Mass Profiles of Clusters of Galaxies: A Comparison of X-ray and Weak Lensing Observations

by

En-Hsin Peng

Submitted to the Department of Physics
in partial fulfillment of the requirements for the degree of

Doctor of Philosophy

at the

MASSACHUSETTS INSTITUTE OF TECHNOLOGY

September 2011

Author .....
Department of Physics
August 31, 2011

Certified by .....
Marshall W. Bautz
Senior Research Scientist
Thesis Supervisor

Certified by .....
Paul L. Schechter
William A. M. Burden Professor of Astrophysics
Thesis Co-Supervisor

Accepted by .....
Krishna Rajagopal
Professor of Physics
Associate Department Head for Education

Mass Profiles of Clusters of Galaxies: A Comparison of X-ray and Weak Lensing Observations

by

En-Hsin Peng

Submitted to the Department of Physics
on August 31, 2011, in partial fulfillment of the
requirements for the degree of
Doctor of Philosophy

Abstract

Clusters of galaxies are useful probes of cosmology because they are the most massive bound systems and fair representatives of the matter composition of the universe. For clusters to be used as tracers of cosmic evolution, one must determine their masses with high accuracy. In this thesis, we provide a detailed comparison of mass estimates from X-rays and weak gravitational lensing for a sample of 32 intermediate low redshift clusters, and study the dependence of the mass profiles derived from these techniques on the dynamical state of the clusters. We analyze *Chandra* X-ray observations and compare the X-ray masses with published weak lensing data (Hoekstra, 2007; Okabe et al., 2010). The temperature, gas density, pressure, gas fraction profiles and their relation to the cluster morphology are also examined. We find that slopes of X-ray pressure and mass profiles vary with cluster morphology. Specifically, clusters with lower third-order power ratios P_3/P_0 (more relaxed) have the steepest profiles while high P_3/P_0 clusters (more disturbed) have the flattest ones. The same trend is not obvious in weak lensing data. Consequently, a correlation between P_3/P_0 and the mass ratio of X-ray to weak lensing estimates M_X/M_{WL}, which in principle indicates the level of non-thermal pressure component in clusters, is found. For the entire sample, we find $M_X/M_{WL} = 1.14 \pm 0.12$ at R_{2500} (at 68% confidence). For apparently unrelaxed, high P_3/P_0 clusters, we find $M_X/M_{WL} = 0.96 \pm 0.12$ at the same radius. For apparently relaxed, low P_3/P_0 clusters, we find $M_X/M_{WL} = 1.32 \pm 0.17$, instead of $M_X/M_{WL} = 1$, expected if these clusters are in hydrostatic equilibrium. This may imply that the gas is hotter than the dark matter in cluster central regions (Rasia et al., 2004).

Thesis Supervisor: Marshall W. Bautz
Title: Senior Research Scientist

Thesis Co-Supervisor: Paul L. Schechter
Title: William A. M. Burden Professor of Astrophysics

Acknowledgments

This work would not have been completed without many individuals. I would like to acknowledge all the help from those important people.

Fisrt and foremost, I would like to thank my advisor, Mark Bautz, for many, many years of support and patient discussions. His guidance is the gravity that keeps things on track. Second, I would like to thank the former member of MIT clusters group Karl Andersson, who was always available for advice and led a fruitful discussion group here at MIT. I am also thankful to other group members: Fred Baganoff, Catherine Grant, and Eric Miller, for their help and answering my questions.

I would also like to express my gratitude to my committee members, Claude Canizares, Paul Schechter, and Saul Rappaport for their invaluable comments on my thesis. I am grateful to my fellow graduate students and postdocs, both former and current, for their friendship, help on general exams, or sharing their expertise and time: Nurit Baytch, Ben Cain, Tamer Elkholy, Li Ji, Dacheng Lin, Jinrong Lin, Ying Liu, Yangsen Yao and many others.

Finally, I would like to thank my friends and family. I thank Yi-wen Huang, Hsin-I Lu, and Chunchun Wu for their wonderful company over the years; my cousin Brook Su for her good humor and always being there for me; my sister Grace and my parents for their unconditional love and support; my parents-in-law for tirelessly taking care of my son Caleb while I was finishing this work; and most of all, my husband Hsin Lin for his considerateness and unwavering support.

Contents

List of Figures

List of Tables

Chapter 1

Introduction

Galaxy clusters are the most massive gravitationally bound structures in the Universe, with masses up to $\sim 10^{15}\mathrm{M}_{\odot}$. They contain tens to hundreds of galaxies, which make up $\sim 3\%$ of the total mass. The intracluster medium (ICM) makes up $10-20\%$ of the mass, while unknown, dark matter (DM) accounts for $80-90\%$ of the total mass. According to the concordance model, structures grow from the gravitational collapse of the primordial density perturbations. Because these perturbations have a larger amplitude on smaller length scales, smallest objects are the first to form and then later built into larger and larger structures. Clusters, the largest virialized systems in the Universe, are therefore the youngest structures. As a result, the theoretical prediction of the cluster density is less complicated by nonlinearities of perturbations or gas dynamics than that of smaller objects, such as galaxies. In addition, the observed abundance of massive halos is exponentially sensitive to the amplitude of density fluctuations σ_8[1], and its evolution highly depends on the matter density of the Universe Ω_M. These features all make clusters powerful probes of cosmological models.

Cluster studies have consistently indicated low values of Ω_M and σ_8 (e.g., Henry & Arnaud, 1991; White et al., 1993; Eke et al., 1998; Borgani et al., 2001; Reiprich & Böhringer, 2002; Schuecker et al., 2003; Vikhlinin et al., 2003; Voevodkin & Vikhlinin, 2004). Including a sufficient number of high-redshift clusters, recent works are able to derive tighter constraints on the dark energy equation of state w (e.g., Vikhlinin et al., 2009b; Mantz et al., 2010b), which is complementary to measurements of the cosmic microwave background (CMB, e.g., Spergel et al., 2003; Komatsu et al., 2011), Type Ia supernovae (SNIa, e.g., Riess et al., 1998; Perlmutter et al., 1999; Hicken et al., 2009; Kessler et al., 2009; Guy et al., 2010), or large scale structures (e.g., Cole et al., 2005; Percival et al., 2010). Figure 1-1 shows the comparison of constraints for w and Ω_M from different methods: the cluster X-ray luminosity function (XLF, Mantz et al., 2010b) with the X-ray luminosity as a mass proxy, cluster gas mass fractions (f_{gas}, Allen et al., 2008), CMB anisotropies from 5-year Wilkinson Microwave Anisotropy Probe data (WMAP5, Dunkley et al., 2009), SNIa (Kowalski et al., 2008), and the large scale clustering of galaxies (Percival et al., 2007) imprinted from the baryonic

[1]See detailed definition in §1.3.1

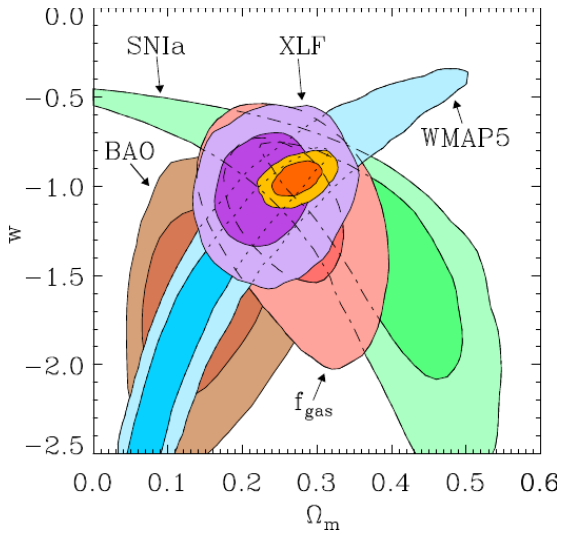

Figure 1-1: Comparison of constraints for the dark energy equation of state w and the matter density Ω_M from cluster XLF (Mantz et al., 2010b), $f_{\rm gas}$ (Allen et al., 2008), WMAP5 (Dunkley et al., 2009), SNIa (Kowalski et al., 2008), and BAO data (Percival et al., 2007). Orange and gold regions show the combined result at 68% and 95% confidence levels, respectively. Reproduced from Mantz et al. (2010b).

acoustic oscillations (BAO) of the primordial plasma (Silk, 1968; Peebles & Yu, 1970). Combining all these data significantly reduces the degeneracy among the parameters, as shown in the gold region of Figure 1-1.

All of the above mentioned cluster cosmological studies rely on accurate mass estimates or reliable mass-observable relations. Calibrating the mass estimate from different observational techniques is essential to estimating systematic errors and is thus necessary for precision cosmology. Our understanding of cluster physics can be greatly improved from this comparison as well. We start with a brief introduction of galaxy clusters in §1.1, describe observational techniques for the mass estimate in §1.2, and explain how cluster data can be used to constrain cosmological parameters in §1.3. This thesis focuses on the detailed comparison of mass estimates from X-rays and weak gravitational lensing, two of the most mature and widely available methods of mass determination. The thesis outline is presented in §1.4.

1.1 Clusters of Galaxies

Galaxy clusters have been known in the optical band for centuries. In the late 1700s, Messier (1784) recognized concentrations of non-cometary fuzzy objects, described by Messier as nebulae without stars, in the constellation Virgo. These objects are now known as galaxies, residing in the Virgo cluster, which is part of the Local Supercluster

containing the Local group, to which our own Milky Way galaxy belongs, along with other hundred galaxy groups and clusters. In the mid 1900s, the first catalog of galaxy clusters in the northern sky was compiled by Abell (1958) from the Palomar sky survey. Later the catalog was expanded to the southern sky with data from the UK Schmidt telescope (Abell et al., 1989), now including 4073 clusters with redshifts z up to $z \sim 0.2$. The Abell catalog, containing most of the known nearby clusters, formed an important foundation for the study of clusters.

In the late 1960s, the X-ray emission was detected from the nearby galaxy M87 in the center of the Virgo cluster (Byram et al., 1966; Bradt et al., 1967), the Perseus cluster (Fritz et al., 1971), and the Coma cluster (Meekins et al., 1971). With the launch of the Uhuru satellite in 1970, the first X-ray satellite devoted entirely to X-ray astronomy (Giacconi et al., 1972), this X-ray emission was revealed to be spatially extended and common in galaxy clusters (Gursky et al., 1972; Kellogg et al., 1972; Forman et al., 1972). In the late 1970s, the detection of the hydrogen- and helium-like iron ion lines at $\sim 7\,\mathrm{keV}$ from nearby clusters (Mitchell et al., 1976; Serlemitsos et al., 1977) confirmed the thermal bremsstrahlung origin of the cluster X-ray emission.

It is now known that intracluster space is permeated by low-density ($\approx 10^{-3}\mathrm{cm}^{-3}$), hot ($10^7 - 10^8$ K) ionized gas, with an X-ray luminosity of $10^{43} - 10^{45}$ erg s^{-1}. The majority of the baryons in the cluster are in this hot plasma, constituting $70 - 90\%$ of the total baryonic mass (e.g., Giodini et al., 2009). The cluster heavy elements like iron are synthesized in stars and ejected into intragalactic space through supernova explosions. The enriched gas in the galaxy may later be stripped during the cluster formation via galaxy mergers and mostly retained in the intracluster space.

In addition to optical and X-ray observations, clusters are detected at radio wavelengths (see Ferrari et al. (2008) for a review). The diffuse radio emission, extending over $\sim 1\,\mathrm{Mpc}$, is not associated with individual member galaxies but with the ICM. The power-law radio spectrum indicates that the emission mechanism is synchrotron, implying the presence of relativistic (Lorentz factor $\gamma \gtrsim 1000$) electrons and magnetic fields of order 1μG in the intracluster space. The extended radio emission, only observed in clusters with complex dynamics (e.g., Cassano et al., 2008; Venturi et al., 2008), could arise from particle acceleration by shocks or turbulence during cluster mergers.

Clusters, as a the multiple component system, thus can be studied in various wavelengths (e.g., Sarazin, 1988). The stars and molecular gas in galaxies emit visible, ultraviolet and infrared light. The hot gas is observed in X-rays. The relativistic particles can be detected in the radio band. Yet the most massive component of clusters, the nonbaryonic dark matter, is invisible in the electromagnetic spectrum. It can be inferred from combining all the above direct observations of cluster baryons with an estimate of the total cluster mass, such as through galaxy velocity dispersion or gravitational lensing (see §1.2).

Zwicky (1933, 1937) was the first to derive cluster masses M from the measured galaxy velocity dispersion, assuming clusters are bound, self-gravitating systems. The system's potential energy and the kinetic energy are related through the virial theo-

rem,

$$\frac{1}{2}\frac{GM^2}{R_G} = \frac{3}{2}M\sigma_r^2, \tag{1.1}$$

where σ_r is the one dimensional galaxy velocity dispersion, G is the gravitational constant, and R_G is the gravitational radius defined as

$$R_G = M^2 \left(\sum_i \sum_{i<j} \frac{m_i m_j}{r_{ij}} \right)^{-1}, \tag{1.2}$$

where r_{ij} is the separation of galaxies i and j, and m_i is the galaxy mass. For a typical rich cluster, $\sigma_r \approx 10^3$km/s and $R_G \approx 1\,$Mpc, one finds $M \approx 10^{15}\mathrm{M}_\odot$ from Eq. 1.1. In §1.2 below we discuss the use of X-ray observations and gravitational lensing to estimate cluster mass; these two techniques provide the foundation for the work described in this thesis.

1.1.1 X-ray emission from clusters

Similar to the above application of the virial theorem by Zwicky (1933), Felten et al. (1966) pointed out that the hot gas in the deep cluster potential can have a temperature as high as $T \sim 10^8\,$K, estimated from

$$\frac{3}{2}\frac{kT}{\mu_g m_p} = \frac{3}{2}\sigma_r^2, \tag{1.3}$$

where k is Boltzmann's constant, μ_g is the mean molecular weight of the gas particle (~ 0.6), and m_p is the proton mass. At such temperatures with the gas density of order 10^{-3} cm^{-3}, the time scale for electrons and ions to reach equilibrium from energy exchange through Coulomb collisions is much shorter than the cooling time of the plasma (e.g., Sarazin, 1988), particles are assumed to have a Maxwell-Boltzmann velocity distribution. With free electrons governed by a Maxwellian distribution at the temperature T, the emissivity, i.e., the emission power per volume and frequency, from electron acceleration in the Coulomb field produced by ions is given by

$$\epsilon_{\nu,\,ff} = \frac{dL}{dV\,d\nu} = \frac{2^5\pi e^6}{3\,m_e\,c^3}\left(\frac{2\pi}{3m_e k\,T}\right)^{1/2} n_e n_i\,Z^2\,g_{ff}(T,Z,\nu)\exp\left(-\frac{h\nu}{k\,T}\right), \tag{1.4}$$

where m_e and n_e are the electron mass and number density, respectively, n_i is the respective ion density, Z is the effective charge of the ion, and g_{ff} is the Gaunt factor, a quantum-mechanically correction to the classically-calculated emissivity. This emission is called thermal bremsstrahlung or free-free emission.

In addition to the predominant thermal bremsstrahlung emission, there are also recombination (bound-free) radiation, two-photon emission (which mostly occurs following a collisional excitation to the metastable $2s$ states of hydrogen- and helium-like ions), and discrete line emission from, e.g., collisional excitation, radiative and dielectronic recombination, resonant excitation, and inner shell collisional ionization.

Three-body (or more) processes are generally ignored because of the low density. Available spectral models calculating line and continuum emissivities for optically thin plasmas in collisional equilibrium include Raymond-Smith (Raymond & Smith, 1977), MEKAL (Mewe et al., 1985, 1986; Kaastra, 1992; Liedahl et al., 1995)[2], APEC (Smith et al., 2001), and CHIANTI (Landi et al., 2006).

The resulting emissivity integrating over all photon frequencies is usually expressed by a cooling function Λ_c,

$$\epsilon = \frac{dL}{dV} = n_e n_p \Lambda_c(T, Z). \tag{1.5}$$

For typical ICM temperatures, $\Lambda_c \sim 10^{-23} \mathrm{erg\,s^{-1}\,cm^3}$. The total luminosity L is thus the integration of Eq. 1.5 over the volume of the emission region, or written as the product of the cooling function and the emission measure EM, defined as

$$EM = \int n_e n_p dV. \tag{1.6}$$

The observed flux S is related to EM and Λ_c through

$$S = \frac{L}{4\pi D_L^2} = \frac{\mathrm{EM}\Lambda_c\,(T, Z)}{4\pi D_L^2}, \tag{1.7}$$

where D_L is the luminosity distance. From the normalization and the shape of the X-ray spectrum, the gas density and temperature can be determined.

1.1.2 The halo mass profile

Simulations of the cold dark matter (CDM) hierarchical halo formation show that the spherically averaged dark matter mass profile can be described by an universal Navarro, Frenk & White (NFW) model (Navarro et al., 1996, 1997):

$$\frac{\rho(r)}{\rho_{\mathrm{crit}}} = \frac{\delta_d}{(r/r_{\mathrm{s}})(1 + r/r_{\mathrm{s}})^2}, \tag{1.8}$$

where δ_d is the dimensionless characteristic density, r_{s} is the scale radius which divides the two distinct regimes of asymptotic mass density slopes $\rho \propto r^{-1}$ and r^{-3}, and ρ_{crit} is the critical density of the universe at the cluster redshift, calculated through

$$\rho_{\mathrm{crit}} = \frac{3H^2(z)}{8\pi G}, \tag{1.9}$$

where $H(z)$ is the Hubble function, evolving in a flat universe as

$$H(z) = H_0 \left[\Omega_M (1+z)^3 + \Omega_R (1+z)^4 + \Omega_\Lambda (1+z)^{3(1+w)}\right]^{1/2}, \tag{1.10}$$

[2]now part of the SPEX package (Kaastra et al., 1996).

where Ω_M, Ω_R, and Ω_Λ are the current matter, radiation, and dark energy density, respectively, $H_0 \equiv 100\,h\mathrm{km\,s^{-1}Mpc^{-1}}$ is the Hubble constant with the Hubble parameter h, and w is the dark energy equation of state. A non-evolving dark energy component (the cosmological constant) corresponds to $w = -1$.

The characteristic density δ_d is related to the concentration parameter c_Δ through

$$\delta_d = \frac{\Delta}{3}\frac{c_\Delta^3}{\ln(1+c_\Delta) - \frac{c_\Delta}{1+c_\Delta}}, \tag{1.11}$$

for any given over density relative to the critical density Δ. The concentration parameter c_Δ, by definition, is the ratio of r_Δ and r_s, where r_Δ is the over-density radius at which the enclosed mean cluster density is Δ times ρ_crit.

Integrating Eq. 1.8, we obtain the mass enclosed in a sphere of radius r,

$$M(r) = M_0 \left[\ln(1 + r/r_\mathrm{s}) + \frac{1}{1 + r/r_\mathrm{s}} - 1\right], \tag{1.12}$$

where $M_0 = 4\pi\rho_\mathrm{crit}\,\delta_d\,r_\mathrm{s}^3$.

1.2 Observational techniques for cluster mass determination

1.2.1 X-ray observations

For optically-thin plasmas as in the ICM, the gas pressure P is written as

$$P = \frac{\rho_g k\,T}{\mu_g m_p}. \tag{1.13}$$

If the ICM is approximately in hydrostatic equilibrium, then the gas pressure gradient is balanced by the gravitational force,

$$\nabla P = -\rho_g \nabla\Phi, \tag{1.14}$$

where Φ is the gravitational potential.

With Poisson's equation which relates Φ with the mass density ρ,

$$\nabla^2\Phi = 4\pi G\rho, \tag{1.15}$$

the total mass density is derived,

$$4\pi G\rho = -\frac{k}{\mu_g m_p}(\nabla^2 T + T\nabla^2 \ln\rho_g + \nabla\ln\rho_g \cdot \nabla T). \tag{1.16}$$

If spherical symmetry is satisfied, integrating ρ over the volume of a sphere of

radius r, we find the total mass enclosed in a sphere of radius r as

$$M = -\frac{k\,T\,r}{G\mu m_p}\left(\frac{d\ln T}{d\ln r} + \frac{d\ln \rho_g}{d\ln r}\right). \tag{1.17}$$

Thus measuring the gas density and temperature profiles provides an estimate of the mass profile.

However, if there is macroscopic gas motion, Eq. 1.14 should include gas motion terms,

$$\nabla P + \nabla\cdot(\rho_g\,\sigma^2) + \rho_g\,(\mathbf{v}\cdot\nabla)\mathbf{v} = -\rho_g\nabla\Phi, \tag{1.18}$$

where $\mathbf{v}$ is the macroscopic gas velocity field and $\rho_g\,\sigma^2$ is the anisotropic gas pressure which changes with random turbulent gas motions, with velocity dispersion tensor σ^2 calculated as

$$\sigma_{ij}^2 = (v_i - \bar{v_i})(v_j - \bar{v_j}). \tag{1.19}$$

Eq. 1.18 is the generalized Euler equation in the static state and equivalent to the Jeans equation.

Evaluating $\nabla\cdot(\rho_g\,\sigma^2)$ in spherical coordinates and applying the divergence theorem, one finds the correction to the total mass from the turbulent motion,

$$\begin{aligned} M_{\rm turb} \;&= -\tfrac{r^2}{G\rho_g}\left(\tfrac{\partial\rho_g\sigma_{rr}^2}{\partial r} + \tfrac{1}{r}\tfrac{\partial\rho_g\sigma_{\theta r}^2}{\partial\theta} + \tfrac{1}{r\sin\theta}\tfrac{\partial\rho_g\sigma_{\phi r}^2}{\partial\phi}\right) \\ &\quad -\tfrac{r}{G}\left(2\sigma_{rr}^2 - \sigma_{\theta\theta}^2 - \sigma_{\phi\phi}^2 + \cot\theta\sigma_{\theta r}^2\right). \end{aligned} \tag{1.20}$$

Other non-random motions from $(\mathbf{v}\cdot\nabla)\mathbf{v}$ produce corrections consisting of $M_{\rm rot}$, the contribution from the rotational motion,

$$M_{\rm rot} = \frac{r(v_\theta^2 + v_\phi^2)}{G}, \tag{1.21}$$

and $M_{\rm stream}$, the contribution from the streaming motion,

$$M_{\rm stream} = -\frac{r}{G}\left(r v_r\frac{\partial v_r}{\partial r} + v_\theta\frac{\partial v_r}{\partial\theta} + \frac{v_\phi}{\sin\theta}\frac{\partial v_r}{\partial\phi}\right). \tag{1.22}$$

Thus the total mass is a sum of four components:

$$M_{\rm tot} = M_{\rm therm} + M_{\rm turb} + M_{\rm rot} + M_{\rm stream}, \tag{1.23}$$

where $M_{\rm therm}$ is from Eq. 1.17. Note we ignore the viscosity and the magnetic field in this derivation. If the gas motion can be directly measured, which requires a sensitive high-resolution X-ray spectrometer, then the accuracy of the X-ray mass estimate should be improved, e.g., as demonstrated in simulation works of Rasia et al. (2004), Fang et al. (2009), and Lau et al. (2009).

1.2.2 Gravitational lensing

The gravitational deflection $\boldsymbol{\alpha}$ of a light ray from a source at the angular position of $\boldsymbol{\beta}$ by a foreground mass concentration can be described by the lens equation (e.g., Bartelmann & Schneider, 2001),

$$\boldsymbol{\alpha}(\boldsymbol{\theta}) = \boldsymbol{\theta} - \boldsymbol{\beta} = \nabla\psi(\boldsymbol{\theta}), \tag{1.24}$$

where $\boldsymbol{\theta}$ is the angular position of a lensed image and ψ is the effective lensing potential, which is related to the dimensionless surface mass density (convergence), $\kappa = \Sigma/\Sigma_{\rm crit}$, through the two-dimensional Poisson equation,

$$\nabla^2\psi(\boldsymbol{\theta}) = 2\kappa(\boldsymbol{\theta}). \tag{1.25}$$

The critical surface mass density $\Sigma_{\rm crit}$ is expressed as

$$\Sigma_{\rm crit} = \frac{c^2}{4\pi G}\frac{D_s}{D_l\, D_{ls}}, \tag{1.26}$$

where D_s, D_l, and D_{ls} are the angular diameter distances of the source, the lens, and between the lens and the source, respectively, and c is the speed of light.

The distortion of the lensed image is governed by the Jacobian matrix $\mathcal{A}$,

$$\mathcal{A}_{ij} = \frac{\partial\boldsymbol{\beta}_i}{\partial\boldsymbol{\theta}_j} = \delta_{ij} - \frac{\partial\boldsymbol{\alpha}_i}{\partial\boldsymbol{\theta}_j} = \delta_{ij} - \frac{\partial^2\psi}{\partial\boldsymbol{\theta}_i\partial\boldsymbol{\theta}_j}, \tag{1.27}$$

which is often written in terms of convergence κ and shear γ,

$$\mathcal{A} = \begin{pmatrix} 1-\kappa-\gamma_1 & -\gamma_2 \\ -\gamma_2 & 1-\kappa+\gamma_1 \end{pmatrix}, \tag{1.28}$$

where $\gamma_1 = (\psi_{,11} - \psi_{,22})/2$ and $\gamma_2 = \psi_{,12}$ are the Cartesian components of the shear, most conveniently treated as a complex number $\gamma = \gamma_1 + i\gamma_2$.

The Jacobian matrix $\mathcal{A}$ has two eigenvalues, $1-\kappa+|\gamma|$ and $1-\kappa-|\gamma|$, which transforms a circular source into an ellipse with an axis ratio of

$$\frac{b}{a} = \frac{1-|g|}{1+|g|}, \tag{1.29}$$

or an ellipticity of

$$\epsilon = \frac{1-b/a}{1+b/a} = |g|, \tag{1.30}$$

where a and b are major and minor axes of the ellipse, respectively, and $g \equiv \gamma/(1-\kappa)$ is the reduced shear. Therefore, the cluster surface mass density Σ can be estimated from the reduced shear of background galaxies. To overcome the intrinsic ellipticities of the galaxies, the shear must be averaged over many background galaxies locally, assuming they are randomly oriented in the field.

1.2.3 Galaxy kinematics

From the Jeans equation for a static spherically symmetric system, the total mass can be estimated from the galaxy velocity dispersion profile (Binney & Tremaine, 1987):

$$M = -\frac{r\sigma_r^2}{G}\left(\frac{d\,\ln n_{\rm gal}}{d\,\ln r} + \frac{d\,\ln \sigma_r^2}{d\,\ln r} + 2\beta\right). \tag{1.31}$$

where $n_{\rm gal}$ is the galaxy number density, σ_r is the radial velocity dispersion, and β is the velocity anisotropy parameter, defined as

$$\beta = 1 - \frac{\sigma_t^2}{\sigma_r^2}, \tag{1.32}$$

where σ_t^2 is the tangential velocity dispersion[3].

To compare with the observations, $n_{\rm gal}$ and σ_r need to be related to the galaxy surface number density $\Sigma_{\rm gal}$ and projected velocity dispersion σ_p,

$$\Sigma_{\rm gal}(R) = 2\int_R^\infty \frac{n_{\rm gal}(r) r dr}{\sqrt{r^2 - R^2}}\ , \tag{1.33}$$

$$\sigma_p^2(R) = \frac{2}{\Sigma_{\rm gal}(R)}\int_R^\infty \frac{n_{\rm gal}(r)\sigma_r^2(r)\left[1 - \beta(r)\frac{R^2}{r^2}\right] r dr}{\sqrt{r^2 - R^2}}\ . \tag{1.34}$$

Since only the line-of-sight velocity dispersion is measured, the velocity anisotropy parameter has either to be assumed, e.g. $\beta = 0$ for isotropic orbits, or modeled, by a functional form with certain free parameters (e.g., Carlberg et al., 1997; Girardi et al., 1998; Lemze et al., 2008b).

1.2.4 The Sunyaev-Zeldovich effect

The cosmic microwave background (CMB) radiation, originated at $z \simeq 1000$ when photons decoupled from matter, can be up-scattered by the hot ICM electrons, resulting a distortion of the CMB spectrum. This phenomenon is predicted by Sunyaev & Zeldovich (1970, 1972), now known as the Sunyaev-Zeldovich (SZ) effect.

The lowest-order temperature change $\Delta T_{\rm SZE}$ for the CMB spectrum is proportional to the Compton parameter y (e.g., Carlstrom et al., 2002),

$$\frac{\Delta T_{\rm SZE}}{T_{\rm CMB}} = f(x)y = f(x)\int n_e \sigma_{\rm T}\frac{k\,T}{m_{\rm e}c^2}dl, \tag{1.35}$$

where $f(x)$ is a frequency dependence of the SZ effect with $x \equiv h\nu/kT_{\rm CMB}$, $\sigma_{\rm T}$ is the Thomson cross-section, $m_{\rm e}$ is the electron mass, n_e is the electron density, $T_{\rm CMB}$ is the CMB temperature, and the integration is along the line-of-sight. Since $\Delta T_{\rm SZE}/T_{\rm CMB}$

[3] $\sigma_t^2 \equiv (\sigma_{\theta\theta}^2 + \sigma_{\phi\phi}^2)/2 = \sigma_{\theta\theta}^2 = \sigma_{\phi\phi}^2$ in spherically symmetric systems, where σ_{ij}^2 is defined in Eq. 1.19.

is independent of the redshift (Eq. 1.35), the SZ survey could be a powerful method to detect high redshift clusters.

The SZ data probe the gas pressure directly, which can be used to estimate the cluster potential if combined with the gas temperature or density from the X-ray data, or through the calibrated $Y_{\rm SZ} - M$ relation, where $Y_{\rm SZ}$ is the y parameter integrated over the whole cluster.

1.3 Cosmology with clusters

1.3.1 Cluster mass function

The cluster mass function, $n_M(M, z)$, which gives the comoving number density of clusters with masses greater than M at redshift z, is sensitive to cosmological parameters. The theoretical framework of the mass function was first developed by Press & Schechter (1974), later extened and refined by Bond et al. (1991), Bower (1991), and Lacey & Cole (1993). The Press-Schechter model predicts a mass function from a linear density field, which applies to structures that have grown to the nonlinear regime. The differential form of the mass function is written as

$$\frac{d\, n_M}{d\, \ln \sigma^{-1}} = \sqrt{\frac{2}{\pi}} \frac{\Omega_M \rho_{\rm crit}}{M} \frac{\delta_c}{\sigma} \exp\left(-\frac{\delta_c^2}{2\sigma^2}\right), \tag{1.36}$$

where δ_c is a threshold for overdense regions to collapse when the density constrast $\delta\rho/\rho$ exceeds this value, and σ is the amplitude of the linear perturbation of the density field on mass scale M,

$$\sigma^2(M, z) \equiv \langle \left(\frac{\delta M}{M}\right)^2 \rangle = \frac{D^2(z)}{(2\pi)^3} \int P(k)\, W^2(k, M)\, d^3k, \tag{1.37}$$

where $P(k)$ is the power spectrum of the density field, $D(z)$ is the growth rate of the density perturbation, and $W(k, M)$ is the Fourier transform of a spherical top-hat window function which is one within radius $r_M = (3M/4\pi\Omega_M\rho_{\rm crit})^{1/3}$ and zero outside. Parameter $\sigma_8 = \sigma(M_8, 0)$ is thus the normalization of $P(k)$ with $r_M = 8h^{-1}$Mpc at $z = 0$.

Figure 1-2 demonstrates the sensitivity of the cluster mass function to the cosmological model. For example, a model with the dark energy density $\Omega_\Lambda = 0$ (*right*) is clearly inconsistent with the data (Vikhlinin et al., 2009b) and over-predicts the abundance of distant massive clusters.

1.3.2 Baryon fraction

Massive clusters contain almost all the matter that was originally extended over ~ 10 Mpc of volume; on this large scale the total matter census should be representative of the universe as a whole. Since most of the cluster baryon is in the form of hot plasmas, measuring the gas mass fraction $f_{\rm gas}$ gives a lower limit on the baryon fraction

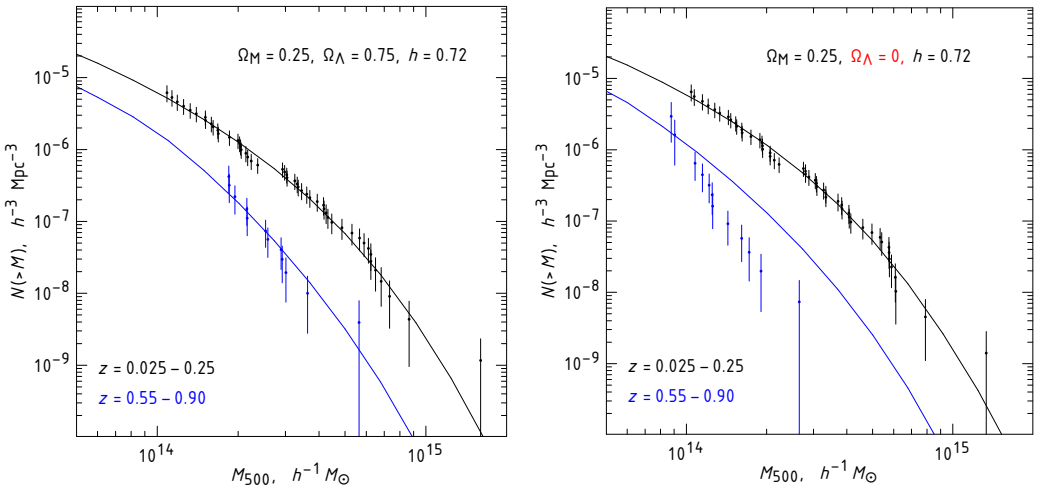

Figure 1-2: The measured cluster mass function (points) in comparison with different cosmological models (curves): a flat ΛCDM model (*left*) and an open OCDM model without the dark energy (*right*). Reproduced from Vikhlinin et al. (2009b).

Ω_b/Ω_M. With a prior on the baryon density Ω_b from $\Omega_b h^2$ (e.g., Burles et al., 2001; Kirkman et al., 2003) and h (e.g., Freedman et al., 2001; Riess et al., 2009), Ω_M can be estimated from $f_{\rm gas}$.

The estimated value of $f_{\rm gas}$ varies with the assumed angular diameter distance D_A as $f_{\rm gas}(z) \propto D_A(z)^{3/2}$, so if $f_{\rm gas}$ does not evolve much with the redshift, as predicted by simulations (e.g., Eke et al., 1998; Crain et al., 2007), clusters can serve as standard candles for distance measurements, just like Type Ia supernovae. Figure 1-3 shows how the measured $f_{\rm gas}$ evolution changes with the assumed cosmology. Under the generally accepted ΛCDM cosmology (*left*), $f_{\rm gas}$ is indeed non-evolving as expected. Assuming $f_{\rm gas}$ does not evolve with the redshift[4], studies on the cluster baryon fraction (Allen et al., 2008; Ettori et al., 2009) have yielded cosmological constraints comparable to those from the mass function (Vikhlinin et al., 2009b; Mantz et al., 2010b). See e.g. Allen et al. (2011) for the comparison.

1.4 Outline of the thesis

Chapter 2 presents an X-ray analysis of A1689. Spectral information is carefully studied in order to explore the long standing discrepancy of X-ray and lensing mass measurements. Chapter 3 presents a detailed comparison of X-ray and weak lensing masses for a sample of 32 intermediate low redshift clusters. The temperature, gas density, pressure, gas fraction profiles and their relation to the cluster morphology are also examined. Chapter 4 gives the result of a novel Smoothed Particle Inference (SPI, Peterson et al., 2007) modeling of X-ray data for the above sample. This technique employs a very flexible modeling for 2-dimensional imaging and spectral

[4]or only weakly evolves, see Allen et al. (2008).

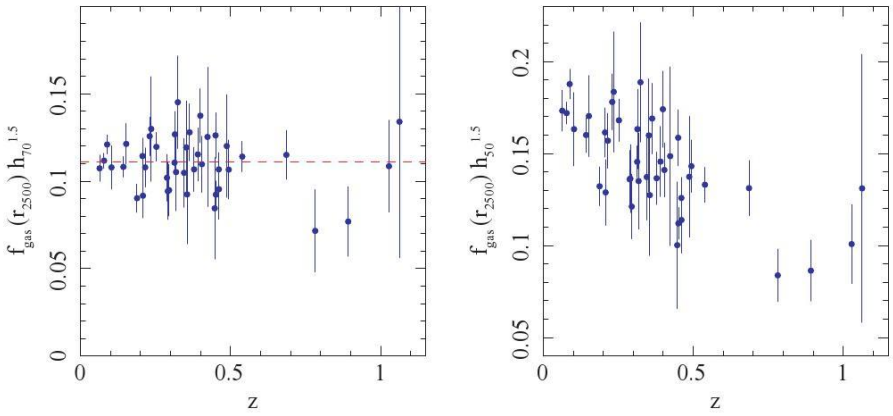

Figure 1-3: The X-ray gas mass fraction measured within R_{2500} as a function of the redshift under ΛCDM (*left*) and SCDM (*right*, $\Omega_M = 1.0$, $\Omega_\Lambda = 0$, $h = 0.5$) cosmologies. Reproduced from Allen et al. (2008).

data and is well suited for clusters with complex structures. The morphological measures used in Chapter 3 are derived from SPI X-ray luminosity maps. Because of various parameter degeneracies, the interpretation of SPI temperature maps is quite challenging. Therefore, we only use data deduced from SPI luminosity maps for analyses in Chapter 3. Finally, conclusions are summarized in Chapter 5.

Chapter 2

X-ray Analysis of Abell 1689

This chapter is an excerpt from "Discrepant Mass Estimates in the Cluster of Galaxies Abell 1689," by Peng, E.-H., Andersson, K., Bautz, M. W., & Garmire, G. P. 2009, ApJ, **701**, 1283.

2.1 Introduction

Abell 1689 is a massive galaxy cluster with the largest known Einstein radius to date, $\theta_E = 45''$ for $z_s = 1$ (e.g., Tyson et al., 1990; Miralda-Escude & Babul, 1995; Broadhurst et al., 2005a,b), located at a moderately low redshift of $z = 0.187$ (Frye et al., 2007). It has a regular X-ray morphology, indicating that the cluster is likely in hydrostatic equilibrium, but the mass derived from the X-ray measurement is often a factor of 2 or more lower than that from gravitational lensing at most radii. Using *XMM-Newton* observations, Andersson & Madejski (2004, A04 hereafter) find an asymmetric temperature distribution and a high redshift structure in A1689, providing evidence for an ongoing merger in this cluster.

A recent joint *Chandra*, HST/ACS, and Subaru/Suprime cam analysis by Lemze et al. (2008a, L08 hereafter) suggested that the temperature of A1689 could be as high as $T = 18$ keV at 100 h^{-1}kpc, almost twice as large as the observed value at that radius. The derived 3D temperature profile was based on the X-ray surface brightness, the lensing shear, and the assumption of hydrostatic equilibrium. From the disagreement between the observed X-ray temperature and the deduced one, L08 concluded that denser, colder, and more luminous small-scale structures could bias the X-ray temperature.

In another study of 192 clusters of galaxies from the *Chandra* archive, Cavagnolo et al. (2008b) find a very high hard-band ($2/(1+z)$-7 keV) to broad-band (0.7-7 keV) temperature ratio for A1689, $1.36^{+0.14}_{-0.12}$ compared to 1.16 ± 0.10 for the whole sample. They also find that merging clusters tend to have a higher temperature ratio, as predicted by Mathiesen & Evrard (2001) where this high ratio is attributed to accreting cool subclusters lowering the broad-band temperature by contributing large amounts of line emission in the soft band. The hard-band temperature, however, should be unaltered by this emission. The simulations of Mathiesen & Evrard (2001)

show an increase of temperature ratios of $\sim 20\%$ in general, which is close to the average of the sample of Cavagnolo et al. (2008b), 16%.

A recent study, using the latest *Chandra* data (Riemer-Sørensen et al., 2009) claim that the cluster harbors a cool core and thus is relaxed based on a hardness-ratio map analysis. They further calculate a mass profile from the X-ray data and conclude that the X-ray and lensing measurements are in good agreement when the substructure to the NE is excluded.

In this work, we examine the possibility of an extra spectral component in the X-ray data and derive an improved gravitational mass profile, including a recent 150 ks *Chandra* observation. §2.2 describes the details of data reduction and examines the possibility of an uncorrected absorption edge in the data. In §2.3, we explore the physical properties of the potential cool substructures under a two-temperature (2T) model and examine if they can be used to explain the high hard-band to broad-band temperature ratio. In §2.4, assuming that the temperature profile derived by L08 is real, we investigate what this implies for the required additional cool component. In §2.5, we derive the mass profile under both one and two temperature-phase assumptions, using both parametric and non-parametric methods. Finally, we discuss our results in §2.6 and summarize in §2.7.

Throughout this paper, we assume $H_0 = 100\,h$ km s^{-1} Mpc^{-1}, $\Omega_m = 0.3$, and $\Omega_\lambda = 0.7$, which gives $1'' = 2.19\ h^{-1}$kpc at the cluster redshift of 0.187. Abundances are relative to the photospheric solar abundances of Anders & Grevesse (1989). All errors are 1 σ unless otherwise stated.

2.2 Data Reduction

Chandra The data were processed through CIAO 4.0.1 with CALDB 3.4.3. Since all of the observations had gone through Repro III in the archive, reprocessing data was not needed. Updated charge-transfer inefficiency and time-dependent gain corrections had already been applied. For data taken in VFAINT telemetry mode, additional screening to reject particle background was used. Events with bad CCD columns and bad grades were removed. Lightcurves were extracted from four I-chips with cluster core and point sources masked in the 0.3-12 keV band and filtered by *lc_clean* which used 3 σ clipping and a cut at 20% above the mean. Finally, *make_readout_bg* were used to generated Out-of-Time event file. These events were multiplied by 1.3% and subtracted from the images or the spectra to correct read-out artifacts. For spectral anlysis, emission-weighted response matrices and effective area files were constructed for each spectral region by *mkacisrmf* and *mkwarf*.

Blank-field data sets were used to estimate the background level. After reprojecting the blank-sky data sets onto the cluster's sky position, the background was scaled by the count rate ratio between the data and the blank-field background in the 9.5-12 keV band to account for the variation of particle induced background. Below 1 keV, the spatial varying galactic ISM emission (Markevitch et al., 2003) could cause a mismatch between the real background and the blank-field data. By analysing the spectra in the same field but sufficiently far from the cluster, tailoring this soft

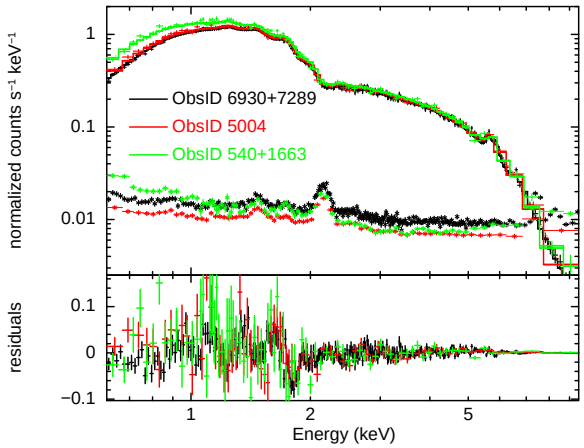

Figure 2-1: The 0.6-9.5 keV *Chandra* spectrum of A1689 from the central 3′ region. The upper panel shows the data, plotted against an absorbed VAPEC model (solid line) with each element's abundance and absorption column density as free parameters. The lower panel shows residuals.

component can be made using an unabsorbed $T \sim 0.2$ keV, solar abundance thermal model (Vikhlinin et al., 2005).

The current available blank-sky data were created from observations before 2005. As the solar cycle gradually reaches its minimum, the particle induced background increases. Therefore, newer observations need a much higher background normalization with a factor of 1.2-1.3. This leads an overestimate of the background in the soft band because other components like cosmic X-ray background (CXB) does not change as the particle induced background does. To correct the over-subtracted CXB and halo emission, an absorbed power law with photon index fixed at 1.4 (De Luca & Molendi, 2004) plus an unabsorbed thermal model was used to fit the blank-field background subtracted spectrum taken at $r > 13'$.

XMM-Newton The data from two MOS detectors were processed with the XMM-SAS 6.1.0 tool, *emchain*. Background flares were removed by a double-filtering method (Nevalainen et al., 2005) from $E > 10$ keV and 1-5 keV light curves. Only events with pixel PATTERNs 0-12 were selected. Since *XMM-Newton* data were only used to crosscheck the result of the multi-component analysis of *Chandra* spectra, extracted from the central region where background modeling is relatively unimportant, we used the simpler local background, taken from 6′-8′. Spectral response files were created by *rmfgen* and *arfgen*. We did not include PN data because the measured mean redshift, 0.169 ± 0.001, was not consistent with those from *XMM-Newton* MOS or *Chandra* data. This could indicate a possible gain offset for PN detector, although A04 did not find any evidence for that.

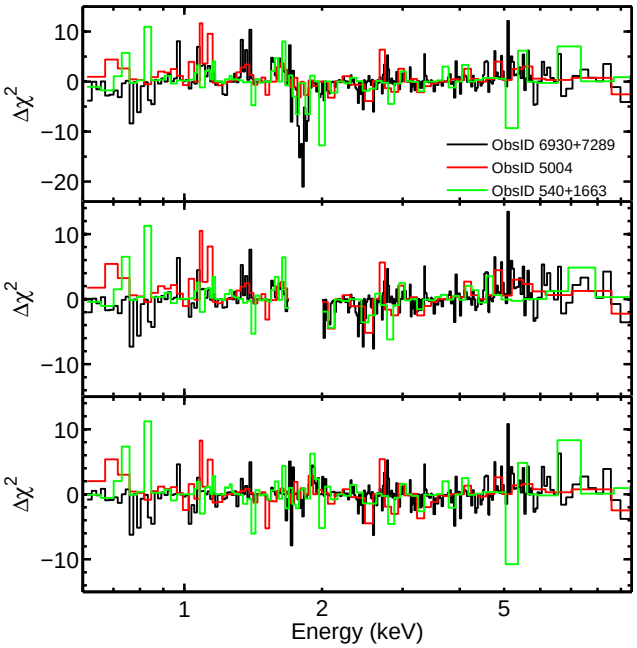

Figure 2-2: Fit residuals, showing each channel's contribution to the total χ^2. *Top*: an absorbed VAPEC model fit to central 3′ spectrum. *Middle*: same as the above, ignoring data in 1.7-2 keV. *Bottom*: adding an absorption edge with E_{thresh} =1.77 keV and τ=0.12.

Chandra Systematic Uncertainties L08 pointed out some issues about previous *Chandra* observations (ObsID 540, 1663, and 5004). The column density from *Chandra* data is much lower than the Galactic value, 1.8×10^{20} cm^{-2} (Dickey & Lockman, 1990), which is also supported by the ROSAT data (Andersson & Madejski, 2004). The temperature difference can be as high as 1.3 keV depending on the choice of column density. In the high energy band, the data is systematically higher than the model prediction. With two long *Chandra* observations, ObsID 6930 and 7289, we clearly see an unusual feature in the datasets which may give clues to problems mentioned before. Figure 2-1 shows an absorbed APEC model (Smith et al., 2001) fit to the central 3′ spectrum. The prominent residual at $\sim$ 1.75 keV is present in all of our observations and appeared as the biggest contributor to the total χ^2 (See Figure 2-2). This residual can not be eliminated by adjusting individual abundances in the cluster or in the absorbing column (the cluster is at high galactic latitude). Because the residual around 1.75 keV is an order of magnitude larger than the background, it is not likely related to the background subtraction. In addition to this absorption, the residuals are systematically rising with the energy from negative to positive values. This trend is not changed when fitting the spectrum with data between 1.7-2.0 keV excluded (Figure 2-2). We found that multiplying a XSPEC Edge model can correct the residual at $\sim$ 1.75 keV, remove steadily rising residuals with the energy, and make the column density agree with the Galactic value.

2.3 Spectral Analysis

2.3.1 Two temperature model

To get some clues to the nature of the claimed cool substructures in A1689, a simple two temperature model was fit to the spectrum extracted from the $r < 3'$ (395 h^{-1}kpc) region where the quality of the data was high enough to test it. We used two absorbed VAPEC models, with variable normalization but linked metallicities between the two phases. The column density was fixed at the Galactic value. To reduce the uncertainty on measuring metallicities, we tied the abundances of α-elements (O, Ne, Mg, Si, S, Ar, and Ca) together and fixed the remaining abundances at the solar value, except for Fe and Ni. Since the hotter phase temperature, $T_{\rm hot}$, was harder to constrain, it was frozen at a certain value above the best-fit single temperature fit, $T_{\rm 1T}$. We changed this increment from 0.5 to 50 keV to explore the whole parameter space.

Figure 2-3 shows the temperature of the cooler gas, $T_{\rm cool}$, and the fractional contribution of the cooler gas, $\rm EM_{cool}/EM_{total}$, as a function of $T_{\rm hot}$. As $T_{\rm hot}$ increases, $T_{\rm cool}$ and $\rm EM_{cool}/EM_{total}$increase as well. $T_{\rm cool}$ eventually becomes $T_{\rm 1T}$ once $T_{\rm hot}$ is greater than 20 keV and very little gas is left in the hot phase, which is also supported by the *XMM-Newton* data. For $T_{\rm hot} \approx 18$ keV, there has to be 30%, 60% of the cool gas at the temperature of 5, 8 keV inferred from *Chandra* and *XMM-Newton* data, respectively. *Chandra* absorption corrected data show similar results as *XMM-Newton* data do at this temperature. Although there is some inconsistency between *Chandra* and *XMM-Newton* data, both indicate that the cool component, if it indeed exists, is not cool at all. $T = 5$ keV is the typical temperature of a medium sized cluster with a mass of $M_{500} = 2.9 \times 10^{14} h^{-1} \rm M_{\odot}$(Vikhlinin et al., 2006).

To quantify how significant the detection of this extra component was, we conducted an F-test from the fits of 1T (the null model) and 2T models. However, because the 2T model reduces to 1T when the normalization of one of the two components hits the parameter space boundary (ie, zero), the assumption of F-test is not satisfied (see Protassov et al., 2002). Therefore, we simulated 1000 1T *Chandra* spectra and performed the same procedure to derive the F-test probability, P_F, based on the F distribution. Figure 2-3 shows the distribution of P_F from simulated data at the 68, 90, 95, and 99 percentile overplotted with P_F from *Chandra* and *XMM-Newton* data. We plot P_F in Figure 2-3 rather than the F statistic, since P_F is a scaler that does not depend on the degrees of freedom of the fits and is ideal to compare observations that have different data bins. For $T_{\rm hot} < 20$ keV, both the edge-corrected *Chandra* data and the *XMM-Newton* data are within the 95 percentile of the simulated 1T model and we conclude that a 2T model is possible but not necessary to describe the data.

2.3.2 Hard-band, broad-band temperature

In addition to multiple-component modeling, measuring the temperature in different band-pass is another way to demonstrate the presence of multiple components. Cavagnolo et al. (2008b) reported a very high hard-band to broad-band temperature

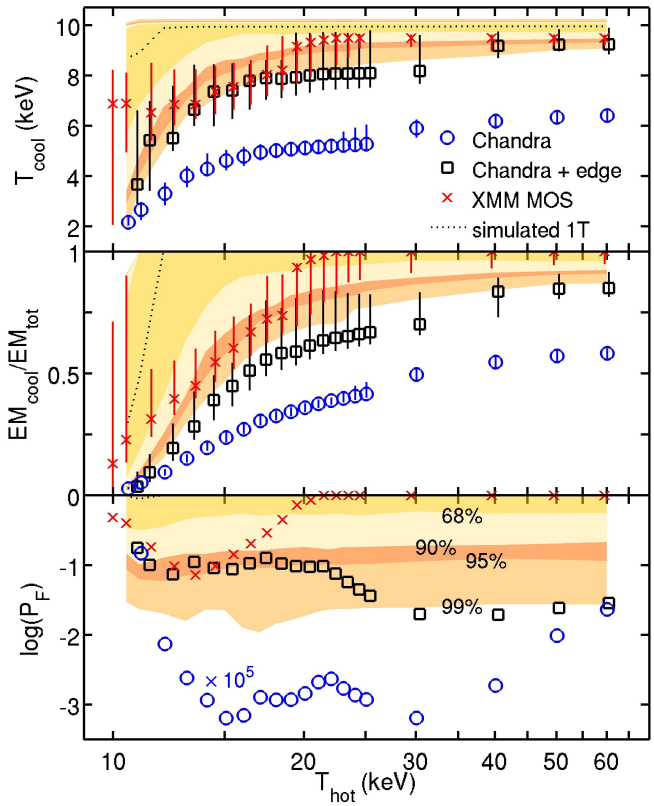

Figure 2-3: The temperature of the cooler gas $T_{\rm cool}$, the emission measure ratio $\rm EM_{cool}/EM_{total}$, and the F-test probability P_F are plotted as a function of $T_{\rm hot}$. The shaded region represents 68%, 90%, 95%, and 99% CL from 1000 simulated $T = 10.1$ keV *Chandra* spectra. The P_F from *Chandra* data without the absorption edge corrected (circles) is multiplied by 10^5.

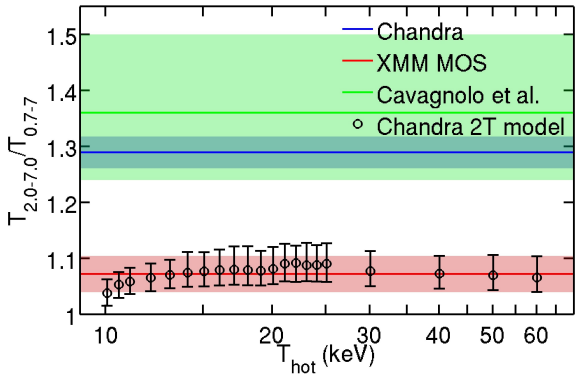

Figure 2-4: The hard-band to broad-band temperature ratio $T_{2.0-7.0}/T_{0.7-7.0}$ of simulated *Chandra* 2T spectra (circles) plotted against $T_{\rm hot}$. The shaded regions show the observed temperature ratios from *Chandra* and *XMM-Newton* MOS data. Also shown is the temperature ratio from 40 ks *Chandra* data by Cavagnolo et al. (2008b).

ratio for A1689, $1.36^{+0.14}_{-0.12}$, from analysis of 40 ks of *Chandra* data, suggesting that this could relate to ongoing or recent mergers. Following the convention in Cavagnolo et al. (2008b), we fit the spectrum in the 0.7-7.0 keV (broad) and 2.0/(1+z)-7.0 keV (hard) band with a single-temperature model. In contrast to C08, we do not use the $r < R_{2500}$ region with the core excised, but simply take the spectrum from the whole central 3′ (395 h^{-1}kpc) region. The hard-band to broad-band temperature ratio from *Chandra* data, 1.29 ± 0.03, strongly disagrees with that of *XMM-Newton* MOS, 1.07 ± 0.03. This result is anticipated since an absorption edge feature found in the *Chandra* spectrum (Figure 2-1) is close to the cut-off of the hard band. After correcting for this absorption, the temperature ratio is in the range of 1 to 1.08 for an absorption depth of $\tau = 0.14 - 0.10$. As a consistency check, we simulated spectra according to the best-fit 2T models (from *Chandra* data) from §2.3.1 to see whether these models can explain such a high temperature ratio. Results are plotted in Figure 2-4. None of the 2T models can reproduce the observed ratio of the uncorrected *Chandra* data. Thus we conclude that there is no evidence from this ratio of the presence of multiple components or merging activity. Furthermore, Leccardi & Molendi (2008) do not find any discrepancy between the hard band (2-10 keV) and broad band (0.7-10 keV) temperature profiles, except for $r < 0.05\ r_{180}$, for a sample of ~ 50 hot, intermediate redshift clusters based on *XMM-Newton* observations. The high hard-band to broad-band temperature ratio seen in A1689, as well as in many other clusters observed with *Chandra* (Cavagnolo et al., 2008b), might be due to the aforementioned calibration uncertainty.

2.3.3 Emission line diagnostics

When fitting the whole spectrum, the temperature is mainly determined by the continuum due to the low amount of line emission at the temperature of A1689. In order

Table 2.1: Emission lines in X-ray spectra

Line	Energy (keV)	Centroid [a] (keV)	Width [a] (eV)
Fe XXV Kα	6.636, 6.668, 6.682, 6.700	6.686	23
Fe XXV Kβ	7.881	7.877	19
Fe 8.3 keV [b]	8.246, 8.252, 8.293, 8.486	8.282	68
Fe XXVI Kα	6.952, 6.973	6.964	14
Fe 8.7 keV [c]	8.698, 8.701, 8.907, 8.909	8.764	97
Ni XXVII Kα	7.765, 7.805	7.793	19
Ni XXVIII Kα	8.074, 8.101	8.090	16

[a]Emissivity-weighted center and one standard deviation. The line emissivity is calculated at $T = 10$ keV from *Chandra* ATOMDB 1.3.1.

[b]including Fe XXVI Kβ, XXV Kγ, and XXV Kδ.

[c]including Fe XXVI Kδ and XXVI Kγ.

to extract the emission line information, which can provide an additional temperature diagnostic, we fit the 4.5-9.5 keV spectrum with an absorbed thermal bremsstrahlung model plus Gaussians. There are 42 lines whose emissivity is greater than 10^{-19} photons cm^{-3}s^{-1} at $kT = 10$ keV from ions of Fe XXV, Fe XXVI, Ni XXVII, Ni XXVIII, according to *Chandra* ATOMDB 1.3.1. Considering the CCD energy resolution, we grouped those lines into seven Gaussians and used the emissivity-weighted centroid and one standard deviation as the line center and width, respectively. The Ni XXVII Kα line is $\sim$ 80 eV away from the Fe XXV Kβ line, not separable under CCD resolution unless we have extremely good data quality. Since we obtained an unusually high Ni/Fe ratio of ~ 9 Ni$_\odot$/Fe$_\odot$ from a VAPEC model fit to the whole spectrum, it is worth investigating this in detail. We therefore modeled Ni XXVII Kα and Fe XXV Kβ lines individually. The model is listed in Table 2.1.

Strictly speaking, using fixed values of line centroids and widths is not correct because those quantities change with temperature. In addition, we approximated the line complex as a Gaussian whose line centroid and width calculated from the model may not be the same after being convolved with the instrument response. To properly compare our fit results with the theory, we simulated spectra and fit them the same way we fit the real data. Figure 2-5 shows the observed line ratios and results from simulated VAPEC spectra with 9 Ni$_\odot$/Fe$_\odot$. 100 spectra were produced at each temperature and the flux was kept at the same level as that of the data. From the good match of fitted results from simulations to the direct model prediction, we confirmed that the fitting is accurate enough to measure the line flux, though only Fe XXV Kα and Fe XXVI Kα lines are precise enough for temperature determination. Table 2.2

Table 2.2: Summary of the emission line analysis

		Chandra	*XMM-Newton* MOS
Continuum			
T	(keV)	$10.3^{+2.2}_{-0.8}$	$9.7^{+0.8}_{-1.1}$
Emission lines			
T [a]	(keV)	$9.6^{+0.5}_{-0.5}$	$10.1^{+0.7}_{-0.7}$
Ni/Fe [b†]	($Ni_\odot/Fe_\odot$)	$8.4^{+3.7}_{-3.6}$	$1.4^{+1.8}_{-1.4}$
Ni/Fe [c†]	($Ni_\odot/Fe_\odot$)	$5.5^{+3.2}_{-3.1}$	$3.7^{+1.6}_{-2.1}$
Fe [d†]	($Z_\odot$)	0.31 ± 0.02	0.32 ± 0.03
Ni [e†]	($Z_\odot$)	$1.23^{+0.50}_{-0.91}$	$1.08^{+0.52}_{-0.65}$

[a]from Fe XXVI Kα/Fe XXV Kα.

[b]from (Ni XXVII Kα+Fe XXV Kβ)/Fe XXVI Kα.

[c]from Ni XXVII Kα/Fe XXVI Kα.

[d]from (Fe XXVI Kα+XXV Kα)/continuum.

[e]from Ni XXVII Kα/continuum.

[†]assuming $T = 10$ keV.

shows the temperature and abundances, inferred from a single-temperature APEC model. The iron line temperature is in very good agreement with the continuum temperature for both *Chandra* and *XMM-Newton* data. All the *Chandra* and *XMM-Newton* observed line fluxes, except Fe XXV Kβ, are consistent with each other (after an overall 9% adjustment to the flux). Using Fe XXV+XXVI Kα and Ni XXVII Kα line flux, we obtain accordant Fe and Ni abundances from both instruments.

As discussed previously, the 2T analysis of *Chandra* data suggested that another spectral component is needed if no absorption edge modeling is applied. Figure 2-6 shows the line ratios predicted by the best-fit models from §2.3.1 over a wide range in temperature for the hot phase. Since the spectral energy range used in this fitting is far enough from the Si edge, it is not necessary to modify the spectral model even if the Si edge indeed needs to be corrected. The broad-band *Chandra* spectrum is not sensitive to the hot phase temperature of the 2T model once it exceeds 15 keV (Figure 2-3). With the good constraint from the Fe XXVI Kα/Fe XXV Kα line ratio, models with $T_{\rm hot} > 20$ keV, which are composed of great amounts of cooler gas, are rejected. Meanwhile, the ratio of higher energy states (Ni XXVIII Kα, Fe XXVI Kβ, Fe XXV Kγ, Kδ) to the well-measured Fe XXVI Kα line suggests that models with lower $T_{\rm hot}$ are preferable.

As for the 2T models based on *Chandra* with an absorption edge model and

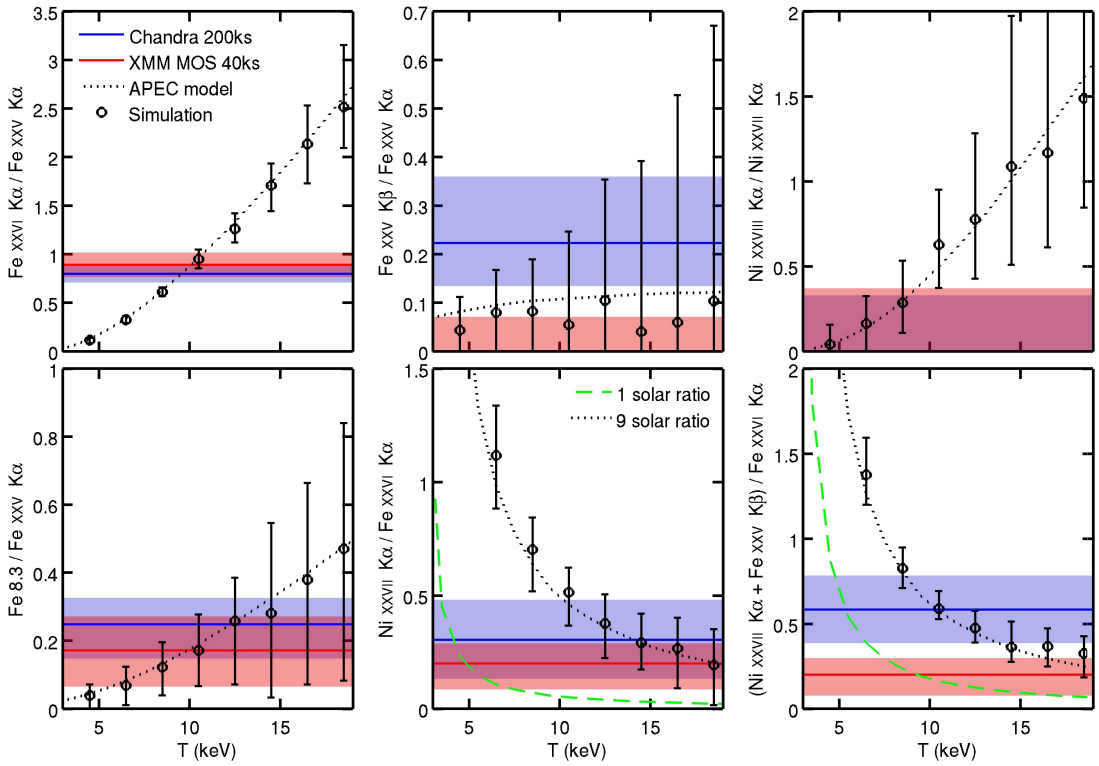

Figure 2-5: The predicted 1T plasma line ratio (dotted line) as a function of temperature, for various lines. The observed ratio and its 1σ confidence are shown as a solid line and shaded region. The circles show the fitted results of 100 simulated *Chandra* spectra drawn from a VAPEC model with 9 $\mathrm{Ni}_{\odot}/\mathrm{Fe}_{\odot}$.

XMM-Newton broad-band spectra, predicted line ratios all agree with the observed value. In fact, models with $T_{\rm hot} > 20$ keV from *XMM-Newton* data are essentially a one temperature model, since the normalization of the hot component in these models is zero. Adding the fact that an additional temperature component does not significantly improve the χ^2 of the fit for those spectra and the remarkably good agreement on the temperature measured by the continuum and the iron lines from both *Chandra* and *XMM-Newton*, we conclude that the simple 1T model is adequate to describe the X-ray emission from the central $3'$ region of A1689.

2.4 Deprojection Analysis

Assuming that the hotter phase gas has the 3D temperature profile of L08, the radial distribution of the cooler gas can be derived. We extracted spectra from concentric annuli up to $8.8'$ (1.2 h^{-1}Mpc). The emission from each shell in three-dimensional space was modeled with an absorbed two-temperature APEC model with $T_{\rm hot}$ fixed at the value of L08 and then projected by the PROJCT model in XSPEC. Because of the complexity of this model, we used coarser annular bins than those used in L08.

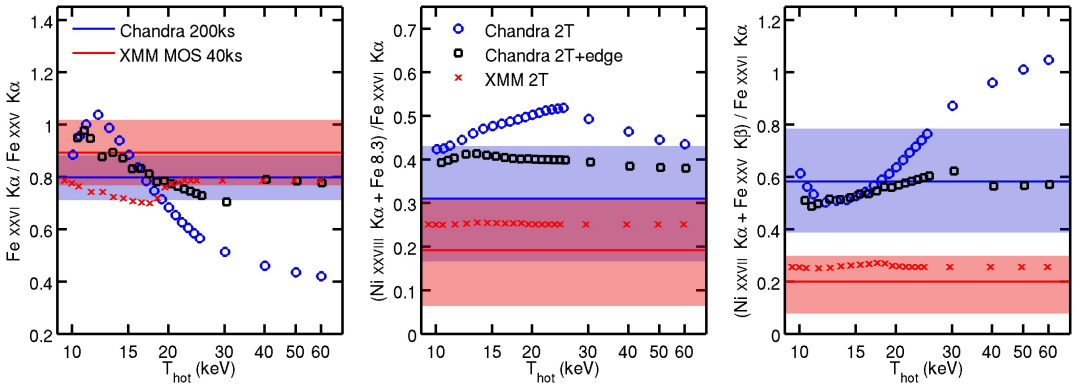

Figure 2-6: The predicted line ratio from the best-fit 2T (VAPEC) models (§2.3.1) as a function of the temperature of the hotter phase $T_{\rm hot}$. The solid line and shaded region shows the observed ratio and its 1σ error. The x-axis is in log scale.

Data of L08 were binned using the weighting scheme of Mazzotta et al. (2004) to produce a spectroscopic-like temperature. $T_{\rm cool}$, abundance, and the normalization of both components were free to vary. The outermost two annuli were background dominated, so spectra were binned to have at least 15 net counts per bin at $r = 4.8'-6.5'$ (625−852 h^{-1}kpc) and 2 net counts at $r = 6.5'-8.8'$ (852−1161 h^{-1}kpc) (see §**??**). L08 predicted the gas temperature only up to 721 h^{-1}kpc, and that temperature was slightly below the observed one. Therefore, we allowed $T_{\rm hot}$ to change in the last two bins. The cold component was removed and the abundance was fixed at 0.2 solar in these regions in order to constrain the rest of the parameters better.

Assuming two phases in pressure equilibrium, the volume filling fraction of the ith component can be obtained from

$$f_i = \frac{{\rm Norm}_i T_i^2}{\sum_j {\rm Norm}_j T_j^2} \tag{2.1}$$

(e.g., Sanders & Fabian, 2002). Once f_i is determined, the gas density $\rho_{gi} = \mu_e m_p n_{ei}$ can be derived from

$${\rm Norm}_i = \frac{10^{-14}}{4\pi((1+z)D_A)^2} \int n_{ei} n_{Hi} f_i dV, \tag{2.2}$$

where n_H/n_e and μ_e are calculated from a fully ionized plasma with the measured abundance (He abundance is primordial, and others are from Anders & Grevesse, 1989). For $Z = 0.3\ Z_\odot$, $n_H/n_e = 0.852$ and $\mu_e = 1.146$. Figure 2-7 shows the results of this deprojected 2T analysis. The 1T modeling, in which emission from each shell has only one component, and the results from L08, are also shown. If the cluster has a temperature profile of L08, then 70−90% of the space within 250 h^{-1}kpc is occupied by the "cool" component with a temperature of ~ 10 keV, based on *Chandra* absorption edge corrected data, and this gas constitutes 90% of the total gas mass.

Kawahara et al. (2007) show that local density and temperature inhomogeneities do not correlate with each other in simulated clusters, which undermines the assumption of two phases in thermal pressure equilibrium. However, other cosmological simulations find that gas motions contribute about 5-20% of the total pressure support (e.g., Faltenbacher et al., 2005; Rasia et al., 2006; Lau et al., 2009). If the pressure balance is off by 20%, it will not significantly change the gas mass fraction ($\lesssim 4\%$) or the volume filling fraction ($\lesssim 8\%$).

2.5 Mass Profile

Given the 3D gas density and temperature profiles, the total cluster mass within a radius r can be estimated from the hydrostatic equilibrium equation (Eq. 1.17). If the gas has two temperatures with two phases in pressure equilibrium, the total mass still can be derived from Eq. 1.17 with ρ_g and T replaced by $\rho_{g_{\rm hot}}$ and $T_{\rm hot}$, respectively.

2.5.1 Nonparametric Method

To evaluate the derivatives in Eq. 1.17, we took the differences of deprojected temperature and the gas density in log space. The radius of each annulus was assigned at $\bar{r}$ such that

$$F_{3D}(\bar{r})\,\frac{4\pi}{3}\left(r_{out}^3 - r_{in}^3\right) = \int_{r_{in}}^{r_{out}} F_{3D}(r)\,4\pi r^2 dr, \tag{2.3}$$

where F_{3D} is the deprojected flux density from a finely binned surface brightness profile, and r_{in} (r_{out}) is the inner (outer) radius of the annulus. The radius r outside of the brackets of Eq. 1.17 is taken at the geometric mean (i.e. the arithmetic mean in log scale) of the radii of two adjacent rings, $r = \sqrt{\bar{r}_i\,\bar{r}_{i+1}}$, and the temperature is linearly interpolated at this radius. Because errors from e.g. T and dT/dr are not independent, standard error propagation is not easily applied. Uncertainties are estimated from the distribution of 1000 Monte-Carlo simulations of T and ρ_g profiles. Figure 2-7 shows the total mass profile from both 1T and 2T models. Two-temperature modeling, based on the T_{hot} of L08, increases the total mass by 30-50% for all radii within 625 h^{-1}kpc. Beyond that radius, the 2T assumption is not held because of the lack of constraint on $T_{\rm hot}$.

Although the inclusion of an absorption edge in the spectral model greatly changes the derived composition of the multi-phase plasma, it does not affect the mass measurement much. This is because we use a fixed $T_{\rm hot}$ profile. Once the temperature is determined, the total mass only depends on the logarithmic scale of the gas density, which produces $\sim 13\%$ difference at most.

2.5.2 Parametric Method

If the temperature does not vary dramatically on small scales, we can obtain a mass profile with higher spatial resolution since the gas density can be measured in detail from the X-ray surface brightness with the assumption of a certain geometry of the

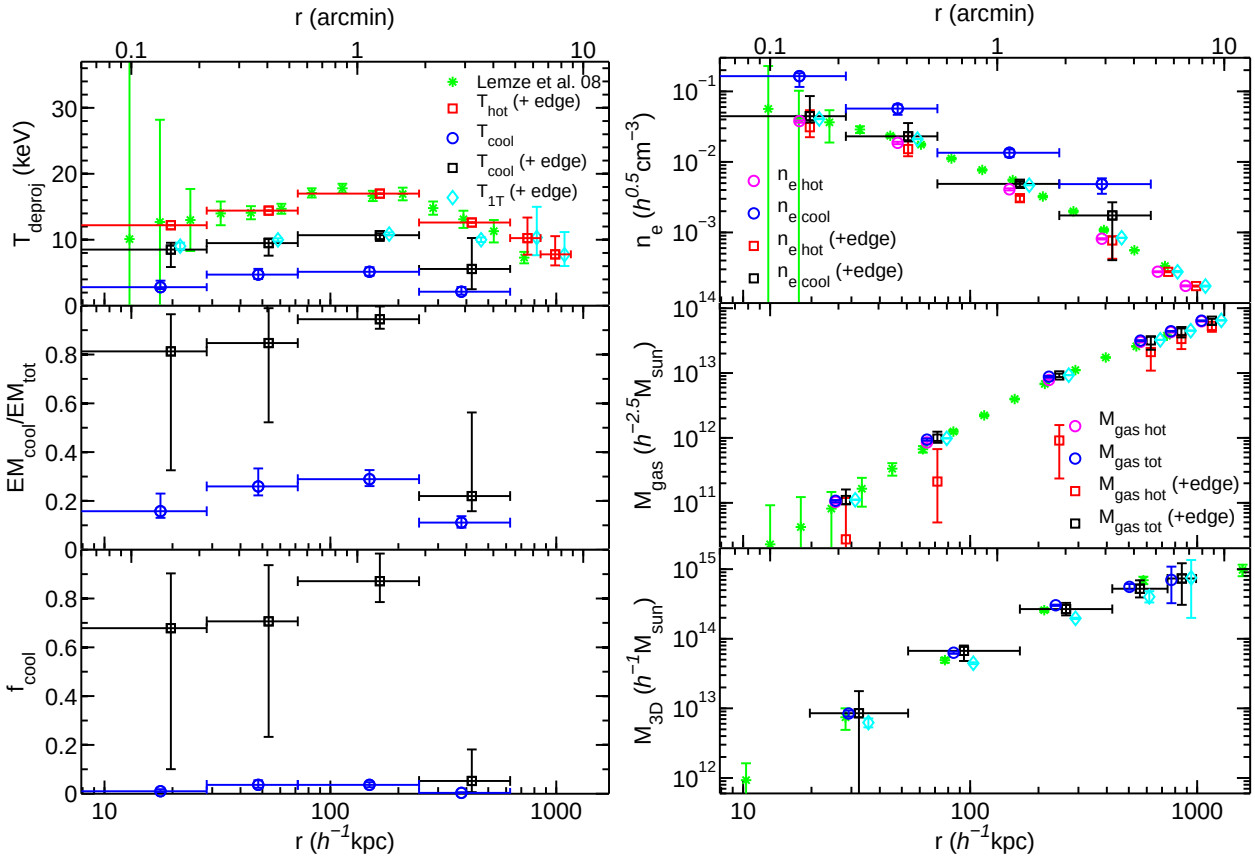

Figure 2-7: Temperature, emission measure ratio of the cool component $EM_{\rm cool}/EM_{\rm tot}$, volume filling fraction of the cool component $f_{\rm cool}$, gas number density n_e, cumulative gas mass $M_{\rm gas}$, and cumulative total mass M_{3D} profiles from the 2T deprojection analysis with an absorption edge correction (squares) and without the correction (circles). Also shown is the 1T analysis (diamonds) and results from Lemze et al. (2008a) (asterisks). $T_{\rm hot}$ of the first 4 annuli was fixed at the value derived from lensing and X-ray brightness data (Lemze et al., 2008a), which were grouped into fewer bins. The cool component of the last 2 bins was frozen at zero. The 2T assumption is held within 625 h^{-1}kpc. X-data points of the 1T and 2T models have been shifted by +10% and -10% for clarity, and their error bars are also omitted.

cluster. To achieve this, modeling of the temperature and the gas density is necessary. Following the procedure of Vikhlinin et al. (2006), we project the 3D temperature and the gas density models along the line of sight and fit with the observed projected temperature and the surface brightness profiles. A weighting method by Mazzotta et al. (2004) and Vikhlinin (2006) is used to predict a single-temperature fit to the projected multi-temperature emission from 3D space. This method has been shown to accurately reproduce density and temperature profiles of simulated clusters (Nagai et al., 2007b).

The gas density model is given by

$$n_p\, n_e = n_0^2\, \frac{(r/r_c)^{-\alpha}}{(1+r^2/r_c^2)^{3\beta-\alpha/2}}\, \frac{1}{(1+r^\gamma/{r_s}^\gamma)^{\varepsilon/\gamma}} + \frac{n_{02}^2}{(1+r^2/r_{c2}^2)^{3\beta_2}}, \tag{2.4}$$

which originates from a β model (Cavaliere & Fusco-Femiano, 1978) modified by a power-law cusp and a steepening at large radii (Vikhlinin et al., 1999). The second term describes a possible component in the center, especially for clusters with small core radius.

The temperature model is given by

$$T_{\rm 3D}(r) = T_0 \frac{(r/r_{\rm cool})^{a_{\rm cool}} + T_{\rm min}/T_0}{1+(r/r_{\rm cool})^{a_{\rm cool}}} \frac{(r/r_t)^{-a}}{(1+(r/r_t)^b)^{c/b}}, \tag{2.5}$$

which is a broken power law with central cooling (Allen et al., 2001). The observed temperature and surface brightness profiles, the best-fit model, and the surface brightness residual are shown in Figure 2-8. The model describes the data very well (χ^2/dof=154.3/155). The best-fit $T_{\rm 3D}$ and n_e models are shown in Figure 2-9. Also plotted are the profiles from the spectral deprojection fitting (§2.5.1). Compared to this nonparametric result, modeling $T_{\rm 3D}$ and n_e can avoid flucutations from the direct spectral deprojection, which is a common problem as the deprojection tends to amplify the noise in the data (see Appendix in Sanders & Fabian, 2007).

Comparing the surface brightness profile of the northeastern (NE) part to the southwestern (SW), Riemer-Sørensen et al. (2009) found that the NE part is 5-15% brighter outside 350 h^{-1}kpc and 25% under-luminous at 70 h^{-1}kpc than the SW. To see if this asymmetry can affect the mass estimate, we fit a symmetric model to the image and iteratively removed any part of the cluster that deviates significantly from the azimuthal mean, mainly the northern clump at 460 h^{-1}kpc, the southern less luminous region at 330 h^{-1}kpc, and possibly some point sources not completely removed beforehand. We did not exclude these regions from our temperature measurement since they were unlikely to bias the average temperature much for such a hot cluster, as shown in Figure 2-3 that at least 10-20% of the total emission measure from another spectral component was needed in order the change the spectroscopic temperature by 1 keV. We find that removing asymmetric parts from the image increases the total mass estimate by $\lesssim 10\%$ around the regions of the removed clumps,

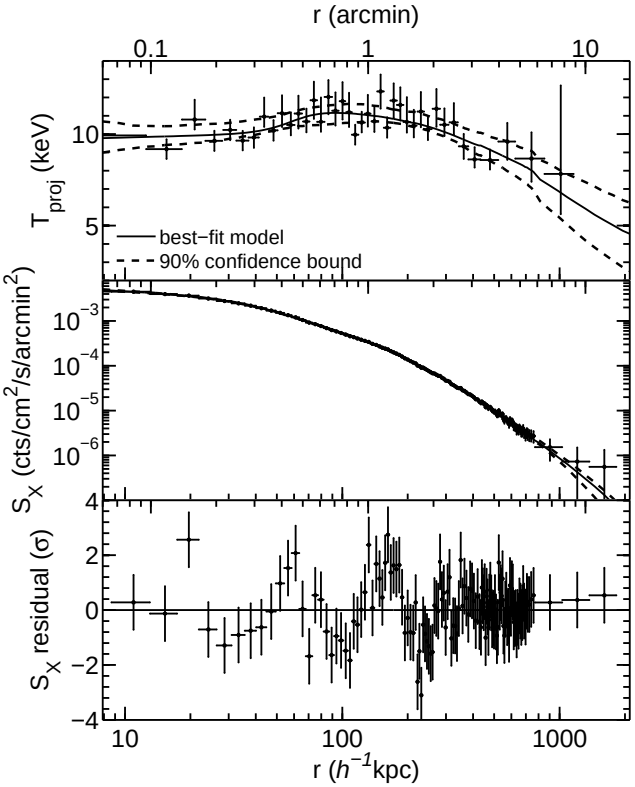

Figure 2-8: Projected temperature and surface brightness profiles with the best-fit model (solid lines) and its 90% confidence bounds (dashed lines). Bottom panel: residual between the surface brightness and the model. This fit gives a χ^2/dof of 154.3/155.

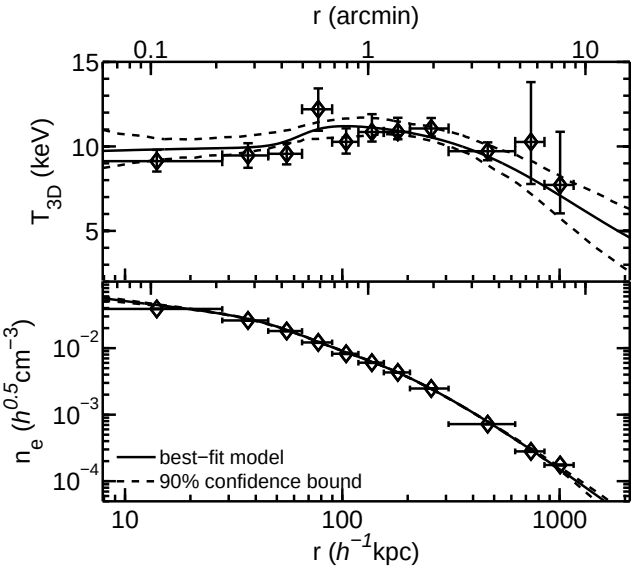

Figure 2-9: Best-fit T_{3D} and n_e models (solid lines) and 90% confidence bounds (dashed lines). Also shown are unparameterized results (diamonds) from §2.5.1.

which is not significant compared to the statistical error.

Figure 2-10 shows a comparison of parametric and non-parametric mass profiles. The non-parametric mass profile is from a more finely binned deprojected data than those shown in Figure 2-7. Results from these two methods are fully consistent with each other, although their errors are quite different. For the non-parametric method, we simply assign the observable, e.g. dT/dr, at a certain radius, so the uncertainty associated with the position is not included in the error on the mass, σ_M, but separately shown on the radius. Therefore, σ_M appears smaller if data are binned more coarsely. For the parametric method, the dependency of σ_M on the data binning is weaker. The departure from the model for any data point is assumed to be random noise and is filtered out through the fitting. Hence, σ_M reflects only the uncertainty of the fitted function and it depends strongly on the modeling.

2.5.3 Comparison with Other Studies

The total mass profiles of A04, based on *XMM-Newton*, and L08, a joint X-ray, strong and weak lensing study are also shown in Figure 2-10. Our result is in good agreement with A04, but disagrees with L08 around $\sim$ 200 h^{-1}kpc. To compare our mass estimate with other lensing works, we derived the total mass density and integrated it along the line-of-sight. The total mass density, ρ, is obtained through the hydrostatic equation, Eq. 1.16. Figure 2-11 shows the surface mass density profiles from both parametric and nonparametric methods, along with the HST/ACS strong lensing analysis of Broadhurst et al. (2005a), and the combined Subaru distortion and depletion data by Umetsu & Broadhurst (2008). Since it requires at least 3 points to calculate the second derivative, ρ at the boundary is unknown. This will

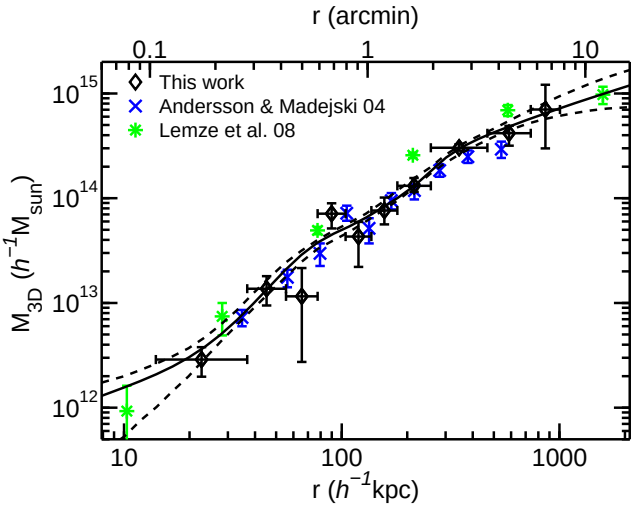

Figure 2-10: The parametric mass profile (solid line) compared to the unparameterized result (diamonds). Dashed lines show the 95% confidence bounds. Also shown are *XMM-Newton* result from A04 (crosses) and combined X-ray, strong and weak lensing analysis of L08 (asterisks). The mass profile of Lemze et al. (2008a) is mainly determined by the lensing data.

introduce additional systematic errors to the inner and the outer projected profile. To demonstrate how this may affect our nonparametric result, we insert two artificial points at $1''$ (2 h^{-1}kpc) and $13'$ (1.7 h^{-1}Mpc) to the nonparametric T and ρ_g profiles with their values estimated from the parametric model. The projected density derived this way is shown in red filled diamonds in Figure 2-11. The X-ray data are consistent with those from the weak lensing, but disagree with the strong lensing analysis. Although the nonparametric data appear to agree with the strong lensing estimate at $r = 80$ h^{-1}kpc, this is probably due to the temperature fluctuation mentioned in §2.5.2.

The mass discrepancy is manifested when comparing the cumulative projected mass profiles, M_{2D}, shown in Figure 2-12. The weak lensing M_{2D} profile of Umetsu & Broadhurst (2008) includes the integration of the data of Broadhurst et al. (2005a) in the inner region. Uncertainties are from Monte-Carlo simulations of the convergence profiles. The last 3 data points of Umetsu & Broadhurst (2008) (1-2.3 h^{-1}Mpc) are discarded since only the upper limits are available. Also shown are parametric strong lensing profiles (Halkola et al., 2006; Limousin et al., 2007), and other X-ray analyses (A04; Riemer-Sørensen et al., 2009). To convert M_{3D} to M_{2D}, A04 assume that the last data point reached the cluster mass limit, which unavoidably leads to underestimations especially at large radii. Riemer-Sørensen et al. (2009) use only the SE part of the cluster and four of the *Chandra* observations (excluding ObsID 540) and derive M_{2D} based on a best-fit NFW model fit to the M_{3D} profile. Their mass profile is generally lower than our estimate at most radii. This is contradictory to most findings that claim that the hydrostatic mass is underestimated in unrelaxed

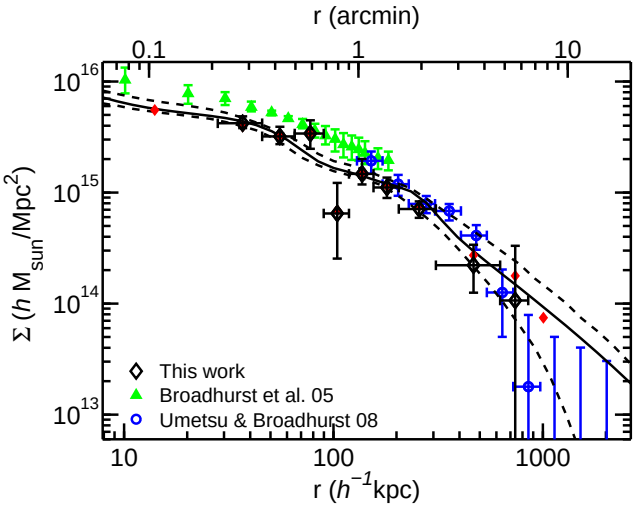

Figure 2-11: Surface mass density profiles from non-parametric (open diamonds) and parametric X-ray model (solid and dashed lines, 95% CL), compared to HST/ACS strong lensing analysis of Broadhurst et al. (2005a) (triangles), and combined Subaru distortion and depletion data by Umetsu & Broadhurst (2008), based on a maximum entropy method (circles). Filled diamonds show the mass from the nonparametric T_{3D} and n_e profiles that include estimations from the parametric result at $1''$ (2 h^{-1}kpc) and $13'$ (1.7 h^{-1}Mpc).

systems (e.g., Jeltema et al., 2008). Using such reasoning, and removing the NE part, presumably disturbed according to Riemer-Sørensen et al. (2009), should increase the overall mass estimate. The X-ray M_{2D} is 25-40% lower than that of lensing within 200 h^{-1}kpc, corresponding to a $\sim 1.4 \times 10^{14}$ $h^{-1}\mathrm{M}_{\odot}$ difference in the total projected mass.

2.5.4 NFW profile parameters

Table 2.3 lists the best-fit NFW parameters, M_{200} and c_{200}, for the total mass from both methods and from other studies, all converted to the adopted cosmology. Compared to other X-ray studies, our derived M_{200} is 30-50% higher, closer to weak lensing results. The differences between our NFW parameters and those of A04 from *XMM-Newton* are primarily attributed to their slightly lower but yet consistent mass at the last data point (Figure 2-10). This demonstrates that the accurate mass measurement at large radii, where systematic errors are usually the greatest, is crucial to the determination of NFW parameters.

Our results are consistent with weak lensing measurements, but with a lower concentration than what recent weak lensing studies seem to suggest (Umetsu & Broadhurst, 2008; Corless et al., 2009). When these analyses are added with strong lensing information, a very tight constraint on the concentration parameter can be obtained, giving $C_{200} = 9.9^{+0.8}_{-0.7}$ (Umetsu & Broadhurst, 2008), which hardly can be

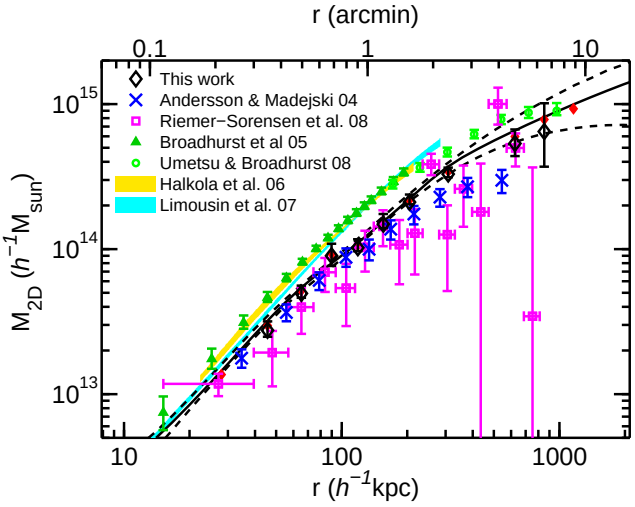

Figure 2-12: Projected mass profiles from non-parametric (open diamonds) and parametric analyses (solid and dashed lines, 95% CL), compared to *XMM-Newton* result from A04 (crosses), *Chandra* result by Riemer-Sørensen et al. (2009) (squares), HST/ACS and Subaru results by Broadhurst et al. (2005a) (triangles) and Umetsu & Broadhurst (2008) (circles). We integrated the lensing surface mass profile (shown in Figure 2-11) and estimated its uncertainties from Monte-Carlo simulations. Also shown are parametric strong lensing profiles of Halkola et al. (2006) and Limousin et al. (2007) (shaded regions, 68% CL). Riemer-Sørensen et al. (2009) used only SW part of the X-ray data and converted M_{3D} to M_{2D} with a NFW profile. A04 assumed that the last data point reached the cluster mass limit. Filled diamonds, same as Figure 2-11.

Table 2.3: Comparison of best-Fit NFW Parameters

Method	Instrument	M_{200} ($10^{15}h^{-1}\mathrm{M}_\odot$)	c_{200}	χ^2/dof	Reference
Spherical model					
X-ray (1T+edge)	Chandra	$1.16^{+0.45}_{-0.27}$	$5.3^{+1.3}_{-1.2}$	6.3/8	this work
X-ray (parametrized T_{3D}, n_e)	Chandra	$0.94^{+0.11}_{-0.06}$	$6.6^{+0.4}_{-0.4}$		this work
X-ray (2T [a])	Chandra	$1.45^{+0.36}_{-0.25}$	$7.6^{+1.3}_{-1.2}$	2.2/3	this work
X-ray (2T [a]+edge)	Chandra	$1.12^{+0.53}_{-0.29}$	$9.3^{+0.7}_{-2.8}$	0.1/3	this work
X-ray (1T)	XMM-Newton	0.63 ± 0.36	$7.6^{+1.7}_{-2.6}$	7.6/8	A04
X-ray (1T)	Chandra	0.55	10.1 [d]	1.6/13	Riemer-Sørensen et al. (2009)
SL	ACS	2.29	$6.3^{+1.8}_{-1.6}$		Broadhurst et al. (2005a)
SL	ACS	2.16 ± 0.32	5.8 ± 0.5	0.8/11	Halkola et al. (2006)
WL	CFHT	0.97 ± 0.13	7.4 ± 1.6		Limousin et al. (2007)
WL	CFHT	0.90 ± 0.17	13.1 ± 7.5		Corless et al. (2009)
WL	Subaru	1.24 ± 0.14	$10.5^{+4.4}_{-2.6}$	332/834	Umetsu & Broadhurst (2008)
SL+WL	ACS+Subaru	1.22 ± 0.13	$10.8^{+1.1}_{-0.9}$	13.3/20	Broadhurst et al. (2005b)
SL+WL	ACS+Subaru	1.31 ± 0.11	$9.9^{+0.8}_{-0.7}$	335/846	Umetsu & Broadhurst (2008)
SL+WL+X-ray (S_X)	ACS+Subaru+Chandra	1.42	$9.7^{+0.8}_{-0.7}$	15.3/24	L08
Triaxial model					
SL+WL [b]	ACS+Subaru	$1.15^{+0.26}_{-0.45}$	$13.4^{+1.8}_{-10.2}$	378/362	Oguri et al. (2005)
WL [c]	CFHT	0.83 ± 0.16	12.0 ± 6.6		Corless et al. (2009)

Note. — see Comerford & Natarajan (2007); Umetsu & Broadhurst (2008); Corless et al. (2009) for a more complete compilation.

[a] with $T_{\rm hot}$ from L08

[b] under a flat prior on the axis ratios.

[c] under a prior on the halo orientation that favors the line-of-sight direction.

[d] converted from best-fit parameters, $\rho_0 = 7.79 \times 10^6 \mathrm{M}_\odot \mathrm{kpc}^{-3}$, $r_s = 174$ kpc ($h = 0.7$, $\Omega_m = 0.28$, and $\Omega_\lambda = 0.72$), of Riemer-Sørensen et al. (2009), not consistent with their quoted value of 5.6 since they did not adopted the commonly defined c_{200}, the concentration at r_{200} where the enclosed mean density is 200 times the critical density (private communication).

reconciled with our value, $5.3^{+1.3}_{-1.2}$. However, if the gas emission is modeled with two spectral components with $T_{\rm hot}$ from L08, the X-ray derived concentration is in a closer agreement to those of combined strong and weak lensing studies, but this also implies that the majority of the gas is in the cool phase and occupies most of the intracluster space (§2.3.1).

2.6 Discussion

Nagai et al. (2007b) show that following the data analysis of Vikhlinin et al. (2006), the hydrostatic mass is underestimated by 14±6% within estimated r_{2500} for simulated clusters visually classified as "relaxed". Based on the X-ray morphology, A1689 is likely to be categorized as a relaxed cluster. The X-ray centroid is within $3''$ of the lensing and optical centers (Andersson & Madejski, 2004), with a very minimal centroid shift or asymmetry (Hashimoto et al., 2007). At the X-ray estimated r_{2500}

Table 2.4: Comparison of M_{500}

Method	M_{500} ($10^{14}h^{-1}\mathrm{M}_\odot$)	r_{500} ($h^{-1}\mathrm{Mpc}$)
parametrized $T_{3\mathrm{D}}$, n_e	$7.3^{+1.3}_{-0.5}$	$1.01^{+0.06}_{-0.03}$
$M_{500} - T_X$ †	7.7 ± 0.2	1.03 ± 0.01
$M_{500} - Y_X$ ‡a	$7.7^{+0.5}_{-1.2}$	$1.03^{+0.02}_{-0.06}$

†Scaling relations from Vikhlinin et al. (2009a) with indices fixed to self-similar theory values. Errors only reflect the measurement uncertainties. Dispersions of the relation is not included. $T_X = 10.1 \pm 0.2$ keV, measured from $r = 1.14' - 7.6'$ ($\approx 0.15 r_{500} - r_{500}$).

[a]By solving Eq. 14 of Vikhlinin et al. (2009a). The final $Y_X = T_X \times M_{\mathrm{gas}}$ determined at r_{500} is $(5.1^{+0.5}_{-1.2}) \times 10^{14}\ h^{-2.5}\mathrm{M}_\odot$ keV.

of 493 h^{-1}kpc, we derive an enclosed hydrostatic mass of $(4.2 \pm 0.3) \times 10^{14} h^{-1}\mathrm{M}_\odot$, $\approx 30\%$ lower than the lensing mass from L08. At $r = 200\ h^{-1}$kpc, this becomes a 50% difference (see Figure 2-10). Such a strong bias is not seen in the relaxed cluster sample of Nagai et al. (2007b), assuming that the lensing mass is unbiased, although this is not unusual for "unrelaxed" clusters, referring to those with secondary maxima, filamentary structures, or significant isophotal centroid shifts.

Table 2.4 shows the comparison of measured M_{500} with others derived from the $M_{500} - Y_X$ and $M_{500} - T_X$ relations of Vikhlinin et al. (2009a), calibrated from 49 low-z and 37 high-z with $\langle z \rangle = 0.5$ clusters observed with *Chandra* and *ROSAT*. A very good agreement has been achieved between these estimates. Since the $M_{500} - Y_X$ relation is insensitive to whether the cluster is relaxed or not (Kravtsov et al., 2006) and merging clusters tend to be cool for their mass (Mathiesen & Evrard, 2001), consistency among these mass estimates indicates that A1689 is relaxed in the sense that it behaves like other "relaxed" clusters on the scaling relation.

On the other hand, projection effects, such as triaxial halos or chance alignments, always have to be taken into account when comparing projected (lensing) and three-dimensional (X-ray) mass estimates. From kinematics of about 200 galaxies in A1689, Łokas et al. (2006) suggest that there could be a few distant, possibly non-interacting, substructures superposed along the line of sight. Lemze et al. (2008b), based on a 0.5×0.5 deg^2 VLT/VIMOS spectroscopic survey from Czoske (2004) which includes ~ 500 cluster members, disagree with this projection view. They conclude that only one identifiable substructure at +3000 km/s, $1.5'$ to the NE (the X-ray clump is at $\sim 3.5'$ NE). This background group is seen in the strong lensing mass analysis (Broadhurst et al., 2005a), but is determined not to be massive ($< 10\%$ of the total mass in the strong lensing region). Nonetheless, the higher than usual velocity dispersion in the cluster center, ~ 2100 km/s, indicates that the central part is quite complex

(Czoske, 2004). This may also imply that the halo is elongated in the line-of-sight direction, as galaxies move faster along the major axis.

For powerful strong lens systems, like A1689, halo sphericity is never a justified assumption (e.g., Hennawi et al., 2007). Oguri & Blandford (2009) show that these "superlens" clusters almost always have their major axes aligned along the line-of-sight, with more circular appearances in projection and $\sim 40-60\%$ larger concentrations than other clusters with similar masses and redshifts. Gavazzi (2005) demonstrates that using a prolate halo with axis ratio ~ 0.4, they were able to explain the mass discrepancy between the lensing and X-ray estimates of cluster MS2137-23. This cluster has a well defined cool core (e.g., Andersson et al., 2009), thus presumably relaxed, and yet a factor of 2 difference in the mass is not lessened with a multiphase model for the core region (Arabadjis et al., 2004). In contrast, triaxial modeling not only solves the mass inconsistency, but also the high concentration problem and the misalignment between stellar and dark matter components in MS2137-23 (Gavazzi, 2005).

To see how the triaxiality changes our mass measurements, we modeled $T_{\rm 3D}$ and ρ_g with prolate profiles, by replacing r in Eq. 2.4 and 2.5 with $(x^2/a^2+y^2/b^2+z^2/c^2)^{1/2}$, where we assumed $a=b<c$ and the major axis, z-axis, is perfectly aligned along the line-of-sight. Following the same analysis outlined in §2.5.2 but with different projection factors, we obtained best-fit $T_{\rm 3D}$ and ρ_g profiles. The derived mass profiles under various axis ratios a/c are shown in Figure 2-13. The uncertainties on $\Sigma(r)$ and $M_{2D}(r)$ are similar to those in Figures 2-11 and 2-12. We integrated the density from $z=-4.5h^{-1}$Mpc to $+4.5h^{-1}$Mpc ($\approx 3r_{200}$ for a/c=1) for all the cases. The uncertainties of $T_{\rm 3D}$ and ρ_g profiles at large radii ($\gtrsim 10\%$ at $r=r_{500}$ and increasing further afterward) does not significantly change the projected mass at smaller radii ($\lesssim 3\%$ within $500h^{-1}$kpc).

The total mass enclosed within a sphere of radius r, $M_{3D}(r)$, and the spherically averaged mass density, $\rho(r)$, are basically unchanged under different assumptions of triaxiality, considering the typical measurement uncertainty. The same conclusion was drawn by Piffaretti et al. (2003) and Gavazzi (2005), though they assumed a β or a NFW model with gas isothermality. For the azimuthally averaged surface mass density $\Sigma(r)$ or the projected mass within a cylinder of radius r, $M_{2D}(r)$, a factor of 2 or more difference can be easily made by increasing the ellipticity. An axis ratio of 0.6, giving $M_{2D}(<45'')=1.4\times10^{14}h^{-1}{\rm M}_\odot$ (by a factor of 1.6 increase), can resolve the central mass discrepancy, but overpredicts the mass by $\sim 40\%$ at large radii. For a ratio of 0.7, the X-ray mass estimate data agrees with those of strong and weak lensing within 1% (-1σ) and 25% ($+1\sigma$), respectively. Since the gas distribution is rounder than that of the DM, a larger axis ratio than the finding of Gavazzi (2005) is expected.

Not only does the projected mass increase with the triaxiality, but so also does the steepness of the profile. This explains a higher than X-ray derived concentration from the lensing data (§2.5.4). Although some attempts have been made to model the lensing mass profile with a 3D triaxial halo (Oguri et al., 2005; Corless et al., 2009), no significant constraint on the concentration parameter is obtained (Table 2.3). To break the degeneracy between the triaxiality and the concentration, observations from

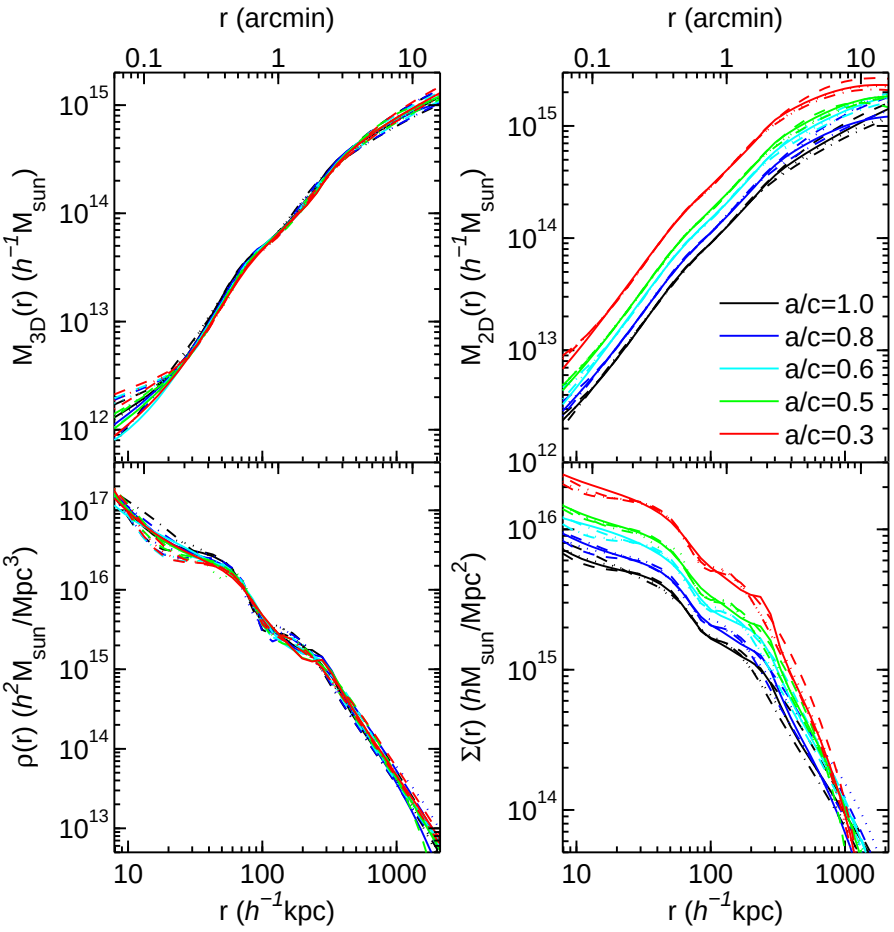

Figure 2-13: Best-fit mass profiles for various axis ratios a/c from Model 1 (dash-dot line), 2 (dotted line), 3 (solid line), and 4 (dashed line). *Top left*: total mass enclose within a sphere of radius r, $M_{3D}(r)$. *Top right*: spherically average mass density $\rho(r)$. *Bottom left*: azimuthally average surface mass density $\Sigma(r)$. *Bottom right*: projected mass within a cylinder of radius r, $M_{2D}(r)$.

different prospective projections, such as X-ray, Sunyaev-Zel'dovich effect, or galaxy kinematics, are always needed.

Riemer-Sørensen et al. (2009) conclude that A1689 harbors a cool core based on the radial temperature profile and a hardness ratio map. From this, they conclude that A1689 is relaxed, excluding the NE half of the cluster, where there is a low mass substructure. Based on the derived temperature profile we disagree that A1689 contains a cool core. The temperature of the cluster varies radially from 9 to 11 keV with a slight drop only after 500 h^{-1}kpc. This can not be characterized as the properties of a cool core cluster. In fact, as shown in Andersson et al. (2009), A1689 is an intermediate stage cluster in terms of central baryon concentration with a minimal core temperature drop. This, does not necessarily provide evidence that the cluster is disturbed but we do not either expect the properties of a cool core

cluster. Hardness-ratio maps are very sensitive to accurate background subtraction, especially for high energy splittings. We suspect that the hardness ratio map ($S/H = E[0.3-6.0]/E[6.0-10.0]$) in Riemer-Sørensen et al. (2009), used as evidence for a cool core, suffers from residual background. The ratio decreases rapidly with radius from a central value of 2.2 and reaches 0.4 already at $3'$. This is an extremely low ratio for any reasonable cluster temperature and it is in disagreement with the observed temperature profile. For comparison, a background-free spectrum from an isothermal cluster at 10 keV would exhibit a count-ratio of ~ 47 in ACIS-I given the energy bands mentioned above. The usage of unsubtracted hardness-ratios in these bands shows that the high-energy band has a significant fractional background contribution and hence, is more spatially flat compared to the low energy band. This does not provide information about the spatial distribution of gas temperatures in the ICM.

2.7 Summary

We have investigated a deep exposure of Abell 1689 using the ACIS-I instrument aboard the *Chandra* X-ray telescope. In order to study the discrepancy of the gravitational mass from estimates from gravitational lensing, to that derived using X-ray data, we test the hypothesis of multiple temperature components in projection. The result of a two-temperature model fit shows that it is very important to take into account all details of the calibration of the instrument. We detect an additional absorption feature at 1.75 keV consistent with an absorption edge with an optical depth of 0.13. In analyzing multiple additional datasets, we find similar parameter values for this edge.

If the edge is not modeled, fitting the cluster data within $3'$ strongly favors an additional plasma component at a different temperature. However, when this absorption feature is modeled, the second component does not improve the statistic significantly and the fit results is in better agreement with the *XMM-Newton* MOS data. In all cases, a second component has to have $T > 5$ keV in order for the hot component to agree with the cluster temperature predicted by Lemze et al. (2008a) which is derived from lensing and S_X profiles. This contradicts the assertion that cool clumps are biasing the X-ray temperature measurements since these substructures would not be cool at all. We also find that, if the temperature profile of the ambient cluster gas is in fact that of Lemze et al. (2008a), the "cool clumps" would have to occupy 70-90% of the space within $250h^{-1}$kpc radius, assuming that the two temperature phases are in pressure equilibrium. In conclusion, we find the scenario proposed by Lemze et al. (2008a) unlikely.

Further studying the ratio of Fe XXVI Kα and Fe XXV Kα emission lines, we conclude that these show no signs of a multi-temperature projection and the best fit of this ratio implies a single temperature consistent with the continuum temperatures from both *XMM-Newton* MOS and the *Chandra* data when the absorption edge is modeled.

The discrepancy between lensing and X-ray mass estimates remains, particularly in the $r < 200\ h^{-1}$kpc region. Our X-ray mass profile shows consistent results com-

pared to those from weak lensing (e.g., Broadhurst et al., 2005b; Limousin et al., 2007; Umetsu & Broadhurst, 2008; Corless et al., 2009). Strong lensing mass profiles from different studies generally give consistent results (e.g., Broadhurst et al., 2005a; Halkola et al., 2006; Limousin et al., 2007), but none of them agrees with those derived from X-ray observations (Xue & Wu, 2002; Andersson & Madejski, 2004; Riemer-Sørensen et al., 2009). Using a simple ellipsoidal modeling of the cluster with the major axis along the line of sight, we find that the projected mass, as derived from the X-ray analysis, increases by a factor of 1.6 assuming an axis-ratio of 0.6. We conclude that the mass discrepancy between lensing and X-ray derived masses can be alleviated by line of sight ellipticity and that this also can explain the high concentration parameter found in this cluster.

Chapter 3

Cluster mass, pressure and baryon profiles from X-ray and Weak lensing observations

3.1 Sample and Analysis

We select 18 clusters from the weak lensing sample of Hoekstra (2007) and 23 from the weak lensing study of Okabe et al. (2010) which have archival X-ray data observed with the *Chandra* Observatory. The former and the latter samples are carried out with the Canada-France-Hawaii Telescope (CFHT) and the Subaru Telescope, respectively. We shall call them CFHT and Subaru samples throughout the paper. The observation details are listed in Table 3.1. Combining the two samples, we have a total of 33 clusters with temperatures in $4 - 11$ keV at $0.15 < z < 0.55$. The merging cluster A115 from the Subaru sample is excluded from the X-ray and weak lensing comparison because the lensing analysis is centered at the southern subcluster while our X-ray measurement is focused on the brighter northern one with a well defined cool core.

Throughout this work, we assume a concordance cosmology with $\Omega_M = 0.3$, $\Omega_\Lambda = 0.7$ and $H_0 = 70$ km s^{-1} Mpc^{-1}.

3.1.1 Lensing data

CFHT sample The sample of Hoekstra (2007) is chosen from the archival CFHT data that have deep exposures in both B and R bands observed by the CFH12k camera. Two clusters A370 and CL0024.0+1652 are included because of the well known strong lensing feature. About a half of the rest are part of the the Canadian Network for Observational Cosmology Cluster Redshift Survey (CNOC, Yee et al., 1996) selected from the Einstein Medium Sensitivity Survey (EMSS, Gioia et al., 1990), and the other half are from a CFH12k lensing survey (Bardeau et al., 2005) drawn from the X-ray Brightest Abell Clusters Survey (XBACS, Ebeling et al., 1996). Therefore this sample is mostly X-ray luminosity selected.

Source galaxies are selected from faint galaxies redder or bluer than the Red

Table 3.1: Summary of sample

Name	RA (J2000)	Dec (J2000)	z	*Chandra* ObsID	WL sample
(1)	(2)	(3)	(4)	(5)	(6)
MS0015.9+1609	00:18:33.4	+16:26:12	0.546	520	CFHT
CL0024.0+1652	00:26:35.8	+17:09:42	0.390	929	CFHT
A68	00:37:06.2	+09:09:33	0.255	3250	CFHT, Subaru
A115	00:55:50.6	+26:24:35	0.197	3233	Subaru
A209	01:31:53.0	−13:36:44	0.206	522,3579	CFHT, Subaru
RXJ0142.0+2131	01:42:03.5	+21:31:20	0.280	10440	Subaru
A267	01:52:42.2	+01:00:36	0.227	3580	CFHT, Subaru
A370	02:39:53.3	−01:34:35	0.373	515	CFHT
A383	02:48:03.4	−03:31:45	0.187	524,2320,2321	CFHT, Subaru
A521	04:54:08.0	−10:14:07	0.247	430,901	Subaru
A586	07:32:20.3	+31:37:56	0.171	530	Subaru
A611	08:00:56.8	+36:03:24	0.288	3194	Subaru
ZwCl0839.9+2937	08:42:55.9	+29:27:26	0.194	2224	Subaru
A697	08:42:57.6	+36:21:56	0.282	4217	Subaru
A750	09:09:12.6	+10:58:33	0.180	924	CFHT
A963	10:17:03.5	+39:02:52	0.206	903	CFHT, Subaru
A1689	13:11:29.5	−01:20:29	0.187	540,1663,5004,6930,7289	CFHT
A1763	13:35:18.9	+41:00:02	0.223	3591	CFHT
MS1358.1+6245	13:59:50.6	+62:31:05	0.329	516	CFHT
A1835	14:01:02.0	+02:52:42	0.253	495,496,6880,6881,7370	Subaru
ZwCl1454.8+2233	14:57:15.1	+22:20:35	0.258	543,4192	CFHT, Subaru
A2009	15:00:19.6	+21:22:11	0.153	10438	Subaru
ZwCl1459.4+4240	15:01:22.4	+42:20:46	0.292	7899	Subaru
MS1512.4+3647	15:14:22.5	+36:36:21	0.373	800	CFHT
MS1621.5+2640	16:23:35.6	+26:34:20	0.427	546	CFHT
A2218	16:35:52.6	+66:12:36	0.171	553,1454,1666	CFHT
A2219	16:40:20.3	+46:42:30	0.228	896	CFHT, Subaru
RXJ1720.1+2638	17:20:10.0	+26:37:30	0.161	304,1453,3224,4361	Subaru
A2261	17:22:27.1	+32:07:57	0.224	550,5007	Subaru
RXJ2129.6+0005	21:29:39.9	+00:05:21	0.234	552,9370	Subaru
A2390	21:53:36.8	+17:41:44	0.231	500,501,4193	CFHT, Subaru
A2485	22:48:30.9	−16:06:29	0.247	10439	Subaru
A2631	23:37:38.5	+00:16:13	0.278	3248	Subaru

Note. — Column (2), (3): the X-ray center, determined from a sum of three 2-dimensional β models fit to the X-ray image.

Cluster Sequence on the color-magnitude diagram. The remaining contamination by blue member clusters is corrected by boosting the shear signal by the fraction of excess number counts of galaxies. The weak lensing mass is determined from the aperture mass densitometry method. The surface mass density of the outermost annulus ($10'-17'$) is estimated from a best-fit NFW model with a halo virial mass and concentration relation from simulations (Bullock et al., 2001). This model is also used to convert the projected mass to the 3D mass. We use the converted 3D mass given at R_{2500}, R_{1000}, and R_{500} from Mahdavi et al. (2008), which is taken from Hoekstra (2007) but with an updated redshift distribution of Ilbert et al. (2006), and refit the mass profile with the NFW model so that the mass at other radii can be determined.

Subaru sample The sample of Okabe et al. (2010) is part of the Local Cluster Substructure Survey (LoCuSS, Smith et al., 2010), selected from the *ROSAT* All-Sky Survey catalogues (Ebeling et al., 1998, 2000; Böhringer et al., 2004), observed with Suprime-Cam camera in i' and V bands. Source galaxies are selected similar to that of Hoekstra (2007) but down to a slightly fainter magnitude, with redshift distributions from Ilbert et al. (2009). Three clusters ZwCl0839.9+2937, A963, and A2009 do not have V band data, so the lensing signal is measured from the faint galaxies. We take the best-fit NFW model for the reduced shear from Okabe et al. (2010) as the lensing mass profile.

3.1.2 X-ray data analysis

We extract the surface brightness profiles in adaptively binned annuli in the $0.7-2.0$ keV energy band, centered at the X-ray centroid determined from a sum of three 2-dimensional β models[1] fit to the exposure corrected, point sources masked X-ray image of the entire field of view of *Chandra* ACIS-I or ACIS-S3. The X-ray center is listed in Table 3.1. Each radial bin is chosen to have a constant signal-to-noise ratio, and this ratio is adjusted depending on the overall quality of the observation. When the bin width is smaller than the PSF size or greater than a certain distance, it is brought back into an appropriate range, so that we can adequately measure the radial profile for the whole cluster. The X-ray spectrum is extracted in similar annuli, but in much coarser bins than those used in the brightness profile.

To measure the projected temperature, we fit the spectrum with an absorbed APEC model (Smith et al., 2001), using Cash statistic (Cash, 1979) in XSPEC (Arnaud, 1996). The background is modeled in a similar way of Leccardi & Molendi (2008), consisting of

- cosmic ray induced background: power-laws plus several Gaussians, quiescent components
- charged particle background: broken power-laws, also flaring components (Markevitch et al., 2003)

[1] $S_X = S_{X_0}\left(1+\frac{r^2}{r_c^2}\right)^{-3\beta+1/2}$ (Cavaliere & Fusco-Femiano, 1978)

- cosmic X-ray background (CXB): absorbed broken power-law
- galactic emission: absorbed thermal and unabsorbed thermal (e.g. Kuntz & Snowden, 2000; Smith et al., 2007; Miller et al., 2008, and references within).

The X-ray backgrounds, charged particle and cosmic ray induced backgrounds, are determined by ACIS-stowed data [2]. The magnitudes of the sky backgrounds, CXB and galactic backgrounds, are measured from blank-sky data [3] with X-ray background components fixed at values determined from ACIS-stowed data. Any mismatch in the galactic background of the cluster pointing and that of blank-sky data is corrected by a spectral fitting in regions far from the cluster emission in the same field. The formal error of the temperature includes the statistical uncertainty and the systematic uncertainty from the amplitude of X-ray and galactic backgrounds. The latter is determined by the change to the best-fit temperature when the background normalization is fixed at $\pm 1\sigma$ from the nominal value for the galactic background or $\pm 2\%$ for the X-ray background (Vikhlinin et al., 2005). These changes are separately added the total uncertainty of the temperature in quadrature.

Following a similar procedure of Vikhlinin et al. (2006), we project the 3D temperature and gas density models (Eqs. 2.4 and 2.5) along the line-of-sight and fit to the observed projected temperature and surface brightness profiles. A weighting method of Vikhlinin (2006), modified from Mazzotta et al. (2004), is used to predict the temperature of a single-temperature fit to the multi-temperature emission from 3D space. For purely continuum spectra, the weighted (projected 2D) temperature can be expressed as the following,

$$\langle T \rangle = \frac{\int w\, T\, dV}{\int w\, dV}, \tag{3.1}$$

where $w = \rho_g^2\, T^{-\alpha}$ and $\alpha \simeq 0.75$. For spectra mixed with lines and continua as in the realistic case, the weighting method is non-analytic. See Vikhlinin et al. (2006) for details.

Ideally fitting 3D temperature and gas density models should be done simultaneously, e.g. as been implemented in Sanderson & Ponman (2010), because converting the count rate to the emission measure $\int n_{\rm e} n_{\rm p} dV$ needs the temperature for the cooling function (Eq. 1.7), and calculating the projected 2D temperature requires the 3D gas density profile (Eq. 3.1). However, we find that the model can not fit the projected temperature well because of the constraint from the surface brightness profile, especially for data of very good quality. In any localized over-luminous region, which can result from cluster asphericity, shock compression, or substructures, the joint model will try decreasing the temperature to increase the emissivity at low energy instead of raising the gas density, which is usually not possible because the gas model is tightly confined by neighboring brightness data. To overcome this, we fit the temperature and the density iteratively. When fitting the temperature, the gas density is fixed at the previously determined value, and versa.

[2] http://cxc.harvard.edu/contrib/maxim/stowed/
[3] http://cxc.harvard.edu/contrib/maxim/acisbg/

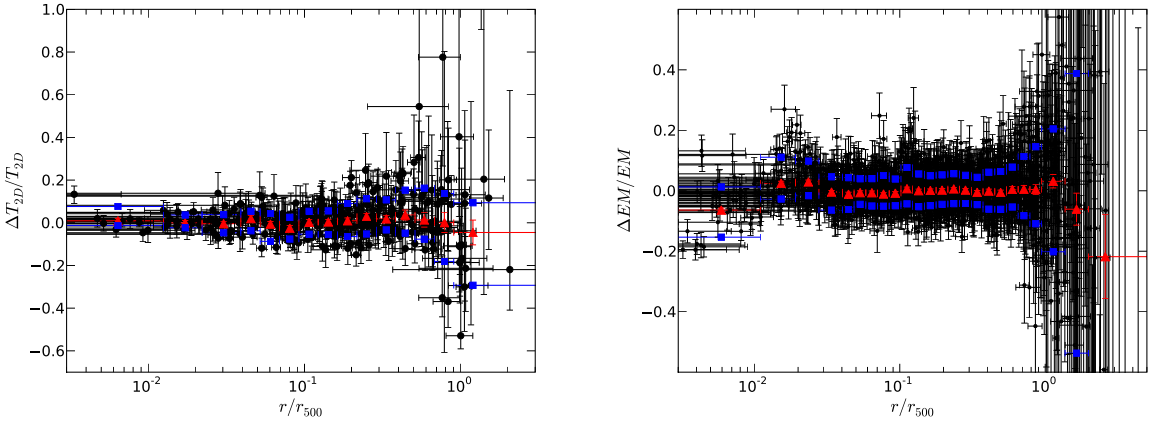

Figure 3-1: Residuals of best-fit projected temperature (left) and emission measure profiles (right), expressed as (data−model)/model. Also shown are mean residuals (red triangles) and root-mean-square residuals (blue squares).

Although data in the central region have great statistical power, systematic uncertainties such as from central AGN activities, the multiphase nature of the ICM, or the validity of the model are difficult to address. Therefore we exclude both temperature and surface brightness data inside of a 12 kpc radius ($\approx 0.01 R_{500}$) from the fit. This cut-off radius may be chosen somewhat arbitrarily: e.g, Vikhlinin et al. (2006) used $5 - 80$ kpc for the temperature data; Sanderson & Ponman (2010) used $5 - 20$ kpc for both temperature and surface brightness data. Ettori et al. (2010) used 50 kpc for temperature data. But it generally does not affect the result at much larger radii.

The fitting is carried out by a Markov chain Monte Carlo (MCMC) method, described in §3.1.3, which is computationally efficient for models with large numbers of parameters (8 parameters in temperature and 10 parameters in gas density), and has the advantage of rejecting unphysical parameters beforehand (e.g. parameters that give negative total mass). The temperature and emission measure profiles along with their best-fit models are shown in Appendix A.1 and A.2. Note that the best-fit projected temperature profile, shown in the blue solid line in A.1, is for the illustrative purpose only. The projected temperature is evaluated through the integration of the 3D temperature and the density over certain radial range. Its profile shape, unlike that of the parametrized 3D temperature, depends on the radial bin adopted. We use the same radial bin at which the projected temperature or the surface brightness are measured when fitting the projected profiles. The integral is summed over to $4.5 R_{500}$ ($\approx 3\, R_{200}$).

In Figure 3-1 we plot the residuals of best-fit projected temperature and emission measure profiles, expressed as (data−model)/model, for our whole sample of 32 clusters (without A115). The mean and root-mean-square residuals in each radial bin are shown in red crosses and blue squares, respectively. The projected temperature profile is modeled with an accuracy of $\approx 2\%$ on average and a scatter of 8%; the emission measure profile is modeled better than 1% in $0.03 - 1\, R_{500}$ with a scatter of 6%. Beyond R_{500}, the deviation of the emission measure profile is about $3 - 10\%$.

3.1.3 The Markov chain Monte Carlo Method

A Markov chain is a sequence of model parameters constructed with the property that the model parameters appear in the chain with a frequency proportional to their posterior probability. The candidate parameter values are drawn from a prior probability distribution, which is a Gaussian function with a variable width in our case. We follow the approach of Peterson et al. (2007) to calculate the adaptive step size which facilitates probing the parameter space. The algorithm also includes some memory loss so that later steps are not heavily influenced by earlier steps. These candidate parameters are accepted into the chain or rejected according to the Metropolis-Hastings criterion (Metropolis et al., 1953; Hastings, 1970). If the likelihood of the new point L_1 is higher than the likelihood of the previous point L_0, then the new point is accepted. Otherwise, the point is accepted only if a uniform random number between 0 and 1 is less than the ratio of likelihoods, L_1/L_0.

The likelihood is defined as

$$\ln L = -\frac{1}{2}\sum_i \frac{\left(T_{\rm data,i} - T_{\rm model,i}\right)^2}{\sigma_{T,i}^2} - \frac{1}{2}\sum_i \frac{\left(S_{\rm X\,data,i} - S_{\rm X\,model,i}\right)^2}{\sigma_{S_{\rm X},i}^2} \tag{3.2}$$

The marginal posterior distribution for a particular parameter is obtained by building the histogram of the parameter values from the chain. We quote the median of the distribution as the best-fit value. The errors are 68% confidence intervals around the median. We then use the whole sets of parameters to construct posterior simulations for other unobserved quantities (e.g., the hydrostatic mass, the thermal pressure, etc). Similarly, the median of the distribution is regarded as the best-fit value and the uncertainty is 68% confidence intervals around the median.

Figure 3-2 shows the comparison of the mass distribution from the Markov chain (solid line) and from the Monte Carlo realization of the original data (dashed line), a commonly used approach for the uncertainty analysis. The latter method simulates projected temperature and surface brightness profiles according to the observed data and their measurement uncertainties. Errors are estimated through the distribution of best-fit parameters from these simulated data. Both methods give consistent results.

3.1.4 Defining cluster morphological measures

The cuspiness parameter measured from the gas density profile, $\alpha = d\ln\rho_g/d\ln r$ at $r = 0.04R_{500}$ (Vikhlinin et al., 2007), can be used to quantify the extent of the ICM cooling. Sanderson et al. (2009) find that the cut at $\alpha = -0.7$ roughly divides clusters into those with central gas entropy greater than 30 keV cm^2 and those under, which is a threshold for the onset of star formation (Rafferty et al., 2008) and for harboring strong Hα and radio emitting brightest cluster galaxies (BCGs) (Cavagnolo et al., 2008a). Using the same classification of Sanderson et al. (2009), we define cool core (CC) and non-cool core (NCC) clusters as those with α below and above -0.7, respectively. The cuspiness parameters are listed in Table 3.2.

To quantify the overall cluster morphology, we adopt power ratio and centroid

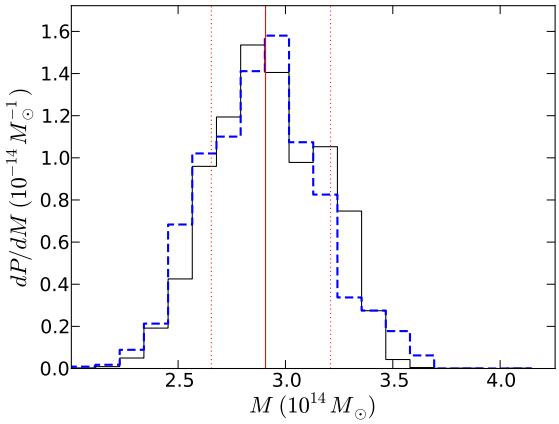

Figure 3-2: Probability distribution of the X-ray mass of A383 at 1 Mpc constructed from the Markov chain. Red solid and dotted lines show the median and its 68% confidence interval, respectively. Also shown by the dashed curve is the distribution from Monte Carlo simulations of the measured profiles.

shift methods. The power ratios P_m/P_0 are the ratio between the power of multipole moments of X-ray luminosity maps, created by a smoothed particle inference (SPI) technique (§4.1). We choose an aperture radius of $0.5R_{500}$ so that most of the area is entirely covered within the field-of-view of *Chandra* ACIS; while the centroid shift, $\langle w \rangle$, is the variation of the centroid with the radius, measured up to R_{500}. Lower values suggest a higher degree of relaxedness of the cluster. Details of the definition and the calculation of power ratios and centroid shifts are described in §4.4 and §4.5. Values are shown in Tables 4.1 and 4.2. Unlike the classification of CC and NCC clusters in which there seems to be a certain threshold value for α, the distributions of P_m/P_0 and $\langle w \rangle$ appear to be unimodal (Figure 4-11). Furthermore, simulations can not match the observed distributions of P_2/P_0 and P_4/P_0 well (Jeltema et al., 2008), and the values of P_m/P_0 highly depend on the chosen aperture. Because of the lack of the reference work tailored to our observations, we divide the sample into halves using the median of the distribution. We shall call those with lower than the median power ratios or centroid shifts the low P_m/P_0 or $\langle w \rangle$ clusters and the high P_m/P_0 or $\langle w \rangle$ clusters if their values are higher than the median.

3.2 X-ray Results

Table 3.2 summarizes X-ray properties of the sample.

3.2.1 Temperature profiles

In Figure 3-3, we plot the best-fit three-dimensional temperature models for the whole sample. The temperature is scaled by T_X, the spectroscopic temperature measured

Table 3.2: Summary of cluster X-ray properties

Name	n_H ($10^{20}\mathrm{cm}^{-2}$)	T_X (keV)	R_{2500} (kpc)	M_{2500} ($10^{14}\mathrm{M}_\odot$)	$f_{\mathrm{gas},2500}$	R_{500} (kpc)	M_{500} ($10^{14}\mathrm{M}_\odot$)	α	CC	Low P_3/P_0
(1)	(2)	(3)	(4)	(5)	(6)	(7)	(8)	(9)	(10)	(11)
MS0015.9+1609	3.99	$7.7^{+0.4}_{-0.4}$	482	$2.9^{+0.2}_{-0.2}$	$0.142^{+0.009}_{-0.011}$	1068	$6.3^{+0.5}_{-0.6}$	-0.32 ± 0.05		
CL0024.0+1652	4.08	$5.1^{+0.6}_{-0.9}$	371	$1.1^{+0.1}_{-0.1}$	$0.077^{+0.009}_{-0.008}$	822	$2.4^{+0.4}_{-0.4}$	-0.73 ± 0.09	✓	
A68	4.83	$7.4^{+1.0}_{-0.9}$	561	$3.2^{+0.4}_{-0.4}$	$0.095^{+0.012}_{-0.010}$	1150	$5.6^{+0.8}_{-0.9}$	-0.44 ± 0.12		✓
A115	5.35	$6.7^{+0.3}_{-0.2}$	438	$1.4^{+0.1}_{-0.1}$	$0.109^{+0.007}_{-0.007}$	1142	$5.2^{+0.5}_{-0.4}$	-1.109 ± 0.005	✓	
A209	1.46	$7.2^{+0.4}_{-0.4}$	500	$2.2^{+0.1}_{-0.1}$	$0.118^{+0.007}_{-0.007}$	1191	$5.9^{+0.4}_{-0.3}$	-0.41 ± 0.06		
RXJ0142.0+2131	6.27	$6.4^{+0.7}_{-0.6}$	511	$2.5^{+0.4}_{-0.3}$	$0.105^{+0.012}_{-0.013}$	1120	$5.3^{+0.7}_{-0.7}$	-0.41 ± 0.05		
A267	2.65	$6.8^{+1.1}_{-0.5}$	540	$2.8^{+0.2}_{-0.2}$	$0.089^{+0.006}_{-0.006}$	1207	$6.3^{+0.7}_{-0.6}$	-0.29 ± 0.05		✓
A370	2.99	$8.2^{+0.5}_{-0.5}$	509	$2.8^{+0.2}_{-0.2}$	$0.099^{+0.006}_{-0.005}$	1186	$7.0^{+0.6}_{-0.6}$	-0.31 ± 0.07		
A383	3.44	$4.5^{+0.2}_{-0.2}$	473	$1.8^{+0.2}_{-0.1}$	$0.093^{+0.007}_{-0.008}$	936	$2.8^{+0.3}_{-0.2}$	-1.13 ± 0.01	✓	✓
A521	4.79	$5.7^{+0.2}_{-0.2}$	283	$0.4^{+0.1}_{-0.1}$	$0.123^{+0.027}_{-0.022}$	1240	$7.0^{+0.5}_{-0.5}$	-0.01 ± 0.12		
A586	4.84	$5.7^{+0.5}_{-0.5}$	505	$2.2^{+0.1}_{-0.1}$	$0.102^{+0.007}_{-0.006}$	1047	$3.9^{+0.4}_{-0.4}$	-0.59 ± 0.04		✓
A611	4.44	$7.2^{+0.5}_{-0.6}$	527	$2.8^{+0.2}_{-0.2}$	$0.096^{+0.007}_{-0.006}$	1203	$6.6^{+0.8}_{-0.8}$	-0.63 ± 0.03		✓
ZwCl0839.9+2937	3.94	$4.1^{+0.5}_{-0.3}$	431	$1.4^{+0.1}_{-0.1}$	$0.082^{+0.006}_{-0.006}$	984	$3.3^{+0.5}_{-0.4}$	-0.88 ± 0.02	✓	✓
A697	2.89	$9.9^{+0.7}_{-0.7}$	585	$3.8^{+0.3}_{-0.3}$	$0.122^{+0.008}_{-0.008}$	1374	$9.8^{+1.0}_{-1.0}$	-0.24 ± 0.03		
A750	3.16	$4.2^{+0.2}_{-0.2}$	458	$1.6^{+0.1}_{-0.1}$	$0.099^{+0.007}_{-0.006}$	915	$2.6^{+0.2}_{-0.2}$	-0.40 ± 0.05		✓
A963	1.27	$5.8^{+0.3}_{-0.3}$	534	$2.7^{+0.2}_{-0.1}$	$0.102^{+0.006}_{-0.008}$	1101	$4.7^{+0.4}_{-0.3}$	-0.67 ± 0.02		✓
A1689	1.82	$9.1^{+0.2}_{-0.2}$	691	$5.7^{+0.3}_{-0.2}$	$0.100^{+0.004}_{-0.005}$	1438	$10.2^{+0.7}_{-0.8}$	-0.882 ± 0.005	✓	✓
A1763	0.82	$7.5^{+0.5}_{-0.5}$	523	$2.5^{+0.1}_{-0.1}$	$0.112^{+0.007}_{-0.006}$	1224	$6.5^{+0.5}_{-0.4}$	-0.27 ± 0.05		
MS1358.1+6245	1.88	$8.0^{+1.0}_{-0.8}$	562	$3.6^{+0.3}_{-0.3}$	$0.079^{+0.006}_{-0.005}$	1294	$8.7^{+1.3}_{-1.9}$	-1.07 ± 0.03	✓	
A1835	2.04	$9.1^{+0.2}_{-0.2}$	673	$5.6^{+0.6}_{-0.3}$	$0.108^{+0.006}_{-0.010}$	1396	$10.0^{+0.8}_{-0.8}$	-1.258 ± 0.002	✓	✓
ZwCl1454.8+2233	3.15	$4.7^{+0.2}_{-0.2}$	432	$1.5^{+0.1}_{-0.1}$	$0.134^{+0.005}_{-0.007}$	906	$2.8^{+0.1}_{-0.1}$	-1.07 ± 0.01	✓	✓
A2009	3.31	$6.3^{+0.4}_{-0.4}$	574	$3.1^{+0.3}_{-0.3}$	$0.087^{+0.008}_{-0.008}$	1102	$4.4^{+0.5}_{-0.6}$	-0.99 ± 0.02	✓	✓
ZwCl1459.4+4240	1.39	$6.5^{+1.4}_{-1.0}$	515	$2.6^{+0.4}_{-0.4}$	$0.091^{+0.015}_{-0.011}$	1067	$4.7^{+1.2}_{-0.9}$	-0.66 ± 0.11		
MS1512.4+3647	1.45	$4.5^{+0.5}_{-0.5}$	351	$0.9^{+0.1}_{-0.1}$	$0.096^{+0.008}_{-0.008}$	905	$3.1^{+0.6}_{-0.4}$	-0.87 ± 0.03	✓	
MS1621.5+2640	3.29	$5.9^{+0.7}_{-0.7}$	414	$1.6^{+0.3}_{-0.2}$	$0.095^{+0.016}_{-0.013}$	875	$3.0^{+0.6}_{-0.5}$	-0.07 ± 0.09		
A2218	2.66	$5.9^{+0.2}_{-0.2}$	517	$2.3^{+0.1}_{-0.1}$	$0.105^{+0.003}_{-0.003}$	1084	$4.3^{+0.2}_{-0.2}$	-0.12 ± 0.06		
A2219	1.68	$11.2^{+0.6}_{-0.4}$	697	$6.1^{+0.2}_{-0.2}$	$0.116^{+0.005}_{-0.004}$	1557	$13.5^{+0.9}_{-1.0}$	-0.22 ± 0.03		
RXJ1720.1+2638	3.45	$7.3^{+0.3}_{-0.3}$	566	$3.0^{+0.2}_{-0.1}$	$0.098^{+0.005}_{-0.007}$	1240	$6.4^{+0.3}_{-0.4}$	-1.109 ± 0.008	✓	✓
A2261	3.18	$6.7^{+0.4}_{-0.3}$	544	$2.9^{+0.2}_{-0.1}$	$0.119^{+0.006}_{-0.007}$	1145	$5.3^{+0.4}_{-0.4}$	-0.73 ± 0.02	✓	
RXJ2129.6+0005	3.69	$6.4^{+0.3}_{-0.3}$	581	$3.5^{+0.4}_{-0.3}$	$0.093^{+0.010}_{-0.009}$	1098	$4.8^{+0.5}_{-0.5}$	-1.06 ± 0.01	✓	✓
A2390	6.19	$11.2^{+0.4}_{-0.4}$	784	$8.6^{+1.0}_{-0.6}$	$0.092^{+0.007}_{-0.009}$	1453	$11.0^{+0.9}_{-1.2}$	-1.035 ± 0.003	✓	✓
A2485	3.05	$5.7^{+0.8}_{-0.7}$	464	$1.8^{+0.2}_{-0.2}$	$0.087^{+0.009}_{-0.008}$	1082	$4.6^{+0.7}_{-0.7}$	-0.59 ± 0.07		✓
A2631	3.64	$6.8^{+0.7}_{-0.6}$	503	$2.4^{+0.3}_{-0.2}$	$0.122^{+0.013}_{-0.012}$	1124	$5.4^{+0.8}_{-0.7}$	-0.26 ± 0.11		

Note. — Column (3): the spectroscopic temperature measured within $0.15 - 1\,R_{500}$; Column (9): the cuspiness parameter at $r = 0.04R_{500}$; Column (10): whether the cluster is a cool core cluster ($\alpha < -0.7$); Column (11): whether P_3/P_0 of the cluster is below the median value of the sample.

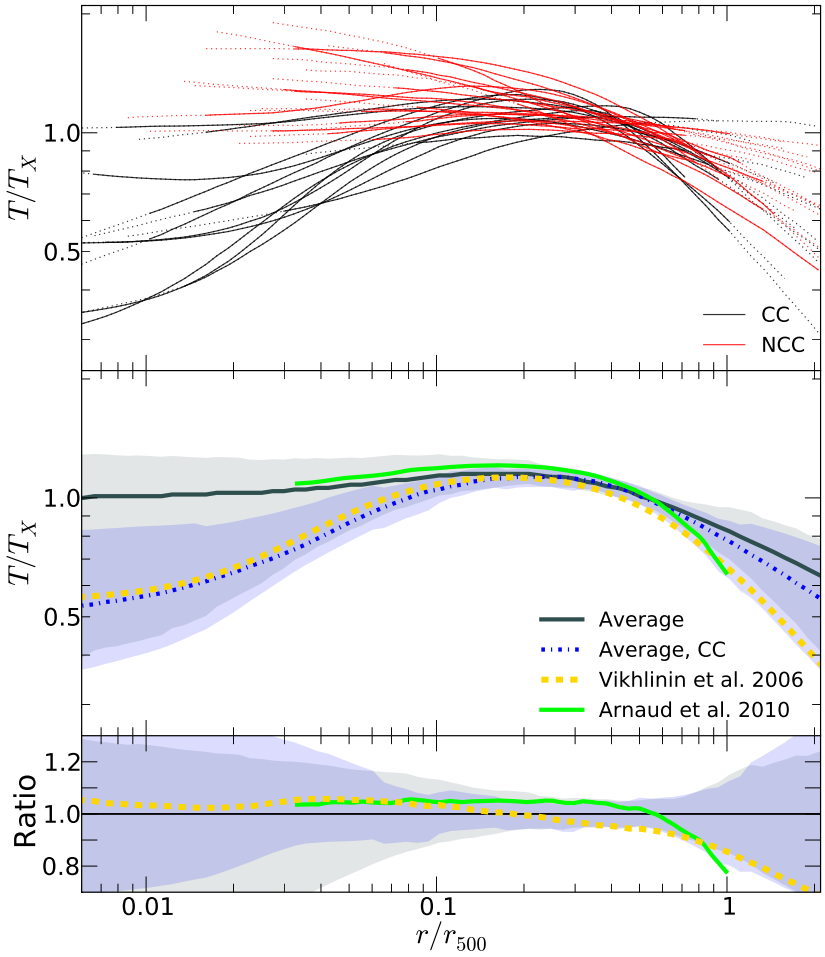

Figure 3-3: *Top:* best-fit three-dimensional temperature profiles. Cool core and non-cool core clusters are plotted in black and red. Solid (dotted) lines show the radial range where the projected temperature (surface brightness) is measured. *Middle:* the average profiles for the total and CC samples, shown in thick solid and dash-dotted lines, respectively. The shaded region represents the rms scatter of the average profile. Also shown are the mean profile of Vikhlinin et al. (2006) (V06), from a sample of nearby *Chandra* relaxed clusters (dashed yellow line), and the median profile of Arnaud et al. (2010) (A10), from a sample of local clusters observed with *XMM-Newton* (solid green line). *Bottom:* the ratio of V06 to the average of our CC sample (dashed yellow) and A10 to the average of our total sample (solid green). The shaded regions shows the scale of the scatter of the average profile.

within $0.15-1\ R_{500}$, where R_{500} is determined iteratively from the self-similar $M_{500}-Y_X$ relation of Vikhlinin et al. (2009a, V09 hereafter) . Given a tentative R_{500}, we determine $Y_X \equiv M_{\rm gas}(< R_{500})\, T_{X\,[0.15-1R_{500}]}$. A new R_{500} can be estimated from the $M_{500}-Y_X$ relation and Y_X is measured again. This procedure is continued until convergence is reached. Values of T_X are listed in Table 3.2. Cool core (CC) and non-cool core (NCC) clusters are plotted in black and red, respectively.

Although we distinguish CC and NCC clusters on the basis of gas density slope alone, cool core clusters also have a stronger decrement in central temperature than non-cool cores. The average temperature of cool core clusters (dash-dotted line) is about 50% lower than that of the total sample (solid line) at $0.01R_{500}$. The average is obtained from the median of temperature profiles, so that the result will not be biased toward the brightest ones, which are all strong cool core clusters. To estimate the uncertainty in the average profile in such a way as to account for the large variation in data quality within our sample (net photon counts range from 4000 to 472000), we generate N sets of samples, Gaussian-distributed around the data point with a dispersion the same as the data uncertainty, which includes errors in scaling quantities T_X and R_{500}. The error of R_{500} comes from Y_X and $\approx 5\%$ statistical error in the normalization of the observed $M_{500}-Y_X$ relation of V09. A median is computed for every realization of the whole cluster sample. The middle 68 percentile of those medians from N realizations is regarded as the uncertainty of the average profile.

Also plotted in Figure 3-3 are the mean profile of Vikhlinin et al. (2006) (V06) [4], from a sample of nearby relaxed *Chandra* clusters which are all CCs by our definition (dashed yellow line), and the median profile of Arnaud et al. (2010) (A10), from a sample of local *XMM-Newton* clusters mixed with CCs and NCCs (solid green line). The average temperature of A10 is scaled by $T_{X\,[0.15-0.75R_{500}]}$, the spectroscopic temperature measured within $0.15-0.75R_{500}$. We convert it to our defined T_X by $T_{X\,[0.15-1R_{500}]}/T_{X\,[0.15-0.75R_{500}]} = 0.97\pm0.01$, a relation found in our sample, consistent with that of Sun et al. (2010), 0.95 ± 0.02.

Our average temperature profile for the total and CC samples agree within 10% of those of A10 and V06, respectively, at $r \lesssim 0.6R_{500}$, but gradually deviate from those beyond that radius. The differences at R_{500} are 21% and 15%, respectively, which are comparable to the 1σ rms scatter of our profiles at that radius (Figure 3-3, *bottom panel*). The temperature at the cluster outskirt is more sensitive to errors in the background modeling, but background uncertainties are expected to produce a systematic bias in the temperature at R_{500} at only the 1-8% level (see Table 3.6 and accompanying discussion below).

This somewhat flatter temperature profile at large radii compared to A10 and

[4] V06 derived a temperature profile scaled by $T_{\rm mg}$, the gas-mass-weighted temperature,

$$\frac{T(x)}{T_{\rm mg}} = 1.35\frac{(x/0.045)^{1.9}+0.45}{(x/0.045)^{1.9}+1}\frac{1}{(1+(x/0.6)^2)^{0.45}}, \tag{3.3}$$

where $x = r/R_{500}$. We convert $T_{\rm mg}$ to T_X by assuming $T_X = 1.11T_{\rm mg}$, an approximation from V06. The index of 0.45 to the second component of the profile was missing in V06, though it can be easily determined from their Figure 16. The corrected form is also explicitly shown in other works (e.g., Vazza et al., 2009; Andersson et al., 2010).

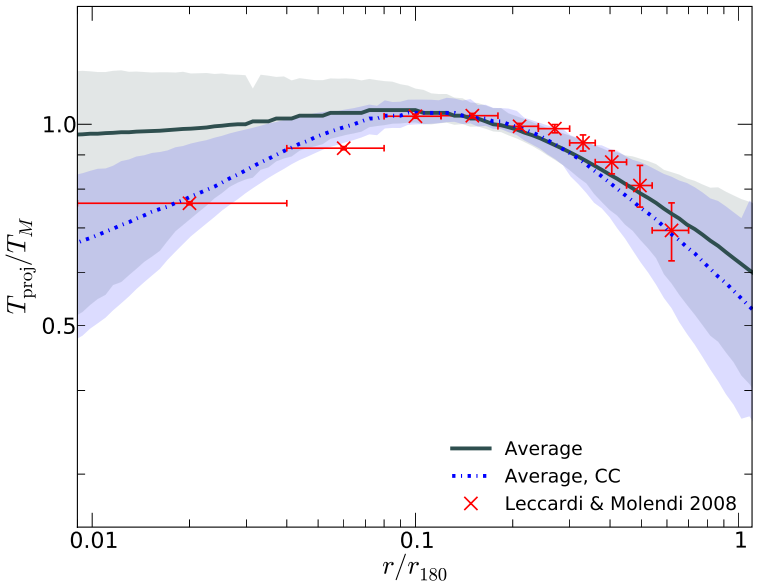

Figure 3-4: Scaled average projected temperature profiles for the total and CC samples, shown in thick solid and dash-dotted lines, respectively. $T_{\rm M}$ is the average projected temperature outside the core. The shaded region represents the rms scatter of the average profile. Also shown is the mean profile of Leccardi & Molendi (2008) (crosses), from a sample of $0.1 \lesssim z \lesssim 0.3$ clusters observed with *XMM-Newton*.

V06 is similar to the finding of Leccardi & Molendi (2008, L08 hereafter) that their average projected temperature profile is the flattest among all other works (De Grandi & Molendi, 2002; Vikhlinin et al., 2005; Pratt et al., 2007) beyond $0.2R_{180}$, measured from ≈ 50 hot, intermediate redshift ($0.1 \lesssim z \lesssim 0.3$) clusters observed with *XMM-Newton*. L08 concluded that the discrepancy, although still within $2-3\sigma$, is probably of systematic origin related to the analysis technique and the background treatment. Since our temperature measurement closely followed the approach of L08 that the background is modeled, instead of subtracted, and the spectral fitting is utilizing the Cash statistic rather than the χ^2, a higher temperature at large radii compared to the measurement from the conventional method is not unexpected (Leccardi & Molendi, 2007).

Figure 3-4 shows the average projected temperature profiles in comparison with L08. The temperature is scaled by $T_{\rm M}$, computed by fitting the projected temperature profile outside the core ($r > 0.15R_{500}$) with a constant, and the radius is scaled by $R_{180} = 1780(T_{\rm M}/5{\rm keV})^{1/2}E(z)^{-1}$ kpc, the same definition used by L08 from Arnaud et al. (2005). The profile of L08 is in good agreement with our average projected temperature profile for the total sample at $r \gtrsim 0.1R_{180}$ (thick solid line) and consistent with that of our CC sample at small radii (dash-dotted line). Although the sample of L08 consists both of CC and NCC clusters, their mean profile is the weighted average one which unavoidable favors CC clusters, thus close to our average CC profile.

Table 3.3: $T_{\rm mg}/T_X$ ratios

$T_{\rm mg}/T_X$	reference	note
X-ray observations		
0.98 ± 0.01	this work	$[0.15, 1]R_{500}$
0.90	Vikhlinin et al. (2006)	$70{\rm kpc}-R_{500}$
0.924 ± 0.004	Arnaud et al. (2010)	T_X: $[0.15, 0.75]R_{500}$, $T_{\rm mg}$: $[0, 1]R_{500}$
SZ observations		
0.82 ± 0.07	Andersson et al. (2010)	$[0, 1]R_{500}$
simulations		
$1.14 - 1.20$	Mathiesen & Evrard (2001)	$[0, 1]R_{500}$, for $3 - 10$ keV clusters [a]
$0.96 - 1.00$	Valdarnini (2006)	$[0, 1]R_{500}$, for $3 - 10$ keV clusters
$0.88 - 0.89$ [b]	Nagai et al. (2007b)	$[0.15, 1]R_{500}$, $T_{\rm mg}$ from mock data
$0.89 - 0.93$ [b]	Nagai et al. (2007b)	$[0.15, 1]R_{500}$, $T_{\rm mg}$ from simulations

[a] $T_{\rm mg}/T_X$ is inversely proportional to T_X.

[b] lower (higher) value for more relaxed (unrelaxed) clusters.

We note that our clusters are more massive and distant ($M \approx 7 \times 10^{14}{\rm M}_\odot$, $z \approx 0.23$) than those of V06 ($M \approx 4 \times 10^{14}{\rm M}_\odot$, $z \approx 0.08$) or A10 ($M \approx 3 \times 10^{14}{\rm M}_\odot$, $z \approx 0.12$), which could contribute to some of the difference in temperature, though L08 do not find a clear evolution in the projected temperature from $z = 0.1$ to 0.3.

Because of differences in the temperature and its slope at large radii, our M_{500} for the CC cluster is expected to be 7% higher than those whose temperature profiles follow that of V06 or 4% lower than those resemble to that of A10 for the total sample, if gas density profiles are similar to ours[5]. In addition to the effect on the hydrostatic mass, the gas mass weighted temperature $T_{\rm mg}$ within R_{500} will be higher than those of V06 and A10 as the temperature does not decrease as much as those at large radii. In Table 3.3 we compare our measured $T_{\rm mg}/T_X$ with values reported in the literature. This ratio is equivalent to $Y_{\rm SZ,sph}/Y_X$ divided by a constant $\frac{\sigma_{\rm T}}{m_{\rm e}c^2}\frac{1}{\mu_{\rm e}m_{\rm p}}$, where $Y_{\rm SZ,sph}$ is the spherically integrated Compton parameter y (Eq. 1.35) over a cluster.

The flatter temperature profile we find makes it even harder to reconcile with the Sunyaev-Zeldovich (SZ) data, as the X-ray data of nearby massive clusters from V06, A10, and V09 have already overpredicted the SZ signal from WMAP data by $20 - 30\%$ (Komatsu et al., 2011). A slightly lower discrepancy of 10% is also found in

[5] The hydrostatic mass at a given overdensity is $M_\Delta \propto -T^{3/2}({\rm d\log T/d\log r} + {\rm d\log n_e/d\log r})^{3/2}$ (see Appendix A of Vikhlinin et al., 2006). Our average ${\rm d\log n_e/d\log r}$ is -1.86 at R_{500} and ${\rm d\log T/d\log r}$ is -0.31 and -0.38 for the total and CC samples, respectively

Andersson et al. (2010) for SZ data of the South Pole Telescope, but an agreement is claimed by Sehgal et al. (2011) with SZ data from the Atacama Cosmology Telescope.

3.2.2 Gas density profiles

Figure 3-5 shows the best-fit gas density profiles scaled by the mean gas density within R_{500}, $\langle n_e \rangle_{R_{500}}$, in comparison with A10 (dashed line). Our average profile agrees within $\approx 10\%$ of that of A10 out to R_{500}.

3.2.3 Thermal pressure profiles

Figure 3-6 shows the thermal pressure profiles of our sample. Following the convention of Nagai et al. (2007a) and A10, we plot the thermal pressure, $P_{\rm th} = n_{\rm gas}\, T$, in terms of the characteristic pressure,

$$P_{500} = n_{\rm gas,\,500}\, T_{500}, \tag{3.4}$$

Also shown is the pressure profile from A10 (dashed line), derived from combining the observed pressure profile of a representative *XMM-Newton* sample of 33 local clusters in the radial range of $0.03 - 1\, R_{500}$ and the simulated pressure profile in $1 - 4\, R_{500}$, which is a generalized NFW (GNFW) model proposed by Nagai et al. (2007a),

$$\frac{P(x)}{P_{500}} = \frac{P_0}{(c_{500}x)^{\gamma}\,[1 + (c_{500}x)^{\alpha}]^{(\beta-\gamma)/\alpha}}, \tag{3.5}$$

where $x = r/R_{500}$, parameters

$$[P_0, c_{500}, \gamma, \alpha, \beta] = [8.130\, {\rm h}_{70}^{-3/2}, 1.156, 0.3292, 1.0620, 5.4807], \tag{3.6}$$

from results based on the $M_{500} - Y_X$ relation of A10 with a standard slope. Although we adopt a different $M_{500} - Y_X$ relation, R_{500} from A10 agrees with that of V09 at 1% level.

Our average pressure profile (solid line) agrees with A10 profile at $\approx 10\%$ level within $0.7R_{500}$, including the core region where A10 is extrapolated. At large radii, it is not as steep as that of A10, just as our temperature profile is flatter than theirs (Figure 3-3). The difference at R_{500}, 20%, is almost the same as the difference in the temperature profile, as expected since the scaled gas density agrees well with A10. Ignoring the discrepancy at large radii which comes from the temperature, the A10 profile indeed characterizes the cluster pressure profiles and clusters do follow the standard self-similar scaling in general. It is also shown that the A10 profile can be applied to local galaxy groups (Sun et al., 2010).

Our average pressure profile can be fit accurately by a GNFW model (dash-dotted line), with parameters

$$[P_0, c_{500}, \gamma, \alpha, \beta] = [16.20^{+7.44}_{-2.30}\, {\rm h}_{70}^{-3/2}, 5.52^{+0.43}_{-2.71}, 0.28^{+0.05}_{-0.11}, 1.47^{+0.18}_{-0.52}, 2.43^{+0.99}_{-0.09}]. \tag{3.7}$$

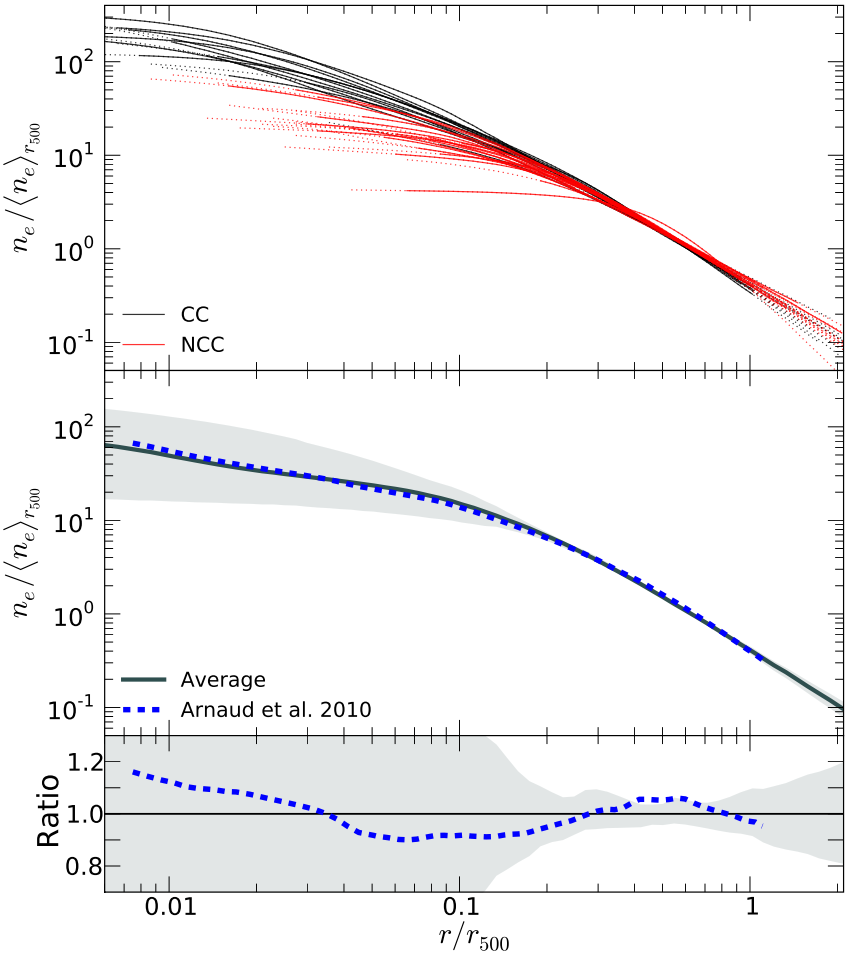

Figure 3-5: *Top:* best-fit gas density profiles scaled by the mean gas density within R_{500}, $\langle n_e \rangle_{R_{500}}$. Cool core and non-cool core clusters are plotted in black and red. Solid (dotted) lines show the radial range where the projected temperature (surface brightness) is measured. *Middle:* the average profile for the total sample. The shaded region represents the rms scatter of the average profile. Also shown is the median profile of Arnaud et al. (2010) (A10), from a sample of local clusters observed with *XMM-Newton* (dashed line). *Bottom:* the ratio of A10 to our average profile (dashed line). The shaded region shows the scale of the scatter of the average profile.

Errors are at 95% CL.

If there are systematic offsets in temperature and gas density between our *Chandra* and A10 *XMM-Newton* sample, then the pressure will not scale the same as each other because $P_{500} \propto M_{500}^{2/3} \propto Y_X^{2/5}$ does not change accordingly to the bias of the pressure. Assuming that T and n_e are overestimated by a constant factor of 10%, for a gas density profile that is similar to ours, R_{500}, $M_{\rm gas}(< R_{500})$, $\langle n_e \rangle_{R_{500}}$, Y_X, and P_{500} will be biased high by 5%, 17%, 1%, 29%, and 11%, respectively (here we ignore subtle changes in T_X due to R_{500}). This shifts the scaled pressure profile P/P_{500} up by 9% and left by 5% from the original. At the same time T/T_X (Figure 3-3) is shifted left by 5% and $n_e/\langle n_e \rangle_{R_{500}}$ (Figure 3-5) is shifted left by 5% and up by 9%, which are not that different from the original regarding the intrinsic scatter in the temperature and gas density.

3.2.4 Systematic errors in X-ray analysis

3.2.4.1 Gas profile modeling

Although the gas density and temperature profiles can be adequately fitted by Eqs. 2.4 and 2.5, there is still $1-5\%$ residual on the surface brightness and projected temperature profiles within $1.5\,R_{500}$ on average (Figure 3-1). To estimate how this deviation affects other X-ray derived quantities, such as the gas mass and the hydrostatic mass, we simulate 3D temperature and gas density profiles centered around the average profile of our sample, assuming the profiles follow the Gaussian distribution at each radial bin. We vary the center and the width of the Gaussian until the simulated 2D temperature and emission measure profiles, projected from simulated 3D profiles, produce similar deviation from the original $2D$ profiles, calculated from the averaged best-fit $3D$ profiles of our sample, as real data exhibit. This procedure is carried out by MCMC (§3.1.3) because of the large number of degrees of freedom in the parameter space ($N = 2\times$ number of radial bins).

Table 3.4 shows the observed fractional residuals of projected temperature and emission measure profiles in comparison with those from simulated $3D$ profiles. Our reconstructed profiles are in good agreement with the observed projected profiles. The mean, in the fractional difference from the original $3D$ profile, and the width, in the fractional difference from the mean, of the Gaussian at different scaled radii are shown in the middle of Table 3.4. The resulting deviations of the hydrostatic mass M_X, gas mass $M_{\rm gas}$, gas mass fraction $f_{\rm gas}$, and gas thermal pressure P_X from the original averaged profiles are listed in the bottom of the table. To avoid bias from parametrizing 3D temperature and density profiles again, we calculate these derived quantities from simulated gas profiles directly rather than from their best-fit gas models.

Because our emission measure profile is fitted fairly well, combined with the fact that the deviation of the gas density profile should be generally less than that of the emission measure profile since the former is from the integration of the gas density, we do not detect any obvious bias in the gas density or the total gas mass within $1.5\,R_{500}$. However, the simulation shows that the $1-3\,\%$ positive residual of the

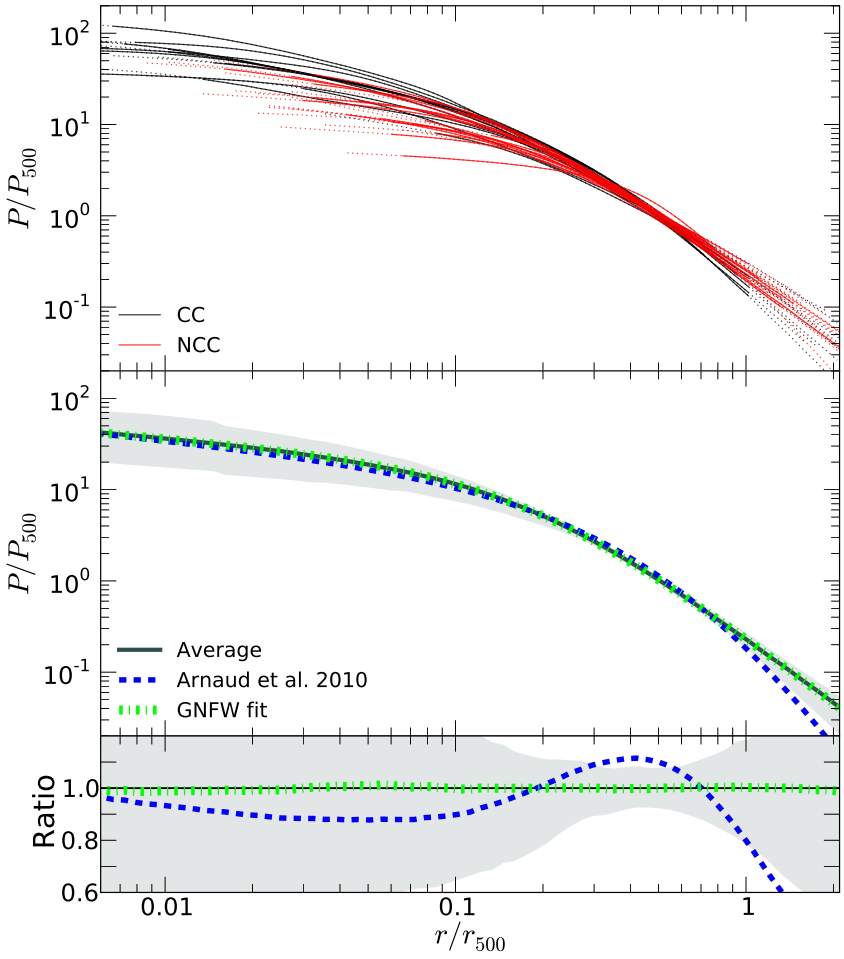

Figure 3-6: *Top:* best-fit thermal pressure profiles. Cool core and non-cool core clusters are plotted in black and red. Solid (dotted) lines show the radial range where the projected temperature (surface brightness) is measured. *Middle:* the average profile for the total sample. The shaded region represents the rms scatter of the average profile. Also shown are the median profile of Arnaud et al. (2010) (A10), from a sample of local clusters observed with *XMM-Newton* (dashed line) and the best-fit GNFW model for our average profile (dash-dotted line). *Bottom:* the ratio of the A10 profile and the best-fit GNFW model to our average profile (dashed and dash-dotted line, respectively). The shaded region show the scale of the scatter of the average profile.

projected temperature at $0.2-0.6R_{500}$ could lead an underestimate of T_{3D} by $2-7\,\%$ around this region, and a corresponding overestimate of the thermal pressure. The effect on M_X is not that clear, because the deviation of M_X depends on the derivative of the temperature and gas density residuals which themselves are not significant compared to the uncertainty. There could be a few percent overestimate at $0.2R_{500}$ and $20 \pm 11\,\%$ underestimate at $1.5R_{500}$.

We also look into how the scatter on the projected profiles widen the uncertainty of other quantities. Similar to the method used above, we simulate 3D profiles to match the observed dispersions of the projected temperature and the emission measure profiles. We fix the center the Gaussian distribution at the value of our averaged 3D profile and adjust the width of the Gaussian. M_X, $M_{\rm gas}$, $f_{\rm gas}$ and P_X are now calculated from the best-fit models of simulated 3D gas profiles instead of from simulated profiles directly, in order to achieve the best measurement results possible. The observed scatter of projected profiles, the dispersion of simulated gas profiles and the spreading of derived quantities are listed in Table 3.5.

The dispersion of T_{3D} is similar to that of T_{2D}. The dispersion of n_e is about a half of that of the emission measure at large radii. At inner radii, where the projection from outer layers attributes some errors, the dispersions are similar.

3.2.4.2 Background subtraction

Although uncertainties associated with X-ray backgrounds affect both temperature and surface brightness measurements, their effect on the derived X-ray quantities is expected to be reduced when calculating the average profile of those quantities. This is because the errors from the backgrounds contribute to the random measurement errors. To address the effect of backgrounds on the average gas profiles, we vary the sky background by $\pm 1\sigma$ and the particle background by 2% separately and perform the same procedure described in §3.1.2 for all our clusters. We average the fractional changes on derived quantities from the nominal best-fit values weighted by the measurement errors of those quantities across the sample. Table 3.6 lists the systematic deviation caused by the backgrounds at different scaled radii.

T_{3D} is more sensitive to the particle background than to the sky background, whereas the opposite is true for n_e. Because T_{3D} and n_e are correlated with the backgrounds in the same way, P_X is the most subject to the background, with $3-9\,\%$ differences at R_{500} for each background change. M_X varies $\mp(4 \pm 2)\%$ with $\pm 2\%$ changes of the particle background at R_{500} , but does not appear to have a clear trend with the variation of the sky background. $f_{\rm gas}$ has similar but inverse changes as M_X does. $M_{\rm gas}$ is least affected by the backgrounds among all the quantities, with a deviation about 1% at R_{500}.

3.2.4.3 Forward v.s. Backward methods

Another commonly used approach to derive X-ray masses is the *backward method*, named by Meneghetti et al. (2010), to be distinguished from our approach called *forward method*. The backward method starts with a functional form of the total

Table 3.4: Systematic deviations from the averaged best-fit profile

	$(X - X_{\rm ave})/X_{\rm ave}$			
	$0.2R_{500}$	$0.45R_{500}$	$1.0R_{500}$	$1.5R_{500}$
Observed and reconstructed projected profiles [a]				
T_{2D} obs.	0.01 ± 0.01	0.03 ± 0.02	-0.03 ± 0.05	-0.05 ± 0.06
T_{2D} rec.	0.01 ± 0.02	0.04 ± 0.02	-0.02 ± 0.06	-0.05 ± 0.06
EM obs.	0.00 ± 0.01	-0.00 ± 0.01	0.03 ± 0.02	-0.02 ± 0.04
EM rec.	0.00 ± 0.00	-0.01 ± 0.01	0.03 ± 0.02	-0.03 ± 0.03
Reconstructed 3D profiles [b]				
T_{3D}	-0.00 ± 0.01	0.07 ± 0.01	0.03 ± 0.01	0.01 ± 0.01
$\sigma_{T_{3D}}$	0.03 ± 0.01	0.02 ± 0.01	0.08 ± 0.01	0.07 ± 0.01
n_e	-0.00 ± 0.01	-0.01 ± 0.01	0.02 ± 0.01	0.01 ± 0.01
σ_{n_e}	0.01 ± 0.01	0.00 ± 0.01	0.02 ± 0.01	0.01 ± 0.01
Deviations of other X-ray derived quantities [c]				
M_X	-0.06 ± 0.06	0.03 ± 0.04	-0.00 ± 0.16	0.20 ± 0.11
$M_{\rm gas}$	-0.00 ± 0.01	-0.00 ± 0.01	0.00 ± 0.01	0.01 ± 0.01
$f_{\rm gas}$	0.08 ± 0.05	0.02 ± 0.04	0.02 ± 0.11	-0.08 ± 6.40
P_X	-0.00 ± 0.03	0.04 ± 0.02	0.06 ± 0.09	0.02 ± 0.07

[a]The observed mean fractional residual of the projected temperature and the emission measure (see Figure 3-1) in comparison with the deviation of the simulated profile from the observed averaged value.

[b]The mean (in the fractional difference from the observed averaged value) and the width (in the fractional difference from the mean) of the Gaussian distribution of simulated 3D profiles.

[c]The fractional deviation of the simulated profile from the observed averaged profile.

Table 3.5: Dispersions from the averaged best-fit profile

	stdev(X)/⟨X⟩			
	$0.15R_{500}$	$0.45R_{500}$	$1.0R_{500}$	$1.5R_{500}$
Observed and reconstructed projected profiles				
T_{2D} obs.	0.08	0.12	0.13	0.14
T_{2D} rec.	0.09	0.12	0.13	0.14
EM obs.	0.05	0.07	0.15	0.33
EM rec.	0.05	0.07	0.15	0.32
Reconstructed 3D profiles				
T_{3D}	0.14	0.17	0.15	0.14
n_e	0.05	0.06	0.09	0.15
Dispersions of other X-ray derived quantities				
M_X	0.05	0.06	0.09	0.10
$M_{\rm gas}$	0.02	0.02	0.02	0.04
$f_{\rm gas}$	0.05	0.05	0.09	0.11
P_X	0.05	0.06	0.08	0.12

mass, with the gas density inferred from the observed surface brightness profile, and moves backward to predict either the projected or deprojected temperature via the hydrostatic equilibrium equation,

$$-G\mu m_p \frac{\rho_g M}{r^2} = \frac{d\left(\rho_g T_{\rm 3D}\right)}{dr}, \tag{3.8}$$

where G is the gravitational constant, $m_{\rm p}$ is the proton mass and μ is the mean molecular weight. The model temperature is then compared with the observed one, with a goodness of fit estimated by

$$\chi^2 = \sum_i \frac{\left(T_{\rm data,i} - T_{\rm model,i}\right)^2}{\sigma^2_{T,i}}, \tag{3.9}$$

where $T_{\rm data}$ is the either projected or deprojected temperature from the spectral fit; $T_{\rm model}$ is predicted value from the hydrostatic equilibrium equation. Further detail of this technique is described in Ettori et al. (2002).

Here we adopt the NFW profile (Eq. 1.12) for the total mass with two free parameters in the backward method. The model 3D temperature is projected by the spectral weighting scheme of Vikhlinin (2006) to be able to compare with the observed temperature. The gas density is predetermined by fitting the surface brightness profile with the projected model of Eq. 2.4 with n_{02} set to zero. We exclude the inner 50 kpc temperature data from the fit, as suggested by Ettori et al. (2010). The comparison of the hydrostatic mass from forward and backward methods at different radii is shown in Figure 3-7.

Table 3.6: Systematic uncertainties from the background subtraction

	$(X - X_{\rm nom})/X_{\rm nom}$			
	$0.2R_{500}$	$0.45R_{500}$	$1.0R_{500}$	$1.5R_{500}$
T_{3D}				
sky bkg. -1σ	-0.01 ± 0.01	-0.00 ± 0.01	-0.01 ± 0.02	-0.02 ± 0.03
sky bkg. $+1\sigma$	-0.01 ± 0.01	-0.01 ± 0.01	-0.02 ± 0.02	-0.01 ± 0.03
particle bkg. -2%	0.00 ± 0.01	0.02 ± 0.01	0.04 ± 0.02	0.06 ± 0.03
particle bkg. $+2\%$	-0.01 ± 0.01	-0.03 ± 0.01	-0.08 ± 0.02	-0.11 ± 0.03
n_e				
sky bkg. -1σ	-0.00 ± 0.01	0.01 ± 0.01	0.03 ± 0.01	0.04 ± 0.01
sky bkg. $+1\sigma$	-0.00 ± 0.01	-0.00 ± 0.01	-0.03 ± 0.01	-0.05 ± 0.01
particle bkg. -2%	-0.00 ± 0.01	0.00 ± 0.01	0.01 ± 0.01	0.01 ± 0.01
particle bkg. $+2\%$	-0.00 ± 0.01	0.00 ± 0.01	-0.01 ± 0.01	-0.02 ± 0.01
M_X				
sky bkg. -1σ	0.01 ± 0.01	-0.02 ± 0.01	-0.02 ± 0.02	-0.03 ± 0.02
sky bkg. $+1\sigma$	0.02 ± 0.01	-0.00 ± 0.01	0.02 ± 0.02	0.02 ± 0.02
particle bkg. -2%	0.01 ± 0.01	0.00 ± 0.01	0.04 ± 0.02	0.05 ± 0.02
particle bkg. $+2\%$	0.01 ± 0.01	-0.01 ± 0.01	-0.04 ± 0.02	-0.06 ± 0.02
$M_{\rm gas}$				
sky bkg. -1σ	0.00 ± 0.01	-0.00 ± 0.01	0.01 ± 0.01	0.02 ± 0.01
sky bkg. $+1\sigma$	0.00 ± 0.01	-0.00 ± 0.01	-0.01 ± 0.01	-0.02 ± 0.01
particle bkg. -2%	0.00 ± 0.01	0.00 ± 0.01	0.01 ± 0.01	0.01 ± 0.01
particle bkg. $+2\%$	-0.00 ± 0.01	-0.00 ± 0.01	-0.00 ± 0.01	-0.01 ± 0.01
$f_{\rm gas}$				
sky bkg. -1σ	-0.01 ± 0.01	0.02 ± 0.01	0.03 ± 0.02	0.05 ± 0.02
sky bkg. $+1\sigma$	-0.01 ± 0.01	0.01 ± 0.01	-0.02 ± 0.02	-0.04 ± 0.02
particle bkg. -2%	-0.00 ± 0.01	0.00 ± 0.01	-0.03 ± 0.02	-0.03 ± 0.02
particle bkg. $+2\%$	-0.00 ± 0.01	0.02 ± 0.01	0.05 ± 0.02	0.07 ± 0.02
P_X				
sky bkg. -1σ	-0.01 ± 0.01	0.00 ± 0.01	0.03 ± 0.02	0.05 ± 0.03
sky bkg. $+1\sigma$	-0.01 ± 0.01	-0.01 ± 0.01	-0.05 ± 0.02	-0.07 ± 0.03
particle bkg. -2%	0.00 ± 0.01	0.02 ± 0.01	0.06 ± 0.02	0.07 ± 0.03
particle bkg. $+2\%$	-0.01 ± 0.01	-0.03 ± 0.01	-0.09 ± 0.02	-0.13 ± 0.03

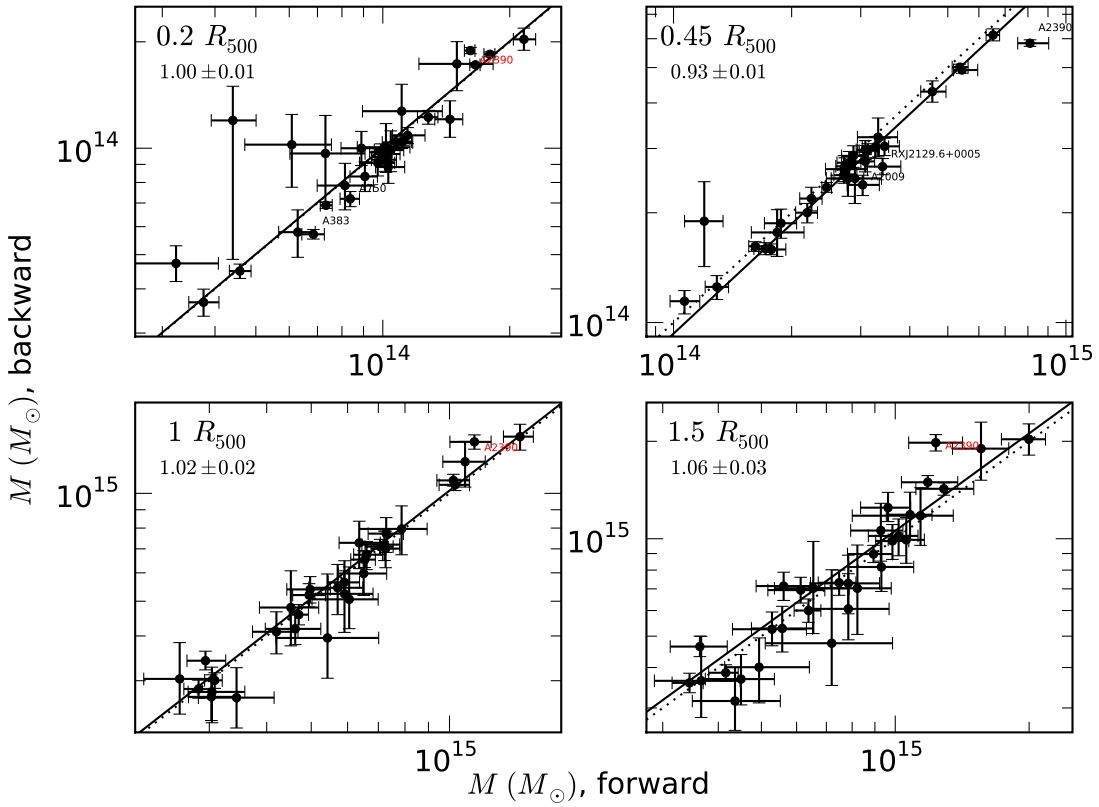

Figure 3-7: Comparison of X-ray masses from forward and backward methods at different radii. The solid line shows the best-fit linear relation and the dotted one shows the line of the equality.

The masses from forward and backward methods are consistent with each other at 0.2 and 1 R_{500}. However, at $0.45R_{500}$ ($\approx R_{2500}$) the mass from the backward method is $7 \pm 1\,\%$ lower than that of the forward method and higher by $6 \pm 3\,\%$ at $1.5R_{500}$ ($\approx R_{200}$). This discrepancy can be fully explained by the residuals inherent from both methods, shown in Figure 3-8. The emission measure profiles for both methods show a similar level of the residual within $0.1 - 1\,R_{500}$, but the projected temperature profiles have somewhat different trends of the deviation.

Similar to what we have done in §3.2.4.1, we start from the residual profiles for the backward method and construct a sample of 3D gas profiles that match the observed deviations. The simulation shows that the resulted mass is biased low by $12 \pm 8\,\%$ at $0.45R_{500}$ and low by $8 \pm 5\,\%$ at $1.5R_{500}$ (Table 3.7). Compared to those from the forward method, low by $3 \pm 4\,\%$ at $0.45R_{500}$ and low by $20 \pm 11\,\%$ at $1.5R_{500}$ (Table 3.4), this explains the $7 \pm 1\,\%$ and $6 \pm 3\,\%$ differences among the two methods at 0.45 and 1.5 R_{500}, respectively. The same argument can be applied to other radii where we have consistent results between the two methods.

The backward method with a simple assumption of the mass profile generally does

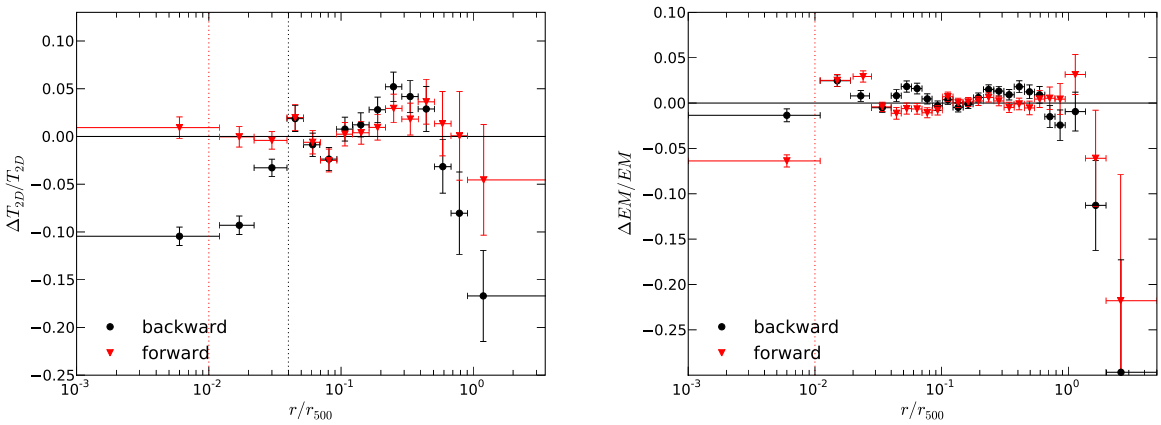

Figure 3-8: Fractional residuals of best-fit projected temperature (left) and emission measure profiles (right) from forward and backward methods. Note that inner 50 kpc ($\approx 0.04\,R_{500}$, dotted black line) temperature data are not included in the fit for the backward method; inner 12 kpc (dotted red line) temperature and surface brightness data are not included for the forward method.

not fit the temperature data as well as the forward method does. It underpredicts T_{2D} by $1-5\,\%$ in $0.1-0.45R_{500}$ and overpredicts it by $3-13\,\%$ in $0.6-1R_{500}$. The residuals suggest that P_X could be biased low by $8\pm3\%$ and high by $5\pm2\,\%$ at 0.45 and 1 R_{500}, respectively.

3.2.4.4 *Chandra* calibration

The calibration work of Nevalainen et al. (2010) show that the *Chandra* ACIS flux is $\sim 2\%$ and $3-11\%$ higher than that of *XMM-Newton* EPIC in the $0.5-2$ keV and $2-7$ keV band, respectively. Since our gas density is measured in the soft band, it should not be very different from the *XMM-Newton* measurement in this energy band. However, if compared to the *XMM-Newton* measurement in other bands, the gas density and the total gas mass can be possibly $1-6\%$ higher than others as $n_e \propto S_{\rm X}^{1/2}$. As to the temperature, the *Chandra* measurement is $8-15\%$ higher than that of *XMM-Newton* when the spectrum is fitted in the $0.5-7.0$ keV band. As a result, P_X, M_X, and $f_{\rm gas}$ can be $11-19\%$ higher, $8-15\%$ higher, and $4-12\%$ lower than those from *XMM-Newton*, respectively. However, the *Chandra* self-calibration indicates that the temperature is at most 6% biased high (Vikhlinin et al., 2009a) and the soft band flux is accurate to 3%[6], corresponding to possible $\pm2\%$, $-1-7\%$, $0-6\%$, and $-7-1\%$ errors in $M_{\rm gas}$, P_X, M_X, and $f_{\rm gas}$, respectively. If M_X is estimated at the overdensity radius, then M_Δ can differ by up to 9% as $\delta M_\Delta/M_\Delta \propto 1.5\delta T/T$ (see Appendix A of Vikhlinin et al., 2006).

[6]http://cxc.harvard.edu/cal/Acis/Cal_prods/qe/qe_memo.ps

Table 3.7: Systematic deviations from the averaged best-fit profile for the backward method

	$(X - X_{\rm ave})/X_{\rm ave}$			
	$0.2R_{500}$	$0.45R_{500}$	$1.0R_{500}$	$1.5R_{500}$
Observed and reconstructed projected profiles [a]				
T_{2D} obs.	0.03 ± 0.01	0.03 ± 0.02	-0.13 ± 0.05	-0.17 ± 0.05
T_{2D} rec.	0.04 ± 0.02	0.03 ± 0.02	-0.13 ± 0.04	-0.17 ± 0.05
EM obs.	0.01 ± 0.01	0.02 ± 0.01	-0.02 ± 0.02	-0.08 ± 0.04
EM rec.	0.01 ± 0.00	0.01 ± 0.01	-0.02 ± 0.01	-0.09 ± 0.05
Reconstructed 3D profiles [b]				
T_{3D}	0.03 ± 0.01	0.09 ± 0.01	-0.05 ± 0.01	-0.09 ± 0.01
$\sigma_{T_{3D}}$	0.03 ± 0.01	0.02 ± 0.01	0.02 ± 0.01	0.04 ± 0.01
n_e	-0.00 ± 0.01	0.01 ± 0.01	-0.00 ± 0.01	-0.01 ± 0.01
σ_{n_e}	0.00 ± 0.01	0.00 ± 0.01	0.00 ± 0.01	0.02 ± 0.01
Deviations of other X-ray derived quantities [c]				
M_X	-0.09 ± 0.06	0.12 ± 0.08	-0.01 ± 0.05	0.08 ± 0.05
$M_{\rm gas}$	-0.00 ± 0.01	0.01 ± 0.01	0.00 ± 0.01	-0.00 ± 0.01
$f_{\rm gas}$	0.12 ± 0.05	-0.07 ± 0.04	0.06 ± 0.03	0.04 ± 0.07
P_X	0.03 ± 0.03	0.08 ± 0.03	-0.05 ± 0.02	-0.10 ± 0.04

[a]The observed stacked fractional residual of the projected temperature and the emission measure (see Figure 3-8) in comparison with the deviation of the simulated profile from the observed averaged value.

[b]The mean (in the fractional difference from the observed averaged value) and the width (in the fractional difference from the mean) of the Gaussian distribution of simulated 3D profiles.

[c]The fractional deviation of the simulated profile from the observed averaged profile.

3.2.5 Comparison with other X-ray studies

3.2.5.1 Gas profiles

Figure 3-9 shows the comparison of temperature and emission measure profiles to those of Vikhlinin et al. (2006) (V06) for A383 and A2390, the only two clusters that are common to both samples. For A383, we have a good agreement with V06 on both profiles between $r_{\rm min}$ and $r_{\rm det}$, where $r_{\rm min}$ is the inner boundary of the radial range for the temperature profile fit and $r_{\rm det}$ is the 3σ detection radius of the surface brightness profile used by V06. However, for A2390, our temperature profile is quite different from V06. Vikhlinin et al. (2005) reported that the column density found in *Chandra* data was $\sim$ 1.6 times higher than the radio value in A2390, but our fit with n_H fixed at the radio value does not yield any obvious residual at the low energy band. Furthermore, the cumulative gas mass fraction of A2390 from V06 is significantly higher from those of other hot clusters in V06 sample, which could indicate that the mass is underestimated because of the low temperature. The extended excess at $r \sim$ 400kpc in the emission profile, which is either ignored or completely excluded from the fit by V06, is likely the result of the central active galactic nucleus (AGN) activities. AGN can produce energetic jets and bubbles, greatly modifying the gas distribution, as observed in other clusters (McNamara et al., 2005).

3.2.5.2 $M_{\rm gas}$

Figure 3-10 compares our estimates of $M_{\rm gas}$ to those from V06, Allen et al. (2008) (A08), Croston et al. (2008) (C08), Maughan et al. (2008) (M08), Ettori et al. (2010) (E10) and Zhang et al. (2010) (Z10)[7]. $M_{\rm gas}$ is calculated within the same R_{2500} or R_{500} from those works. Our $M_{\rm gas}$ is consistent with V06[8] and E10, but 9% lower than A08, 7% higher than M08 and 11% higher than C08. The greatest discrepancy is found when comparing with Z08 from *XMM-Newton* measurements. Our $M_{\rm gas}$ is consistently higher by 27% at both R_{2500} and R_{500}. We can not explain this disagreement since the systematic error from the background or modeling is typically at 1% level and the uncertainty from the *Chandra* and *XMM-Newton* cross calibration is approximately 6% (§3.2.4).

3.2.5.3 M_X

Figure 3-11 compares our X-ray hydrostatic mass with those from other X-ray works. The average ratio between our M_X and others, $M_{\rm reference}$, determined from FITEXY fitting routine (Press et al., 1992), are listed in Table. 3.8. The comparison is taken at the same radius quoted in the literature.

Because we have a distinctly different profile for one of the two clusters that are in common with the sample of Vikhlinin et al. (2006) (V06), A2390 (§3.2.5.1), we do not include it for the comparison. For the other cluster, A383, our M_{2500} and M_{500} are consistent to those of V06 and errors of M_X are comparable to theirs. We

[7] $M_{\rm gas}$ from V06, A10, and E10 are converted from $f_{\rm gas}$ and M_X

[8] Our $M_{\rm gas}$ is slightly higher than V06 because of A2390.

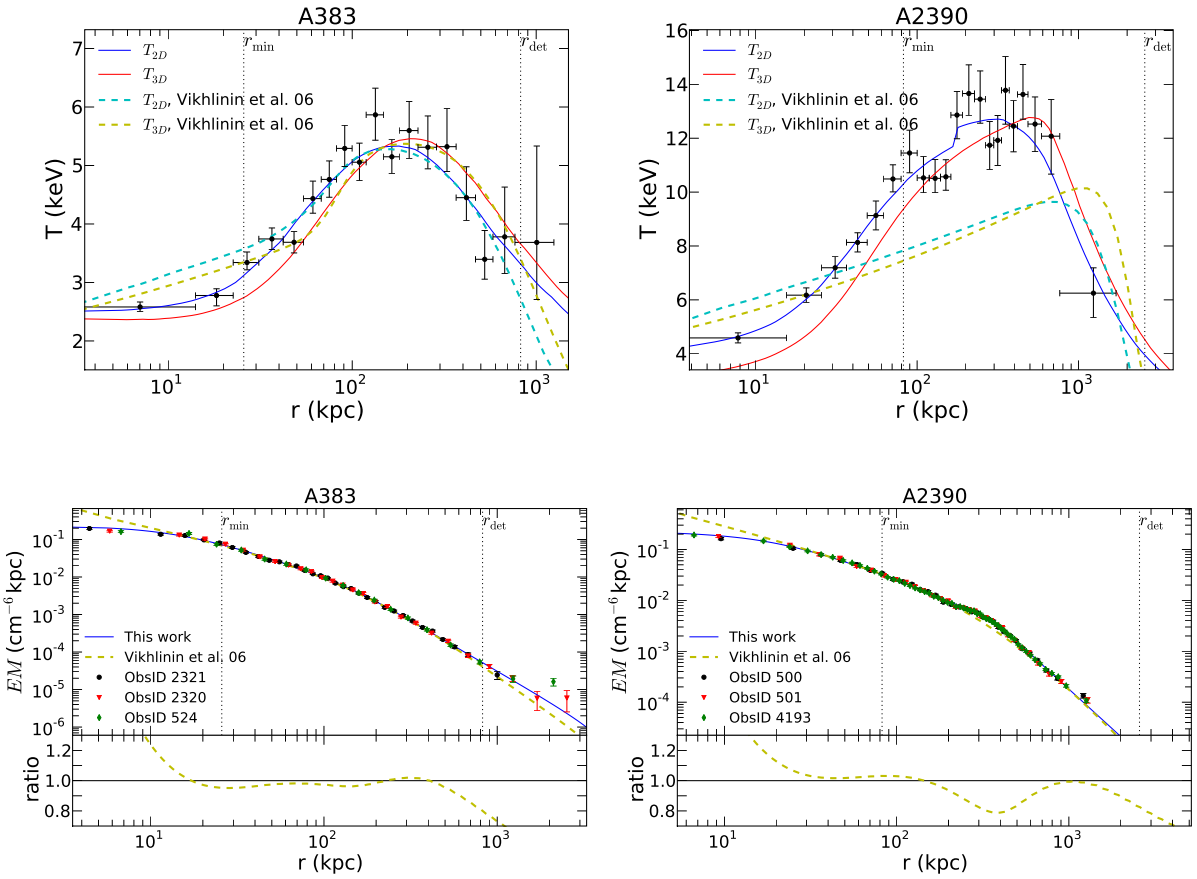

Figure 3-9: Comparison of temperature (*top*) and emission measure (*bottom*) profiles to the result of Vikhlinin et al. (2006) for A383 and A2390. $r_{\rm min}$ and $r_{\rm det}$ denote the inner boundary of the radial range for the temperature profile fit and 3σ detection radius of the surface brightness profile used by Vikhlinin et al. (2006), respectively.

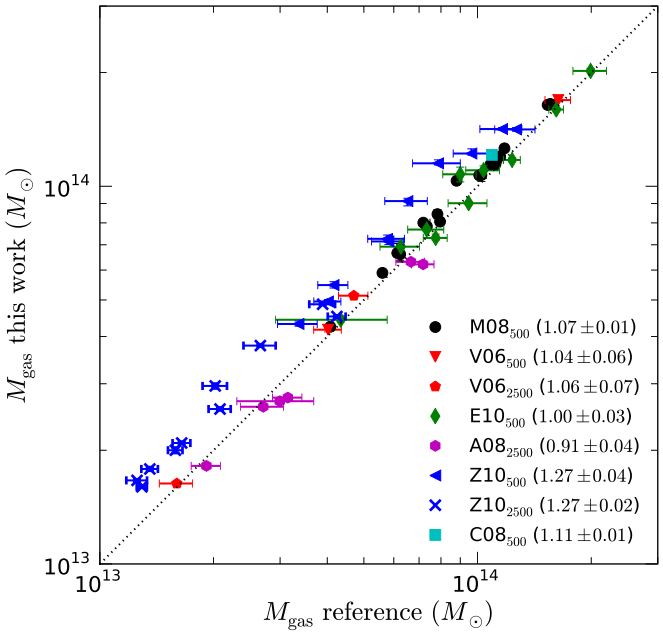

Figure 3-10: Comparison of $M_{\rm gas}$ with those of Vikhlinin et al. (2006) (V06), Allen et al. (2008) (A08), Croston et al. (2008) (C08), Maughan et al. (2008) (M08), Ettori et al. (2010) (E10) and Zhang et al. (2010) (Z10). $M_{\rm gas}$ is calculated within the same radius from the reference works. Subscripts next to the plot label indicate the radius (R_{2500} or R_{500}) and numbers in the parentheses are the average ratios of our $M_{\rm gas}$ to others. The dotted line shows the line of the equality.

use the same *Chandra* data for A383, but employ a different error analysis. Our uncertainty is estimated from the distribution of the Markov chain, whereas V06 use Monte Carlo realizations of the original data. Both approaches yield comparable results as expected (§3.1.3).

Our result is in good agreement with that of Mahdavi et al. (2008) at R_{1000} and R_{500}, but $12\pm3\,\%$ higher than theirs at R_{2500}. Even with A2390 excluded, whose mass seems to be higher compared to all other works, our mass is still $9\pm3\,\%$ higher. We note that Mahdavi et al. (2008) use the backward method with a NFW mass profile, which could underestimate M_{2500} by $12\pm8\,\%$ or differ from our forward method by $7\pm1\,\%$ (§3.2.4.3). These numbers happen to explain the difference at R_{2500}. Yet this discrepancy is not found when comparing our M_{2500} to that of Allen et al. (2008), who use a backward method as well.

Compared to 10 clusters[9] of Zhang et al. (2010) (Z10) observed with *XMM-Newton*, our masses are high by $13-26\,\%$ at $1-2\sigma$ level between R_{2500} and R_{500}. Part of the disagreement could arise from the systematic difference between *XMM-Newton* and *Chandra* temperatures, causing $8-15\%$ errors (§3.2.4.4). However, contrary to the high mass found in comparison with Z10, our M_{500} is $7\pm4\,\%$ lower than that of Ettori et al. (2010) from 10 *XMM-Newton* clusters. This suggests that there is at least a $\approx 10\%$ error from the analysis itself among these works.

We also compare the projected mass within 250 kpc ($\approx 0.2R_{500}$ for our sample) to that of Richard et al. (2010). The projected mass is integrated up to $4.5R_{500}$. Since the gas models of Vikhlinin et al. (2006) do not guarantee the convergence of the projected mass and the mass at $r \lesssim 1.5R_{500}$ is purely an extrapolated value, we include additional uncertainty of the mass estimated from the difference between $M_{2D}(< 1.5R_{500})$ and $M_{2D}(< 4.5R_{500})$, which is usually less than few percents. Our result is consistent within $4\pm2\,\%$ of that of Richard et al. (2010). Clusters with masses differed more than 2σ are A68 and A2390, where our masses are 1.8 and 1.2, respectively, higher than theirs.

3.2.5.4 $f_{\rm gas}$

In this section we perform the sample-to-sample comparison of the cumulative gas mass fraction $f_{\rm gas} = M_{\rm gas}(< r)/M(< r)$. Since $f^{\rm X}_{\rm gas}$ is found to correlate with the cluster mass or temperature (e.g., Mohr et al., 1999; Sanderson et al., 2003; Vikhlinin et al., 2006; Sun et al., 2009; Pratt et al., 2010), we restrict the comparison to those measured from hot clusters ($T \gtrsim 5$ keV). Figure 3-12 plots $f_{\rm gas}$ with the total mass from M_X, $f^{\rm X}_{\rm gas}$, as a function of the overdensity, along with those from Vikhlinin et al. (2006) (V06)[10]. The sample of V06 is from nearby relaxed clusters, which are all CC as well. Our $f^{\rm X}_{\rm gas}$ from CC clusters (solid black lines) are fully consistent with those of V06 (thick blue lines) at all radii.

In Table 3.9, we compile the average $f_{\rm gas}$ at R_{2500} from the literature. Our $f^{\rm X}_{\rm gas}$ is in good agreement with that of V06[11], but $13-20\%$ lower than those of Allen et al.

[9] not including A115 because we analyze A115N instead of A115S

[10] not including A2390 from V06

[11] Strictly speaking, we should compare our $f^{\rm X}_{\rm gas}$ from the CC sample, 0.093 ± 0.003, to that of

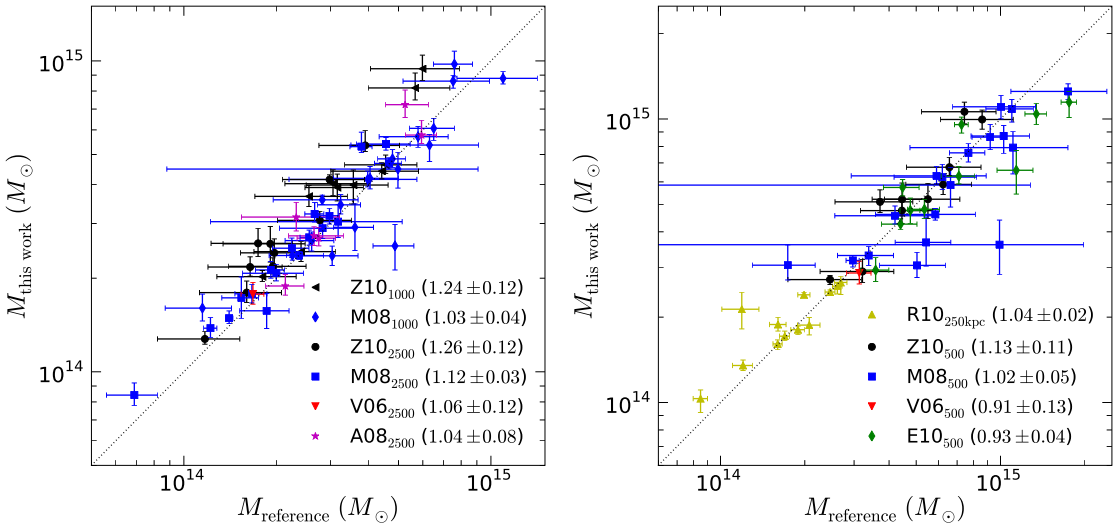

Figure 3-11: Comparison of M_X with those of Vikhlinin et al. (2006) (V06), Allen et al. (2008) (A08), Mahdavi et al. (2008) (M08), Zhang et al. (2010) (Z10), Ettori et al. (2010) (E10), and Richard et al. (2010) (R10). M_X is calculated at the same radius quoted in reference works. Subscripts next to the plot label indicate the radius (250 kpc, R_{2500}, R_{1000} or R_{500}) and numbers in the parentheses are the average ratios of our M_X to others. The mass of E10 is the projected rather than the 3D mass. The dotted line shows the line of the equality.

Table 3.8: Comparison of X-ray hydrostatic Masses

Reference	Data	# of obj.	$M_X/M_{\rm reference}$ 250kpc [b]	R_{2500}	R_{1000}	R_{500}	$\sigma_M/\sigma_{M,\rm ref}$ [a] R_{2500}	R_{500}
Zhang et al. (2010)	*XMM*	10 [c]	···	1.26 ± 0.12	1.24 ± 0.12	1.13 ± 0.11	0.34 ± 0.16	0.36 ± 0.15
Mahdavi et al. (2008)	*Chandra*	18	···	1.12 ± 0.03	1.03 ± 0.04	1.02 ± 0.05	0.73 ± 0.49	0.37 ± 0.27
Vikhlinin et al. (2006)	*Chandra*	1 [d]	···	1.06 ± 0.12	···	0.91 ± 0.13	0.99	0.84
Ettori et al. (2010)	*XMM*	10	···	···	···	0.93 ± 0.04	···	0.78 ± 0.38
Allen et al. (2008)	*Chandra*	6	···	1.04 ± 0.08	···	···	0.54 ± 0.20	···
Richard et al. (2010)	*Chandra*	12	1.04 ± 0.02	···	···	···	···	···

[a]The ratio and its error are simply the mean and the standard deviation of the distribution of $\sigma_M/\sigma_{M,\rm ref}$.

[b]projected mass

[c]exclude A115.

[d]exclude A2390.

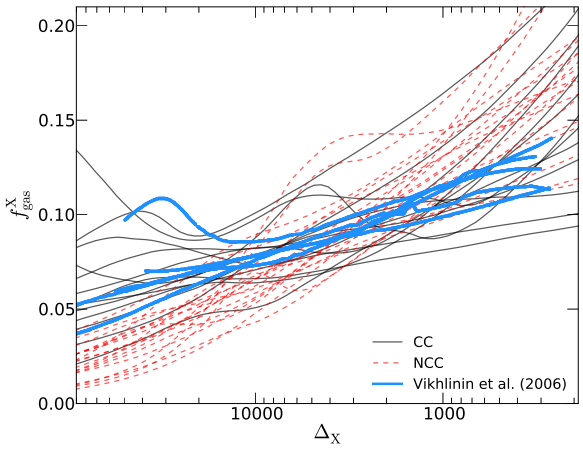

Figure 3-12: Cumulative gas mass fraction as a function of the overdensity, determined from M_X. The solid black and dashed red lines show the gas mass fraction from cool core and non-cool core clusters, respectively. Also shown in thick blue lines are $f_{\rm gas}^{\rm X}$ from Vikhlinin et al. (2006).

(2008) and Mahdavi et al. (2008). Allen et al. (2008) and Mahdavi et al. (2008) use the backward method, which parametrizes the mass profile, instead of the forward method modeling the temperature, as used by V06 and us. Our Monte Carlo analysis of residual gas profiles for the backward method indicates that $f_{\rm gas}^{\rm X}$ is biased high by $7 \pm 4\%$, compared to $2 \pm 4\%$ low in the forward method (§3.2.4.1, §3.2.4.3). Although not enough to solve the discrepancy, this difference is in the right direction. Note that the above statement depends on the radial range used for the fitting and the specific parametric models. It does not necessarily apply to the comparison to those works. Nonetheless, it is generally expected that using fewer parameters with a wider radial range causes a larger difference from our result.

Our average $f_{\rm gas}^{\rm X}$ is consistent with that of Zhang et al. (2010), but it is probably from a cancellation effect of M_X and $M_{\rm gas}$ being biased by the same factor of $\sim 27\%$ (§3.2.5.2, §3.2.5.3). If comparing $f_{\rm gas}$ with the total mass from weak lensing, $f_{\rm gas}^{\rm WL}$, we find that our result is 18% higher than their $f_{\rm gas}^{\rm WL}$, again suggesting that our M_X is higher since their weak lensing mass M_{WL} and part of our M_{WL} are both taken from Okabe et al. (2010).

3.3 Lensing Results

3.3.1 Best-fit masses and concentrations

Table 3.10 and 3.11 list the best-fit NFW mass and concentration parameters of CFHT and Subaru samples, respectively. Small changes to the mass of Hoekstra

V06. Nevertheless, $f_{\rm gas}^{\rm X}$ from the total and CC samples are both consistent with that of V06.

Table 3.9: Comparison of $f_{\rm gas}$ at R_{2500}

Method	Instrument	value	Reference
$f_{\rm gas}^{\rm X}$	*Chandra*	0.096 ± 0.002	This work
$f_{\rm gas}^{\rm X}$	*Chandra*	0.095 ± 0.002	Vikhlinin et al. (2006)
$f_{\rm gas}^{\rm X}$	*Chandra*	0.110 ± 0.002	Allen et al. (2008)
$f_{\rm gas}^{\rm X}$	*Chandra*	0.119 ± 0.006	Mahdavi et al. (2008)
$f_{\rm gas}^{\rm X}$	*XMM*	0.101 ± 0.010	Zhang et al. (2010)
$f_{\rm gas}^{\rm WL}$	*Chandra*+CFHT+Subaru	0.117 ± 0.007	This work
$f_{\rm gas}^{\rm WL}$	*XMM*+Subaru	0.099 ± 0.008	Zhang et al. (2010)

Note. — derived from $T \gtrsim 5$keV clusters with $h = 0.7$.

(2007) and Okabe et al. (2010) are made due to slightly different cluster redshifts used here. Figure 3-13 shows the mass and concentration relation from these samples. The CFHT sample (squares) is less concentrated than the Subaru sample (circles) on average. The former adopted a simulated $M_{200} - c_{200}$ relation (Bullock et al., 2001) to convert the projected mass to the 3D mass, while the latter treated the concentration as a free parameter (see §3.1.1). The $M_{200} - c_{200}$ relation of Bullock et al. (2001) (dotted line) predicts a relatively lower concentration for halos of the same mass than a more current simulation of Duffy et al. (2008) (dash-dotted line) does, which agrees to the Subaru sample better.

3.3.2 Comparison between Suburu and CFHT samples

There are eight clusters that are both selected into the Subaru and CFHT samples. In Figure 3-14, we compare the difference in M_{WL} from these samples as a function of the overdensity radius of those clusters. The ratio between the two mass estimates of the same cluster is first calculated, and then a weighted average is computed across the overlapping sample. We also plot the mass ratio for different types of clusters, CC/NCC, high/low power ratios P_m/P_0 and high/low centroid shifts $\langle w \rangle$, in Figure 3-14.

The CFHT weak lensing mass is systematically higher than the Subaru sample: from a factor of 1.19 ± 0.16 higher at R_{200} gradually decreasing to 1.00 ± 0.13 at R_{5000}, where the overdensity radius is estimated from the CFHT sample. This difference is probably from the concentration parameter measured or assumed in the mass profile (Figure 3-13). As demonstrated in Mandelbaum et al. (2010), if the concentration parameter is underestimated, the total mass will be biased high and vice versa. Since the surface mass density can be determined up to a constant (e.g., Kaiser & Squires, 1993), this constant is particularly crucial to the absolute mass at large radii. There is no significant correlation between the deviation in mass and the type of the cluster,

Table 3.10: Best-fit M_{200} and c_{200} of M_{WL} for CFHT sample

Name	M_{200} $(10^{14}\mathrm{M}_{\odot})$	c_{200}
A68	$9.90^{+8.06}_{-2.09}$	$3.58^{+0.02}_{-0.02}$
A209	$12.2^{+5.3}_{-5.1}$	$2.15^{+1.27}_{-1.35}$
A267	$9.20^{+6.37}_{-1.80}$	$3.21^{+0.04}_{-0.03}$
A370	$21.0^{+13.4}_{-4.1}$	$2.48^{+0.07}_{-0.11}$
A383	$9.00^{+10.81}_{-7.26}$	$1.35^{+0.66}_{-0.81}$
A963	$6.19^{+5.25}_{-2.30}$	$3.05^{+0.32}_{-0.14}$
A1689	$21.7^{+5.1}_{-4.8}$	$2.96^{+0.80}_{-0.28}$
A1763	$16.1^{+11.6}_{-3.5}$	$2.41^{+0.01}_{-0.01}$
A2218	$8.55^{+4.34}_{-1.79}$	$4.81^{+1.16}_{-0.42}$
A2219	$16.6^{+4.5}_{-7.4}$	$2.58^{+0.06}_{-0.07}$
A2390	$13.6^{+5.0}_{-4.3}$	$3.17^{+0.03}_{-0.01}$
CL0024.0+1652	$15.0^{+11.4}_{-3.0}$	$2.79^{+0.10}_{-0.07}$
MS0015.9+1609	$38.6^{+32.3}_{-13.2}$	$1.46^{+0.07}_{-0.08}$
MS1358.1+6245	$10.2^{+9.3}_{-2.4}$	$2.98^{+0.01}_{-0.00}$
ZwCl1454.8+2233	$7.60^{+6.16}_{-2.38}$	$2.79^{+0.05}_{-0.02}$
MS1512.4+3647	$4.84^{+10.01}_{-3.19}$	$1.96^{+0.02}_{-0.03}$
MS1621.5+2640	$13.8^{+10.8}_{-4.5}$	$2.19^{+1.36}_{-1.45}$
A750	$17.0^{+6.3}_{-5.9}$	$1.56^{+0.80}_{-1.22}$

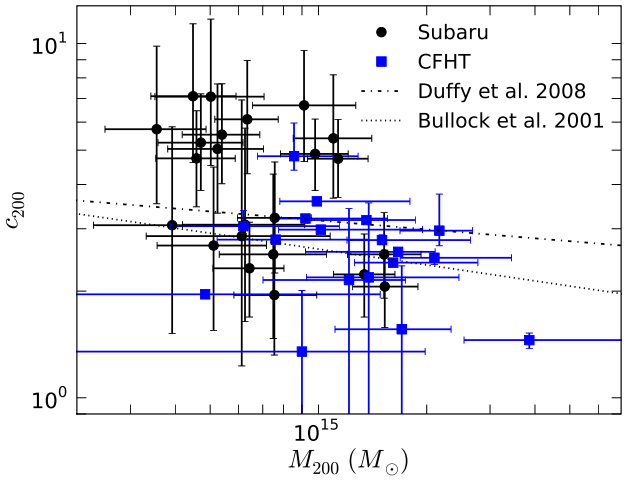

Figure 3-13: Best-fit mass and concentration parameters of Subaru (circles) and CFHT (squares) samples. Also shown are the simulated relations of Bullock et al. (2001) and Duffy et al. (2008) at $z = 0.23$.

Table 3.11: Best-fit M_{200} and c_{200} of M_{WL} for Subaru sample

Name	M_{200} ($10^{14}\mathrm{M}_{\odot}$)	c_{200}
A68	$6.25^{+2.91}_{-2.06}$	$3.08^{+2.69}_{-1.44}$
A209	$15.3^{+3.6}_{-2.8}$	$2.06^{+0.55}_{-0.48}$
RXJ0142.0+2131	$5.39^{+1.48}_{-1.21}$	$5.53^{+2.17}_{-1.51}$
A267	$4.58^{+1.29}_{-1.05}$	$4.74^{+1.72}_{-1.28}$
A383	$4.48^{+1.42}_{-1.06}$	$7.10^{+4.27}_{-2.49}$
A521	$6.43^{+1.59}_{-1.34}$	$2.32^{+0.81}_{-0.63}$
A586	$9.12^{+3.58}_{-2.57}$	$6.69^{+2.88}_{-2.05}$
ZwCl0839.9+2937	$3.55^{+1.32}_{-1.00}$	$5.73^{+4.10}_{-2.20}$
A611	$7.56^{+1.99}_{-1.61}$	$3.22^{+1.41}_{-0.97}$
A697	$13.4^{+2.9}_{-2.4}$	$2.23^{+0.67}_{-0.54}$
A963	$7.54^{+2.35}_{-1.72}$	$1.95^{+0.80}_{-0.63}$
A1835	$15.2^{+4.1}_{-3.2}$	$2.54^{+0.79}_{-0.63}$
ZwCl1454.8+2233	$3.92^{+2.30}_{-1.55}$	$3.07^{+2.75}_{-1.55}$
A2009	$4.71^{+1.46}_{-1.13}$	$5.25^{+1.96}_{-1.40}$
ZwCl1459.4+4240	$5.24^{+1.79}_{-1.43}$	$5.04^{+2.65}_{-1.72}$
RXJ1720.1+2638	$5.02^{+2.04}_{-1.51}$	$7.08^{+4.64}_{-2.55}$
A2219	$11.0^{+3.1}_{-2.5}$	$5.40^{+2.76}_{-1.74}$
A2261	$11.3^{+2.4}_{-2.0}$	$4.73^{+1.38}_{-1.05}$
RXJ2129.6+0005	$7.49^{+3.05}_{-2.19}$	$2.54^{+1.74}_{-1.07}$
A2390	$9.79^{+2.31}_{-1.95}$	$4.88^{+1.24}_{-1.03}$
A2485	$5.11^{+2.06}_{-1.55}$	$2.69^{+1.79}_{-1.14}$
A2631	$6.34^{+1.39}_{-1.19}$	$6.11^{+2.84}_{-1.82}$

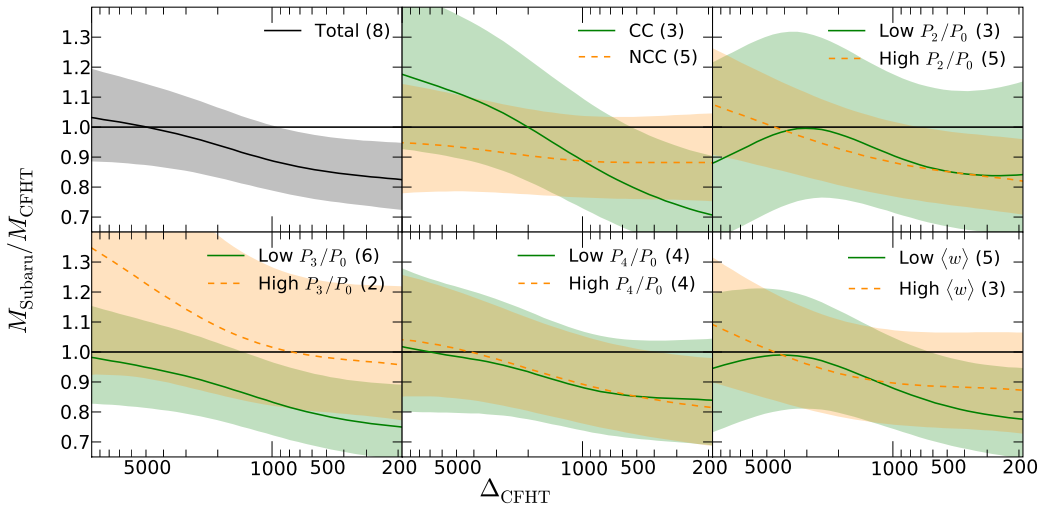

Figure 3-14: Weak lensing mass ratios between CFHT and Subaru samples as a function of overdensity from CFHT data. Shaded regions show the 1σ uncertainty of the ratios.

except possibly for high and low P_3/P_0 clusters. $M_{\rm CFHT}/M_{\rm Subaru}$ for the high P_3/P_0 group is uniformly lower than that of low P_3/P_0 group, though the statistical error is so large that this trend is not statistically significant in this relatively small sample.

3.3.3 Systematic errors in weak lensing analysis

3.3.3.1 Miscentering effect

An offset between the true mass center and the chosen one (here the BCG location) leads a underestimate of the total mass. As the center moves farther from the true position, the mass is underestimated more. Using the distribution of the offset between the BCG and X-ray center (Bildfell et al., 2008) as an estimate for that of the true offset, Hoekstra et al. (2011) quantify the bias generally less than 5% for M_{2500} if the shear at $r < 200$ kpc is not used. The error on M_{500} should be far less than that. Excluding more central data can lessen the bias from the miscentering but will unfortunately increase the statistical error of the mass estimate.

3.3.3.2 Source redshifts

The conversion of the lensing signal to the absolute value of the mass requires the redshift distribution of source galaxies. Since the redshift of individual source galaxies is often unavailable, the redshift distribution is typically estimated from detailed photometric redshift surveys in other fields. The current uncertainty of the photometric redshift calibration is about 1-6% (Ilbert et al., 2009), depending on the magnitude and the redshift of the galaxy. For a crude estimate, a 4% change in the source redshift corresponds to a 2% change in the distance ratio $D_{\rm ls}/D_s$ for a mean

source redshift of 0.6 at $z = 0.2$. In addition to the redshift accuracy, the field-to-field variation also needs to be taken into account. This may be estimated by comparing different pointings from the surveys, but it does not include the effect of the clustering of source galaxies (Hoekstra et al., 2010). The number of sources is smaller at small radii, resulting in a bigger variance in the redshift distribution in these regions. Hoekstra et al. (2010) use a ray-tracing simulation up to $z = 3$ to study the effect of distant LSS and the variation of the source redshift on the weak lensing measurement. They find that the source variation alone causes 2% and 5% scatters in the best-fit mass and concentration parameters, respectively, for $z = 0.2$ clusters. Based on their result, we estimate that the 3D mass errors from the source redshift distribution are 3% and 2% at R_{2500} and R_{500}, respectively. Together with the photometric redshift uncertainty, the total errors are 4% and 3% for M_{2500} and M_{500}, respectively.

3.3.3.3 Signal dilution from member galaxies

Lacking redshift information, the sample of source galaxies may unavoidably contain unlensed objects from the foreground or the cluster itself, which dilute the lensing signal. The contamination by foreground galaxies can be counter accounted by $\langle D_{\rm ls}/D_s \rangle$, calculated from a correct estimate of the redshift distribution in the field. Since the cluster galaxy population is not included in such an estimate, it should be removed from the source sample. Member galaxies, if included, can potentially lead a mass underestimate as high as 50% especially in the inner region (e.g., Broadhurst et al., 2005b). The source galaxies of Subaru and CFHT sample are both selected from faint galaxies redder or bluer than the Red Cluster Sequence (Okabe et al., 2010; Hoekstra, 2007). Although this removes most of the cluster members, faint and blue members may still be present. To account for this, Hoekstra (2007) apply an additional correction from the excess of the source number density relative to the background level to boost the observed shear, which increases the mass by a few percent. Okabe et al. (2010) do not correct for this, but their stacked number density of source galaxies for the whole sample is close to a constant profile, suggesting that member galaxies are properly excluded.

3.3.3.4 Shape measurement

The atmospheric seeing and PSF anisotropy distort the image and thus can possibly bias the lensing signal if not properly corrected. However, since tests on simulated data shows that the shear measurement can achieve an accuracy of $1 - 2\%$ under the best analysis methods (Heymans et al., 2006; Massey et al., 2007), we shall assume that it is not a major concern on the systematic error. Another consideration is the shape noise from the intrinsic ellipticity of the galaxy, which is part of the statistical error already and can be combated with a higher source galaxy density from deeper observations. Simulations of Becker & Kravtsov (2010) suggest that M_{WL} can be biased more for low source galaxy densities. Their result shows that the mass bias reduces from -9% to -6% when the source galaxy density of 10 galaxies/arcmin^2 increases to 40 galaxies/arcmin^2 for a NFW fit in the radial range of $[1', 20']$ in 12

logarithmic bins. A similar trend is observed in other fit ranges or numbers of data bins used. Most of the bias is from the NFW modeling (§3.7.4), so we gauge an about 2% underestimate of the mass from the shape measurement for typical ground-based observations with the source density between $10 - 20$ galaxies/arcmin^2.

3.3.3.5 Weak lensing limit

The weak lensing distortion signal is from the reduced shear $g = \gamma/(1-\kappa)$, rather than the tangential shear γ. In the weak lensing limit where the convergence $\kappa \ll 1$, γ can be approximated by g. However, if this $(1-\kappa)$ factor is ignored at small radii, the cluster mass will be overestimated by a few percent in these regions. Generally this factor is neglected in the non-parametric measurement because the correction requires an additional modeling, but it has been taken into account in the CFHT sample by Hoekstra (2007). As to the Subaru sample, since the mass is from the best-fit NFW model, the $(1-\kappa)$ factor has been modeled when fitting the reduced shear profile.

3.4 X-ray vs. lensing mass profiles

Following the convention of Mahdavi et al. (2008), we calculate $a_\Delta = M_X/M_{WL}$ at different overdensity radii r_Δ using FITEXY fitting routine (Press et al., 1992), which minimizes an effective χ^2 defined as

$$\chi^2 = \sum \frac{(M_X - a_\Delta M_{WL})^2}{\sigma_{M_X}^2 + a_\Delta^2 \sigma_{M_{WL}}^2} \,, \tag{3.10}$$

where σ_{M_X} and $\sigma_{M_{WL}}$ are the errors of the X-ray and lensing masses at r_Δ and the summation sums over all the clusters in our sample. The uncertainty is estimated by locating the value of a_Δ at which $\chi^2 - \chi_{\rm min} = 1$, which corresponds to the 68% confidence interval under the assumption of the χ^2 distribution. r_Δ, where the enclosed mass is Δ times the critical density, is calculated from the best-fit NFW model of weak lensing data. M_X/M_{WL} as a function of r_Δ is plotted in Figure 3-15 and summarized in Table 3.12.

We find that M_X/M_{WL} in general decreases with the radius, as also found in Mahdavi et al. (2008) and the relaxed sample of Zhang et al. (2010) (but not the total sample). However, there are large differences in the absolute scale of M_X/M_{WL} between Suburu and CFHT samples and in comparison with other studies as well. The mass ratio from the Subaru sample is systematically higher than that of the CFHT sample, from $31 \pm 9\%$ higher at R_{500}, gradually decreasing to $10 \pm 11\%$ at R_{5000}. This discrepancy resembles the difference of M_{WL} seen in clusters that are common to both samples (§3.3.2), from $15 \pm 11\%$ at R_{500} to $0 \pm 14\%$ at R_{5000}. If we add this difference in M_{WL} to all M_{WL} in CHFT sample, M_X/M_{WL} from both samples are consistent with each other for the full radial range.

Zhang et al. (2010) from 12 LoCuSS clusters with M_{WL} from Subaru data (Okabe et al., 2010) and M_X from *XMM-Newton* derived mass ratios of 1.01 ± 0.07, 0.97 ± 0.05,

and 0.99 ± 0.07 at R_{2500}, R_{1000}, and R_{500}, respectively. These values are $\approx 20-35\%$ lower than those of our Subaru sample, whose M_X is also from Okabe et al. (2010), at $2-3\sigma$ significance. As found in §3.2.5.3 that their M_X are systematically lower than ours by $15-30\%$ from object-to-object comparisons, this should explain most of the difference in M_X/M_{WL}. Mahdavi et al. (2008) from 18 *Chandra* clusters with M_{WL} from Hoekstra (2007) found ratios of 1.03 ± 0.07, 0.90 ± 0.09, and 0.78 ± 0.09 at R_{2500}, R_{1000}, and R_{500}, respectively. Compared to our CFHT sample, which is identical to theirs, our values are 10% higher than theirs at R_{1000} and R_{500}, but still agree at 1σ. At R_{2500}, the 20% difference in M_X/M_{WL} is about 2σ. Again, this is likely from the $\approx 12\%$ higher M_X we have at this radius (§3.2.5.3).

Many simulations suggest that gas motions (Evrard et al., 1996; Rasia et al., 2004, 2006; Dolag et al., 2005; Nagai et al., 2007b; Lau et al., 2009) or other sources of non-thermal pressure (cosmic rays, AGN bubbles, magnetic field, etc.) provides additional support to the ICM. As a result, the hydrostatic mass is expected to be lower than the true mass by $5-20\%$. The bias in M_X is further found to correlate with cluster structures, mostly with P_3/P_0, the power ratio of the hexapole moment of the multipole expansion of the X-ray image (Jeltema et al., 2008). To test whether M_X/M_{WL} is linked to ICM properties, we show in Figure 3-15 how M_X/M_{WL} changes with different classifications of the cluster: CC/NCC, power ratios P_2/P_0, P_3/P_0, P_4/P_0, and centroid shifts $\langle w \rangle$.

Despite the uncertainty on the overall scale of M_X/M_{WL}, both the CFHT and Subaru samples agree that there is no significant difference in M_X/M_{WL} between cool core (CC) and non-cool core (NCC) samples, consistent with the finding of Mahdavi et al. (2008). Both samples show that clusters with high P_3/P_0 have lower M_X/M_{WL} than those with low P_3/P_0. Although correlated with P_3/P_0, P_4/P_0 does not have a strong correlation with M_X/M_{WL}. The centroid shift, even though measured out to R_{500}, turns out only sensitive in discerning cluster inner regions ($r \lesssim R_{5000}$).

Given these qualitative similarities, combining two samples to form a tighter constraint seems to be reasonable. To do so, we multiply all M_{WL} from the CFHT sample by an average ratio $M_{WL,\,\mathrm{Subaru}}/M_{WL,\,\mathrm{CFHT}}$ from the comparison of M_{WL} from 8 clusters that are common to both samples (§3.3.2). We adjust M_{WL} from the CFHT sample rather than those of the Subaru simply because the Subaru sample is slightly larger than the other. This systematic uncertainty will be addressed later in §3.7. Figure 3-16 shows the combined result.

To find out where the variation in M_X/M_{WL} comes from, we compare M_X and M_{WL} with a "standard" mass profile from simulations. The standard mass profile is determined from a NFW model fit to M_{WL} under the constraint of the mass and concentration relation of Duffy et al. (2008),

$$c_{200} = 5.71 \left(\frac{M_{200}}{2 \times 10^{12} h^{-1} \mathrm{M}_\odot} \right)^{-0.084} (1+z)^{-0.47}. \tag{3.11}$$

This $M_{200} - C_{200}$ relation is the average relation for all halos including unrelaxed ones from N-body simulations with the best-fit parameters of the WMAP5 cosmology (Komatsu et al., 2009). Figure 3-17 plots M_X (*top*) and M_{WL} (*bottom*) relative to this

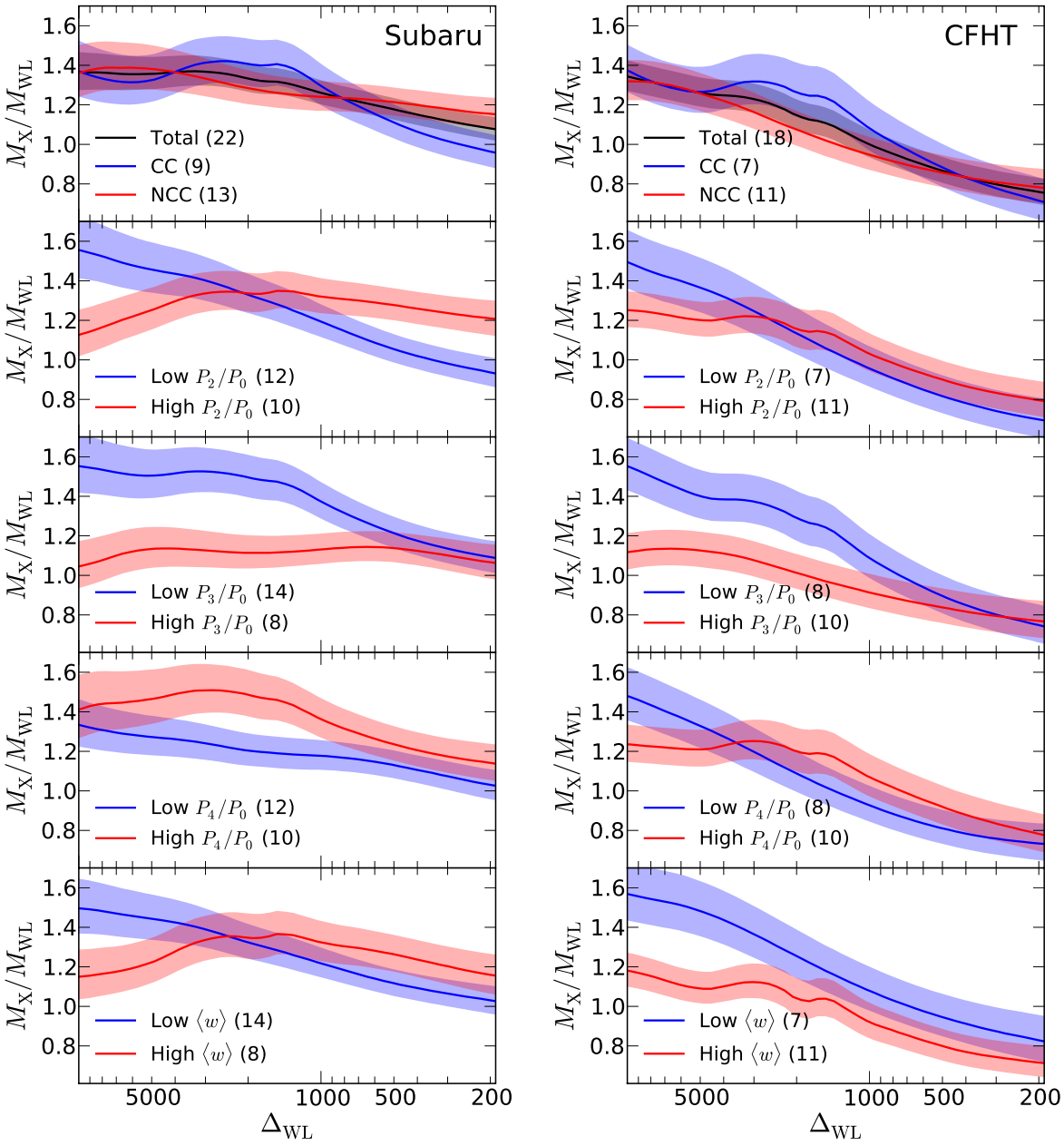

Figure 3-15: The ratio between the hydrostatic X-ray mass and the lensing mass as a function of overdensity Δ_{WL}, calculated from best-fit weak lensing NFW profiles. The 1σ uncertainties are shown in shaded regions. *Left:* Subaru sample; *Right:* CFHT sample. *From top to bottom:* CC vs. NCC, low vs. high P_2/P_0, low vs. high P_3/P_0, low vs. high P_4/P_0, and low vs. high $\langle w \rangle$.

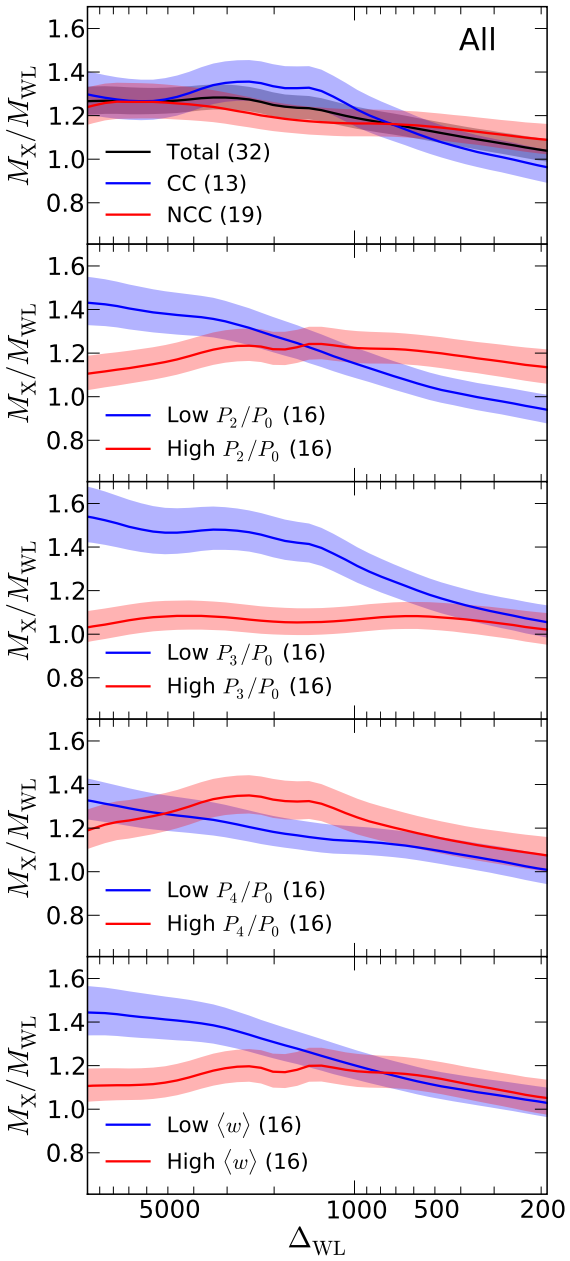

Figure 3-16: The ratio between the hydrostatic X-ray mass and the lensing mass as a function of overdensity $\Delta_{\rm WL}$, calculated from best-fit weak lensing NFW profiles. The 1σ uncertainties are shown in shaded regions.

Table 3.12: Comparison of X-ray and weak-lensing mass estimates

Sample	M_X/M_{WL}			
	R_{5000}	R_{2500}	R_{1000}	R_{500}
Subaru sample (22)				
Total	1.36 ± 0.08	1.36 ± 0.07	1.26 ± 0.06	1.18 ± 0.05
CC	1.33 ± 0.12	1.42 ± 0.12	1.30 ± 0.10	1.11 ± 0.09
NCC	1.38 ± 0.11	1.31 ± 0.09	1.24 ± 0.07	1.21 ± 0.07
low P_2/P_0	1.46 ± 0.13	1.37 ± 0.11	1.19 ± 0.08	1.05 ± 0.07
high P_2/P_0	1.25 ± 0.11	1.34 ± 0.10	1.32 ± 0.09	1.28 ± 0.08
low P_3/P_0	1.50 ± 0.12	1.52 ± 0.11	1.37 ± 0.09	1.21 ± 0.08
high P_3/P_0	1.13 ± 0.10	1.12 ± 0.09	1.13 ± 0.08	1.14 ± 0.08
low P_4/P_0	1.27 ± 0.10	1.22 ± 0.09	1.18 ± 0.08	1.13 ± 0.07
high P_4/P_0	1.46 ± 0.14	1.51 ± 0.12	1.36 ± 0.10	1.24 ± 0.09
low $\langle w \rangle$	1.44 ± 0.11	1.36 ± 0.09	1.22 ± 0.08	1.12 ± 0.07
high $\langle w \rangle$	1.22 ± 0.11	1.35 ± 0.11	1.32 ± 0.10	1.26 ± 0.09
CFHT sample (18)				
Total	1.26 ± 0.07	1.20 ± 0.07	1.00 ± 0.07	0.87 ± 0.07
CC	1.27 ± 0.12	1.31 ± 0.13	1.08 ± 0.12	0.88 ± 0.11
NCC	1.26 ± 0.10	1.12 ± 0.09	0.95 ± 0.08	0.86 ± 0.08
low P_2/P_0	1.37 ± 0.14	1.20 ± 0.12	0.96 ± 0.10	0.82 ± 0.10
high P_2/P_0	1.20 ± 0.09	1.20 ± 0.09	1.03 ± 0.10	0.90 ± 0.09
low P_3/P_0	1.40 ± 0.12	1.35 ± 0.12	1.09 ± 0.11	0.90 ± 0.10
high P_3/P_0	1.13 ± 0.09	1.05 ± 0.09	0.91 ± 0.09	0.84 ± 0.09
low P_4/P_0	1.33 ± 0.12	1.15 ± 0.11	0.93 ± 0.09	0.81 ± 0.09
high P_4/P_0	1.21 ± 0.09	1.24 ± 0.10	1.07 ± 0.11	0.92 ± 0.10
low $\langle w \rangle$	1.48 ± 0.14	1.32 ± 0.13	1.08 ± 0.11	0.95 ± 0.11
high $\langle w \rangle$	1.09 ± 0.08	1.11 ± 0.09	0.92 ± 0.09	0.80 ± 0.08
Total (32)				
Total	1.27 ± 0.06	1.27 ± 0.06	1.19 ± 0.05	1.13 ± 0.05
CC	1.28 ± 0.09	1.36 ± 0.09	1.23 ± 0.09	1.09 ± 0.07
NCC	1.26 ± 0.08	1.21 ± 0.07	1.16 ± 0.06	1.15 ± 0.06
low P_2/P_0	1.38 ± 0.10	1.32 ± 0.08	1.15 ± 0.07	1.04 ± 0.06
high P_2/P_0	1.16 ± 0.07	1.23 ± 0.07	1.22 ± 0.07	1.20 ± 0.07
low P_3/P_0	1.47 ± 0.11	1.47 ± 0.09	1.32 ± 0.08	1.17 ± 0.07
high P_3/P_0	1.08 ± 0.07	1.07 ± 0.06	1.07 ± 0.06	1.08 ± 0.06
low P_4/P_0	1.26 ± 0.08	1.21 ± 0.07	1.14 ± 0.06	1.10 ± 0.06
high P_4/P_0	1.27 ± 0.09	1.35 ± 0.09	1.25 ± 0.08	1.16 ± 0.07
low $\langle w \rangle$	1.41 ± 0.10	1.34 ± 0.08	1.20 ± 0.07	1.11 ± 0.06
high $\langle w \rangle$	1.12 ± 0.07	1.20 ± 0.07	1.18 ± 0.08	1.14 ± 0.07

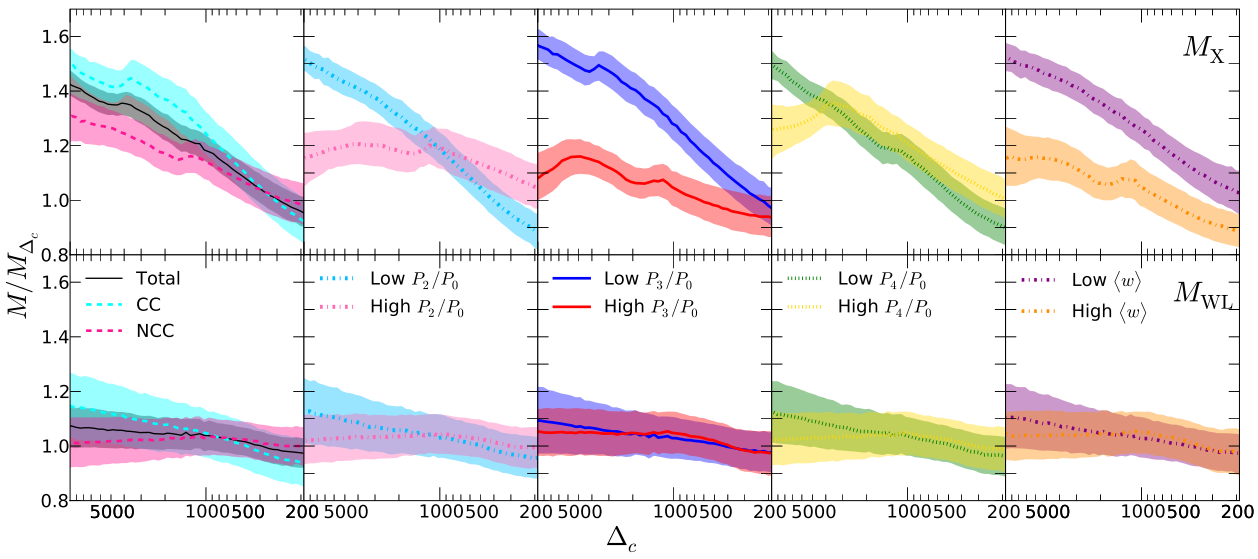

Figure 3-17: Mass profiles relative to the best-fit NFW model of M_{WL} under the constraint of the $M_{200} - C_{200}$ relation of Duffy et al. (2008), M_{Δ_c}, as a function of the overdensity Δ_c, determined from M_{Δ_c}. *Top:* average M_X profiles. *Bottom:* average M_{WL} profiles. *From left to right:* mass profiles of CC/NCC, high and low P_m/P_0 and $\langle w \rangle$ clusters. The shaded area shows the 1σ error of the average profile.

standard mass profile M_{Δ_c} as a function of the overdensity Δ_c estimated from the standard profile.

The relative mass profile from M_{WL} is much flatter than that of M_X. The former also has less scatters among different subsamples compared to the latter. The only type of clusters that seems to be different from others in M_{WL} is the CC sample, which has the steepest relative overdensity. The enclosed mass at R_{7000} is 15% higher than the prediction of Duffy et al. (2008). This finding, although not significant, is not unexpected because gas physics is not taken into account in simulations of Duffy et al. (2008). When the gas cools, it contracts and pulls the dark matter farther into the core, resulting a steeper density profile than the original (Blumenthal et al., 1986; Gnedin et al., 2004). Barkana & Loeb (2010) show that the cluster mass can increase by an order of 20% at $0.1R_{\rm vir}$ ($\approx R_{7000}$) depending on the fraction of mass in the satellite halos. The relative mass profile for the CC sample from M_X, on the other hand, is not the highest among all at small radii. The low P_3/P_0 sample, instead, has the steepest mass profile. Low and high P_3/P_0 samples have a 10% higher and a 15% lower mass compared to the average sample at R_{5000}, respectively.

Dividing the averaged relative mass profile from the X-ray to that of the weak lensing, we obtain the averaged X-ray to weak lensing mass ratio $\langle M_X \rangle / \langle M_{WL} \rangle$, plotted in Figure 3-18. Likewise shown in Figure 3-16 which plots M_X/M_{WL} averaged across the sample, P_3/P_0 is the structure measure that correlates with mass ratios the most, centroid shifts and P_2/P_0 the next, and P_4/P_0 and CC/NCC the least. The error of $\langle M_X \rangle / \langle M_{WL} \rangle$ is much larger than M_X/M_{WL} in Figure 3-16 because the

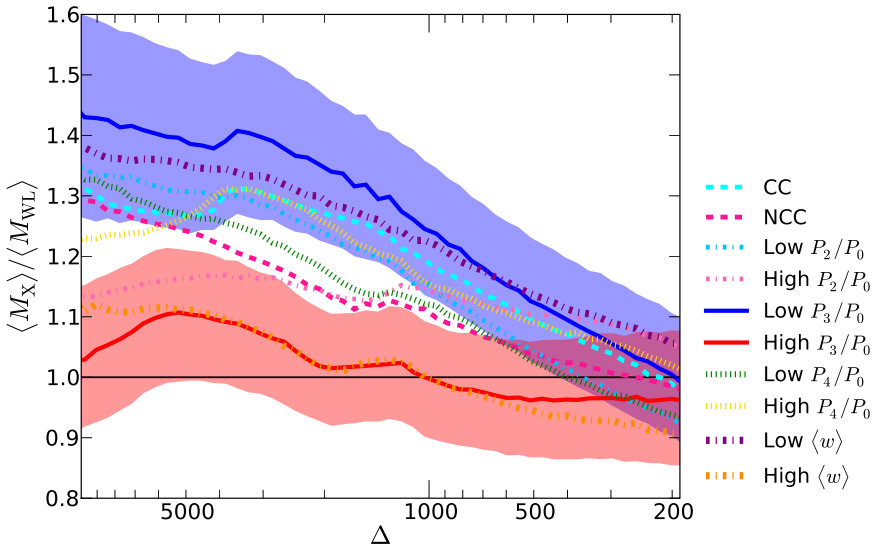

Figure 3-18: Ratios of averaged X-ray mass profiles to those of weak lensing. Blue and pink shaded regions show the 1σ uncertainty of the ratio of low and high P_3/P_0 groups, respectively. Errors for other types of clusters are omitted for clarity.

same uncertainty of M_{Δ_c} is included both in M_X/M_{Δ_c} and M_{WL}/M_{Δ_c} and subsequently double-counted in $\langle M_X \rangle / \langle M_{WL} \rangle$. The consistent finding from $\langle M_X \rangle / \langle M_{WL} \rangle$ and $\langle M_X / M_{WL} \rangle$ shows that the mass ratio is robust. Figure 3-17 suggests that the change in the mass ratio is mostly likely from the X-ray measurement as $\langle M_{WL} \rangle$ profiles from each individual type of clusters are quite similar to one another and approximately follow the $M_{200} - C_{200}$ relation of Duffy et al. (2008). Although the relative M_X and M_{WL} profiles are determined from a weak lensing based M_{Δ_c}, which overlooks the intrinsic scatter in M_{WL} and therefore could overestimate the scatter in M_X, our conclusion is the same if the scaled quantity is from the X-ray measurement, as will be shown in §3.5.

3.5 X-ray vs. lensing pressure profiles

Comparing the thermal pressure $P_{\rm th}$, measured from X-ray data, with the total gas pressure $P_{\rm tot}$ balanced by the gravitational force, inferred from lensing data, is a way to estimate the nonthermal pressure in clusters. Other more direct methods for constraining nonthermal pressure rely on emission line measurements (e.g., Churazov et al., 2004; Werner et al., 2009; Sanders et al., 2010), which are difficult with currently available instrumentation. The total pressure is obtained by integrating the mass profile from M_{WL}, given by

$$P_{\rm tot}(r) = -\int_{r_0}^{r} \frac{G\rho_{\rm gas} M_{\rm tot}(r')}{r'^2} dr' + P_{\rm tot}(r_0). \tag{3.12}$$

Since the pressure is a strong decreasing function of the radius, choosing $r_0 \to \infty$ lessens the dependence of this undetermined total pressure at r_0. However, we do not measure the gas density out to very large radii and M_{WL} from the NFW profile gives a divergent total mass, so we set $P_{\rm tot} = 1.25P_{\rm th}$ at $1.5R_{500}$ with a 10% scatter, a crude estimate from the simulation of Lau et al. (2009). To better distinguish the measured value from the true pressure, we henceforth replace the symbols $P_{\rm th}$ and $P_{\rm tot}$ with P_X and P_{WL}, respectively. Note P_{WL} still needs the gas density measured from X-ray data.

Figure 3-19 shows P_X/P_{WL} as a function of the radius scaled by R_{500}, determined from the $M_{500} - Y_X$ relation of Vikhlinin et al. (2009a), for the combined sample. Also plotted are ratios by setting $P_{WL} = P_X$ at $1.5R_{500}$ (dashed lines). We find that this 25% difference of P_{WL} at $1.5R_{500}$ causes less than 4% difference in P_X/P_{WL} within $0.7R_{500}$, showing that the measurement is very robust in these regions. Unlike a ratio of $0.4 - 0.6$ found in A1689 (Kawaharada et al., 2010) or $0.7 - 0.95$ predicted from simulations (e.g., Dolag et al., 2005; Lau et al., 2009) if P_X/P_{WL} traces $P_{\rm th}/P_{\rm tot}$, our P_X/P_{WL} is actually greater than 1 for most radii, just as $M_X/M_{WL} > 1$. Nonetheless, we find that the ratio correlates with cluster structures, particular with P_3/P_0 that high P_3/P_0 clusters have a lower ratio.

Following the same analysis in §3.2.3, we plot the average scaled pressure profiles of P_X (*left*) and P_{WL} (*right*) for different cluster structure samples in Figure 3-20. The low P_3/P_0 sample has the steepest P_X profile while the high P_3/P_0 sample has the shallowest. Low P_2/P_0, P_4/P_0, $\langle w \rangle$, or CC clusters also have steeper than average P_X profiles, just not as steep as low P_3/P_0 clusters. The similar trend is seen in scaled P_{WL} profiles, but the slope change is not as much as those of P_X. In the very center, CC, rather than low P_3/P_0, clusters have the highest P_{WL} among all, consistent with the finding in §3.4 that CC clusters have the densest cores.

Figure 3-21 shows the ratio of the average scaled pressure profile of P_X over P_{WL}, $\langle P_X \rangle / \langle P_{WL} \rangle$. The result is comparable to $\langle P_X/P_{WL} \rangle$ profiles plotted in Figure 3-19. Both plots agree that P_3/P_0 is the most sensitive structure measure. Although the scatter in P_{WL}, scaled by X-ray determined P_{500}, is considerably larger than that of M_{WL} (Figure 3-17), normalized by a weak lensing based overdenstiy, it is still evident that the slope change in P_X is the main reason for the difference in P_X/P_{WL} between low and high P_3/P_0 clusters.

3.6 Gas mass fractions

Figure 3-22 plots the cumulative gas mass fraction $f_{\rm gas}^{\rm X}$ (*left*) with the total mass from M_X and $f_{\rm gas}^{\rm WL}$ (*right*) with the mass from M_{WL}, as a function of the overdensity Δ. Different from Figure 3-15 in which we fit a linear relation to M_X and M_{WL} across the sample at each overdensity radius, we calculate $f_{\rm gas} = M_{\rm gas}/M$ first for every cluster and then average $f_{\rm gas}$ across the sample at each overdensity radius.

Morphologically more disturbed (high P_m/P_0 or $\langle w \rangle$) clusters all have a higher than average $f_{\rm gas}^{\rm X}$ or $f_{\rm gas}^{\rm WL}$ at large radii. Since gas clumping can enhance the measured $M_{\rm gas}$ (Mathiesen et al., 1999), this could be the reason for high $f_{\rm gas}^{\rm X}$ and $f_{\rm gas}^{\rm WL}$ in these

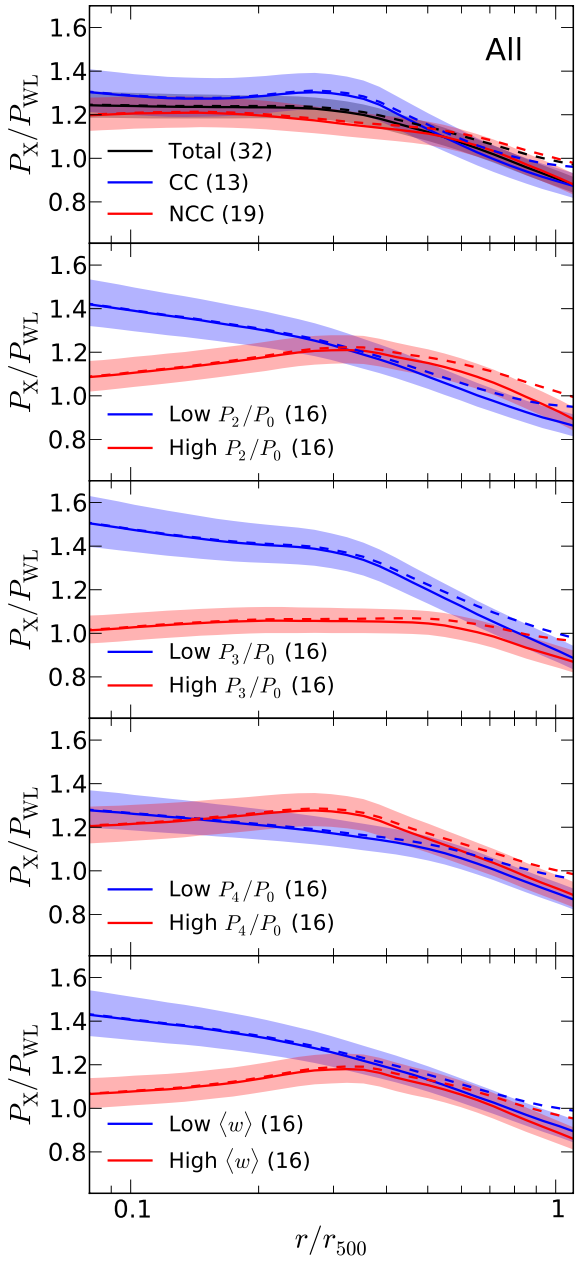

Figure 3-19: Ratio of P_X to P_{WL}. Solid lines show the pressure ratios by enforcing $P_{WL} = 1.25P_X$ at $1.5R_{500}$. The 1σ uncertainties are shown in shaded regions. Also shown are the ratios with $P_{WL} = P_X$ at $1.5R_{500}$ (dashed lines).

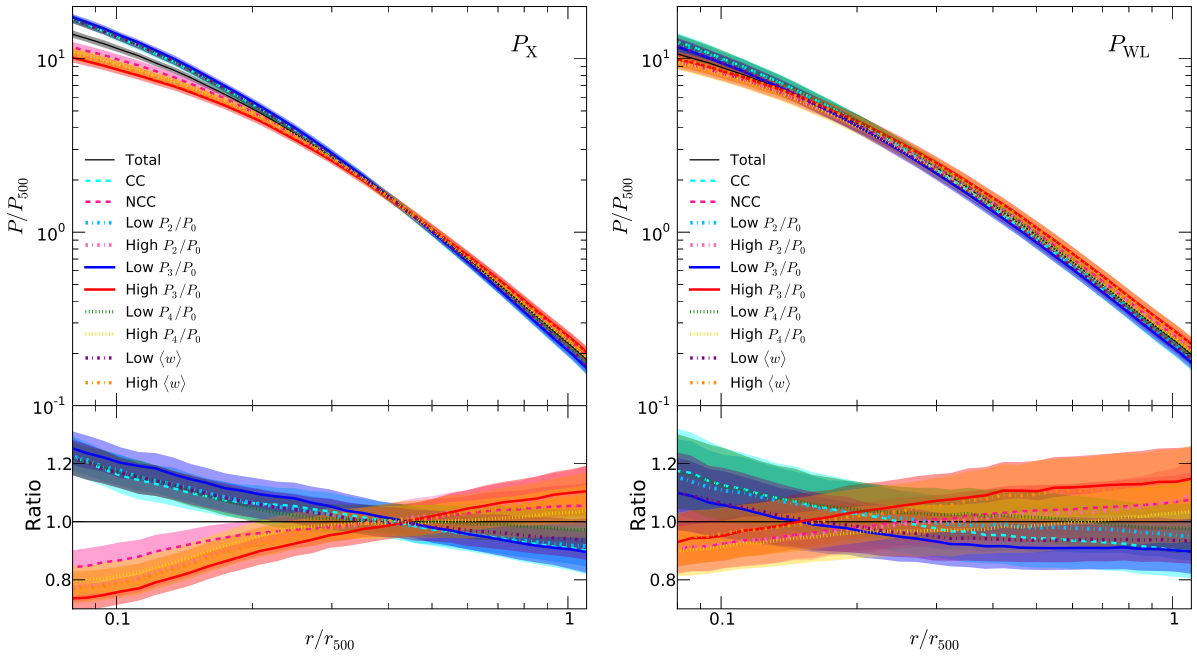

Figure 3-20: *Top*, averaged X-ray (*left*) and weak lensing (*right*) scaled pressure profiles. P_{500} and r_{500} are estimated from the $M_{500,\rm X} - Y_X$ relation of Vikhlinin et al. (2009a). The shaded area shows the 1σ error of the average profile. *Bottom*, the ratio of the profile from the subtype cluster to that of the total sample.

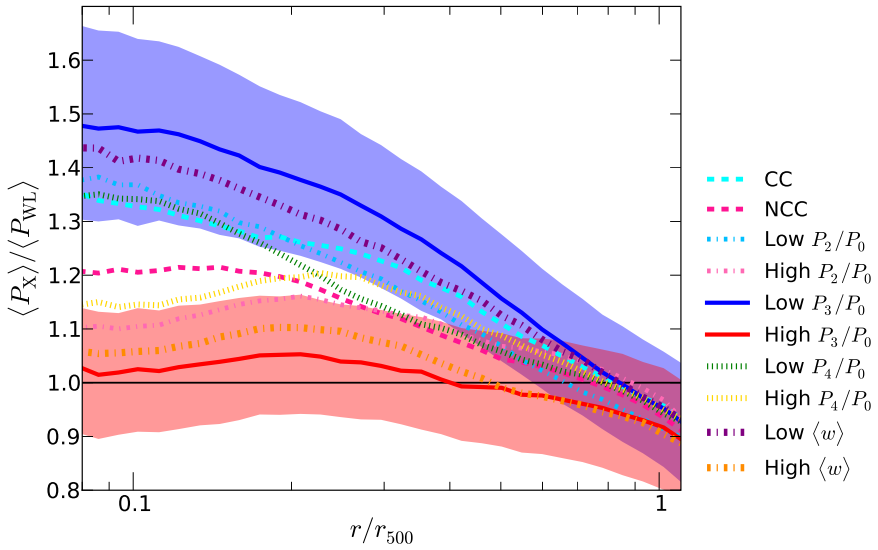

Figure 3-21: Ratios of averaged X-ray pressure profiles to those of weak lensing. Blue and pink shaded regions show the 1σ uncertainty of the ratio of low and high P_3/P_0 groups, respectively. Errors for other groups of clusters are omitted for clarity.

clusters. The gas clumping is also suspected at the outskirt of the Perseus cluster, as Simionescu et al. (2011) find that $f_{\rm gas}^{\rm X}$ greatly exceeds the cosmic mean value from *Suzaku* data. Our $f_{\rm gas}^{\rm X}$ is roughly consistent with the cosmic mean baryon fraction (Komatsu et al., 2011) at R_{200}, shown in the dotted line in Figure 3-22. Since there is about 12% known stellar mass in the total baryon budget (Giodini et al., 2009), the measured $f_{\rm gas}^{\rm X}$ is probably overestimated at least at this level.

For $f_{\rm gas}^{\rm WL}$, the difference is more obvious using P_2/P_0 and P_4/P_0 structure measures. Because observed M_{WL} highly depends on the assumed cluster shape and these measures tend to select elliptical clusters in the projection, which generally accompanies by a shortening in the line-of-sight, M_{WL} is underestimated more in these clusters, resulting a high $f_{\rm gas}^{\rm WL}$. We will discuss this further in §3.7.1 and §3.8.1. At small radii, $f_{\rm gas}^{\rm WL}$ of morphologically regular clusters (low P_m/P_0 or $\langle w \rangle$) shows a flattening in the core which raises $f_{\rm gas}^{\rm WL}$ above that of disturbed clusters. This trend, however, is not seen in $f_{\rm gas}^{\rm X}$ at small radii except in the CC sample. As shown in §3.4, all regular, but not CC, clusters have higher M_X/M_{WL} in the core compared to their counterparts, which leads the difference between $f_{\rm gas}^{\rm X}$ and $f_{\rm gas}^{\rm WL}$ in the core.

3.7 Modeling and Measurement Biases

In this section, we discuss the possible bias and scatter in the modeling and measurements, and summarize in Table 3.13. Some of the systematic uncertainties in X-ray measurements have been discussed in §3.2.4.

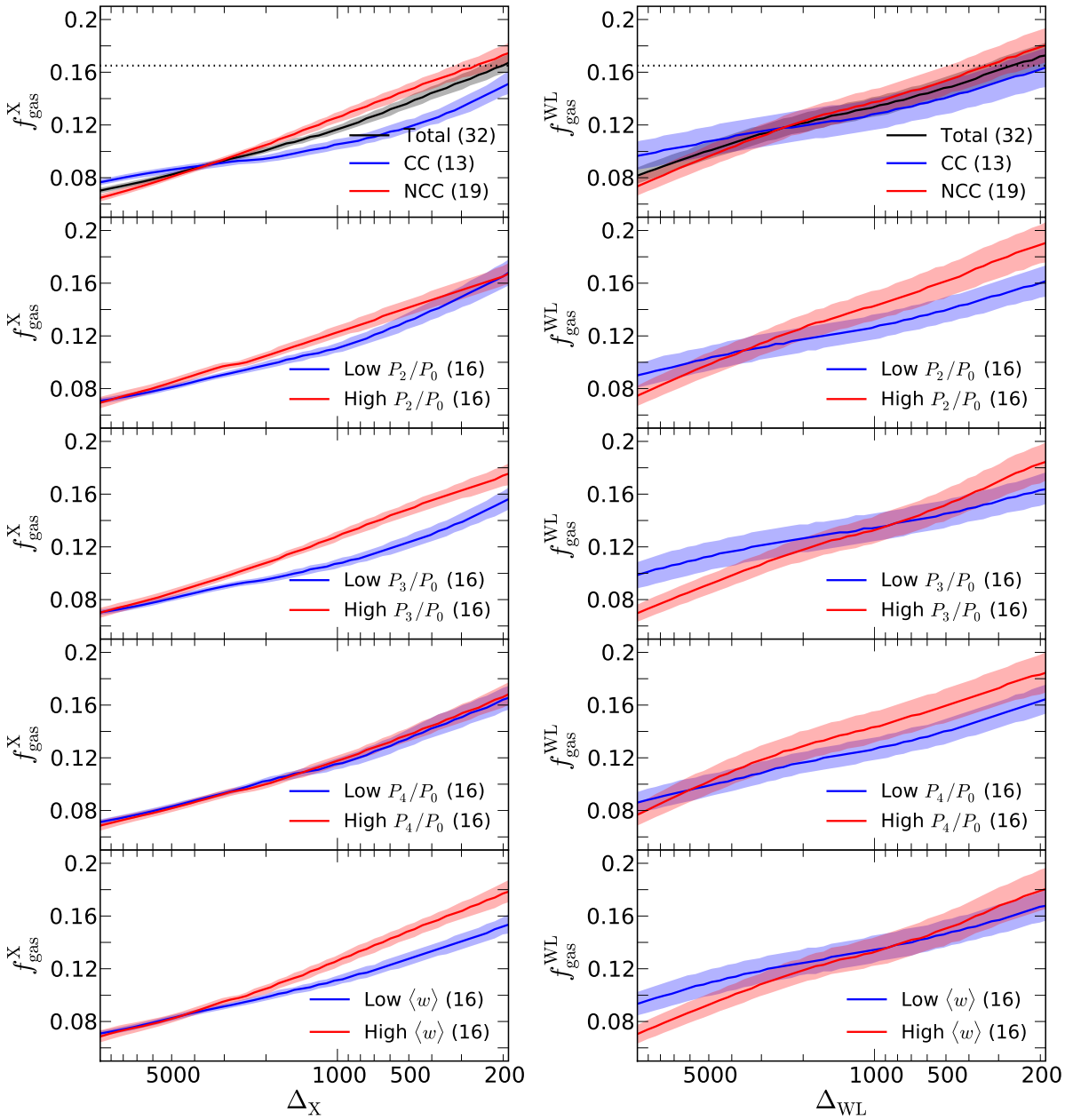

Figure 3-22: Enclosed gas mass fraction as a function of the overdensity, with the total mass from M_X (*left*) and M_{WL} (*right*). The horizontal dotted line shows the cosmic mean baryon fraction from WMAP7 (Komatsu et al., 2011).

3.7.1 Shapes of DM halos and ICM

The previously derived mass and pressure profiles are based on the simple assumption of spherical symmetry. A certain geometry has to be assumed when, for example, converting the projected lensing mass to the 3D mass or calculating the gas density from the X-ray flux. However, observed clusters often exhibit some degree of ellipticity (Figure B-1) and simulated halos are better fitted with a triaxial model (e.g., Jing & Suto, 2002). Prolate (cigar shaped) halos with major axes aligned along the line-of-sight, if modeled as spherical ones, lead the 3D mass (and the concentration) to be overestimated; while oblate (pancake shaped) halos have the opposite effect (e.g., Oguri et al., 2005). The inferred 3D lensing mass therefore highly depends on the viewing angle (e.g., Clowe et al., 2004). Lacking the information about shapes and orientations, the erroneous modeling creates the scatter around the true mass and the effect is strongest at small radii because of the little enclosed mass.

N-body simulations show that cold dark matter halos tend to be prolate, with a tendency slightly increasing with the halo mass (e.g., Shaw et al., 2006; Allgood et al., 2006; Bett et al., 2007). Corless & King (2007) using the distribution of halo axis ratios from Shaw et al. (2006) with random orientations derived the scatter of best-fit NFW parameters from the weak lensing simulations, $\sigma_{M_{200}} = 1.8 \times 10^{14}\mathrm{M}_{\odot}$ and $\sigma_{c_{200}} = 0.8$, for $M_{200} = 10^{15}\mathrm{M}_{\odot}$ and $c_{200} = 4$ clusters, which is consistent with the analysis of Meneghetti et al. (2010) that the error of M_{200} due to triaxiality is of the order of 20%. The parameter distribution is nearly Gaussian with a mean equal to the true value but a long tail toward high values. With such dispersions, we estimate that errors on M_{2500} and M_{500} are 28% and 19%, respectively. These errors include the uncertainty of R_{2500} and R_{500}. If masses are evaluated at a fixed radius, errors reduce to 16% and 13%, respectively.

The X-ray mass estimate, on the other hand, is less affected by the halo triaxiality (Piffaretti et al., 2003; Gavazzi, 2005). Churazov et al. (2008) proved analytically that if the ICM is isothermal and the gas density's radial dependence is a power law ($\rho_{\rm gas} \propto r^{-\gamma}$), treating clusters with arbitrary shapes and orientations as spherical systems will not cause any bias on the hydrostatic mass enclosed by a sphere of the same radius. Peng et al. (2009) who used more flexible gas profiles of Vikhlinin et al. (2006) and modeled ICM with different degrees of flattening along the line-of-sight found that M_X only changes by $2-4\%$ between 0.1 and 1 R_{500}, in agreement with the estimate of Piffaretti et al. (2003), derived from a simpler modeling with the gas isothermality and a β model for the gas density. Using the same analysis of Peng et al. (2009), we find that $M_{\rm gas}$ changes about 6% and 5% at R_{2500} and R_{500}, respectively.

The derived scatter of M_{WL} above may be somewhat overestimated because gas dissipation, not included in the simulation of Shaw et al. (2006), makes clusters more spherical (e.g, Kazantzidis et al., 2004; Fang et al., 2009; Lau et al., 2010). It is also found that observed P_2/P_0 and P_4/P_0 from X-ray images are smaller than the prediction from simulations without cooling (Jeltema et al., 2008), suggesting that clusters in reality are not as triaxial as predicted from dissipationless N-body simulations. Moreover, Lau et al. (2010) show that with gas cooling, the ICM core ($r \lesssim 0.1R_{500}$) is quite oblate as a resualt of the gas rotation, qualitatively consistent with the find-

ing of Fang et al. (2009); while the DM shape in the cluster core remains relatively spherical. Because unrelaxed clusters have large gas random motions relative to the rotation, the oblateness of the ICM core can be potentially used as a diagnostic of the cluster dynamical state. If the ICM core, but not the DM, is indeed oblate, it is expected that the ensemble average of the gas density and thermal pressure at small radii both to be underestimated by a similar fashion because the temperature is less affected by the projection, leaving P_X/P_{WL} unchanged. This effect is hardly detected in M_X/M_{WL}, either, because the measured M_X enclosed within a sphere does not depend much on the assumed halo shape. The large gas rotation and the oblate ICM core, meanwhile, are likely overstated from radiative simulations as well, since the average observed ICM ellipticity profile does not show an increase toward the cluster center as predicted (Fang et al., 2009; Kawahara, 2010).

3.7.2 Large scale structures

The observed lensing signal is the combination of the light deflection by the cluster and those from the intervening structures. The distant large scale structures (LSS) add non-negligible uncertainties to the cluster mass estimate (Hoekstra, 2001, 2003), but do not bias M_{WL} on average since the universe is isotropic and homogeneous at large scales, making the ensemble average of the distortion caused by these structures vanish. Hoekstra et al. (2011) using ray-tracing results from cosmological simulations of Hilbert et al. (2009) measure the scatter of NFW model fits due to distant LSS, which is consistent with the semi-analytic calculation of Hoekstra (2003). Based on their result that $\sigma_{M_{\rm vir}} = 2.1 \times 10^{14}{\rm M}_\odot$ and $\sigma_{c_{\rm vir}} = 0.59$ for $M_{\rm vir} = 10^{15}{\rm M}_\odot$, $c_{\rm vir} = 4.1$, $z = 0.2$ clusters, we estimate that errors on the 3D mass from distant LSS are 14% and 15% at R_{2500} and R_{500}, respectively. This error increases slightly with the distance from the cluster center because the cluster shear decreases with radius, but this cosmic noise is not significantly reduced by averaging over large areas due to its correlated nature, unlike the shape noise from the galaxy (see Dodelson, 2004). Note that the percentage error depends on the cluster mass and the outer fit radius (here $25'$), again for the same reason. Errors are smaller if the cluster is more massive or the fit range is narrower (for $z > 0.1$ clusters, Hoekstra et al., 2011). It also depends on the cluster redshift, the redshift distribution of source galaxies (thus the depth of the observation), and the adopted cosmology, particularly the power spectrum normalization σ_8. The estimated cosmic noise is likely at the high end because the chosen value of Hoekstra et al. (2011), $\sigma_8 = 0.9$, is higher than the currently favored one (Komatsu et al., 2011). The above assumed cluster mass at R_{500} is about $5.4 \times 10^{14}{\rm M}_\odot$, close to the median M_{500} of our sample. The source galaxy is chosen from a magnitude cut of $r_{\rm SDSS} < 25$.

At smaller scales, filaments structures surrounding the cluster can potentially bias M_{WL}. Early works by Cen (1997) and Metzler et al. (2001) suggested that M_{WL} was overestimated by a few to tens of percents due to these correlated LSS. However, Clowe et al. (2004) pointed out that this conclusion was obtained by comparing the total mass projected in a cylinder to that enclosed by a sphere. M_{WL} is generally unbiased by correlated LSS if the mass is determined by fitting the shear with a

projected cluster mass model such as the NFW profile (Clowe et al., 2004; Becker & Kravtsov, 2010), thanks to the otherwise unwanted mass-sheet degeneracy. The simulation of Becker & Kravtsov (2010) find a 19% scatter caused by correlated LSS and the halo triaxiality for $M_{500} = 2-9 \times 10^{14} h^{-1} \mathrm{M}_{\odot}$ clusters. Our estimated scatter by the halo shape alone (§3.7.1) is comparable to that of Becker & Kravtsov (2010) from the combined effect. Because spherical halos tend to cluster more compared to aspherical ones (Faltenbacher & White, 2010) and spherical halos are not subject to the projection effect, it is possible that the combined effect of correlated LSS and the halo shape is not significantly different from the sole effect from either one of them. Therefore, we do not consider separately the additional contribution from correlated LSS.

3.7.3 Substructures

A certain fraction of the cluster mass is retained within substructures. These substructures, if massive enough, can significantly change the mass profile from the universal NFW model, leading to a bias in the mass estimate through the parametric modeling or from converting nonparametric M_{2D} to M_{3D} with a NFW model. From N-body simulations, King et al. (2001) find that the best-fit NFW scale radius, $r_s = R_{200}/c_{200}$, can be recovered within 3% for a typical substructure model comprising 12% the total mass for $z = 0.2$ clusters. This corresponds to a $\approx 3\%$ uncertainty in the 3D mass, not a substantial change. Even if the substructure amplitude is doubled, the parameter dispersion is still within 10%, roughly a 11% error in mass. Meanwhile, the amplitude can be overestimated, as the subhalo mass function is found to be smaller in simulations including the gas than in the DM only version (Dolag et al., 2009).

As to the X-ray measurement, simulations including observational effects show that the gas mass is biased high by approximately 1% and 5% at R_{2500} and R_{500}, respectively (Nagai et al., 2007b; Meneghetti et al., 2010), because of the asymmetry or clumping of the gas distribution. The deviation is related to the dynamical state of the cluster such that relaxed clusters are generally biased less. Although other studies find that the gas mass can be biased up to $\sim 10\%$ (e.g., Hallman et al., 2006; Jeltema et al., 2008), we still choose the lower estimate from Nagai et al. (2007b) because the obvious point sources or small clumps are masked out from the X-ray data, just as done in Nagai et al. (2007b). It is expected that the bias in the gas mass does not affect M_X much because the hydrostatic mass depends on the logarithmic gradient of the gas density rather than the overall scale of the gas mass.

However, the temperature can be significantly biased because of cool substructures (e.g., Mathiesen & Evrard, 2001), and thus lower M_X. Yet the finding of Meneghetti et al. (2010) shows that M_X measured from the mock data is comparable to M_{HEQ}, the hydrostatic mass directly calculated from the gas density and temperature profiles of simulated particles, suggesting that the X-ray data can determine M_X quite accurately. Note again Meneghetti et al. (2010) removed all the identifiable clumps from their X-ray analysis. Therefore, we ignore the error of M_X due to substructures.

3.7.4 NFW modeling

The NFW profile was originally proposed for virialized halos within R_{200} (Navarro et al., 1997). Since lensing signals are sensitive to all the matter along the line-of-sight, any incorrect modeling at large radii will bias the inferred enclosed 3D mass at small radii. N-body simulations find that the mass density actually declines faster than the r^{-3} model assumption at $r \gtrsim R_{\rm vir}$ (Clowe et al., 2004; Busha et al., 2005), probably due to the tidal stripping. Baltz et al. (2009) suggest a smoothly truncated NFW model with an additional parameter corresponding to the tidal radius that is later found to fit the simulated lensing data best (Oguri & Hamana, 2011). Recently, Becker & Kravtsov (2010) studied the bias in M_{WL} introduced by fitting a NFW model to the reduced shear profiles generated from N-body simulations. They find that the overprediction at $r \gtrsim R_{\rm vir}$ causes a $2-4\%$ underestimate on the 3D mass at $r \ll R_{\rm vir}$, based on fits to the range of $1' - 20'$ for $z = 0.25$ clusters with a source galaxy density of 20 galaxies/arcmin^2 and a dispersion of the image ellipticity per galaxy of 0.3, typical for the deep ground-based observations. Furthermore, the bias increases with the expanding of the radial range for the fitting as the inner shear is now more underestimated in exchange for the less biased outer shear.

Despite the fairly good approximation provided by the NFW model within R_{200}, later simulations find that the logarithmic slope of the density profile decreases more slowly with decreasing radius than the prediction and the profile is better fitted with the Einasto model (Einasto, 1965), $\mathrm{d}\log\rho/\mathrm{d}\log\mathrm{r} \propto -\mathrm{r}^{\alpha}$ (Navarro et al., 2004; Prada et al., 2006; Merritt et al., 2006). As a result, the halo density is systematically underestimated by $\approx 2-20\%$ within $0.1R_{\rm vir}$ if the NFW model is fitted in the typical radial range where the weak lensing shear is measured, $0.1-1R_{\rm vir}$ (see Figure 1 of Gao et al., 2008). Outside $0.1R_{\rm vir}$, the errors are a few percent and should not significantly bias the 3D mass evaluated in this region.

The previously discussed simulations are all based on pure N-body runs that do not include baryons. The cooling of gas in the cluster core is expected to lead the adiabatic compression of the dark matter, resulting a steeper density profile (Blumenthal et al., 1986; Gnedin et al., 2004). However, the effect of baryons seems to resemble merely a change in the concentration parameter as suggested by simulations (Rasia et al., 2004). These is no indication of the deviation from the NFW model in lensing observations, either (e.g., Okabe et al., 2010; Umetsu et al., 2011). Therefore, we conclude that overall the NFW modeling introduces a $2-4\%$ bias due to the deviation at $r \gtrsim R_{\rm vir}$ in M_{WL} between R_{2500} and R_{500}.

3.8 Discussion

In Table 3.14, we list the measured mass ratio, gas mass fraction along with the values corrected for the systematic errors shown in Table 3.13. The correction at R_{500} does not include uncertainties in M_X from the temperature measurement (§3.2.1) or differences in M_{WL} between CFHT and Subaru samples (§3.3.2), which are mentioned separately. When correcting M_X/M_{WL}, the uncertainty from M_X is slightly reduced

Table 3.13: Summary of systematic uncertainties on M_{WL}, M_X, and $M_{\rm gas}$ at R_{2500} and R_{500}

source of errors [b]:bias, [s]:scatter	uncertainty R_{2500}, R_{500}	reference
M_{WL}		
[b] NFW modeling	$[2, 4]\%$	§3.7.4
[b] miscentering	$[0, 5]\%$, $\ll 5\%$	§3.3.3.1
[b] source redshift	$\pm 4\%$, $\pm 3\%$	§3.3.3.2
[b] shape measurement	2%	§3.3.3.4
[b] cross calibration [a]	$(4 \pm 12)\%$, $(15 \pm 11)\%$	§3.3.2
[s] triaxiality	$\pm 28\%$, $\pm 19\%$	§3.7.1
[s] large scale structures	$\pm 14\%$, $\pm 15\%$	§3.7.2
[s] substructures	$\pm 3\%$	§3.7.3
total bias [b]	$(7.5 \pm 4.8)\%$, $(5.0 \pm 3.2)\%$	
total scatter (32) [c]	5.6%, 4.3%	
M_X		
[b] parametric modeling	$(3 \pm 4)\%$, $(0 \pm 16)\%$	§3.2.4.1
[b] background	$\pm 2\%$, $\pm 5\%$	§3.2.4.2
[b] temperature measurement	≈ 0, $[-7, 4]\%$	§3.2.1
[b] *Chandra* calibration	$[-9, 0]\%$	§3.2.4.4
[s] triaxiality	$\pm 3\%$	§3.7.1
total bias [b]	$-(4.5 \pm 4.9)\%$, $-(4.5 \pm 6.7)\%$	
total scatter (32) [c]	0.5%, 0.5%	
$M_{\rm gas}$		
[b] parametric modeling	$(0 \pm 1)\%$	§3.2.4.1
[b] background	$\pm 1\%$	§3.2.4.2
[b] substructures	-1%, $\approx -5\%$	§3.7.3
[b] *Chandra* calibration	$\pm 2\%$	§3.2.4.4
[s] triaxiality	$\pm 6\%$, $\pm 5\%$	§3.7.1
total bias [b]	$-(1.0 \pm 2.2)\%$, $-(5.0 \pm 2.2)\%$	
total scatter (32) [c]	1.1%, 0.9%	

Note. — If there is only one number given, then quantities at R_{2500} and R_{500} are both subject to the same uncertainty.

[a]comparison between CFHT and Subaru samples.

[b]not including cross calibration, parametric modeling, or temperature measurement.

[c]divided by the square root of the sample size of 32.

Table 3.14: Summary of measurements at R_{2500} and R_{500}

quantity	sample	raw value	corrected value [a]
R_{2500}			
M_X/M_{WL}	total	1.27 ± 0.06	1.14 ± 0.12
M_X/M_{WL}	low P_3/P_0	1.47 ± 0.09	1.32 ± 0.17
M_X/M_{WL}	high P_3/P_0	1.07 ± 0.06	0.96 ± 0.12
$M_{\rm gas}/M_{WL}$	total	0.117 ± 0.007	0.107 ± 0.011
$M_{\rm gas}/M_{WL}$	low P_3/P_0	0.124 ± 0.011	0.113 ± 0.016
$M_{\rm gas}/M_{WL}$	high P_3/P_0	0.112 ± 0.008	0.102 ± 0.013
$M_{\rm gas}/M_X$	total	0.096 ± 0.002	0.099 ± 0.006
$M_{\rm gas}/M_X$	low P_3/P_0	0.093 ± 0.002	0.096 ± 0.006
$M_{\rm gas}/M_X$	high P_3/P_0	0.102 ± 0.003	0.106 ± 0.007
R_{500}			
M_X/M_{WL}	total	1.13 ± 0.05	1.04 ± 0.10
M_X/M_{WL}	low P_3/P_0	1.17 ± 0.07	1.08 ± 0.13
M_X/M_{WL}	high P_3/P_0	1.08 ± 0.06	0.99 ± 0.11
$M_{\rm gas}/M_{WL}$	total	0.148 ± 0.008	0.133 ± 0.012
$M_{\rm gas}/M_{WL}$	low P_3/P_0	0.145 ± 0.010	0.131 ± 0.015
$M_{\rm gas}/M_{WL}$	high P_3/P_0	0.152 ± 0.012	0.137 ± 0.016
$M_{\rm gas}/M_X$	total	0.137 ± 0.005	0.136 ± 0.011
$M_{\rm gas}/M_X$	low P_3/P_0	0.124 ± 0.005	0.123 ± 0.010
$M_{\rm gas}/M_X$	high P_3/P_0	0.149 ± 0.005	0.148 ± 0.012

[a] M_X and M_{WL} at R_{500} may suffer additional [-7, 4]% and $\approx$ 15% uncertainties from the X-ray temperature and the concentration assumed, respectively.

from the number listed in Table 3.13 since M_X is evaluating at the overdensity radius determined from M_{WL} rather than M_X itself. Our estimate should be regarded as somewhat conservative because the scatter from LSS has already been included to the statistical error of M_{WL} for the CFHT sample (Hoekstra, 2007) and the uncertainty from the X-ray background has been added in M_X.

3.8.1 The mass ratio

From the combined CFHT weak lensing sample of Hoekstra (2007) and Subaru sample of Okabe et al. (2010) and our *Chandra* X-ray analysis, we derive $M_X/M_{WL} = 1.27 \pm 0.06$ at R_{2500}. When all possible systematic uncertainties are taken into account, this ratio reduces to 1.14 ± 0.12, marginally consistent with unity. The ratio is roughly a constant above one between R_{5000} and R_{2500} and gradually decreases to 1.04 ± 0.10 at R_{500} (1.13 ± 0.05 uncorrected for the bias). Additional uncertainties

from the X-ray temperature measurement at large radii (§3.2.1), when comparing our temperature profile to those of Vikhlinin et al. (2006) and Arnaud et al. (2010), can potentially change the ratio by [-7, 4]% at R_{500}. Meanwhile the weak lensing mass discrepancy between CFHT and Subaru samples at large radii (§3.2.1), likely from the concentration parameter, can lower the value by $\approx 15\%$ if M_{WL} from the CFHT sample is more correct.

The measured M_X/M_{WL} is very sensitive to the cluster shape. For example, if the clusters in our sample turn out to be more oblate in general, then M_X/M_{WL} can be reduced below 1 while keeping the similar radial trend, which seems to agree with simulations better as the turbulent pressure is expected to dominate at cluster outskirts (e.g., Lau et al., 2009). However, the measured projected aperture mass to the best-fit NFW 3D mass $M_{\rm 2D}^{\rm ap}/M_{\rm 3D}^{\rm NFW}$ for the Subaru sample is consistent with the expectation of a $c_{\rm vir} \sim 4$ halo (Okabe et al., 2010) and agrees with the true $M_{\rm 2D}/M_{\rm 3D}$ of Meneghetti et al. (2010) from simulations. This suggests that our sample is not from clusters with unusual shapes. On the other hand, because the measured total X-ray luminosity is hardly changed by the viewing angle as it is integrated over a large aperture radius and the luminosity decreases strongly with the radius, it is unlikely that this mostly X-ray selected sample suffers much from the projection effect.

Although the excess of M_X at $r < R_{2500}$ is not significant for the whole sample when most of the potential systematic errors are considered, it is evident in the low P_3/P_0 sample, containing the most "relaxed" and regular clusters, with a ratio of 1.32 ± 0.17 (1.47 ± 0.09 uncorrected). Note we increase the uncertainty from the triaxiality, LSS, and substructures because of the reduced sample size. This finding seems to contradict the consensus from current simulations that the hydrostatic mass is always biased low even for relaxed clusters (e.g, Rasia et al., 2006; Nagai et al., 2007b; Meneghetti et al., 2010), due to ubiquitous gas bulk motions (Evrard et al., 1996) or other non-thermal pressure supports. Inside of R_{2500}, the additional pressure from the gas motion is relatively small according to simulations (e.g, Lau et al., 2009). The specific kinetic energy of DM is approximately equal to the specific thermal energy of the gas (e.g, see Figure 1 of Host et al., 2009, and references within), indicating an equilibrium between two species is reached. Unlike those including the radiative cooling, feedback, or pre-heating, however, the non-radiative simulation of Rasia et al. (2004) actually finds that the estimated mass from the ICM (either through the hydrostatic equation or hydrodynamic equation) is higher than the true mass and the gas is hotter than DM at $r \lesssim 0.1R_{\rm vir}$, in line with our result. The explanation is the following: during the mergers, shocks prevent the collisional gas from reaching the core, but the collisionless DM accumulates there. This spatial lag produces a net transfer of the energy from DM to the gas which subsequently converts to the gas thermal energy as gas particles feel a slightly stronger gravitational field than before (Navarro & White, 1993; Navarro et al., 1995; Rasia et al., 2004). A similar discovery is made by Pearce et al. (1994) that the central gas carries extra energy at the expense of DM in the final state of their merger simulations. Specifically, non-radiative simulations of a two equal-mass cluster merger by Lin et al. (2006) show that DM can transfer $\approx 7\%$ of its initial total energy to the gas across the cosmic time, which corresponds a 40% gain of the total energy of the gas assuming that the

total energy of the gas to that of DM is approximately equal to $M_{\rm gas}/M_{\rm DM} \sim 0.18$ from the virial theorem. If the transferred energy mostly releases as heat, this 40% change seems to account for a factor of 1.3 higher than expected M_X in low P_3/P_0 sample.

Our finding of $M_X/M_{WL} > 1$ at R_{2500} is also consistent with the result of Hoekstra et al. (2011) who measure the weak lensing mass of 25 moderate X-ray luminosity clusters at $0.3 < z < 0.6$. The normalization of their $M_{2500}-L_{\rm X}$ relation is $\approx 10-20\%$ lower than those derived from M_X (Reiprich & Böhringer, 2002; Stanek et al., 2006; Vikhlinin et al., 2009a; Mantz et al., 2010a), though the differences are not significant.

Recently, Lemze et al. (2011) find that the velocity dispersion of DM is smaller than that of the cluster galaxies at $r \lesssim 0.3R_{\rm vir}$ from the galaxy kinematics, strong and weak lensing analyses of A1689. Although they assume spherical symmetry, DM can be even cooler in the core if the halo is elongated along the line-of-sight, as suspected by many studies (e.g., Xue & Wu, 2002; Andersson & Madejski, 2004; Oguri et al., 2005), because the kinematics is less affected by the projection compared to the lensing (Gavazzi, 2005). This is also revealed in the galaxy density profile which flattens in the core region, unlike the steepening DM density profile (Lemze et al., 2011). If the seemingly collisionless galaxies are hotter than DM, then the truly collisional gas should be much hotter than that.

For the morphologically more disturbed high P_3/P_0 sample, we obtain $M_X/M_{WL} = 0.96\pm0.12$ (1.07 ± 0.06 uncorrected), 27% lower or 1.7σ different (3.7σ for uncorrected ratios) than that of the low P_3/P_0 sample and much closer to unity compared to the high P_3/P_0 sample. As shown in §3.4 and §3.5, this difference is probably from the X-ray measurement because the shape of P_X and M_X profiles is very different from clusters to clusters, unlike that of P_{WL} and M_{WL}. The lower M_X could arise from the incomplete thermalization of the gas, biased broad band spectroscopic temperature by cool merging substructures (Mathiesen & Evrard, 2001), or simply mixing that actually brings the gas and DM into a better equilibrium. If our measurement does not suffer further systematic uncertainties, then the word "unrelaxed" in the observer's view may have the opposite meaning.

As discussed in §3.3.3, the offset between the assumed center, the BCG location, and the true one can lower the weak lensing mass estimate, especially at small radii. If high P_3/P_0 clusters happen to be those having the largest BCG offsets, this can explain the relatively lower M_X/M_{WL} in the center. Although we do not know where the true mass center is [12], small offsets between the X-ray centroid and the BCG generally indicate that the true offsets are small, too. However, there appears to be no correlation between P_3/P_0 and the offset of the BCG from the X-ray center (Figure 4-9), except that the biggest four offsets are all from high P_3/P_0 clusters (A521, A2218, A370, A2631[13]). Excluding those four clusters, the difference in M_X/M_{WL} between low and high P_3/P_0 samples remains. This suggests that the miscentering is not the reason for the discrepant M_X/M_{WL} at small radii.

[12]It can be estimated from fitting a symmetric model to the 2D lensing shear map (e.g., Oguri et al., 2010).

[13]not including A115

Since clusters are better described by a triaxial model, it is expected that the more elliptical cluster in the projection may tend to have a lower best-fit M_{WL} from a spherical model but with M_X roughly unchanged (§3.7.1). This speculation is in agreement with our result that the generally more elliptical high P_2/P_0 sample has a higher M_X/M_{WL} than the low P_2/P_0 sample at R_{500}. The $M_{\rm gas}/M_{WL}$ plot (Figure 3-22) shows the same trend, too. An anticorrelation between the best-fit M_{WL} at R_{200} and the ellipticity is also detected in simulations of Clowe et al. (2004). However, if the cluster shape is the only difference in high and low P_2/P_0 samples, then a higher mass ratio is anticipated for the high P_2/P_0 sample at all radii, which is not seen in our data. In point of fact, M_X/M_{WL} is lower for the high P_2/P_0 sample at small radii, just as the high P_3/P_0 sample, suggesting that elliptical clusters are also more "unrelaxed" on average, in the sense of having a relatively lower M_X.

Although the finding $M_X/M_{WL} > 1$ at small radii is generally in agreement with the simulation of Rasia et al. (2004), the observed excess happens at somewhat larger than the predicted radius[14]. Since the gas gains the energy from DM through the transient spatial offset between them during mergers, any process that holds the gas particle longer, such as the ICM viscosity, should increase the transfer of energy to the gas. The higher viscosity may transfer the kinetic energy into the thermal energy more quickly and heat the gas to larger radii. In fact, physical viscosity is ignored in the work of Rasia et al. (2004), just as many other simulations which commonly treat the gas as an inviscid fluid. Implementing physical viscosity in cosmological simulations, Sijacki & Springel (2006) find that the gas temperature can be raised to a much higher level in the core compared to simulations without viscosity. Although the central gas density decreases because of the viscosity, the increase of the temperature surpasses the logarithmic change of the gas density (see their Figure 5 of a isolated halo for a clearer comparison), thus resulting a higher M_X. In addition, the shear force from the viscosity can effectively strip the gas content of the infalling substructure, smooth out the gas distribution, and leave gaseous tails behind the infalling DM. Viscosity will also damp turbulence, reducing non-thermal pressure from gas motions. The multiple bubbles from episodes of the AGN flaring observed in the Perseus cluster (e.g., Fabian et al., 2006) indicate that they are stable against the hydrodynamical instability, which can be sufficiently suppressed by the ICM viscosity (Kaiser et al., 2005; Reynolds et al., 2005; Sijacki & Springel, 2006). Another example is the long and straight cold fronts seen at the sides of the bullet subcluster (Markevitch et al., 2002), which again suggests that the ICM is highly viscous. Other mechanisms, however, such as the magnetic shielding around the moving gas parcel, can also inhibit the instability (Markevitch & Vikhlinin, 2007, and references within).

3.8.2 The gas mass fraction

After adding systematic uncertainties and correcting for possible bias (which includes 1% and 5% for $M_{\rm gas}$ at R_{2500} and R_{500}, respectively), we obtain $f_{\rm gas}^{\rm X} = 0.123 \pm 0.010$ and 0.148 ± 0.012 for low and high P_3/P_0 samples at R_{500}, respectively. This corresponds

[14] $0.1R_{\rm vir} \approx R_{7000}$, $R_{2500} \approx 0.2R_{\rm vir}$

to a $\sim 20\%$ difference in $f_{\rm gas}^{\rm X}$ with a 1.6σ significance. Since a major systematic uncertainty comes from the calibration, which in principle affects the sample uniformly, our result should be more significant than that (e.g., 3.5σ in uncorrected $f_{\rm gas}^{\rm X}$). $f_{\rm gas}^{\rm WL}$ for high P_3/P_0 clusters is also slightly higher than that of low P_3/P_0 clusters at R_{500}, but with a much lower significance. Part of the reason is the greater statistical accuracy of X-ray data while the other part is that high P_3/P_0 clusters also have slightly lower M_X/M_{WL} at R_{500}. In any case, higher $f_{\rm gas}$ found in morphologically more disturbed clusters likely indicates that $M_{\rm gas}$ is affected by the gas clumping or asphericity. From the difference between $f_{\rm gas}^{\rm WL}$ in low and high P_3/P_0 samples, these effects are estimated to be $\approx 5\%$ in $f_{\rm gas}$ at R_{500}.

The gas clumping, however, is certainly not the only reason for a higher $f_{\rm gas}$, as this is found in NCC clusters at large radii, too. Since M_X/M_{WL} profiles are approximately the same for CC and NCC clusters and the cuspiness parameter only correlates weakly with P_3/P_0 (Figure 4-12, 7 out of 19 NCC clusters have low P_3/P_0), this implies that $M_{\rm gas}$ could also be affected by the gas cooling. The cooling may bring more outer gas toward the core, resulting a flatter $f_{\rm gas}$ profile. The flattening is as well seen in other CC clusters from a nearby sample of Pratt et al. (2010) (see Figure 2 of Young et al., 2011).

At small radii, $f_{\rm gas}^{\rm X}$ shows a distinctly different radial trend from $f_{\rm gas}^{\rm WL}$ between low and high P_3/P_0 clusters. Low P_3/P_0 clusters have 10% higher $f_{\rm gas}^{\rm WL}$ than their counterparts at R_{2500}, but for $f_{\rm gas}^{\rm X}$ the opposite is true. The flattened $f_{\rm gas}^{\rm WL}$ profile in the core in low P_3/P_0 clusters very much resembles that of CC clusters, yet the disparity between $f_{\rm gas}^{\rm X}$ and $f_{\rm gas}^{\rm WL}$ at small radii is not seen in CC/NCC samples. This seems to suggest that the morphologically regular cluster has developed a compact gas core, but the massive radiative cooling is not yet turned on so that it still has a relatively high temperature in the core, unlike CC clusters. In other words, this hints at a possible source to power the cool core, the excess energy gaining from DM.

From 12 LoCuSS clusters, Zhang et al. (2010) conclude that $f_{\rm gas}^{\rm WL}$ does not reflect the relaxedness of the cluster, defined from the ICM morphology. Because the differences in $f_{\rm gas}^{\rm WL}$ between low and high P_3/P_0 samples are only $0.9\,\sigma$ and $0.5\,\sigma$ at R_{2500} and R_{500}, respectively, from the original data not including the additional systematic uncertainty, it is not surprising that they do not find it in a sample that is 2.7 times smaller than ours.

3.9 Summary

We study the X-ray and weak lensing measurements of cluster mass, pressure and gas mass profiles and their relations to the ICM morphology, which is quantified by the cuspiness parameter, power ratios P_m/P_0, and centroid shifts $\langle w \rangle$. The cuspiness parameter is used to define whether the cluster is CC or NCC; while low (high) power ratio or centroid shift clusters are those with the measures below (above) the median of the total sample. A lower value indicates a higher degree of regularity of the cluster. Our main results can be summarized as follows:

- Comparing X-ray hydrostatic and weak lensing mass estimates, we obtain

$M_X/M_{WL} = 1.14 \pm 0.12$ at R_{2500} and 1.04 ± 0.10 at R_{500}. Additional uncertainties at R_{500} from the X-ray temperature measurement at large radii (§3.2.1, [-7, 4]%) and from the discrepant concentration parameter of the M_{WL} profile (§3.2.1, $\approx -15\%$) should be considered as well.

- We find a clear correlation of M_X/M_{WL} with P_3/P_0 such that the low P_3/P_0 cluster have a higher M_X/M_{WL}, particularly at small radii, which makes the ratio well above unity, implying that the gas may be hotter than DM. The ICM viscosity, commonly ignored in simulations, could be the reason for the hotter gas.

- M_X/M_{WL} also correlates with P_2/P_0 such that high P_2/P_0 clusters have higher than average M_X/M_{WL} at large radii. Because these clusters are more elliptical in projection, suggesting a shortening along the line-of-sight on average, this erroneous modeling leads to an underestimate of M_{WL}.

- There is no significant difference in M_X/M_{WL} between CC and NCC samples, which agrees with the finding of Mahdavi et al. (2008). However, CC clusters are still special in the sense that they seem to have the most concentrated M_{WL} profiles, possibly providing evidence for the adiabatic compression (Blumenthal et al., 1986).

- We find that morphologically more disturbed (high P_m/P_0 or $\langle w \rangle$) clusters tend to have a higher $f_{\rm gas}^{\rm X}$ or $f_{\rm gas}^{\rm WL}$ at large radii compared to the undisturbed ones, but in the core the latter have a higher $f_{\rm gas}^{\rm WL}$ while their $f_{\rm gas}^{\rm X}$ is still relatively lower.

- Unlike other classifications, $f_{\rm gas}^{\rm X}$ and $f_{\rm gas}^{\rm WL}$ profiles are very similar for CC or NCC clusters at all radii. Both $f_{\rm gas}^{\rm X}$ and $f_{\rm gas}^{\rm WL}$ are flattening in the core for CC clusters, but continue decreasing toward the center for NCC clusters.

- Our scaled thermal pressure profile agrees with that of Arnaud et al. (2010) within $\approx 10\%$ at $r < 0.7R_{500}$, but is not as steep as theirs at large radii because our temperature profile differs from theirs (§3.2.1). The higher pressure or temperature we find at large radii, however, is in tension with with SZ data (Komatsu et al., 2011; Andersson et al., 2010).

- Low P_3/P_0 clusters have the steepest P_X profiles among our sample; CC clusters seem to have the steepest P_{WL} profiles.

- P_3/P_0 is more sensitive to to the cluster dynamic state than $\langle w \rangle$ in general, as concluded by Jeltema et al. (2008).

- The known $\gtrsim 10\%$ difference in $f_{\rm gas}^{\rm X}$ measurements at R_{2500} between those of Vikhlinin et al. (2006) and Allen et al. (2008) (and also ours compared to those of Allen et al. (2008) and Mahdavi et al. (2008)) is likely the result of the different parametrization of gas or mass models. Since the former approach, which we have followed here, adopts very flexible gas profiles, the bias is generally less

than the latter backward method. However, the magnitude of the discrepancy also depends on the specific parametrization and the radial range used in the fitting. From the present work we learn that M_X and M_{WL} are quite different in the core. In addition, the commonly assumed NFW model for the total mass in the backward method is controversial at small radii (§3.7.4) where the X-ray data quality is good. Therefore, we conclude that the former technique is better suited for the X-ray analysis. The implications of the assumed functional form of the gas profiles on cluster masses and scaling relations have been discussed in detail by Mantz & Allen (2011). Although we agree with these authors that the implicit priors in the modeling do affect the result, we disagree that using a semi-parametric approach, which models M_X with a NFW profile without any parametrization on gas profiles (similar to the backward method used here), helps to alleviate the bias. As shown in §3.2.4.3, the backward method with a two-parameter NFW model and a hydrostatic assumption does not fit the temperature profile as well as the forward method. Parametrizing the mass profile is in fact parametrizing the gas temperature profile if hydrostatic equilibrium is imposed.

Chapter 4

X-ray Monte Carlo analysis

4.1 Smoothed Particle Inference

The Smoothed Particle Inference (SPI) technique developed by Peterson et al. (2007) is a forward-folding method with a kilo-parametric model that describes clusters as hundreds of smoothed particles of plasma by two-dimensional spatial Gaussians. Each particle has its own temperature, normalization, spatial position, Gaussian width, redshift, and a set of elemental abundances. The particles are propagated through an instrument model and generate photons at certain CCD positions and pulse-height energies to be compared with raw data. The Markov chain Monte Carlo method (similar to §3.1.3) is used to construct probable sets of parameters.

This kilo-parametric cluster model is needed to cope with complex phenomena, such as cold fronts and shock fronts. Figure 4-1 shows an example of SPI modeling of MS1358.1+6245. The luminosity map reveals a sharp edge close to the west of the bright core and the temperature map shows a sudden jump at this region. This feature is on the scale of $10''$. A sophisticated modeling like SPI is required, otherwise it will be smoothed out.

The SPI method is essentially a multi-temperature model. Particles can be overlapping, so the spectra at any spatial point will consist of multiple temperature components from different blobs. To disentangle these components, the instrument has be to sensitive to the temperature of each component. Yet there is still some degree of the degeneracy that can not be overcome by the perfect detector. The SPI modeling generally gives higher average temperatures than the standard single-temperature analysis does (Andersson et al., 2009). This is expected since the temperature from a single-temperature fit to the multi-temperature plasma (which is always present because we are measuring the projected emission along the line of sight) is usually lower than the average or the emission weighted average of those temperature components because current detectors are more sensitive to the lower temperature component (Mazzotta et al., 2004). However, determining the true temperature distribution is often hampered by the spectral resolution of the instrument, the quality of the data, and the innate degeneracy. We find that the measured temperature distribution depends sensitively on the range of temperatures for the assumed prior distribution, so

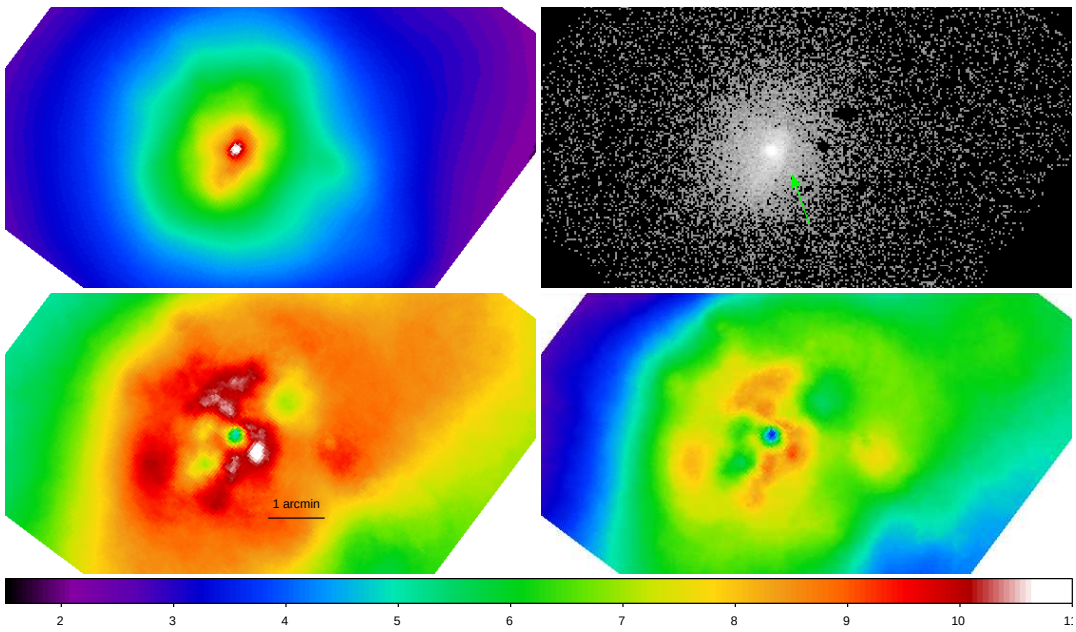

Figure 4-1: MS1358.1+6245. *Top left*, emission measure map constructed from the median of the SPI distribution for all samples at each spatial point; *top right*, raw ACIS-S3 image with point sources excluded; *bottom left*, median emission-measure weighted temperature map; *bottom right*, median spectroscopic-like temperature map.

quoting the average of the temperature distribution may not be meaningful unless the degeneracy inherent in this technique has fully been addressed.

Instead, we produce the spectroscopic-like temperature $T_{\rm spec-like}$ from the SPI model using the weighting scheme of Vikhlinin (2006) (see also §3.1.2). $T_{\rm spec-like}$ is a prediction for the single-temperature fit to the multi-temperature plasma. It is not that sensitive to the prior temperature range and is more nearly comparable to the temperature obtained from the standard analysis. However, there is some limitation on the weighting method of Vikhlinin (2006). It is only accurate if the dynamic range of the temperature is not too large, $T_{\rm max}/T_{\rm min} \lesssim 2$. For bimodal spectra with larger temperature differences, the single-temperature fit tends to ignore the weaker component and model only the brighter one. Nonetheless, $T_{\rm spec-like}$ still provides qualitatively useful information, such as identifying temperature substructures. A future implementation will include a direct single temperature fit to the SPI model convolved with the instrument response.

4.2 Temperature and luminosity maps

The SPI reconstructed luminosity and spectroscopic-like temperature maps for the whole sample are shown in Appendix B.1 and B.2. The value of each pixel of each map is the median from the Markov chain. Details of creating median parameter maps are described in Andersson et al. (2007). The luminosity is calculated in the $0.3-10$ keV band in the observer frame. We show the luminosity in the chosen energy band instead of the bolometric luminosity because the latter is integrated to high energies and thus strongly depends on the temperature of the particle. As mentioned before, we do not constrain the temperature distribution very well, especially at high energies. To reduce the uncertainty, the luminosity is only calculated within the energy range we observe.

To quantitatively compare SPI results with the standard analysis, we extract particles from circular annuli to produce radial profiles. A histogram of particle properties is constructed from the stationary part of the Markov chain. The median of the distribution is regarded as the best value and errors are the 68% confidence intervals around the median. Figure 4-2 shows the comparison of SPI results with the standard analysis (Chapter 3) for projected temperature (*left*) and emission measure (*right*) profiles of four clusters in our sample. For A383 and A1689, the SPI projected temperature and its uncertainty (circles) are comparable to the standard 1D analysis of the single temperature fitting (squares). For A2219 and A1835, however, the SPI result greatly disagrees with the standard analysis. The former two and the latter two represent the best and the worst SPI results in our sample, respectively. As explained earlier, the formula of Vikhlinin (2006) to produce $T_{\rm spec-like}$ is only accurate for the unimodal spectral distribution within the limited temperature range. Yet the disagreement found in A1835 and A2219 does not necessarily mean that the X-ray spectra are highly bimodal, since the calibration uncertainty, not accounted here, could cause the model to favor an unphysical spectral distribution, especially for high-quality data. Our prior probability distribution for particle temperatures

is set in the range of $0.5 - 30$ keV. Such a wide energy range is to accommodate a variety of observed cluster temperatures (e.g., $20 - 30$ keV found in 1E 0657−56, Markevitch & Vikhlinin, 2007). However, this also increases the degeneracy between different temperature components and weaken the validity of $T_{\rm spec-like}$ derived from Vikhlinin (2006). Despite the discrepant temperature, the emission measure profile agrees well with that from a best-fit gas density model (Eq. 2.4) from the standard analysis (solid line). Moreover, the SPI modeling has the advantage of presenting the gas profile in a non-parametric way that captures all subtle features of the profile. In addition, it is very easy to extract the gas profile in regions of interest, unlike the traditional method that the same analysis has to be repeated for spectra taken from other regions.

4.3 Pressure profile

To derive 3D properties of the ICM, such as the gas density or the pressure, the z coordinate in the line of sight direction, not constrained by the data, must be given to the 2D Gaussian blob. Following the work of Andersson (2007), a z coordinate is randomly assigned to each blob so that the 3D spatial distribution of all the particles matches an assumed profile. For simplicity, we assume a spherical symmetry of the particle distribution. We have made some improvements of the deprojection of Andersson (2007). The z coordinate is drawn from a newly calculated distribution of each iteration, instead of a completely random distribution, which makes the convergence faster. Second, the spatial extent of the blob is taken into account. The resulting spherically average thermal pressure profile from SPI (squares) is shown in Figure 4-3, in comparison with a best-fit model from the standard analysis (solid lines). The ratio of the SPI result to that of the standard analysis is plotted in the bottom panel. The agreement is generally good for A383 and A1689, but not for A2219 and A1835 because of the temperature problem (§4.2).

4.4 Power ratios

The power ratio method introduced by Buote & Tsai (1996) is a well established method to quantify substructures in clusters. It is a multipole expansion of the X-ray surface brightness $\Sigma(r, \phi)$ around the cluster centroid with the moments a_m and b_m determined as

$$a_m(R) = \int_{r \le R} \Sigma(r, \phi)\, r^m \cos m\phi \, r{\rm d}r{\rm d}\phi \tag{4.1}$$

$$b_m(R) = \int_{r \le R} \Sigma(r, \phi)\, r^m \sin m\phi \, r{\rm d}r{\rm d}\phi, \tag{4.2}$$

and the powers in the multipole m calculated as

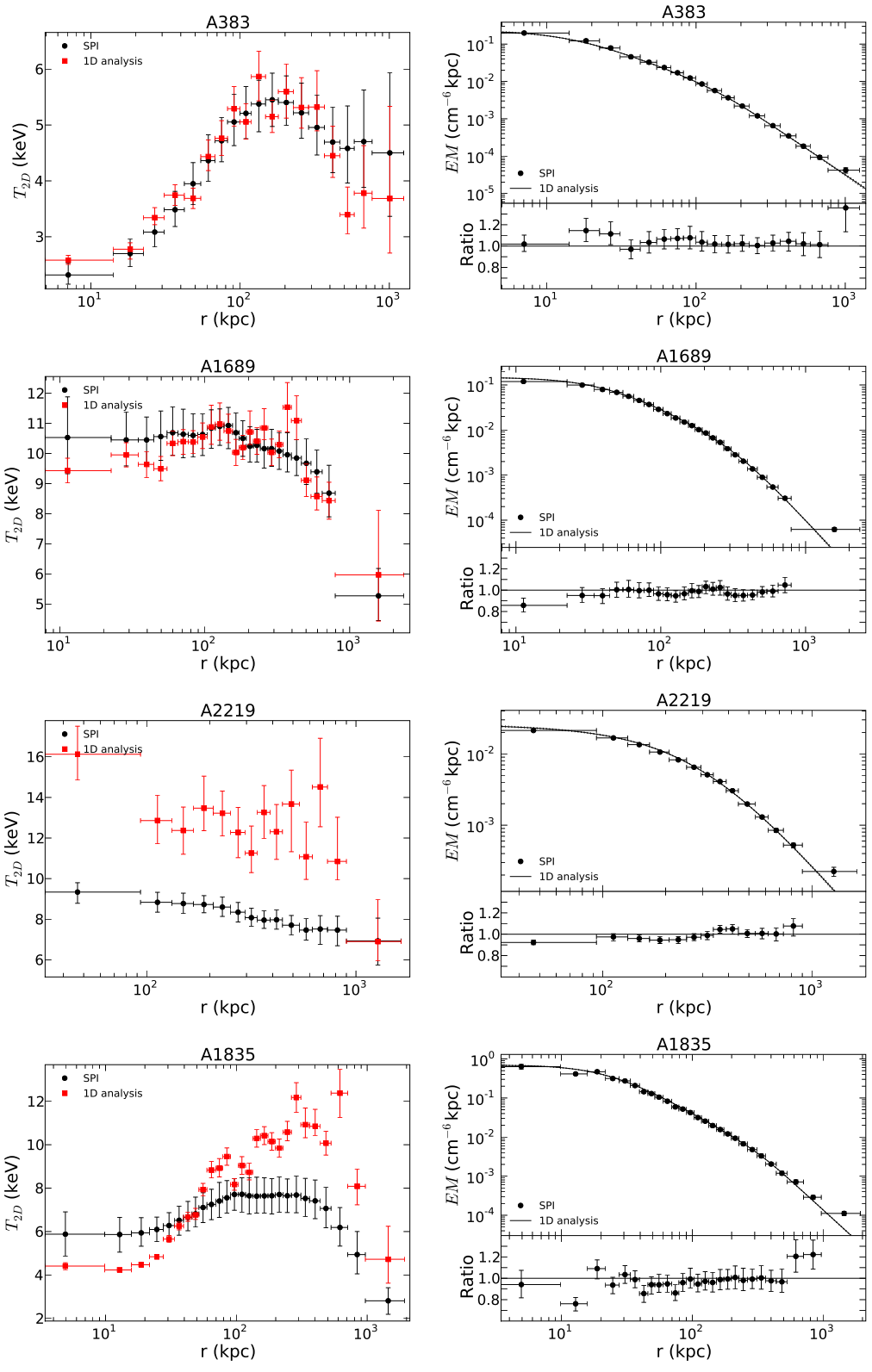

Figure 4-2: Comparison of SPI results with the standard analysis for projected temperature (*left*) and emission measure (*right*) profiles. The bottom panel of the emission measure plot shows the ratio of the SPI result to that of the standard analysis, which is from a best-fit gas density model (Eq. 2.4) fitted to the surface brightness profile.

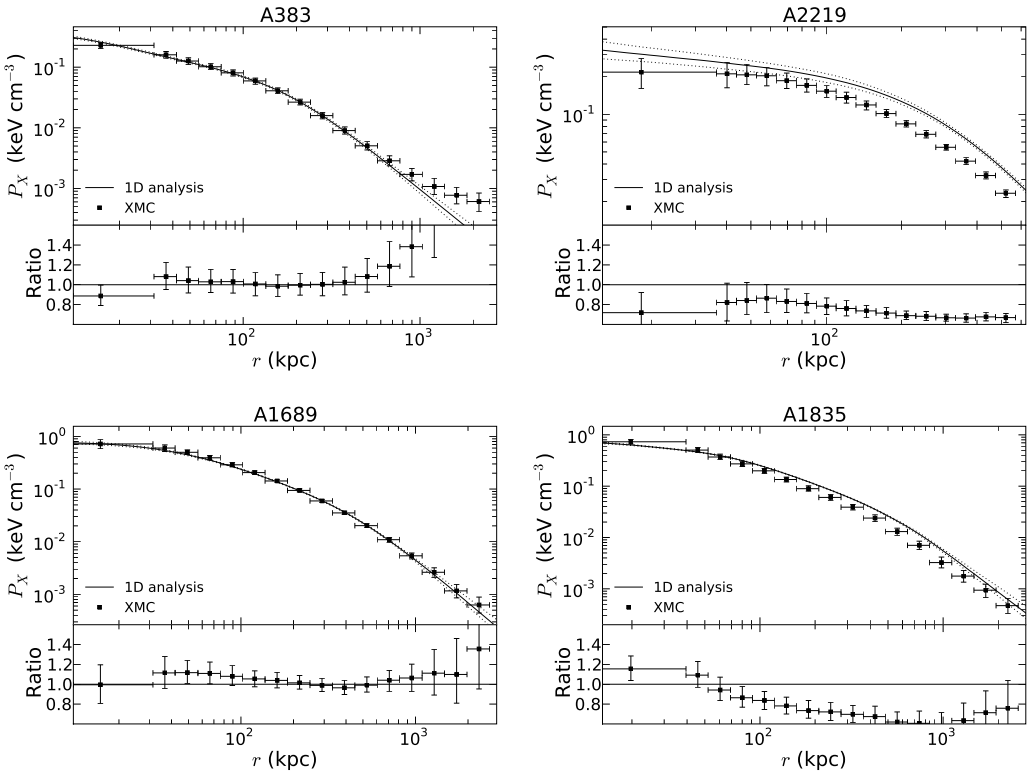

Figure 4-3: Comparison of SPI results with the standard analysis for the X-ray pressure profile. The ratio of the SPI result to that of the standard analysis is shown in the bottom panel.

$$P_0 = (a_0 \ln(R))^2 \tag{4.3}$$

$$P_m = \frac{1}{2m^2 R^{2m}} \left(a_m^2 + b_m^2\right). \tag{4.4}$$

Since P_m is proportional to the total flux, P_0, it is divided by P_0 to form the power ratio, P_m/P_0. Note power ratios, despite of being normalized by P_0, are dependent on the aperture radius R. Since the surface brightness drops quickly with the radius for most clusters, a_m and b_m are unlikely to grow faster than R^m. Consequently, power ratios decrease with the aperture radius in general. However, for some highly disturbed clusters, increasing R may result in more inclusions of major substructures, and thus an increase in power ratios.

The power ratio method has been used in Jeltema et al. (2005); Andersson et al. (2009); Böhringer et al. (2010) for samples of *Chandra* and *XMM-Newton* clusters. Jeltema et al. (2005) find that high-redshift clusters have significantly higher P_3/P_0 and P_4/P_0 than low-redshift ones. Andersson et al. (2009) confirm an increase with z for P_3/P_0, but not for P_2/P_0. Because P_2/P_0 can be large for elliptical but regular clusters, P_3/P_0 is thus expected to be the lowest power ratio moment to clearly indicate substructures.

Here, we define the cluster centroid as the center at which P_1 vanishes for the chosen aperture radius. The power ratio is calculated from the luminosity in the 0.3-10 keV energy range. The luminosity map from an single iteration of the chain, while consistent with the data beacuse of the noisy simulation, is not ideal to compute the power ratio since we want to find real structures but not photon fluctuations. Yet if using the average map of all iterations, we have no other sample for the error estimate. Therefore, we take a subset of the chain, create a median luminosity map from this subset, and calculate the power ratio for this map. The final result is from the distribution of power ratios measured from the maps of those subsets, with the median of the distribution as the best value and the 68% confidence intervals around the median as errors. To choose the adequate size of the subset, we start from a small number and steadily increase the size until the final power ratio does not vary from the previous run by 5%. It typically requires $10 - 30$ iterations from a chain to achieve this.

Figure 4-4 compares our power ratios to the results of Jeltema et al. (2005) (J05) from *Chandra* data and Andersson et al. (2009) (A09) from *XMM-Newton* data for the same objects. The aperture radius is 500 kpc, identical to those used in J05 and A09. J05 measured P_m/P_0 from adaptively binned raw images (Sanders & Fabian, 2001) corrected for the exposure. A09 used the same SPI modeling as we do. Our values generally agree with J05, though the scatter is quite large, especially for P_3/P_0 and P_4/P_0. Our power ratios are uniformly lower by a factor of 2 or more than those of A09, possibly because these authors calculated the ratio from a single iteration map instead of the smoothed map from a subset of the chain. Since both A09 and our results show the same trend from low to high values and only the relative power ratio is needed to classify the sample, this difference in the absolute value is not important

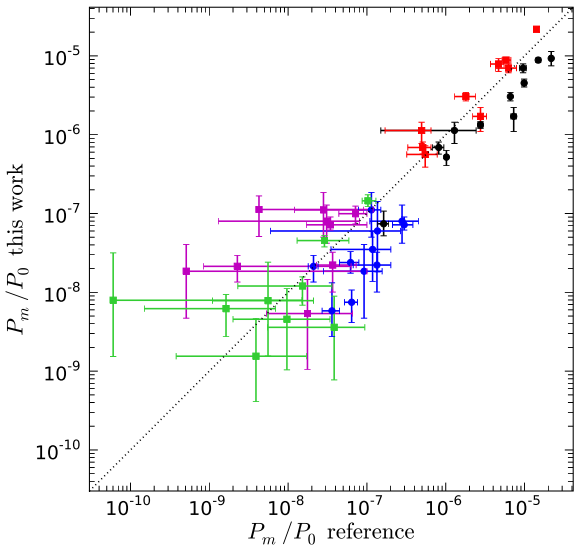

Figure 4-4: Comparison of power ratios for clusters that are common to the sample of Jeltema et al. (2005) (squares) and Andersson et al. (2009) (circles) for an aperature radius of 500 kpc. P_2/P_0, P_3/P_0 and P_4/P_0 of Jeltema et al. (2005) are shown in red, magenta and green colors, respectively. P_2/P_0 and P_3/P_0 of Andersson et al. (2009) are shown in black and blue colors, respectively. The dotted line is the line of the equality.

for our analysis.

Figure 4-5 shows comparisons of P_3/P_0 in 3 different radii: 500 kpc, 0.5 and 0.9 R_{500}. Only clusters that are completely covered by the 0.9 R_{500} aperture are shown (Figure 4-5 *left*). P_3/P_0 measured in 0.9 R_{500} radius is systematically smaller that in 0.5 R_{500}, as expected, except for one obvious outlier, A115, a merging cluster with two roughly equal massive subclusters, separated by $5'$ ($\approx 0.75R_{500}$) in projection and colliding with a speed of 1600 km s^{-1} (Barrena et al., 2007; Gutierrez & Krawczynski, 2005). The difference between 500 kpc and 0.5 R_{500} apertures is relatively small. The average 0.5 R_{500} for our sample is 1.2 times 500 kpc, with a scatter of 20%. However, the gravitational potential of clusters is known to exhibit self-similarity (Navarro et al., 1997), so the use of the scaled version of radii, the overdensity radius, should provide a fair comparison for clusters with different masses and redshifts. For this reason, we choose $0.5R_{500}$ as the aperture radius for the analysis in Chapter 3 and for the subsequent study. Values are listed in Table 4.1. Also pointed out by Jeltema et al. (2008), if the power ratio is measured within a constant physical radius, the evolution in the cluster structure could be hidden since the viral radius decreases with the redshift.

Table 4.1: Power ratios measured within $0.5R_{500}$

Name	RA [a] (J2000)	Dec [a] (J2000)	P_2/P_0 (10^{-7})	P_3/P_0 (10^{-7})	P_4/P_0 (10^{-7})
MS0015.9+1609	00:18:33.5	+16:26:14	$66.2^{+18.0}_{-5.5}$	$1.35^{+0.98}_{-0.73}$	$0.24^{+0.22}_{-0.14}$
CL0024.0+1652	00:26:35.7	+17:09:38	$24.5^{+6.9}_{-10.2}$	$2.35^{+1.29}_{-1.43}$	$0.13^{+0.23}_{-0.09}$
A68	00:37:06.1	+09:09:35	$71.0^{+12.2}_{-10.3}$	$0.25^{+0.41}_{-0.18}$	$0.46^{+0.32}_{-0.21}$
A115	00:55:53.1	+26:24:27	121^{+9}_{-11}	$4.21^{+0.99}_{-0.74}$	$0.57^{+0.18}_{-0.16}$
A209	01:31:52.3	−13:36:37	$45.0^{+6.9}_{-5.7}$	$0.60^{+0.28}_{-0.28}$	$0.06^{+0.05}_{-0.04}$
RXJ0142.0+2131	01:42:03.6	+21:31:22	$30.7^{+9.9}_{-8.7}$	$1.28^{+0.98}_{-0.83}$	$0.26^{+0.22}_{-0.19}$
A267	01:52:42.1	+01:00:30	$45.3^{+12.0}_{-8.7}$	$0.30^{+0.35}_{-0.23}$	$0.06^{+0.11}_{-0.04}$
A370	02:39:53.1	−01:34:32	175^{+18}_{-19}	$6.33^{+1.62}_{-1.84}$	$1.83^{+0.49}_{-0.48}$
A383	02:48:03.3	−03:31:47	$0.71^{+0.30}_{-0.21}$	$0.23^{+0.08}_{-0.06}$	$0.02^{+0.01}_{-0.01}$
A521	04:54:07.8	−10:14:01	$77.6^{+6.0}_{-5.2}$	$2.19^{+0.31}_{-0.44}$	$0.04^{+0.05}_{-0.03}$
A586	07:32:20.4	+31:37:55	$4.77^{+2.48}_{-1.72}$	$0.16^{+0.17}_{-0.10}$	$0.04^{+0.05}_{-0.03}$
A611	08:00:56.9	+36:03:27	$6.12^{+2.02}_{-2.03}$	$0.12^{+0.17}_{-0.09}$	$0.04^{+0.04}_{-0.03}$
ZwCl0839.9+2937	08:42:55.9	+29:27:27	$5.07^{+0.94}_{-0.74}$	$0.14^{+0.06}_{-0.04}$	$0.01^{+0.02}_{-0.01}$
A697	08:42:57.6	+36:21:55	$51.6^{+8.4}_{-8.8}$	$1.01^{+0.65}_{-0.57}$	$0.12^{+0.17}_{-0.08}$
A750	09:09:12.7	+10:58:37	$24.2^{+2.8}_{-3.4}$	$0.35^{+0.19}_{-0.15}$	$0.03^{+0.03}_{-0.03}$
A963	10:17:03.7	+39:02:49	$3.64^{+0.55}_{-0.62}$	$0.22^{+0.08}_{-0.08}$	$0.08^{+0.03}_{-0.03}$
A1689	13:11:29.6	−01:20:25	$9.49^{+0.57}_{-0.53}$	$0.05^{+0.02}_{-0.02}$	$0.05^{+0.01}_{-0.01}$
A1763	13:35:19.3	+41:00:02	$59.5^{+13.7}_{-10.5}$	$0.98^{+0.64}_{-0.66}$	$0.42^{+0.34}_{-0.21}$
MS1358.1+6245	13:59:50.9	+62:31:03	$12.8^{+3.4}_{-2.1}$	$0.39^{+0.17}_{-0.17}$	$0.05^{+0.05}_{-0.03}$
A1835	14:01:01.9	+02:52:39	$2.62^{+0.72}_{-0.68}$	$0.03^{+0.06}_{-0.03}$	$0.03^{+0.03}_{-0.01}$
ZwCl1454.8+2233	14:57:15.0	+22:20:33	$7.09^{+1.20}_{-1.17}$	$0.21^{+0.08}_{-0.06}$	$0.01^{+0.01}_{-0.01}$
A2009	15:00:19.7	+21:22:12	$11.7^{+4.0}_{-2.9}$	$0.12^{+0.15}_{-0.09}$	$0.03^{+0.05}_{-0.02}$
ZwCl1459.4+4240	15:01:22.0	+42:20:51	$50.9^{+14.0}_{-9.6}$	$0.48^{+0.59}_{-0.34}$	$0.06^{+0.10}_{-0.04}$
MS1512.4+3647	15:14:22.4	+36:36:24	$33.3^{+6.5}_{-4.9}$	$0.46^{+0.45}_{-0.20}$	$0.16^{+0.13}_{-0.11}$
MS1621.5+2640	16:23:35.6	+26:34:21	$3.93^{+3.15}_{-2.90}$	$1.57^{+0.84}_{-0.90}$	$1.21^{+0.52}_{-0.66}$
A2218	16:35:52.3	+66:12:36	$18.5^{+4.9}_{-4.2}$	$0.64^{+0.60}_{-0.28}$	$0.03^{+0.07}_{-0.02}$
A2219	16:40:20.5	+46:42:30	137^{+7}_{-7}	$0.70^{+0.11}_{-0.11}$	$0.73^{+0.09}_{-0.09}$
RXJ1720.1+2638	17:20:10.0	+26:37:29	$5.60^{+1.30}_{-1.44}$	$0.04^{+0.07}_{-0.03}$	$0.03^{+0.03}_{-0.03}$
A2261	17:22:27.1	+32:07:57	$8.27^{+2.35}_{-2.14}$	$0.81^{+0.36}_{-0.31}$	$0.03^{+0.03}_{-0.02}$
RXJ2129.6+0005	21:29:39.7	+00:05:19	$18.8^{+3.1}_{-3.0}$	$0.22^{+0.18}_{-0.11}$	$0.08^{+0.05}_{-0.05}$
A2390	21:53:37.3	+17:41:43	$59.8^{+3.5}_{-3.3}$	$0.16^{+0.04}_{-0.03}$	$0.26^{+0.04}_{-0.03}$
A2485	22:48:30.9	−16:06:27	$7.84^{+3.73}_{-2.70}$	$0.19^{+0.26}_{-0.13}$	$0.08^{+0.05}_{-0.05}$
A2631	23:37:38.6	+00:16:17	$61.9^{+15.1}_{-11.1}$	$2.45^{+1.14}_{-1.08}$	$0.18^{+0.23}_{-0.12}$

[a]X-ray centroids, determined by minimizing P_1.

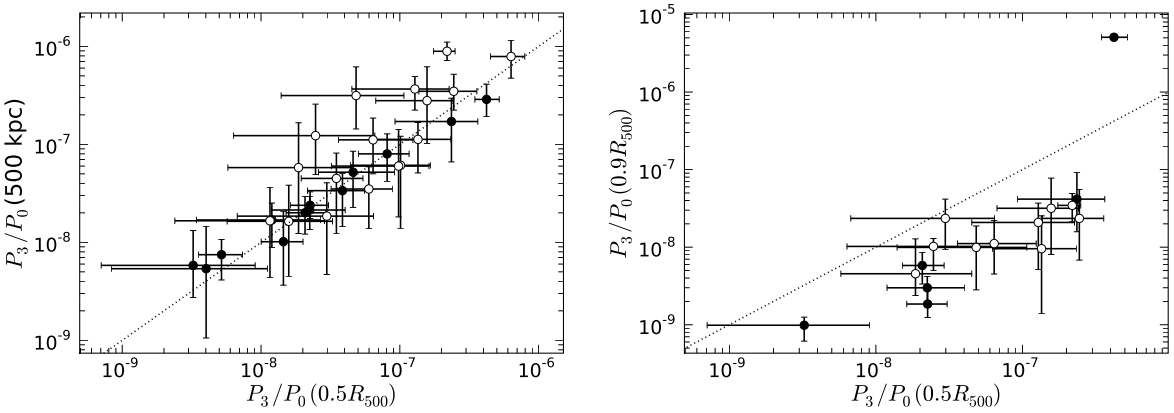

Figure 4-5: Comparison of P_3/P_0 in different aperture radii: 500kpc, 0.5 and 0.75 R_{500}. The dotted line is the line of the equality. Open (filled) symbols show NCC (CC) clusters. The merging cluster, A115, is the only one with a P_3/P_0 measured within $0.9R_{500}$ significantly higher than that of $0.5R_{500}$.

4.5 Centroid Shifts

The centroid shift, calculated from the variation of the centroid with the radius, is another measure of cluster morphology. This measure is more robust against the projection then the power ratio method, but somewhat less sensitive to detect departure from the hydrostatic equilibrium (Jeltema et al., 2008). Following Jeltema et al. (2008) who modified the method from Poole et al. (2006) and Maughan et al. (2008), the centroid is determined within a series of circular apertures centered on the X-ray peak with radii increasing in steps of $0.05R_{500}$ from $0.1R_{500}$ to R_{500}. The centroid shift, $\langle w \rangle$, is then the standard deviation of the separation between the X-ray peak and the centroid of various apertures normalized by R_{500},

$$\langle w \rangle = \left[\frac{1}{N-1} \sum_i \left(\Delta_i - \bar{\Delta} \right)^2 \right]^{1/2} \frac{1}{R_{500}}, \tag{4.5}$$

where Δ_i is the distance between the X-ray peak and the centroid of the ith aperture. Δ_i is only measured out to a radius that the entire cluster is within the *Chandra* field of view.

Here, the aperture is fixed at the centroid of $0.05R_{500}$ aperture, instead of the X-ray peak used by Poole et al. (2006) and Maughan et al. (2008), as suggested by Jeltema et al. (2008). The cluster peak is sometimes hard to define because of presence of small, brightly peaked substructures, so choosing the centroid should provide a better sense of the overall cluster center. To enhance the detection of faint structures at larger radii, the inner $0.05R_{500}$ region is excluded from the centroid (but not the inner most centroid for the X-ray peak) measurement, though Jeltema et al. (2008) find that the centroid shifts are very similar regardless of the removal of the

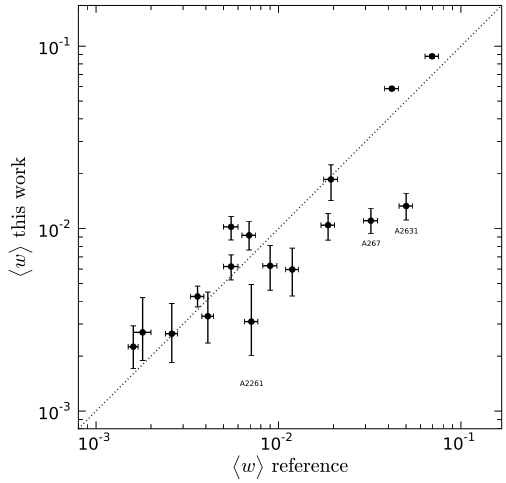

Figure 4-6: Comparison of centroid shifts to the result of Maughan et al. (2008). The dotted line is the line of the equality.

central region for most of the clusters. The measured centroid shifts are listed in Table 4.2.

In Figure 4-6, we compare our result to the centroid shift measured by Maughan et al. (2008), who analyzed the morphology of 115 galaxy clusters from *Chandra* ACIS-I observations. The agreement is generally good except for A267 and A2631, two clusters that have elongated cores. Maughan et al. (2008) used the X-ray peak and excluded central 30 kpc region, and these differences could contribute to the discrepancy. Nonetheless, this uncertainty will not hinder our classification of the cluster because we only divide clusters into two groups: high and low $\langle w \rangle$. Both works agree on the result of the grouping.

4.6 Correlation between morphological measures and cluster properties

Figure 4-7 shows the correlation among P_2/P_0, P_3/P_0, and P_4/P_0 for $0.5R_{500}$ aperture. Also plotted are 40 clusters from J05 in $0.1 < z < 0.9$, measured within 500 kpc. The relation and the scatter of the power ratio are similar to those of J05.

Figure 4-8 shows a plot of $\langle w \rangle$ versus P_3/P_0 measured in $0.5R_{500}$. Also plotted are a sample of nearby clusters from Böhringer et al. (2010), observed with *XMM-Newton*. Although their P_3/P_0 is calculated from a much larger aperture, R_{500}, the correlation between P_3/P_0 and $\langle w \rangle$ is quite similar to ours.

Figures 4-9 and 4-10 plot P_3/P_0 and $\langle w \rangle$, respectively, against BCG offsets and cluster redshifts. The offset is the the displacement between the position of the brightest cluster galaxy (BCG) and the X-ray center, determined from a sum of three 2-dimensional β models fit to the X-ray image, listed in Table 3.1. This is also the

Table 4.2: Centroid shifts

Name	RA [a] (J2000)	Dec [a] (J2000)	$\langle w \rangle$ (10^{-2})
MS0015.9+1609	00:18:33.4	+16:26:10	$0.63^{+0.18}_{-0.17}$
CL0024.0+1652	00:26:35.7	+17:09:42	$0.71^{+0.18}_{-0.16}$
A68	00:37:06.4	+09:09:32	$0.60^{+0.18}_{-0.17}$
A115	00:55:50.3	+26:24:35	$8.80^{+0.19}_{-0.18}$
A209	01:31:53.1	−13:36:45	$1.02^{+0.14}_{-0.16}$
RXJ0142.0+2131	01:42:03.2	+21:31:15	$1.19^{+0.19}_{-0.19}$
A267	01:52:42.2	+01:00:39	$1.11^{+0.19}_{-0.16}$
A370	02:39:53.2	−01:34:40	$1.40^{+0.59}_{-0.40}$
A383	02:48:03.4	−03:31:46	$0.27^{+0.15}_{-0.08}$
A521	04:54:06.5	−10:13:14	$5.85^{+0.12}_{-0.11}$
A586	07:32:20.4	+31:37:55	$0.27^{+0.12}_{-0.08}$
A611	08:00:56.8	+36:03:24	$0.43^{+0.09}_{-0.09}$
ZwCl0839.9+2937	08:42:55.8	+29:27:27	$0.28^{+0.07}_{-0.07}$
A697	08:42:57.6	+36:21:57	$0.33^{+0.12}_{-0.09}$
A750	09:09:12.8	+10:58:33	$0.83^{+0.21}_{-0.18}$
A963	10:17:03.6	+39:02:52	$0.26^{+0.07}_{-0.06}$
A1689	13:11:29.6	−01:20:30	$0.42^{+0.06}_{-0.05}$
A1763	13:35:18.3	+40:59:56	$0.92^{+0.17}_{-0.16}$
MS1358.1+6245	13:59:50.4	+62:31:04	$0.40^{+0.08}_{-0.06}$
A1835	14:01:01.9	+02:52:42	$0.27^{+0.09}_{-0.07}$
ZwCl1454.8+2233	14:57:15.0	+22:20:33	$0.31^{+0.06}_{-0.06}$
A2009	15:00:19.6	+21:22:10	$0.29^{+0.09}_{-0.07}$
ZwCl1459.4+4240	15:01:22.3	+42:20:45	$1.36^{+0.33}_{-0.35}$
MS1512.4+3647	15:14:22.4	+36:36:22	$0.96^{+0.29}_{-0.32}$
MS1621.5+2640	16:23:35.3	+26:34:29	$1.86^{+0.38}_{-0.44}$
A2218	16:35:51.0	+66:12:37	$1.04^{+0.17}_{-0.18}$
A2219	16:40:20.1	+46:42:35	$0.29^{+0.04}_{-0.05}$
RXJ1720.1+2638	17:20:09.9	+26:37:31	$0.23^{+0.07}_{-0.05}$
A2261	17:22:27.3	+32:07:59	$0.31^{+0.19}_{-0.11}$
RXJ2129.6+0005	21:29:40.0	+00:05:22	$0.62^{+0.10}_{-0.10}$
A2390	21:53:36.6	+17:41:43	$0.72^{+0.04}_{-0.05}$
A2485	22:48:31.0	−16:06:27	$0.53^{+0.25}_{-0.17}$
A2631	23:37:38.4	+00:16:07	$1.33^{+0.22}_{-0.22}$

[a]X-ray centroids, determined from the $0.05R_{500}$ aperature.

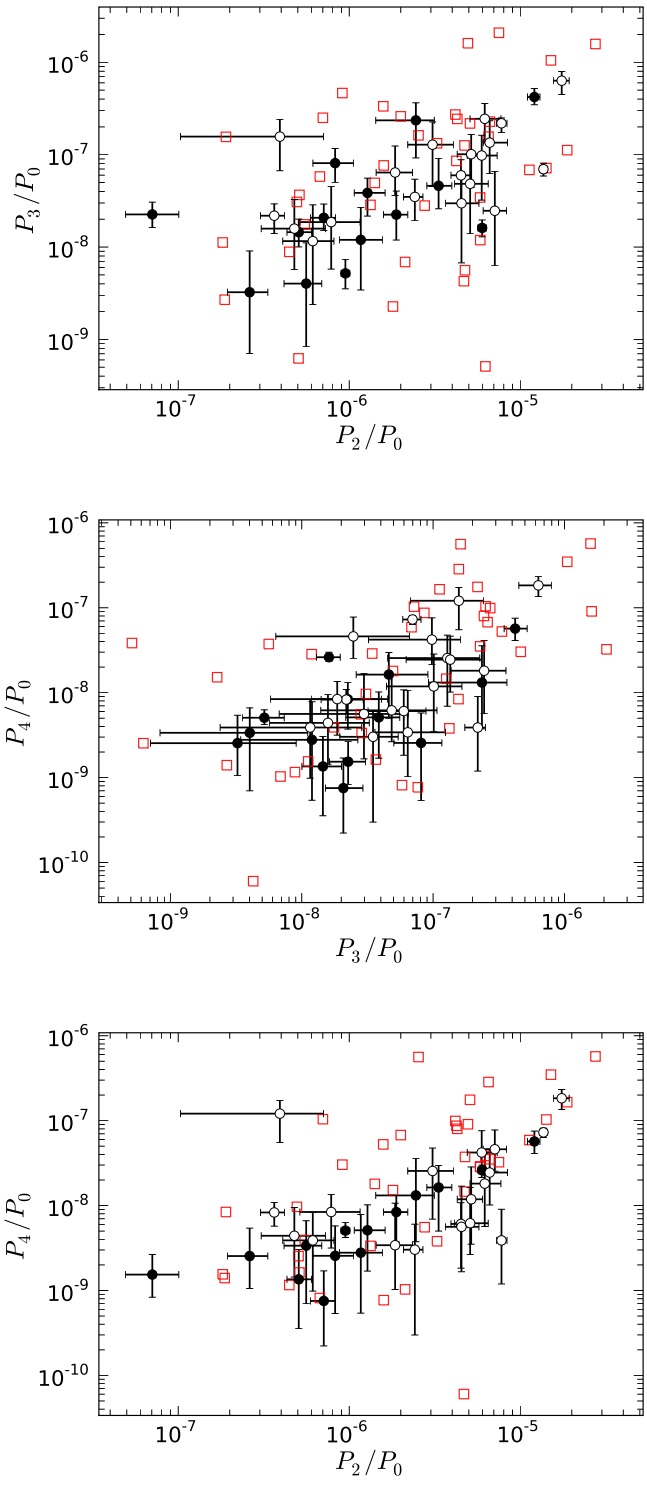

Figure 4-7: Correlations among the power ratios for $0.5R_{500}$ aperture. Cool core and non-cool core clusters are shown in filled and open circles, respectively. Also shown in red squares are 40 clusters observed with *Chandra* from Jeltema et al. (2005) measured within 500 kpc.

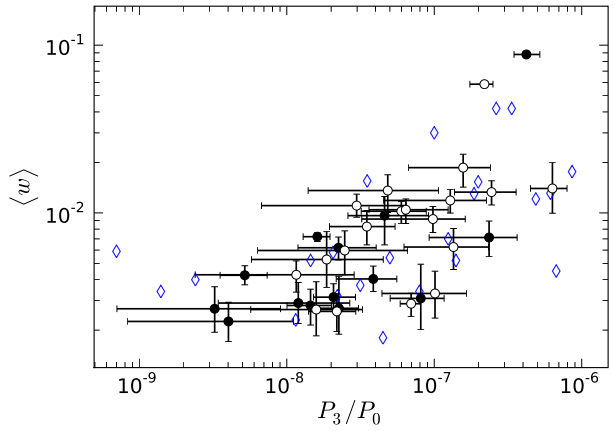

Figure 4-8: Centroid shift plotted against P_3/P_0. Open (filled) symbols show NCC (CC) clusters. Also plotted in diamonds are nearby clusters from Böhringer et al. (2010), observed with *XMM-Newton*.

center for the radial gas density and temperature profiles (§3.1.2). A115 is excluded from this plot because the X-ray center and the BCG belong to distinctly different subclusters, A115N and A115S, respectively. BCG positions are from Hoekstra (2007), Zhang et al. (2010), Richard et al. (2010), and Stott et al. (2008). We find that clusters with highest redshifts ($z > 0.3$) or biggest BCG offsets ($> 0.25'$) among the sample all have larger P_3/P_0 or $\langle w \rangle$, but once removing those, there is hardly a correlation with z or the BCG offset for P_3/P_0 and $\langle w \rangle$.

Figure 4-11 plots the distribution of P_m/P_0 and $\langle w \rangle$ for our sample, in comparison with those of Jeltema et al. (2005) and Böhringer et al. (2010).

Figure 4-12 plots P_m/P_0 and $\langle w \rangle$ against the cuspiness parameter α of the gas density at $0.04R_{500}$. P_3/P_0 and $\langle w \rangle$ is weakly correlated with α.

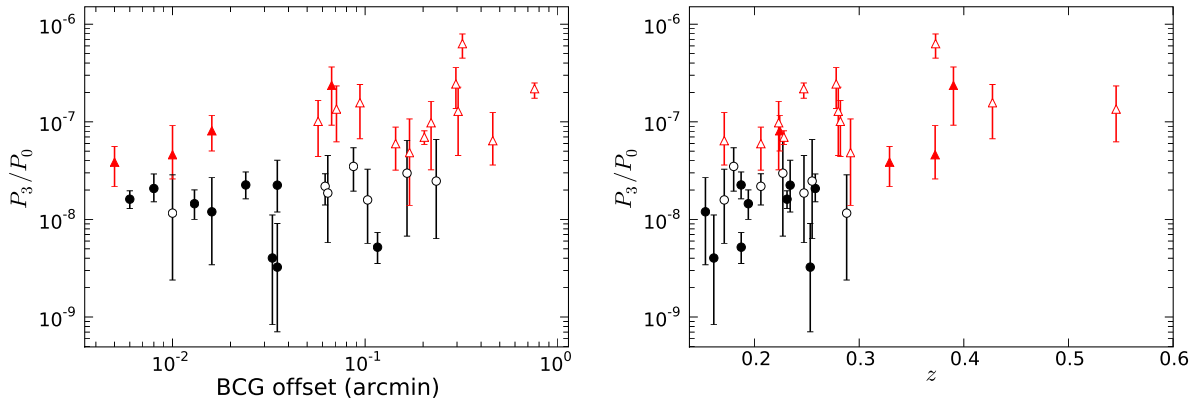

Figure 4-9: P_3/P_0 versus the offset between BCG position and X-ray center (*left*) and the redshift (*right*). Clusters having higher (lower) than the median P_3/P_0 are plotted in red triangles (black circles). Open (filled) symbols show NCC (CC) clusters.

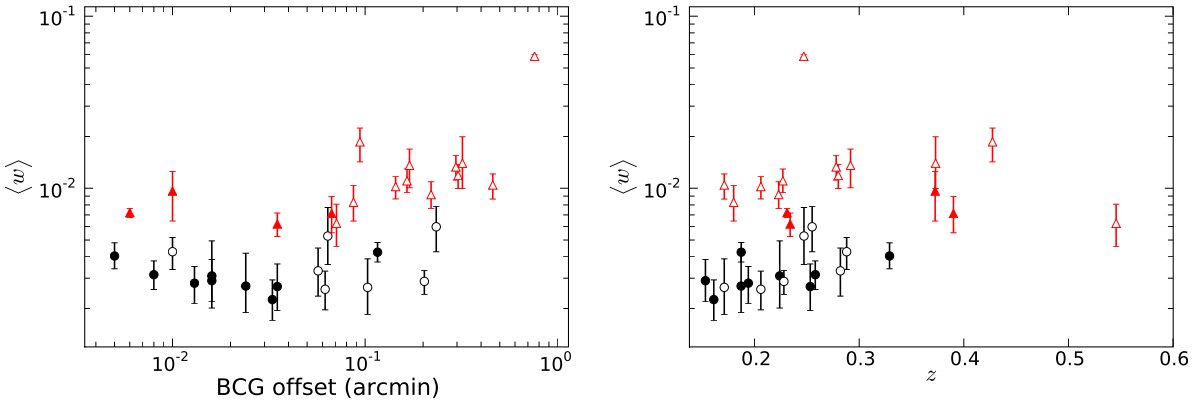

Figure 4-10: Centroid shift versus the offset between BCG position and X-ray center (*left*) and the redshift (*right*). Clusters having higher (lower) than the median $\langle w \rangle$ are plotted in red triangles (black circles). Open (filled) symbols show NCC (CC) clusters.

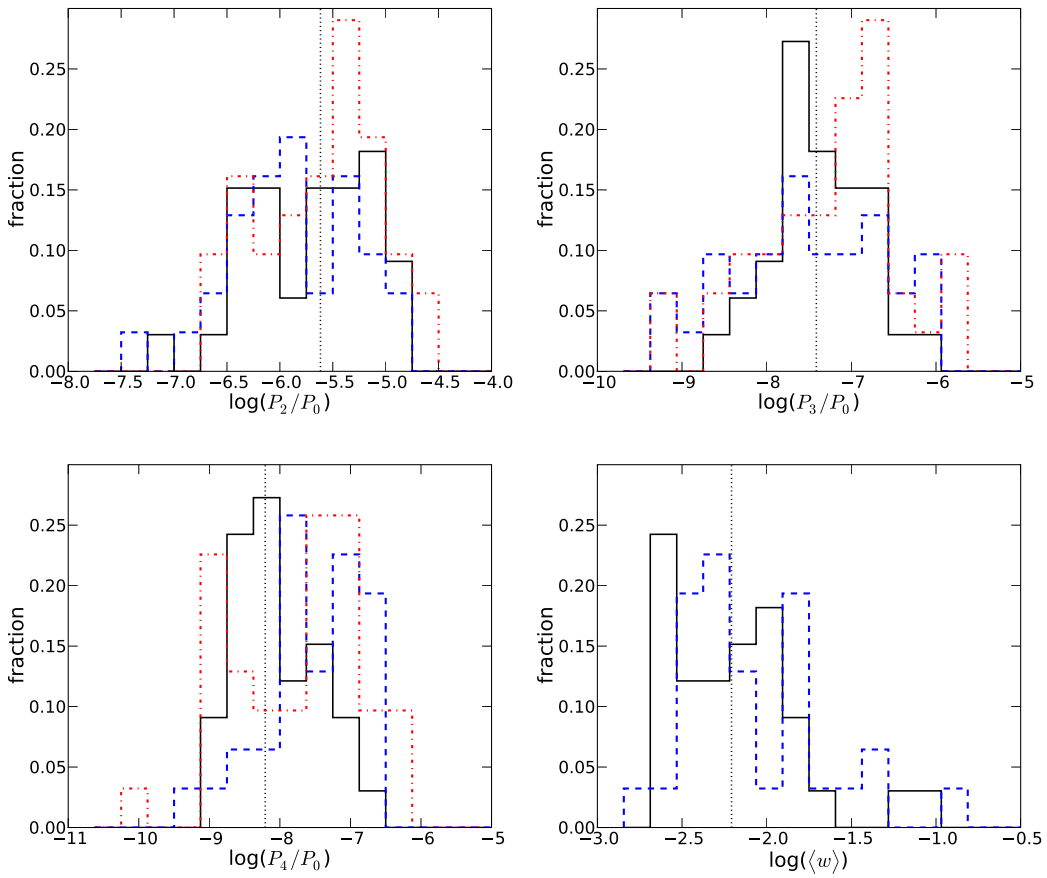

Figure 4-11: The distributions of power ratios, measured within $0.5R_{500}$, and centroid shifts (solid line). The dotted vertical line is the median value of the distribution. Also shown are power ratios of Jeltema et al. (2005) computed in a 500kpc aperture (dash-dotted line) and results from Böhringer et al. (2010) whose power ratios are measured within R_{500} (dashed line).

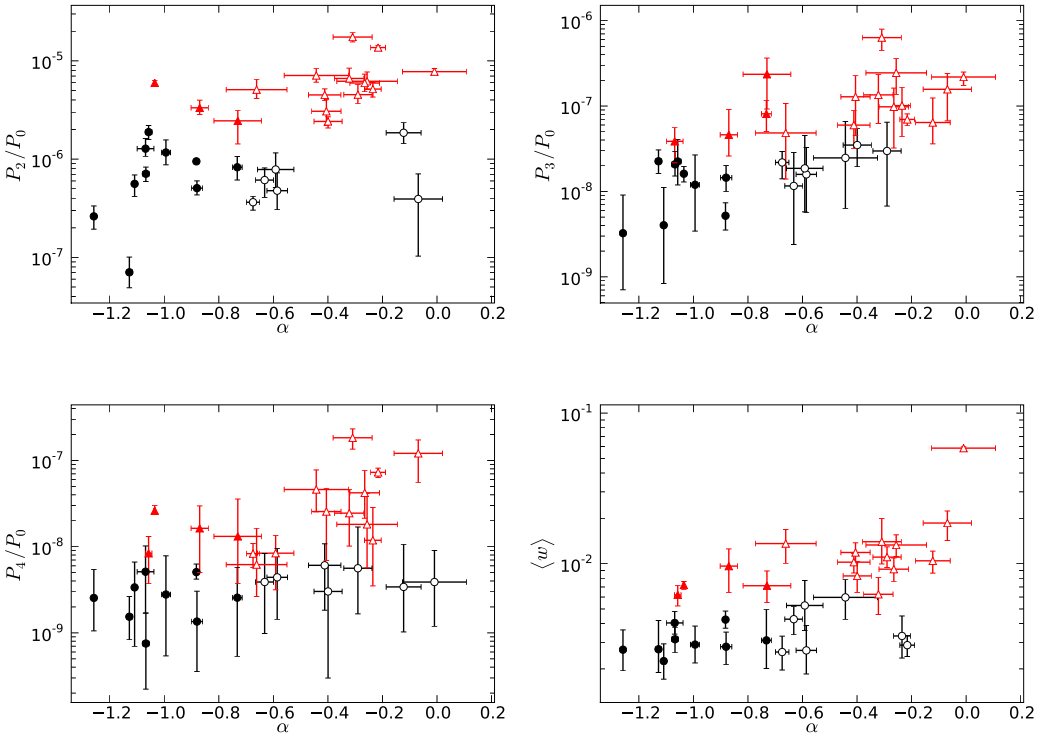

Figure 4-12: Correlations between power ratios P_m/P_0, centroid shifts $\langle w \rangle$ with the cuspiness parameter α. Clusters having higher (lower) than the median P_m/P_0 or $\langle w \rangle$ are plotted in red triangles (black circles). Open (filled) symbols show NCC (CC) clusters.

Chapter 5

Summary and Conclusion

In Chapter 2, we presented a detailed X-ray spectral analysis of Abell 1689, a well known cluster with discrepant X-ray and lensing masses. We tested the hypothesis that multiple temperature components in projection result in a lower X-ray mass estimate. We found that an additional temperature component does not improve the fit significantly. If the temperature of the hot component is to agree with the cluster temperature predicted from the combined lensing and X-ray surface brightness profiles by Lemze et al. (2008a), then the implied temperature of the cooler component is greater than 5 keV and it occupies 70-90% of the space within $250h^{-1}$kpc radius, assuming that the two temperature phases are in pressure equilibrium. Therefore, the scenario that "cool" clumps biasing the X-ray temperature measurements proposed by Lemze et al. (2008a) seems to be unlikely. Other explanations for the mass discrepancy include the projection effect and the unrelaxed state of the cluster.

In Chapter 3, we analyzed a sample of 32 intermediate redshift massive X-ray clusters and compared *Chandra* X-ray data with the weak lensing studies of Hoekstra (2007) and Okabe et al. (2010). We found that the mass ratio between M_X and M_{WL} does not depend on how cuspy the gas density profile is at $0.04R_{500}$, our discriminant between cool core and non-cool core clusters. This is contrary to the common belief that cool core clusters are more relaxed than non-cool core clusters in general. In addition, we found that the power ratio P_3/P_0, a measure of substructures, correlates with M_X/M_{WL}, such that low P_3/P_0 clusters (less substructures) have a higher M_X/M_{WL}, particularly at small ratii. However, instead of a mass ratio close to one, expected if the ICM is in hydrostatic equilibrium, we found that these apparently relaxed low P_3/P_0 clusters actually have a ratio $M_X/M_{WL} = 1.32 \pm 0.17$ higher than unity, after correcting for all known biases and scatter we consider, from *Chandra* calibration to halo triaxiality. This surprising result is in fact in qualitative agreement with the non-radiative simulations of Rasia et al. (2004), who show that at $r \lesssim 0.1R_{\rm vir}$, the gas may be hotter than the dark matter. The collisional gas particles gain energy from the collisionless dark matter from the transient spatial offset between the two species during the mergers. It should be noted, however, that later works (e.g., Rasia et al., 2006) including radiative cooling and other feedback processes suggest that hydrostatic X-ray masses can be low by 10-20%, if the ICM viscosity is neglected. On the other hand, the ICM viscosity, a property commonly ignored in cosmological

simulations, will raise the gas temperature (Sijacki & Springel, 2006), which will tend to increase X-ray mass estimates.

Our result shows that $f_{\rm gas}$ is related to cluster morphology, for both cool core/non-cool core and P_3/P_0 measures. Combined with the finding that cluster structure may evolve over cosmic time (Jeltema et al., 2005; Vikhlinin et al., 2007; Andersson et al., 2009), the robustness of the use of $f_{\rm gas}$ as a cosmological probe will depend on the sample selection, which is rarely addressed in detail since there is no consensus on which measure is best suited for selecting standard clusters. Although an attempt has been made to correct the biased M_X or $M_{\rm gas}$ with observable structure measures from simulations (Jeltema et al., 2008), the feasibility of this approach is limited by the current knowledge of gas physics. As shown by Young et al. (2011), the baryon fraction evolves and changes with different models of gas heating and cooling incorporated in simulations. Another potential concern arises from the difference between M_X and M_{WL} mentioned above. $f_{\rm gas}$ is usually measured at R_{2500} where the radius is large enough to avoid complex physical processes in the core and yet not far enough to be complicated by the background or gas clumping. We found that at this radius, M_X is $\sim 10-30\%$ higher than M_{WL} from an average cluster to a low P_3/P_0 cluster. This uncertainty should be included in $f_{\rm gas}$ for cosmological studies if the total mass is from M_X.

In Chapter 4, we provide X-ray luminosity and temperature maps for our sample from the Smoothed Particle Inference (SPI) technique (Peterson et al., 2007), which models the cluster with hundreds of particles, forward folds the model to compare with data and samples the parameter space with the Markov chain Monte Carlo method. Each particle has its own temperature and spatial extent, composing a very flexible kilo-parametric cluster model. The power ratio and the centroid shift used in Chapter 3 are measured from the SPI luminosity map. The SPI temperature map is for demonstration only and not included in this study because of the great degeneracy between different temperature phases. Although quantitatively not correct for some clusters, the map is still qualitatively worthwhile. With a better understanding of the degeneracy and constraints from deeper observations and more sensitive instruments, SPI should be a powerful tool to study ICM. The Monte Carlo approach also makes it straightforward to combine data from different instruments or even with observations from the Sunyaev-Zeldovich effect.

Appendix A

Gas profiles and best-fit models

A.1 Temperature profiles

A.2 Gas density profiles

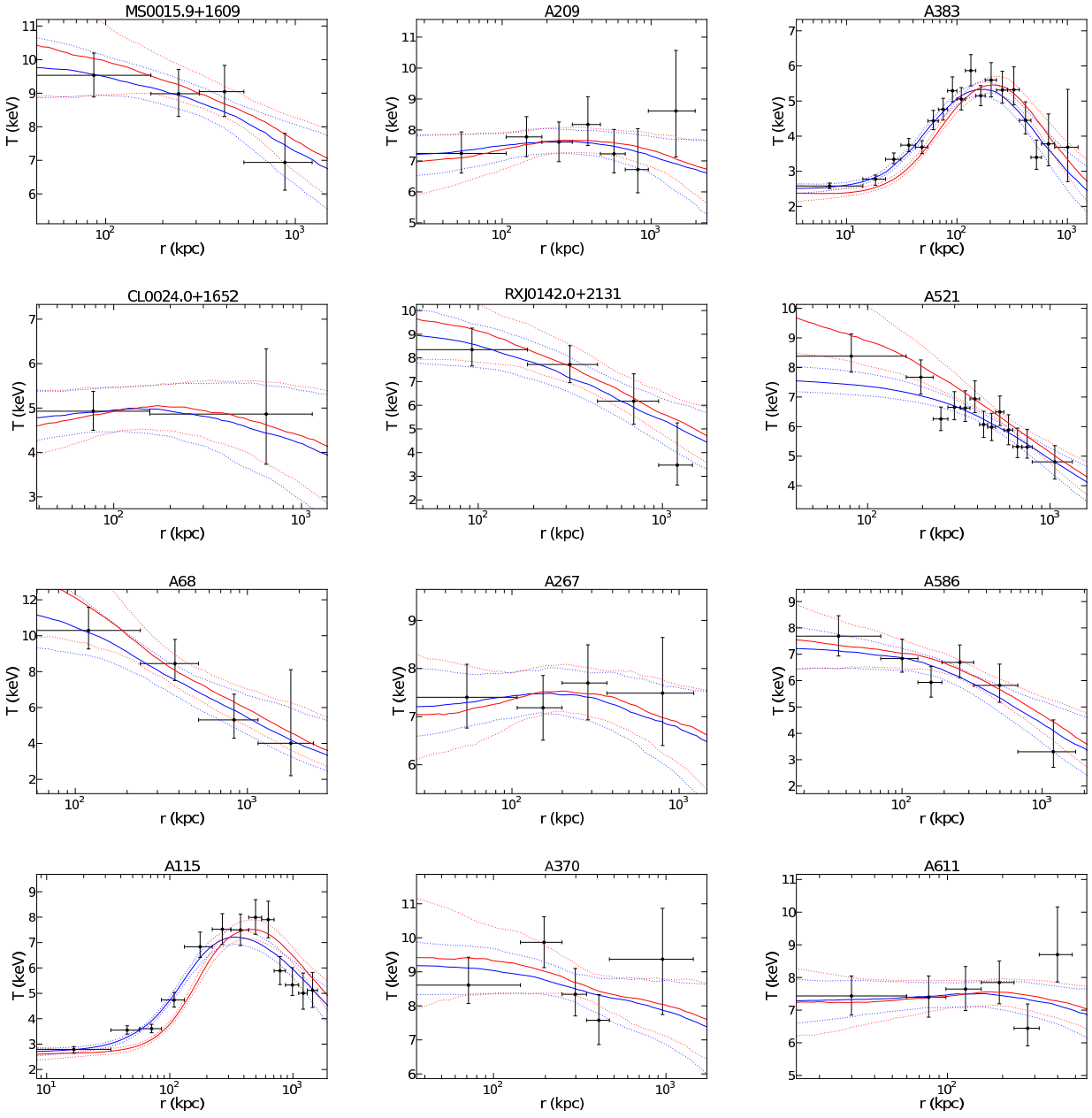

Figure A-1: Temperature profiles. Observed projected temperatures are shown in crosses. Solid red and blue lines show the best-fit three-dimensional model and the corresponding projected profile, respectively. Dotted lines show 1σ errors. The best-fit projected temperature profile shown in the blue solid line is for the illustrative purpose only (see text).

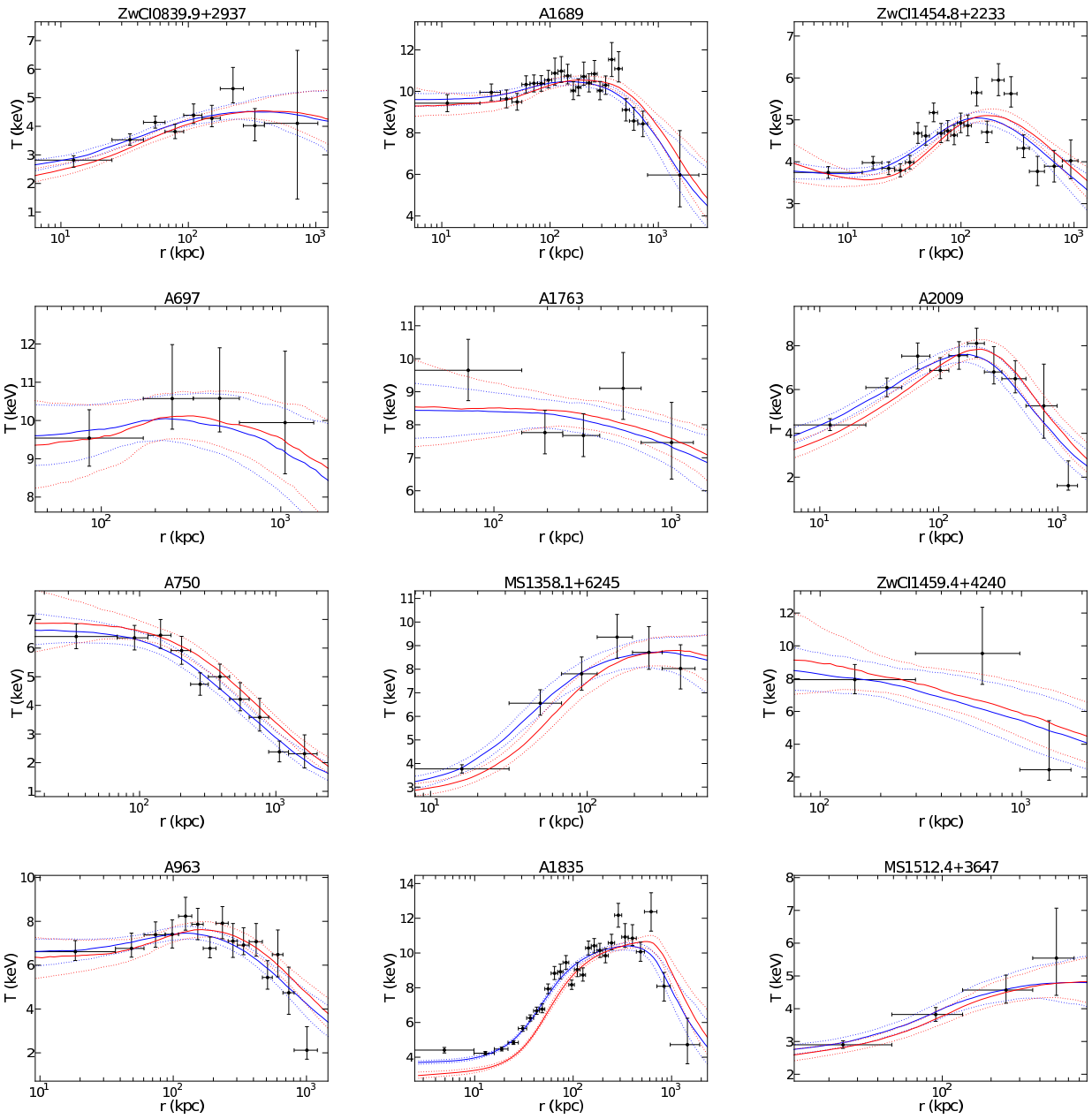
ZwCl0839.9+2937
A1689
ZwCl1454.8+2233
A697
A1763
A2009
A750
MS1358.1+6245
ZwCl1459.4+4240
A963
A1835
MS1512.4+3647
T (keV)
r (kpc)

Figure A-1:

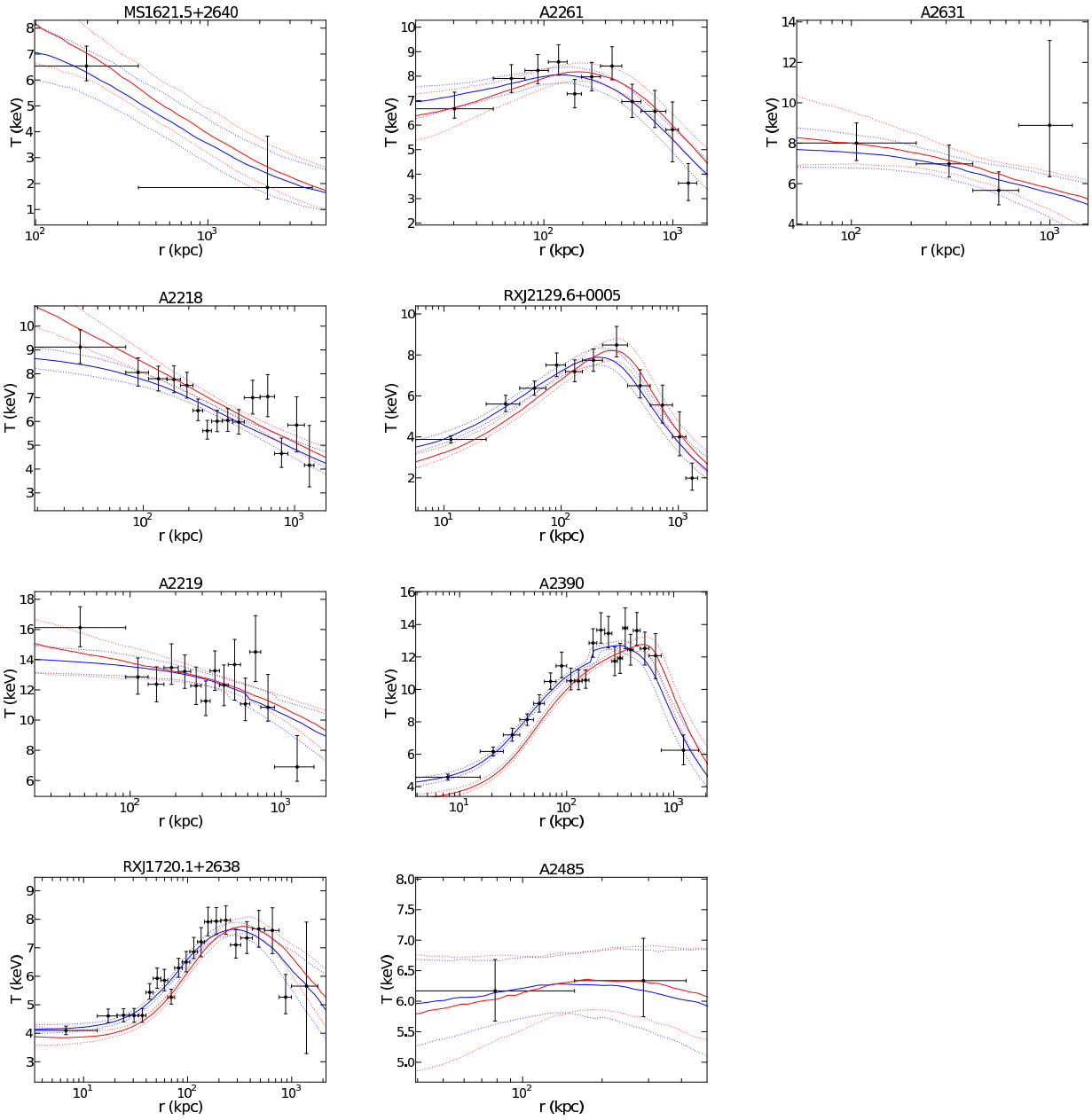
MS1621.5+2640
A2261
A2631
A2218
RXJ2129.6+0005
A2219
A2390
RXJ1720.1+2638
A2485
T (keV)
r (kpc)

Figure A-1:

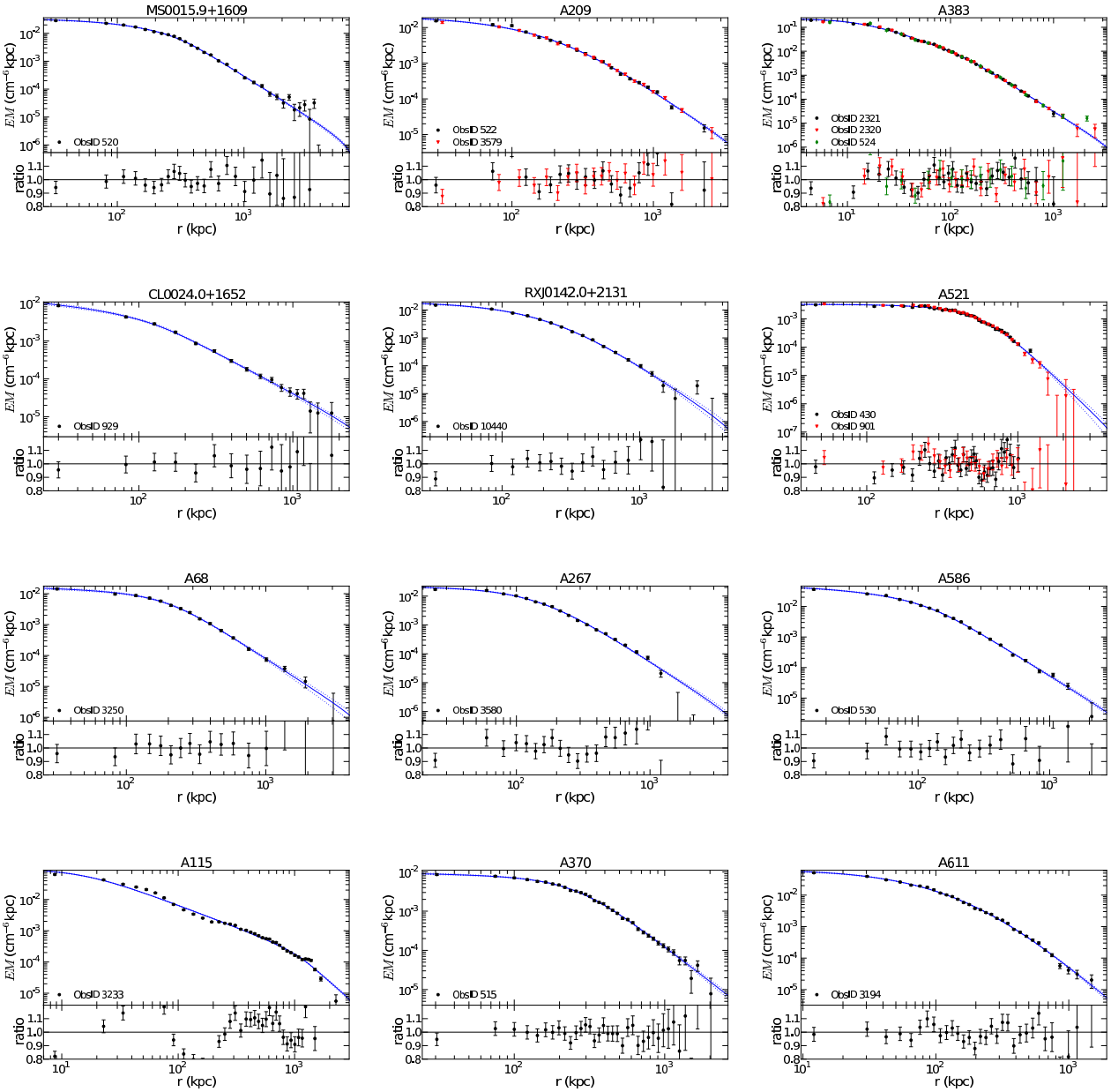

Figure A-2: *Top*, observed projected emissivity profiles are shown in point markers. Solid and dotted lines show the best fit and 1σ errors to the three-dimensional gas density profile. *Bottom*, the residuals.

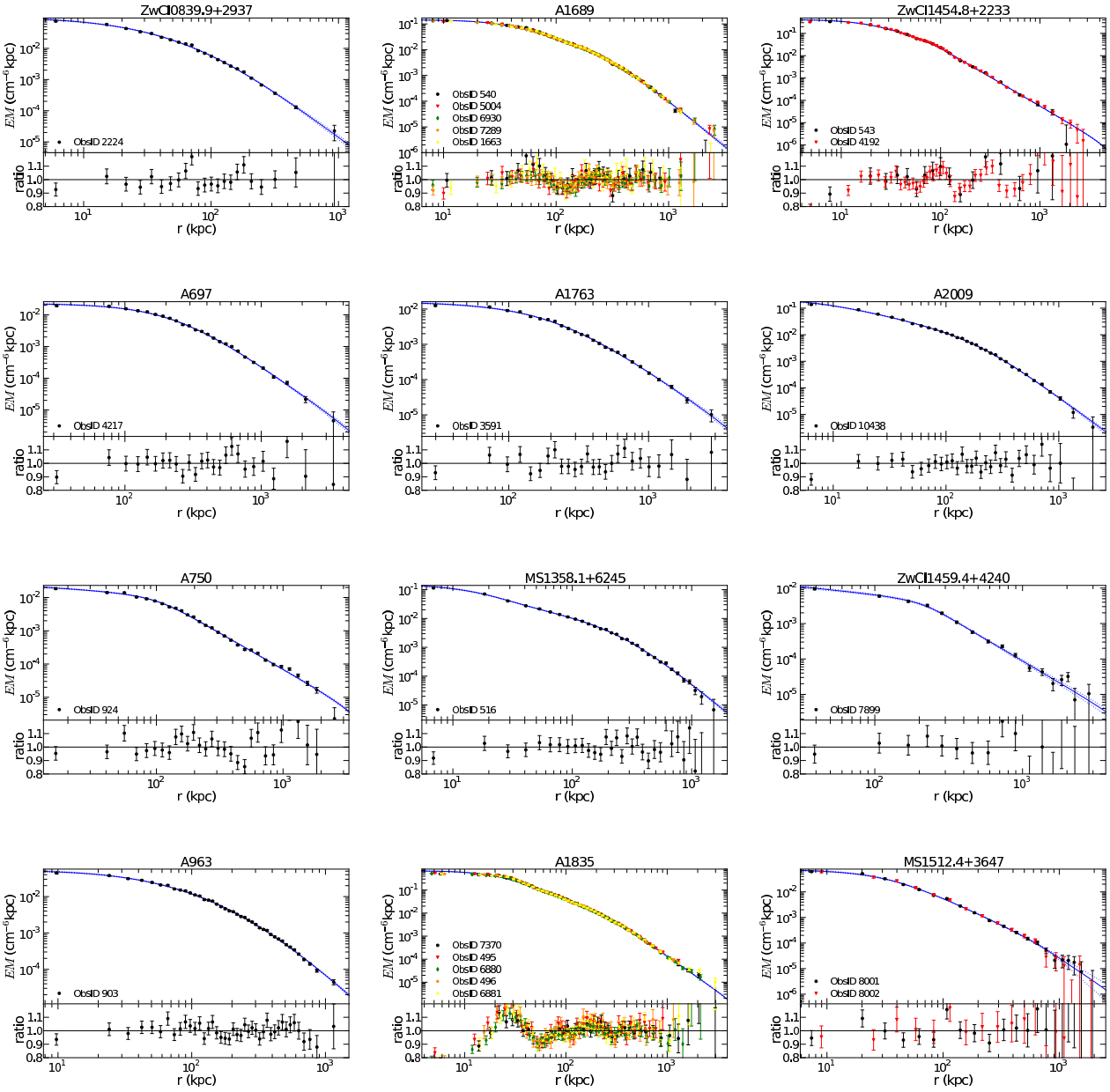
ZwCl0839.9+2937
ObsID 2224
A1689
ObsID 540
ObsID 5004
ObsID 6930
ObsID 7289
ObsID 1663
ZwCl1454.8+2233
ObsID 543
ObsID 4192
A697
ObsID 4217
A1763
ObsID 3591
A2009
ObsID 10438
A750
ObsID 924
MS1358.1+6245
ObsID 516
ZwCl1459.4+4240
ObsID 7899
A963
ObsID 903
A1835
ObsID 7370
ObsID 495
ObsID 6880
ObsID 496
ObsID 6881
MS1512.4+3647
ObsID 8001
ObsID 8002
EM (cm⁻⁶ kpc)
ratio
r (kpc)

Figure A-2:

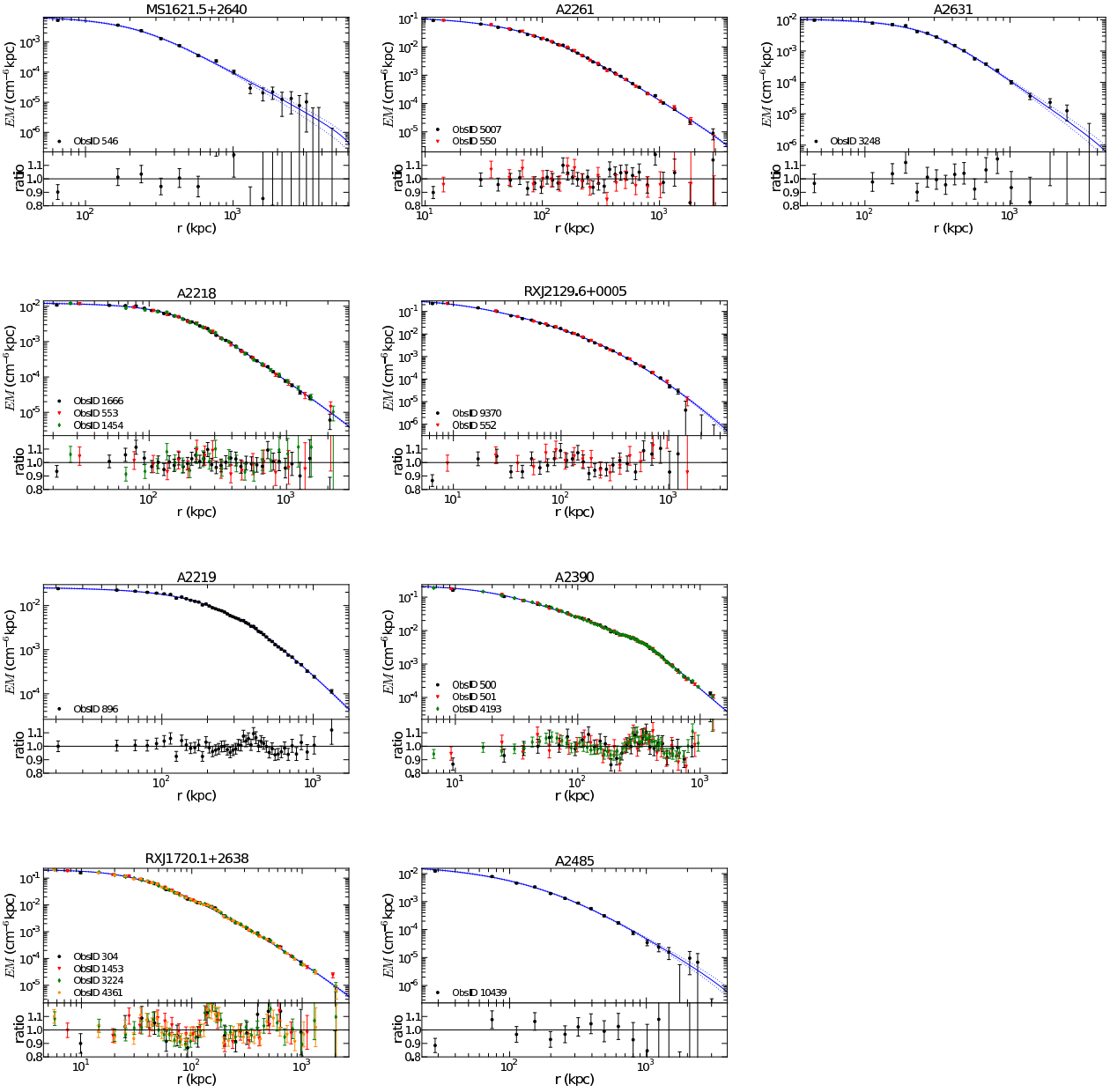
MS1621.5+2640
ObsID 546
A2261
ObsID 5007
ObsID 550
A2631
ObsID 3248
A2218
ObsID 1666
ObsID 553
ObsID 1454
RXJ2129.6+0005
ObsID 9370
ObsID 552
A2219
ObsID 896
A2390
ObsID 500
ObsID 501
ObsID 4193
RXJ1720.1+2638
ObsID 304
ObsID 1453
ObsID 3224
ObsID 4361
A2485
ObsID 10439
EM (cm^{-6} kpc)
ratio
r (kpc)

Figure A-2:

Appendix B

Luminosity and Temperature maps

B.1 Luminosity maps

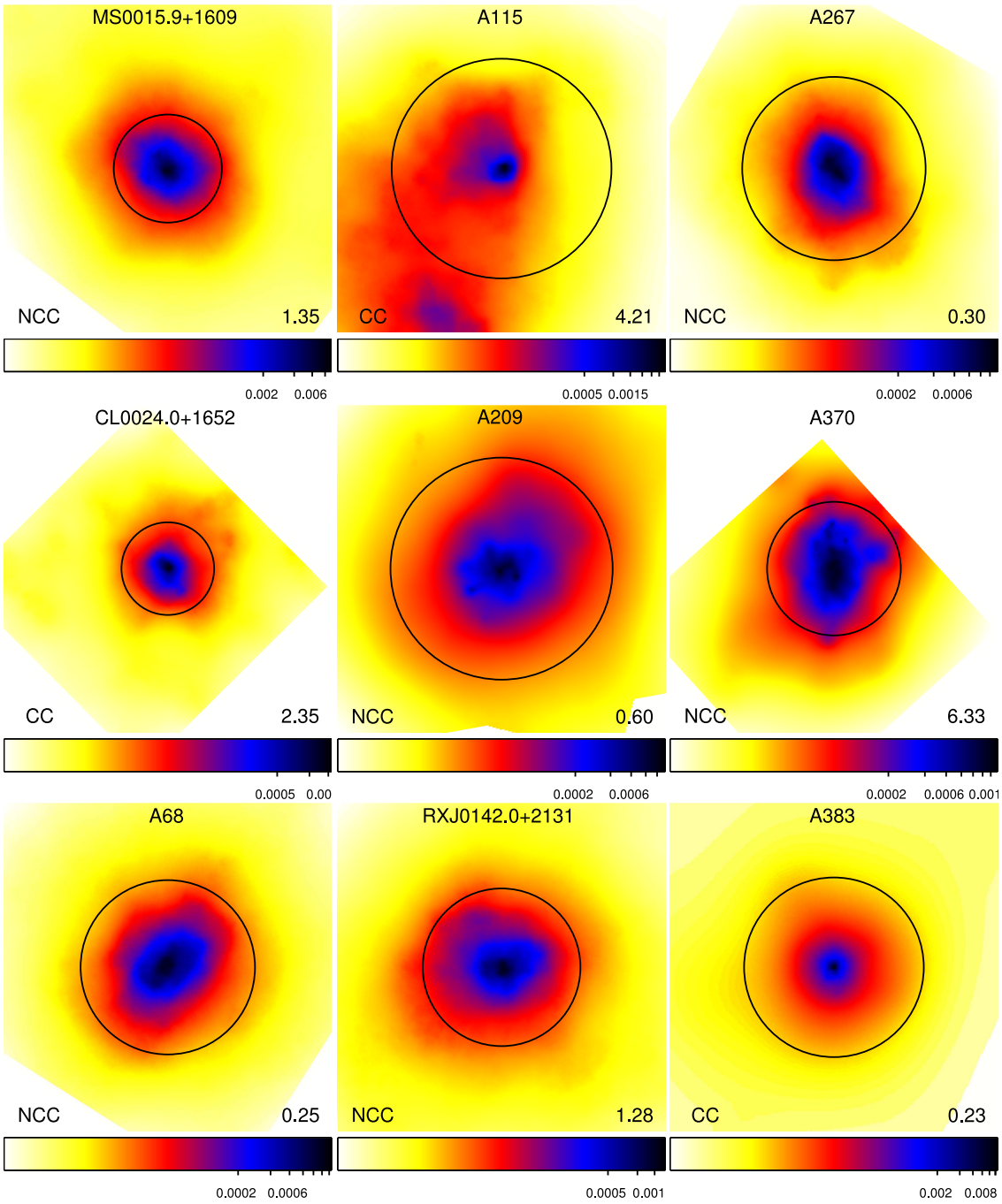

Figure B-1: Median luminosity maps in units of 10^{44} erg s$^{-1}(''')^{-2}$ in the $0.3-10$ keV (observer frame) energy band. Images are $10' \times 10'$ in size. Circles show $0.5R_{500}$ radii. The number at the lower left corner is the value of P_3/P_0 measured within $0.5R_{500}$, in units of 10^{-7}. The median value of our sample, 3.9×10^{-8}, is used to divide the sample into high and low P_3/P_0 sub-samples.

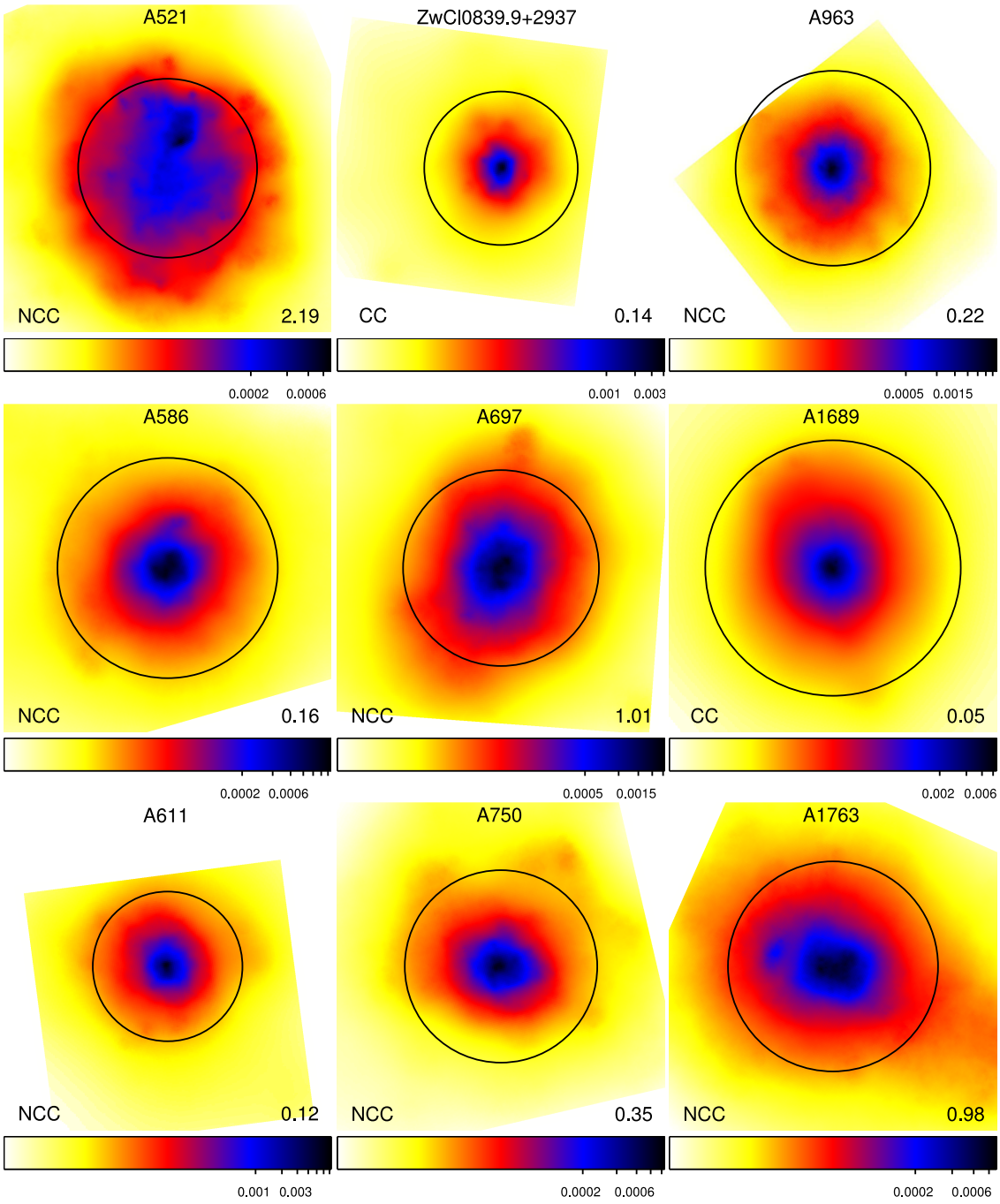
A521
NCC
2.19
0.0002
0.0006
ZwCl0839.9+2937
CC
0.14
0.001
0.003
A963
NCC
0.22
0.0005
0.0015
A586
NCC
0.16
0.0002
0.0006
A697
NCC
1.01
0.0005
0.0015
A1689
CC
0.05
0.002
0.006
A611
NCC
0.12
0.001
0.003
A750
NCC
0.35
0.0002
0.0006
A1763
NCC
0.98
0.0002
0.0006

Figure B-1:

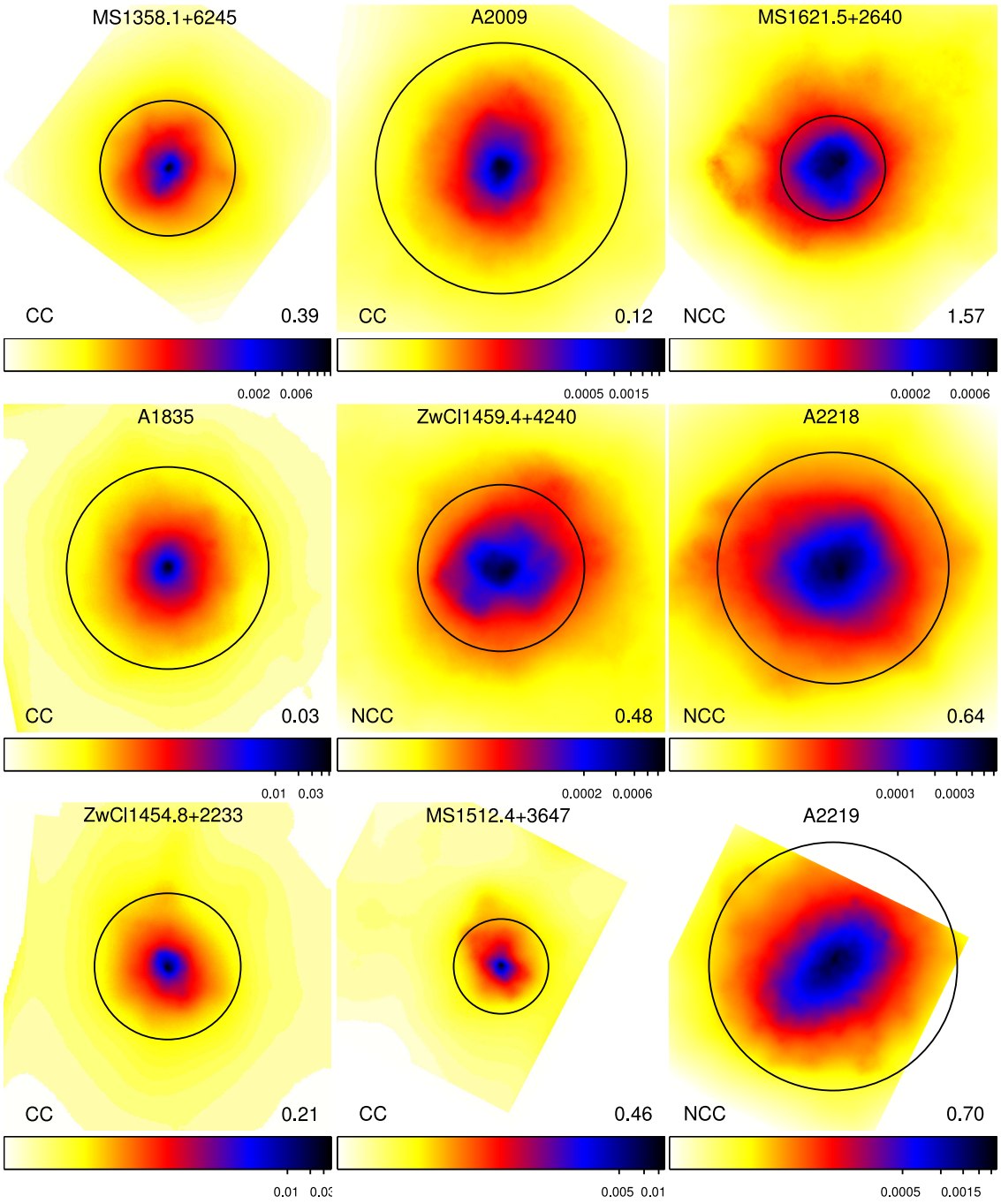
MS1358.1+6245
CC
0.39
0.002 0.006
A2009
CC
0.12
0.0005 0.0015
MS1621.5+2640
NCC
1.57
0.0002 0.0006
A1835
CC
0.03
0.01 0.03
ZwCl1459.4+4240
NCC
0.48
0.0002 0.0006
A2218
NCC
0.64
0.0001 0.0003
ZwCl1454.8+2233
CC
0.21
0.01 0.0
MS1512.4+3647
CC
0.46
0.005 0.01
A2219
NCC
0.70
0.0005 0.0015

Figure B-1:

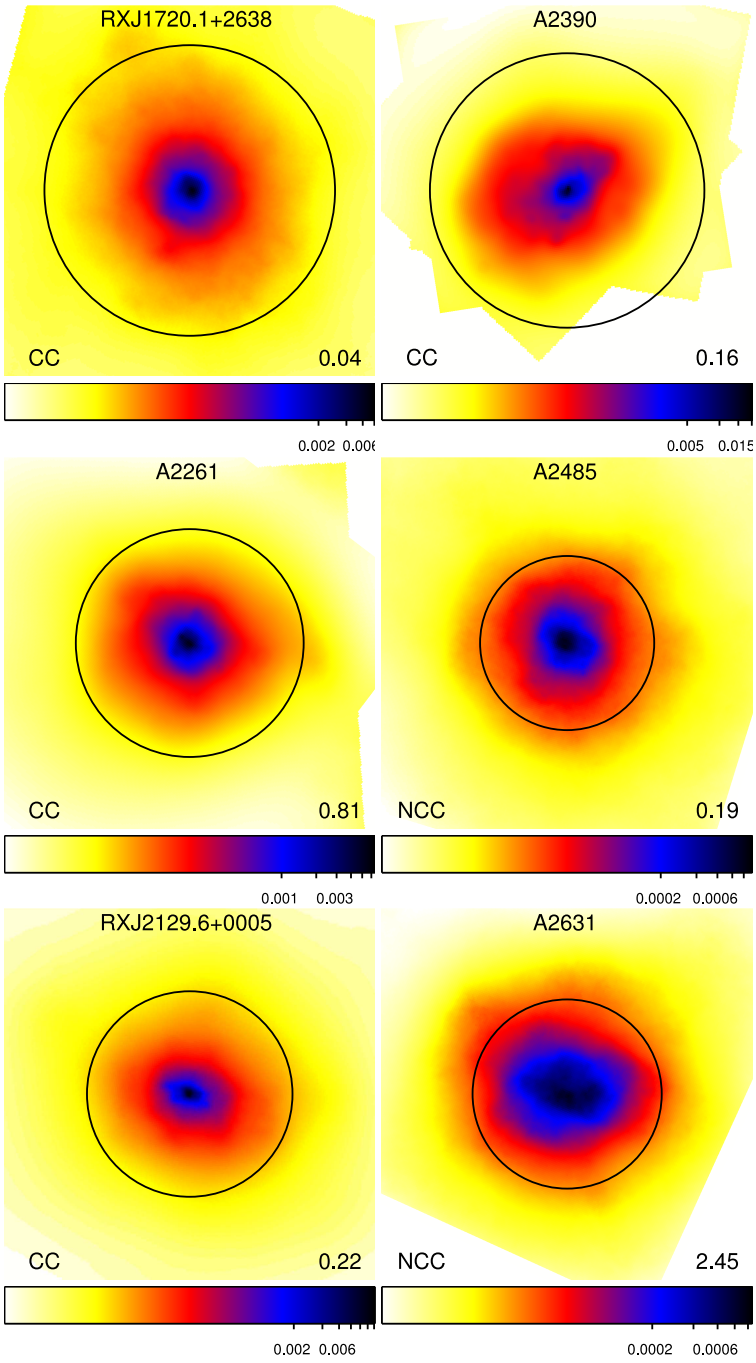
RXJ1720.1+2638
CC
0.04
0.002 0.006
A2390
CC
0.16
0.005 0.015
A2261
CC
0.81
0.001 0.003
A2485
NCC
0.19
0.0002 0.0006
RXJ2129.6+0005
CC
0.22
0.002 0.006
A2631
NCC
2.45
0.0002 0.0006

Figure B-1:

B.2 Spectroscopic-like temperature maps

Because of the degeneracy between different temperature components (§4.1), the temperature map is not currently used in any analysis of this work.

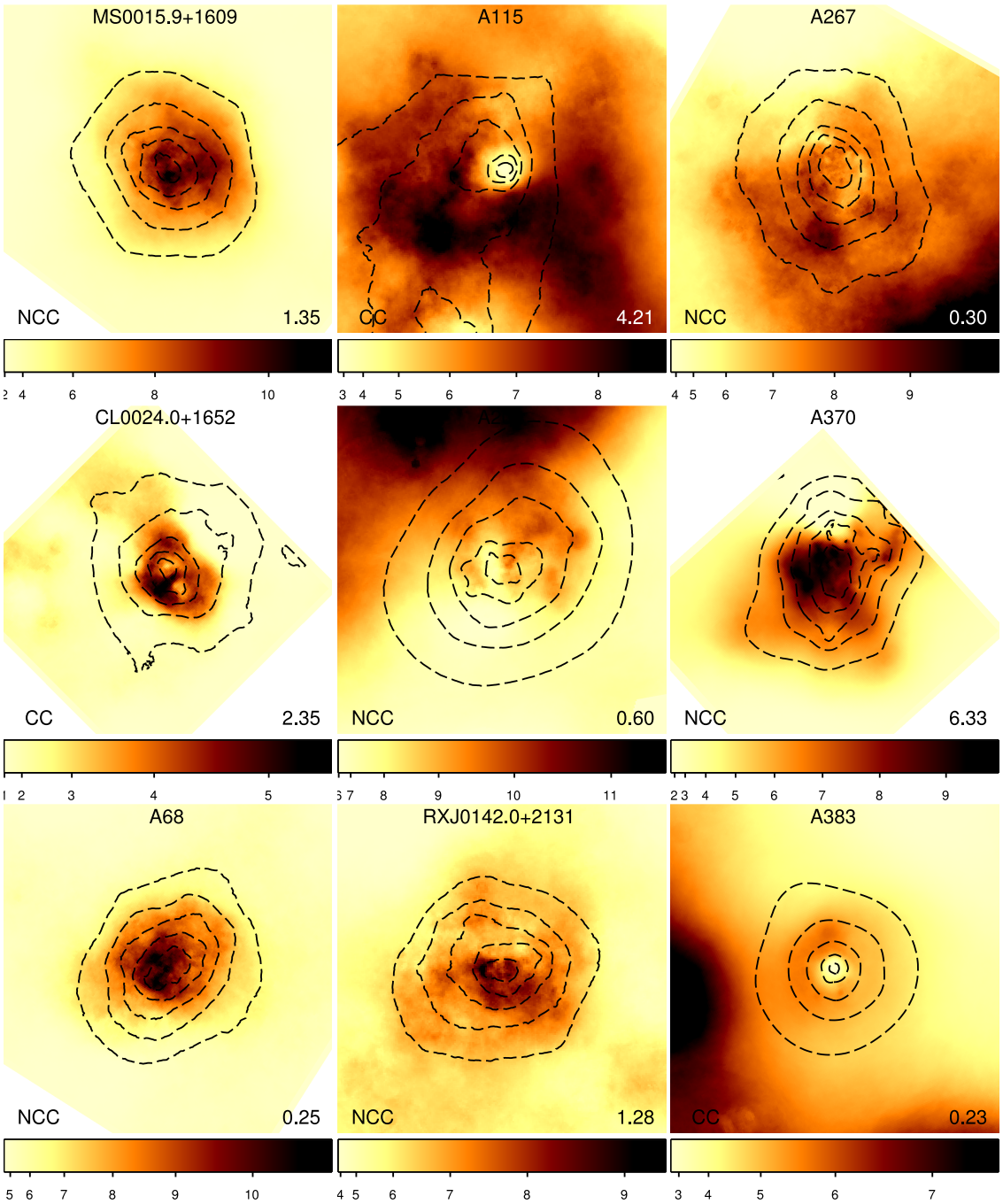

Figure B-2: Median spectroscopic-like temperature maps in units of keV, overlaid with X-ray luminosity contours. The contour levels are logarithmically spaced. Images are $10' \times 10'$ in size. The number at the lower left corner is the value of P_3/P_0 measured within $0.5R_{500}$, in units of 10^{-7}. The median value of our sample, 3.9×10^{-8}, is used to divide the sample into high and low P_3/P_0 sub-samples.

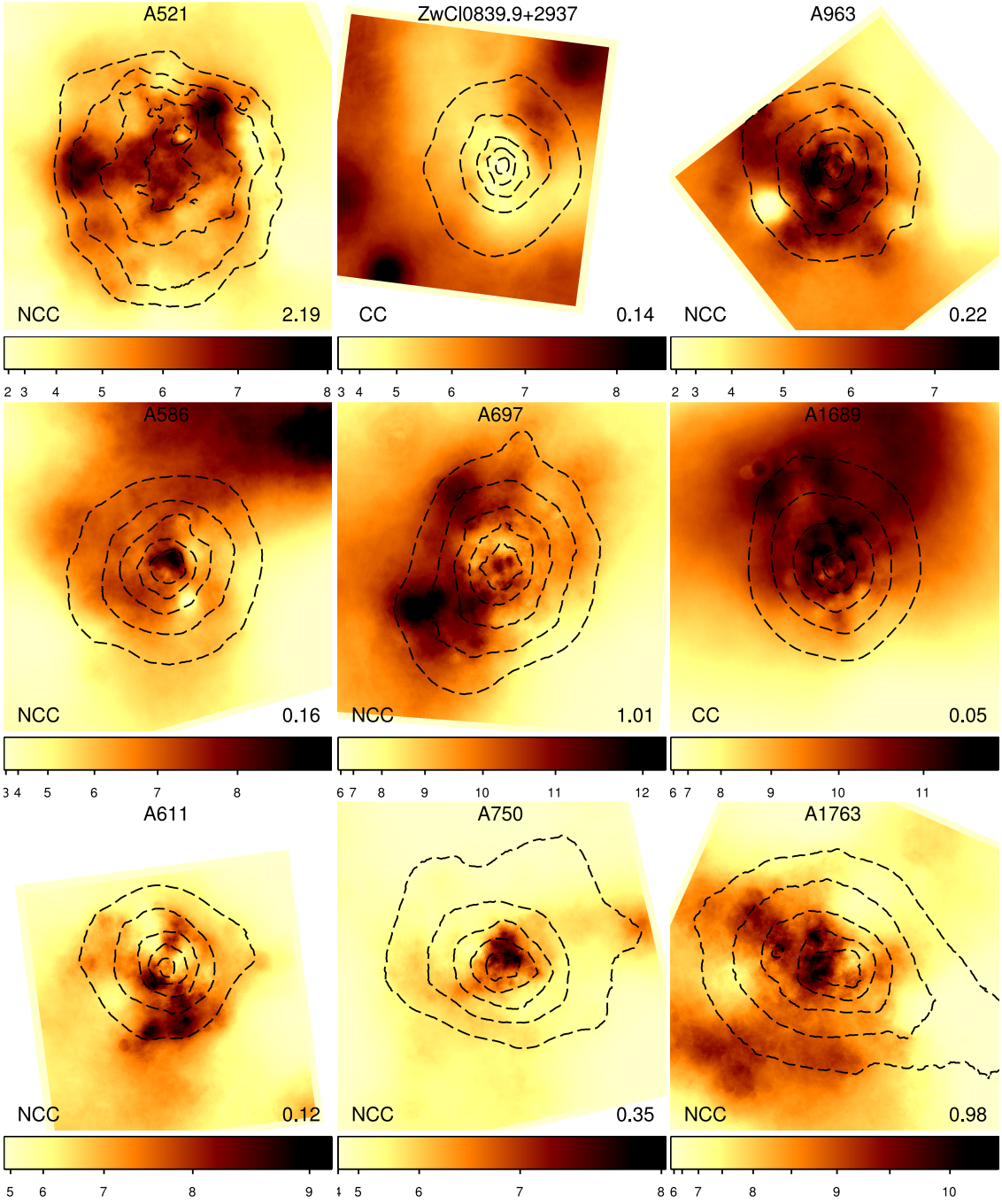
A521
NCC
2.19
ZwCl0839.9+2937
CC
0.14
A963
NCC
0.22
A586
NCC
0.16
A697
NCC
1.01
A1689
CC
0.05
A611
NCC
0.12
A750
NCC
0.35
A1763
NCC
0.98

Figure B-2:

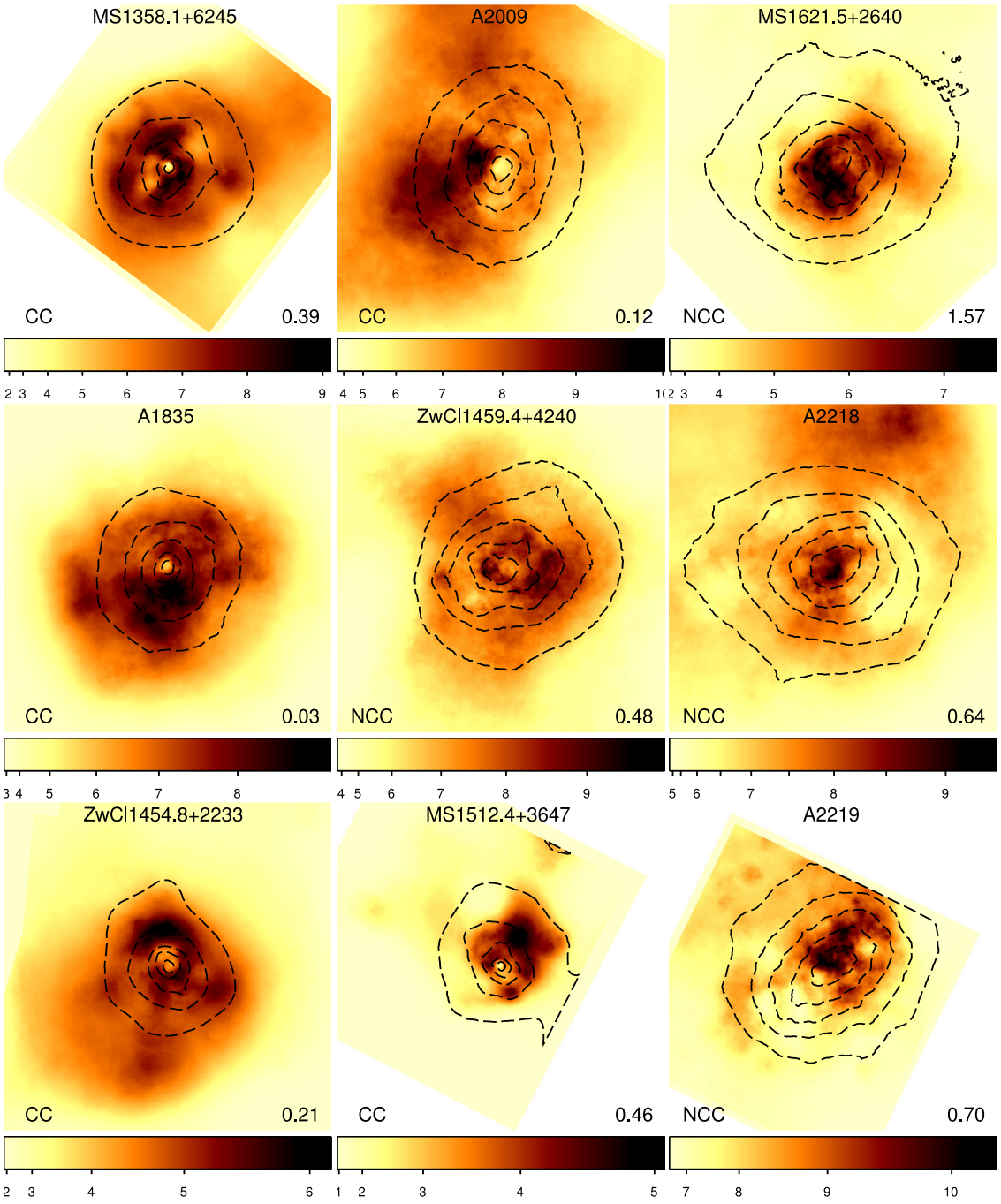
MS1358.1+6245
CC
0.39
2 3 4 5 6 7 8 9
A2009
CC
0.12
4 5 6 7 8 9 10
MS1621.5+2640
NCC
1.57
2 3 4 5 6 7
A1835
CC
0.03
3 4 5 6 7 8
ZwCl1459.4+4240
NCC
0.48
4 5 6 7 8 9
A2218
NCC
0.64
5 6 7 8 9
ZwCl1454.8+2233
CC
0.21
2 3 4 5 6
MS1512.4+3647
CC
0.46
1 2 3 4 5
A2219
NCC
0.70
7 8 9 10

Figure B-2:

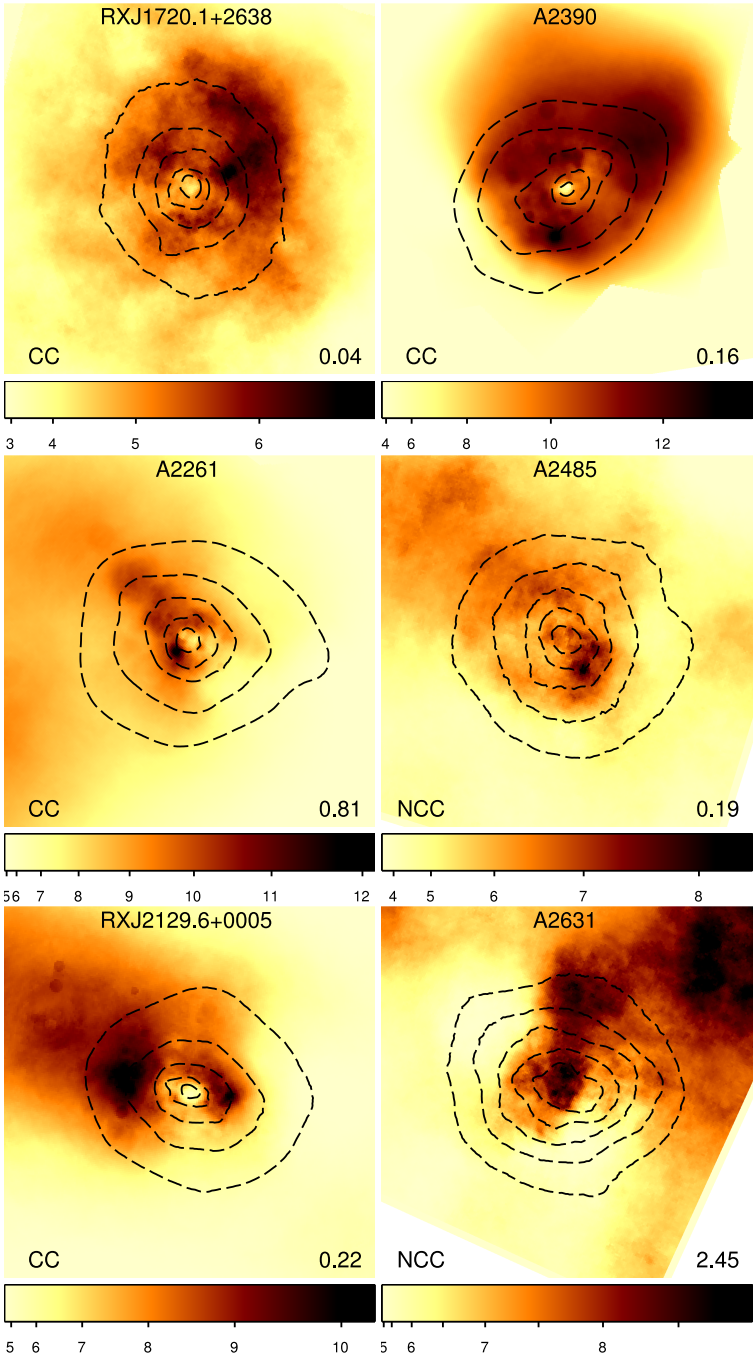
RXJ1720.1+2638
CC
0.04
3 4 5 6
A2390
CC
0.16
4 6 8 10 12
A2261
CC
0.81
56 7 8 9 10 11 12
A2485
NCC
0.19
4 5 6 7 8
RXJ2129.6+0005
CC
0.22
5 6 7 8 9 10
A2631
NCC
2.45
5 6 7 8

Figure B-2:

Bibliography

Abell, G. O. 1958, ApJS, 3, 211

Abell, G. O., Corwin, Jr., H. G., & Olowin, R. P. 1989, ApJS, 70, 1

Allen, S. W., Evrard, A. E., & Mantz, A. B. 2011, ArXiv e-prints

Allen, S. W., Rapetti, D. A., Schmidt, R. W., Ebeling, H., Morris, R. G., & Fabian, A. C. 2008, MNRAS, 383, 879

Allen, S. W., Schmidt, R. W., & Fabian, A. C. 2001, MNRAS, 328, L37

Allgood, B., Flores, R. A., Primack, J. R., Kravtsov, A. V., Wechsler, R. H., Faltenbacher, A., & Bullock, J. S. 2006, MNRAS, 367, 1781

Anders, E., & Grevesse, N. 1989, Geochim. Cosmochim. Acta, 53, 197

Andersson, K. 2007, Ph.D. Thesis, Stockholm University

Andersson, K., Benson, B. A., Ade, P. A. R., Aird, K. A., Armstrong, B., Bautz, M., Bleem, L. E., Brodwin, M., Carlstrom, J. E., Chang, C. L., Crawford, T. M., Crites, A. T., de Haan, T., Desai, S., Dobbs, M. A., Dudley, J. P., Foley, R. J., Forman, W. R., Garmire, G., George, E. M., Gladders, M. D., Halverson, N. W., High, F. W., Holder, G. P., Holzapfel, W. L., Hrubes, J. D., Jones, C., Joy, M., Keisler, R., Knox, L., Lee, A. T., Leitch, E. M., Lueker, M., Marrone, D. P., McMahon, J. J., Mehl, J., Meyer, S. S., Mohr, J. J., Montroy, T. E., Murray, S. S., Padin, S., Plagge, T., Pryke, C., Reichardt, C. L., Rest, A., Ruel, J., Ruhl, J. E., Schaffer, K. K., Shaw, L., Shirokoff, E., Song, J., Spieler, H. G., Stalder, B., Staniszewski, Z., Stark, A. A., Stubbs, C. W., Vanderlinde, K., Vieira, J. D., Vikhlinin, A., Williamson, R., Yang, Y., & Zahn, O. 2010, ArXiv e-prints

Andersson, K., Peterson, J. R., & Madejski, G. 2007, ApJ, 670, 1010

Andersson, K., Peterson, J. R., Madejski, G., & Goobar, A. 2009, ApJ, 696, 1029

Andersson, K. E., & Madejski, G. M. 2004, ApJ, 607, 190

Arabadjis, J. S., Bautz, M. W., & Arabadjis, G. 2004, ApJ, 617, 303

Arnaud, K. A. 1996, in Astronomical Society of the Pacific Conference Series, Vol. 101, Astronomical Data Analysis Software and Systems V, ed. G. H. Jacoby & J. Barnes, 17–+

Arnaud, M., Pointecouteau, E., & Pratt, G. W. 2005, A&A, 441, 893

Arnaud, M., Pratt, G. W., Piffaretti, R., Böhringer, H., Croston, J. H., & Pointecouteau, E. 2010, A&A, 517, A92+

Baltz, E. A., Marshall, P., & Oguri, M. 2009, J. Cosmology Astropart. Phys., 1, 15

Bardeau, S., Kneib, J.-P., Czoske, O., Soucail, G., Smail, I., Ebeling, H., & Smith, G. P. 2005, A&A, 434, 433

Barkana, R., & Loeb, A. 2010, MNRAS, 405, 1969

Barrena, R., Boschin, W., Girardi, M., & Spolaor, M. 2007, A&A, 469, 861

Bartelmann, M., & Schneider, P. 2001, Phys. Rep., 340, 291

Becker, M. R., & Kravtsov, A. V. 2010, ArXiv e-prints

Bett, P., Eke, V., Frenk, C. S., Jenkins, A., Helly, J., & Navarro, J. 2007, MNRAS, 376, 215

Bildfell, C., Hoekstra, H., Babul, A., & Mahdavi, A. 2008, MNRAS, 389, 1637

Binney, J., & Tremaine, S. 1987, Galactic dynamics, ed. Binney, J. & Tremaine, S.

Blumenthal, G. R., Faber, S. M., Flores, R., & Primack, J. R. 1986, ApJ, 301, 27

Böhringer, H., Pratt, G. W., Arnaud, M., Borgani, S., Croston, J. H., Ponman, T. J., Ameglio, S., Temple, R. F., & Dolag, K. 2010, A&A, 514, A32+

Böhringer, H., Schuecker, P., Guzzo, L., Collins, C. A., Voges, W., Cruddace, R. G., Ortiz-Gil, A., Chincarini, G., De Grandi, S., Edge, A. C., MacGillivray, H. T., Neumann, D. M., Schindler, S., & Shaver, P. 2004, A&A, 425, 367

Bond, J. R., Cole, S., Efstathiou, G., & Kaiser, N. 1991, ApJ, 379, 440

Borgani, S., Rosati, P., Tozzi, P., Stanford, S. A., Eisenhardt, P. R., Lidman, C., Holden, B., Della Ceca, R., Norman, C., & Squires, G. 2001, ApJ, 561, 13

Bower, R. G. 1991, MNRAS, 248, 332

Bradt, H., Mayer, W., Naranan, S., Rappaport, S., & Spada, G. 1967, ApJ, 150, L199+

Broadhurst, T., Benítez, N., Coe, D., Sharon, K., Zekser, K., White, R., Ford, H., Bouwens, R., Blakeslee, J., Clampin, M., Cross, N., Franx, M., Frye, B., Hartig, G., Illingworth, G., Infante, L., Menanteau, F., Meurer, G., Postman, M., Ardila, D. R., Bartko, F., Brown, R. A., Burrows, C. J., Cheng, E. S., Feldman, P. D., Golimowski, D. A., Goto, T., Gronwall, C., Herranz, D., Holden, B., Homeier, N., Krist, J. E., Lesser, M. P., Martel, A. R., Miley, G. K., Rosati, P., Sirianni, M., Sparks, W. B., Steindling, S., Tran, H. D., Tsvetanov, Z. I., & Zheng, W. 2005a, ApJ, 621, 53

Broadhurst, T., Takada, M., Umetsu, K., Kong, X., Arimoto, N., Chiba, M., & Futamase, T. 2005b, ApJ, 619, L143

Bullock, J. S., Kolatt, T. S., Sigad, Y., Somerville, R. S., Kravtsov, A. V., Klypin, A. A., Primack, J. R., & Dekel, A. 2001, MNRAS, 321, 559

Buote, D. A., & Tsai, J. C. 1996, ApJ, 458, 27

Burles, S., Nollett, K. M., & Turner, M. S. 2001, ApJ, 552, L1

Busha, M. T., Evrard, A. E., Adams, F. C., & Wechsler, R. H. 2005, MNRAS, 363, L11

Byram, E. T., Chubb, T. A., & Friedman, H. 1966, Science, 152, 66

Carlberg, R. G., Yee, H. K. C., Ellingson, E., Morris, S. L., Abraham, R., Gravel, P., Pritchet, C. J., Smecker-Hane, T., Hartwick, F. D. A., Hesser, J. E., Hutchings, J. B., & Oke, J. B. 1997, ApJ, 485, L13+

Carlstrom, J. E., Holder, G. P., & Reese, E. D. 2002, ARA&A, 40, 643

Cash, W. 1979, ApJ, 228, 939

Cassano, R., Brunetti, G., Venturi, T., Setti, G., Dallacasa, D., Giacintucci, S., & Bardelli, S. 2008, A&A, 480, 687

Cavagnolo, K. W., Donahue, M., Voit, G. M., & Sun, M. 2008a, ApJ, 683, L107

—. 2008b, ApJ, 682, 821

Cavaliere, A., & Fusco-Femiano, R. 1978, A&A, 70, 677

Cen, R. 1997, ApJ, 485, 39

Churazov, E., Forman, W., Jones, C., Sunyaev, R., & Böhringer, H. 2004, MNRAS, 347, 29

Churazov, E., Forman, W., Vikhlinin, A., Tremaine, S., Gerhard, O., & Jones, C. 2008, MNRAS, 388, 1062

Clowe, D., De Lucia, G., & King, L. 2004, MNRAS, 350, 1038

Cole, S., Percival, W. J., Peacock, J. A., Norberg, P., Baugh, C. M., Frenk, C. S., Baldry, I., Bland-Hawthorn, J., Bridges, T., Cannon, R., Colless, M., Collins, C., Couch, W., Cross, N. J. G., Dalton, G., Eke, V. R., De Propris, R., Driver, S. P., Efstathiou, G., Ellis, R. S., Glazebrook, K., Jackson, C., Jenkins, A., Lahav, O., Lewis, I., Lumsden, S., Maddox, S., Madgwick, D., Peterson, B. A., Sutherland, W., & Taylor, K. 2005, MNRAS, 362, 505

Comerford, J. M., & Natarajan, P. 2007, MNRAS, 379, 190

Corless, V. L., & King, L. J. 2007, MNRAS, 380, 149

Corless, V. L., King, L. J., & Clowe, D. 2009, MNRAS, 393, 1235

Crain, R. A., Eke, V. R., Frenk, C. S., Jenkins, A., McCarthy, I. G., Navarro, J. F., & Pearce, F. R. 2007, MNRAS, 377, 41

Croston, J. H., Pratt, G. W., Böhringer, H., Arnaud, M., Pointecouteau, E., Ponman, T. J., Sanderson, A. J. R., Temple, R. F., Bower, R. G., & Donahue, M. 2008, A&A, 487, 431

Czoske, O. 2004, in IAU Colloq. 195: Outskirts of Galaxy Clusters: Intense Life in the Suburbs, ed. A. Diaferio, 183–187

De Grandi, S., & Molendi, S. 2002, ApJ, 567, 163

De Luca, A., & Molendi, S. 2004, A&A, 419, 837

Dickey, J. M., & Lockman, F. J. 1990, ARA&A, 28, 215

Dodelson, S. 2004, Phys. Rev. D, 70, 023008

Dolag, K., Borgani, S., Murante, G., & Springel, V. 2009, MNRAS, 399, 497

Dolag, K., Vazza, F., Brunetti, G., & Tormen, G. 2005, MNRAS, 364, 753

Duffy, A. R., Schaye, J., Kay, S. T., & Dalla Vecchia, C. 2008, MNRAS, 390, L64

Dunkley, J., Komatsu, E., Nolta, M. R., Spergel, D. N., Larson, D., Hinshaw, G., Page, L., Bennett, C. L., Gold, B., Jarosik, N., Weiland, J. L., Halpern, M., Hill, R. S., Kogut, A., Limon, M., Meyer, S. S., Tucker, G. S., Wollack, E., & Wright, E. L. 2009, ApJS, 180, 306

Ebeling, H., Edge, A. C., Allen, S. W., Crawford, C. S., Fabian, A. C., & Huchra, J. P. 2000, MNRAS, 318, 333

Ebeling, H., Edge, A. C., Bohringer, H., Allen, S. W., Crawford, C. S., Fabian, A. C., Voges, W., & Huchra, J. P. 1998, MNRAS, 301, 881

Ebeling, H., Voges, W., Bohringer, H., Edge, A. C., Huchra, J. P., & Briel, U. G. 1996, MNRAS, 281, 799

Einasto, J. 1965, Trudy Inst. Astrofiz. Alma-Ata, 51, 87

Eke, V. R., Cole, S., Frenk, C. S., & Patrick Henry, J. 1998, MNRAS, 298, 1145

Ettori, S., De Grandi, S., & Molendi, S. 2002, A&A, 391, 841

Ettori, S., Gastaldello, F., Leccardi, A., Molendi, S., Rossetti, M., Buote, D., & Meneghetti, M. 2010, A&A, 524, A68+

Ettori, S., Morandi, A., Tozzi, P., Balestra, I., Borgani, S., Rosati, P., Lovisari, L., & Terenziani, F. 2009, A&A, 501, 61

Evrard, A. E., Metzler, C. A., & Navarro, J. F. 1996, ApJ, 469, 494

Fabian, A. C., Sanders, J. S., Taylor, G. B., Allen, S. W., Crawford, C. S., Johnstone, R. M., & Iwasawa, K. 2006, MNRAS, 366, 417

Faltenbacher, A., Kravtsov, A. V., Nagai, D., & Gottlöber, S. 2005, MNRAS, 358, 139

Faltenbacher, A., & White, S. D. M. 2010, ApJ, 708, 469

Fang, T., Humphrey, P., & Buote, D. 2009, ApJ, 691, 1648

Felten, J. E., Gould, R. J., Stein, W. A., & Woolf, N. J. 1966, ApJ, 146, 955

Ferrari, C., Govoni, F., Schindler, S., Bykov, A. M., & Rephaeli, Y. 2008, Space Sci. Rev., 134, 93

Forman, W., Kellogg, E., Gursky, H., Tananbaum, H., & Giacconi, R. 1972, ApJ, 178, 309

Freedman, W. L., Madore, B. F., Gibson, B. K., Ferrarese, L., Kelson, D. D., Sakai, S., Mould, J. R., Kennicutt, Jr., R. C., Ford, H. C., Graham, J. A., Huchra, J. P., Hughes, S. M. G., Illingworth, G. D., Macri, L. M., & Stetson, P. B. 2001, ApJ, 553, 47

Fritz, G., Davidsen, A., Meekins, J. F., & Friedman, H. 1971, ApJ, 164, L81+

Frye, B. L., Coe, D., Bowen, D. V., Benítez, N., Broadhurst, T., Guhathakurta, P., Illingworth, G., Menanteau, F., Sharon, K., Lupton, R., Meylan, G., Zekser, K., Meurer, G., & Hurley, M. 2007, ApJ, 665, 921

Gao, L., Navarro, J. F., Cole, S., Frenk, C. S., White, S. D. M., Springel, V., Jenkins, A., & Neto, A. F. 2008, MNRAS, 387, 536

Gavazzi, R. 2005, A&A, 443, 793

Giacconi, R., Murray, S., Gursky, H., Kellogg, E., Schreier, E., & Tananbaum, H. 1972, ApJ, 178, 281

Giodini, S., Pierini, D., Finoguenov, A., Pratt, G. W., Boehringer, H., Leauthaud, A., Guzzo, L., Aussel, H., Bolzonella, M., Capak, P., Elvis, M., Hasinger, G., Ilbert, O., Kartaltepe, J. S., Koekemoer, A. M., Lilly, S. J., Massey, R., McCracken, H. J., Rhodes, J., Salvato, M., Sanders, D. B., Scoville, N. Z., Sasaki, S., Smolcic, V., Taniguchi, Y., Thompson, D., & the COSMOS Collaboration. 2009, ApJ, 703, 982

Gioia, I. M., Maccacaro, T., Schild, R. E., Wolter, A., Stocke, J. T., Morris, S. L., & Henry, J. P. 1990, ApJS, 72, 567

Girardi, M., Giuricin, G., Mardirossian, F., Mezzetti, M., & Boschin, W. 1998, ApJ, 505, 74

Gnedin, O. Y., Kravtsov, A. V., Klypin, A. A., & Nagai, D. 2004, ApJ, 616, 16

Gursky, H., Solinger, A., Kellogg, E. M., Murray, S., Tananbaum, H., Giacconi, R., & Cavaliere, A. 1972, ApJ, 173, L99+

Gutierrez, K., & Krawczynski, H. 2005, ApJ, 619, 161

Guy, J., Sullivan, M., Conley, A., Regnault, N., Astier, P., Balland, C., Basa, S., Carlberg, R. G., Fouchez, D., Hardin, D., Hook, I. M., Howell, D. A., Pain, R., Palanque-Delabrouille, N., Perrett, K. M., Pritchet, C. J., Rich, J., Ruhlmann-Kleider, V., Balam, D., Baumont, S., Ellis, R. S., Fabbro, S., Fakhouri, H. K., Fourmanoit, N., González-Gaitán, S., Graham, M. L., Hsiao, E., Kronborg, T., Lidman, C., Mourao, A. M., Perlmutter, S., Ripoche, P., Suzuki, N., & Walker, E. S. 2010, A&A, 523, A7+

Halkola, A., Seitz, S., & Pannella, M. 2006, MNRAS, 372, 1425

Hallman, E. J., Motl, P. M., Burns, J. O., & Norman, M. L. 2006, ApJ, 648, 852

Hashimoto, Y., Böhringer, H., Henry, J. P., Hasinger, G., & Szokoly, G. 2007, A&A, 467, 485

Hastings, W. K. 1970, Biometrika, 57, 97

Hennawi, J. F., Dalal, N., Bode, P., & Ostriker, J. P. 2007, ApJ, 654, 714

Henry, J. P., & Arnaud, K. A. 1991, ApJ, 372, 410

Heymans, C., Van Waerbeke, L., Bacon, D., Berge, J., Bernstein, G., Bertin, E., Bridle, S., Brown, M. L., Clowe, D., Dahle, H., Erben, T., Gray, M., Hetterscheidt, M., Hoekstra, H., Hudelot, P., Jarvis, M., Kuijken, K., Margoniner, V., Massey, R., Mellier, Y., Nakajima, R., Refregier, A., Rhodes, J., Schrabback, T., & Wittman, D. 2006, MNRAS, 368, 1323

Hicken, M., Wood-Vasey, W. M., Blondin, S., Challis, P., Jha, S., Kelly, P. L., Rest, A., & Kirshner, R. P. 2009, ApJ, 700, 1097

Hilbert, S., Hartlap, J., White, S. D. M., & Schneider, P. 2009, A&A, 499, 31

Hoekstra, H. 2001, A&A, 370, 743

—. 2003, MNRAS, 339, 1155

—. 2007, MNRAS, 379, 317

Hoekstra, H., Donahue, M., Conselice, C. J., McNamara, B. R., & Voit, G. M. 2011, ApJ, 726, 48

Hoekstra, H., Hartlap, J., Hilbert, S., & van Uitert, E. 2010, ArXiv e-prints

Host, O., Hansen, S. H., Piffaretti, R., Morandi, A., Ettori, S., Kay, S. T., & Valdarnini, R. 2009, ApJ, 690, 358

Ilbert, O., Arnouts, S., McCracken, H. J., Bolzonella, M., Bertin, E., Le Fèvre, O., Mellier, Y., Zamorani, G., Pellò, R., Iovino, A., Tresse, L., Le Brun, V., Bottini, D., Garilli, B., Maccagni, D., Picat, J. P., Scaramella, R., Scodeggio, M., Vettolani, G., Zanichelli, A., Adami, C., Bardelli, S., Cappi, A., Charlot, S., Ciliegi, P., Contini, T., Cucciati, O., Foucaud, S., Franzetti, P., Gavignaud, I., Guzzo, L., Marano, B., Marinoni, C., Mazure, A., Meneux, B., Merighi, R., Paltani, S., Pollo, A., Pozzetti, L., Radovich, M., Zucca, E., Bondi, M., Bongiorno, A., Busarello, G., de La Torre, S., Gregorini, L., Lamareille, F., Mathez, G., Merluzzi, P., Ripepi, V., Rizzo, D., & Vergani, D. 2006, A&A, 457, 841

Ilbert, O., Capak, P., Salvato, M., Aussel, H., McCracken, H. J., Sanders, D. B., Scoville, N., Kartaltepe, J., Arnouts, S., Le Floc'h, E., Mobasher, B., Taniguchi, Y., Lamareille, F., Leauthaud, A., Sasaki, S., Thompson, D., Zamojski, M., Zamorani, G., Bardelli, S., Bolzonella, M., Bongiorno, A., Brusa, M., Caputi, K. I., Carollo, C. M., Contini, T., Cook, R., Coppa, G., Cucciati, O., de la Torre, S., de Ravel, L., Franzetti, P., Garilli, B., Hasinger, G., Iovino, A., Kampczyk, P., Kneib, J.-P., Knobel, C., Kovac, K., Le Borgne, J. F., Le Brun, V., Fèvre, O. L., Lilly, S., Looper, D., Maier, C., Mainieri, V., Mellier, Y., Mignoli, M., Murayama, T., Pellò, R., Peng, Y., Pérez-Montero, E., Renzini, A., Ricciardelli, E., Schiminovich, D., Scodeggio, M., Shioya, Y., Silverman, J., Surace, J., Tanaka, M., Tasca, L., Tresse, L., Vergani, D., & Zucca, E. 2009, ApJ, 690, 1236

Jeltema, T. E., Canizares, C. R., Bautz, M. W., & Buote, D. A. 2005, ApJ, 624, 606

Jeltema, T. E., Hallman, E. J., Burns, J. O., & Motl, P. M. 2008, ApJ, 681, 167

Jing, Y. P., & Suto, Y. 2002, ApJ, 574, 538

Kaastra, J. S. 1992, Internal SRON-Leiden Report

Kaastra, J. S., Mewe, R., & Nieuwenhuijzen, H. 1996, in UV and X-ray Spectroscopy of Astrophysical and Laboratory Plasmas, ed. K. Yamashita & T. Watanabe, 411–414

Kaiser, C. R., Pavlovski, G., Pope, E. C. D., & Fangohr, H. 2005, MNRAS, 359, 493

Kaiser, N., & Squires, G. 1993, ApJ, 404, 441

Kawahara, H. 2010, ApJ, 719, 1926

Kawahara, H., Suto, Y., Kitayama, T., Sasaki, S., Shimizu, M., Rasia, E., & Dolag, K. 2007, ApJ, 659, 257

Kawaharada, M., Okabe, N., Umetsu, K., Takizawa, M., Matsushita, K., Fukazawa, Y., Hamana, T., Miyazaki, S., Nakazawa, K., & Ohashi, T. 2010, ApJ, 714, 423

Kazantzidis, S., Kravtsov, A. V., Zentner, A. R., Allgood, B., Nagai, D., & Moore, B. 2004, ApJ, 611, L73

Kellogg, E., Gursky, H., Tananbaum, H., Giacconi, R., & Pounds, K. 1972, ApJ, 174, L65+

Kessler, R., Becker, A. C., Cinabro, D., Vanderplas, J., Frieman, J. A., Marriner, J., Davis, T. M., Dilday, B., Holtzman, J., Jha, S. W., Lampeitl, H., Sako, M., Smith, M., Zheng, C., Nichol, R. C., Bassett, B., Bender, R., Depoy, D. L., Doi, M., Elson, E., Filippenko, A. V., Foley, R. J., Garnavich, P. M., Hopp, U., Ihara, Y., Ketzeback, W., Kollatschny, W., Konishi, K., Marshall, J. L., McMillan, R. J., Miknaitis, G., Morokuma, T., Mörtsell, E., Pan, K., Prieto, J. L., Richmond, M. W., Riess, A. G., Romani, R., Schneider, D. P., Sollerman, J., Takanashi, N., Tokita, K., van der Heyden, K., Wheeler, J. C., Yasuda, N., & York, D. 2009, ApJS, 185, 32

King, L. J., Schneider, P., & Springel, V. 2001, A&A, 378, 748

Kirkman, D., Tytler, D., Suzuki, N., O'Meara, J. M., & Lubin, D. 2003, ApJS, 149, 1

Komatsu, E., Dunkley, J., Nolta, M. R., Bennett, C. L., Gold, B., Hinshaw, G., Jarosik, N., Larson, D., Limon, M., Page, L., Spergel, D. N., Halpern, M., Hill, R. S., Kogut, A., Meyer, S. S., Tucker, G. S., Weiland, J. L., Wollack, E., & Wright, E. L. 2009, ApJS, 180, 330

Komatsu, E., Smith, K. M., Dunkley, J., Bennett, C. L., Gold, B., Hinshaw, G., Jarosik, N., Larson, D., Nolta, M. R., Page, L., Spergel, D. N., Halpern, M., Hill, R. S., Kogut, A., Limon, M., Meyer, S. S., Odegard, N., Tucker, G. S., Weiland, J. L., Wollack, E., & Wright, E. L. 2011, ApJS, 192, 18

Kowalski, M., Rubin, D., Aldering, G., Agostinho, R. J., Amadon, A., Amanullah, R., Balland, C., Barbary, K., Blanc, G., Challis, P. J., Conley, A., Connolly, N. V., Covarrubias, R., Dawson, K. S., Deustua, S. E., Ellis, R., Fabbro, S., Fadeyev, V., Fan, X., Farris, B., Folatelli, G., Frye, B. L., Garavini, G., Gates, E. L., Germany, L., Goldhaber, G., Goldman, B., Goobar, A., Groom, D. E., Haissinski, J., Hardin, D., Hook, I., Kent, S., Kim, A. G., Knop, R. A., Lidman, C., Linder, E. V., Mendez, J., Meyers, J., Miller, G. J., Moniez, M., Mourão, A. M., Newberg, H.,

Nobili, S., Nugent, P. E., Pain, R., Perdereau, O., Perlmutter, S., Phillips, M. M., Prasad, V., Quimby, R., Regnault, N., Rich, J., Rubenstein, E. P., Ruiz-Lapuente, P., Santos, F. D., Schaefer, B. E., Schommer, R. A., Smith, R. C., Soderberg, A. M., Spadafora, A. L., Strolger, L.-G., Strovink, M., Suntzeff, N. B., Suzuki, N., Thomas, R. C., Walton, N. A., Wang, L., Wood-Vasey, W. M., & Yun, J. L. 2008, ApJ, 686, 749

Kravtsov, A. V., Vikhlinin, A., & Nagai, D. 2006, ApJ, 650, 128

Kuntz, K. D., & Snowden, S. L. 2000, ApJ, 543, 195

Lacey, C., & Cole, S. 1993, MNRAS, 262, 627

Landi, E., Del Zanna, G., Young, P. R., Dere, K. P., Mason, H. E., & Landini, M. 2006, ApJS, 162, 261

Lau, E. T., Kravtsov, A. V., & Nagai, D. 2009, ApJ, 705, 1129

Lau, E. T., Nagai, D., Kravtsov, A. V., & Zentner, A. R. 2010, ArXiv e-prints

Leccardi, A., & Molendi, S. 2007, A&A, 472, 21

—. 2008, A&A, 486, 359

Lemze, D., Barkana, R., Broadhurst, T. J., & Rephaeli, Y. 2008a, MNRAS, 386, 1092

Lemze, D., Broadhurst, T., Rephaeli, Y., Barkana, R., & Umetsu, K. 2008b, ArXiv e-prints

Lemze, D., Rephaeli, Y., Barkana, R., Broadhurst, T., Wagner, R., & Norman, M. L. 2011, ApJ, 728, 40

Liedahl, D. A., Osterheld, A. L., & Goldstein, W. H. 1995, ApJ, 438, L115

Limousin, M., Richard, J., Jullo, E., Kneib, J.-P., Fort, B., Soucail, G., Elíasdóttir, Á., Natarajan, P., Ellis, R. S., Smail, I., Czoske, O., Smith, G. P., Hudelot, P., Bardeau, S., Ebeling, H., Egami, E., & Knudsen, K. K. 2007, ApJ, 668, 643

Lin, W. P., Jing, Y. P., Mao, S., Gao, L., & McCarthy, I. G. 2006, ApJ, 651, 636

Łokas, E. L., Prada, F., Wojtak, R., Moles, M., & Gottlöber, S. 2006, MNRAS, 366, L26

Mahdavi, A., Hoekstra, H., Babul, A., & Henry, J. P. 2008, MNRAS, 384, 1567

Mandelbaum, R., Seljak, U., Baldauf, T., & Smith, R. E. 2010, MNRAS, 405, 2078

Mantz, A., & Allen, S. W. 2011, ArXiv e-prints

Mantz, A., Allen, S. W., Ebeling, H., Rapetti, D., & Drlica-Wagner, A. 2010a, MNRAS, 406, 1773

Mantz, A., Allen, S. W., Rapetti, D., & Ebeling, H. 2010b, MNRAS, 406, 1759

Markevitch, M., Bautz, M. W., Biller, B., Butt, Y., Edgar, R., Gaetz, T., Garmire, G., Grant, C. E., Green, P., Juda, M., Plucinsky, P. P., Schwartz, D., Smith, R., Vikhlinin, A., Virani, S., Wargelin, B. J., & Wolk, S. 2003, ApJ, 583, 70

Markevitch, M., Gonzalez, A. H., David, L., Vikhlinin, A., Murray, S., Forman, W., Jones, C., & Tucker, W. 2002, ApJ, 567, L27

Markevitch, M., & Vikhlinin, A. 2007, Phys. Rep., 443, 1

Massey, R., Heymans, C., Bergé, J., Bernstein, G., Bridle, S., Clowe, D., Dahle, H., Ellis, R., Erben, T., Hetterscheidt, M., High, F. W., Hirata, C., Hoekstra, H., Hudelot, P., Jarvis, M., Johnston, D., Kuijken, K., Margoniner, V., Mandelbaum, R., Mellier, Y., Nakajima, R., Paulin-Henriksson, S., Peeples, M., Roat, C., Refregier, A., Rhodes, J., Schrabback, T., Schirmer, M., Seljak, U., Semboloni, E., & van Waerbeke, L. 2007, MNRAS, 376, 13

Mathiesen, B., Evrard, A. E., & Mohr, J. J. 1999, ApJ, 520, L21

Mathiesen, B. F., & Evrard, A. E. 2001, ApJ, 546, 100

Maughan, B. J., Jones, C., Forman, W., & Van Speybroeck, L. 2008, ApJS, 174, 117

Mazzotta, P., Rasia, E., Moscardini, L., & Tormen, G. 2004, MNRAS, 354, 10

McNamara, B. R., Nulsen, P. E. J., Wise, M. W., Rafferty, D. A., Carilli, C., Sarazin, C. L., & Blanton, E. L. 2005, Nature, 433, 45

Meekins, J. F., Fritz, G., Chubb, T. A., & Friedman, H. 1971, Nature, 231, 107

Meneghetti, M., Rasia, E., Merten, J., Bellagamba, F., Ettori, S., Mazzotta, P., Dolag, K., & Marri, S. 2010, A&A, 514, A93+

Merritt, D., Graham, A. W., Moore, B., Diemand, J., & Terzić, B. 2006, AJ, 132, 2685

Messier, C. 1784, Connaissance des Temps (Paris)

Metropolis, N., Rosenbluth, A. W., Rosenbluth, M. N., Teller, A. H., & Teller, E. 1953, J. Chem. Phys., 21, 1087

Metzler, C. A., White, M., & Loken, C. 2001, ApJ, 547, 560

Mewe, R., Gronenschild, E. H. B. M., & van den Oord, G. H. J. 1985, A&AS, 62, 197

Mewe, R., Lemen, J. R., & van den Oord, G. H. J. 1986, A&AS, 65, 511

Miller, E. D., Tsunemi Hiroshi, Bautz, M. W., McCammon, D., Fujimoto, R., Hughes, J. P., Katsuda, S., Kokubun, M., Mitsuda, K., Porter, F. S., Takei, Y., Tsuboi, Y., & Yamasaki, N. Y. 2008, PASJ, 60, 95

Miralda-Escude, J., & Babul, A. 1995, ApJ, 449, 18

Mitchell, R. J., Culhane, J. L., Davison, P. J. N., & Ives, J. C. 1976, MNRAS, 175, 29P

Mohr, J. J., Mathiesen, B., & Evrard, A. E. 1999, ApJ, 517, 627

Nagai, D., Kravtsov, A. V., & Vikhlinin, A. 2007a, ApJ, 668, 1

Nagai, D., Vikhlinin, A., & Kravtsov, A. V. 2007b, ApJ, 655, 98

Navarro, J. F., Frenk, C. S., & White, S. D. M. 1995, MNRAS, 275, 720

—. 1996, ApJ, 462, 563

—. 1997, ApJ, 490, 493

Navarro, J. F., Hayashi, E., Power, C., Jenkins, A. R., Frenk, C. S., White, S. D. M., Springel, V., Stadel, J., & Quinn, T. R. 2004, MNRAS, 349, 1039

Navarro, J. F., & White, S. D. M. 1993, MNRAS, 265, 271

Nevalainen, J., David, L., & Guainazzi, M. 2010, A&A, 523, A22+

Nevalainen, J., Markevitch, M., & Lumb, D. 2005, ApJ, 629, 172

Oguri, M., & Blandford, R. D. 2009, MNRAS, 392, 930

Oguri, M., & Hamana, T. 2011, ArXiv e-prints

Oguri, M., Takada, M., Okabe, N., & Smith, G. P. 2010, MNRAS, 405, 2215

Oguri, M., Takada, M., Umetsu, K., & Broadhurst, T. 2005, ApJ, 632, 841

Okabe, N., Takada, M., Umetsu, K., Futamase, T., & Smith, G. P. 2010, PASJ, 62, 811

Pearce, F. R., Thomas, P. A., & Couchman, H. M. P. 1994, MNRAS, 268, 953

Peebles, P. J. E., & Yu, J. T. 1970, ApJ, 162, 815

Peng, E.-H., Andersson, K., Bautz, M. W., & Garmire, G. P. 2009, ApJ, 701, 1283

Percival, W. J., Nichol, R. C., Eisenstein, D. J., Weinberg, D. H., Fukugita, M., Pope, A. C., Schneider, D. P., Szalay, A. S., Vogeley, M. S., Zehavi, I., Bahcall, N. A., Brinkmann, J., Connolly, A. J., Loveday, J., & Meiksin, A. 2007, ApJ, 657, 51

Percival, W. J., Reid, B. A., Eisenstein, D. J., Bahcall, N. A., Budavari, T., Frieman, J. A., Fukugita, M., Gunn, J. E., Ivezić, Ž., Knapp, G. R., Kron, R. G., Loveday, J., Lupton, R. H., McKay, T. A., Meiksin, A., Nichol, R. C., Pope, A. C., Schlegel, D. J., Schneider, D. P., Spergel, D. N., Stoughton, C., Strauss, M. A., Szalay, A. S., Tegmark, M., Vogeley, M. S., Weinberg, D. H., York, D. G., & Zehavi, I. 2010, MNRAS, 401, 2148

Perlmutter, S., Aldering, G., Goldhaber, G., Knop, R. A., Nugent, P., Castro, P. G., Deustua, S., Fabbro, S., Goobar, A., Groom, D. E., Hook, I. M., Kim, A. G., Kim, M. Y., Lee, J. C., Nunes, N. J., Pain, R., Pennypacker, C. R., Quimby, R., Lidman, C., Ellis, R. S., Irwin, M., McMahon, R. G., Ruiz-Lapuente, P., Walton, N., Schaefer, B., Boyle, B. J., Filippenko, A. V., Matheson, T., Fruchter, A. S., Panagia, N., Newberg, H. J. M., Couch, W. J., & The Supernova Cosmology Project. 1999, ApJ, 517, 565

Peterson, J. R., Marshall, P. J., & Andersson, K. 2007, ApJ, 655, 109

Piffaretti, R., Jetzer, P., & Schindler, S. 2003, A&A, 398, 41

Poole, G. B., Fardal, M. A., Babul, A., McCarthy, I. G., Quinn, T., & Wadsley, J. 2006, MNRAS, 373, 881

Prada, F., Klypin, A. A., Simonneau, E., Betancort-Rijo, J., Patiri, S., Gottlöber, S., & Sanchez-Conde, M. A. 2006, ApJ, 645, 1001

Pratt, G. W., Arnaud, M., Piffaretti, R., Böhringer, H., Ponman, T. J., Croston, J. H., Voit, G. M., Borgani, S., & Bower, R. G. 2010, A&A, 511, A85+

Pratt, G. W., Böhringer, H., Croston, J. H., Arnaud, M., Borgani, S., Finoguenov, A., & Temple, R. F. 2007, A&A, 461, 71

Press, W. H., & Schechter, P. 1974, ApJ, 187, 425

Press, W. H., Teukolsky, S. A., Vetterling, W. T., & Flannery, B. P. 1992, Numerical recipes in FORTRAN. The art of scientific computing, ed. Press, W. H., Teukolsky, S. A., Vetterling, W. T., & Flannery, B. P.

Protassov, R., van Dyk, D. A., Connors, A., Kashyap, V. L., & Siemiginowska, A. 2002, ApJ, 571, 545

Rafferty, D. A., McNamara, B. R., & Nulsen, P. E. J. 2008, ApJ, 687, 899

Rasia, E., Ettori, S., Moscardini, L., Mazzotta, P., Borgani, S., Dolag, K., Tormen, G., Cheng, L. M., & Diaferio, A. 2006, MNRAS, 369, 2013

Rasia, E., Tormen, G., & Moscardini, L. 2004, MNRAS, 351, 237

Raymond, J. C., & Smith, B. W. 1977, ApJS, 35, 419

Reiprich, T. H., & Böhringer, H. 2002, ApJ, 567, 716

Reynolds, C. S., McKernan, B., Fabian, A. C., Stone, J. M., & Vernaleo, J. C. 2005, MNRAS, 357, 242

Richard, J., Smith, G. P., Kneib, J., Ellis, R. S., Sanderson, A. J. R., Pei, L., Targett, T. A., Sand, D. J., Swinbank, A. M., Dannerbauer, H., Mazzotta, P., Limousin, M., Egami, E., Jullo, E., Hamilton-Morris, V., & Moran, S. M. 2010, MNRAS, 404, 325

Riemer-Sørensen, S., Paraficz, D., Ferreira, D. D. M., Pedersen, K., Limousin, M., & Dahle, H. 2009, ApJ, 693, 1570

Riess, A. G., Filippenko, A. V., Challis, P., Clocchiatti, A., Diercks, A., Garnavich, P. M., Gilliland, R. L., Hogan, C. J., Jha, S., Kirshner, R. P., Leibundgut, B., Phillips, M. M., Reiss, D., Schmidt, B. P., Schommer, R. A., Smith, R. C., Spyromilio, J., Stubbs, C., Suntzeff, N. B., & Tonry, J. 1998, AJ, 116, 1009

Riess, A. G., Macri, L., Casertano, S., Sosey, M., Lampeitl, H., Ferguson, H. C., Filippenko, A. V., Jha, S. W., Li, W., Chornock, R., & Sarkar, D. 2009, ApJ, 699, 539

Sanders, J. S., & Fabian, A. C. 2001, MNRAS, 325, 178

—. 2002, MNRAS, 331, 273

—. 2007, MNRAS, 381, 1381

Sanders, J. S., Fabian, A. C., & Smith, R. K. 2010, MNRAS, 1534

Sanderson, A. J. R., Edge, A. C., & Smith, G. P. 2009, MNRAS, 398, 1698

Sanderson, A. J. R., & Ponman, T. J. 2010, MNRAS, 402, 65

Sanderson, A. J. R., Ponman, T. J., Finoguenov, A., Lloyd-Davies, E. J., & Markevitch, M. 2003, MNRAS, 340, 989

Sarazin, C. L. 1988, X-ray emission from clusters of galaxies (Cambridge Astrophysics Series, Cambridge: Cambridge University Press, 1988)

Schuecker, P., Böhringer, H., Collins, C. A., & Guzzo, L. 2003, A&A, 398, 867

Sehgal, N., Trac, H., Acquaviva, V., Ade, P. A. R., Aguirre, P., Amiri, M., Appel, J. W., Barrientos, L. F., Battistelli, E. S., Bond, J. R., Brown, B., Burger, B., Chervenak, J., Das, S., Devlin, M. J., Dicker, S. R., Bertrand Doriese, W., Dunkley, J., Dünner, R., Essinger-Hileman, T., Fisher, R. P., Fowler, J. W., Hajian, A., Halpern, M., Hasselfield, M., Hernández-Monteagudo, C., Hilton, G. C., Hilton, M., Hincks, A. D., Hlozek, R., Holtz, D., Huffenberger, K. M., Hughes, D. H., Hughes, J. P., Infante, L., Irwin, K. D., Jones, A., Baptiste Juin, J., Klein, J., Kosowsky, A., Lau, J. M., Limon, M., Lin, Y.-T., Lupton, R. H., Marriage, T. A., Marsden, D., Martocci, K., Mauskopf, P., Menanteau, F., Moodley, K., Moseley, H., Netterfield, C. B., Niemack, M. D., Nolta, M. R., Page, L. A., Parker, L., Partridge, B., Reid, B., Sherwin, B. D., Sievers, J., Spergel, D. N., Staggs, S. T., Swetz, D. S., Switzer, E. R., Thornton, R., Tucker, C., Warne, R., Wollack, E., & Zhao, Y. 2011, ApJ, 732, 44

Serlemitsos, P. J., Smith, B. W., Boldt, E. A., Holt, S. S., & Swank, J. H. 1977, ApJ, 211, L63

Shaw, L. D., Weller, J., Ostriker, J. P., & Bode, P. 2006, ApJ, 646, 815

Sijacki, D., & Springel, V. 2006, MNRAS, 371, 1025

Silk, J. 1968, ApJ, 151, 459

Simionescu, A., Allen, S. W., Mantz, A., Werner, N., Takei, Y., Morris, R. G., Fabian, A. C., Sanders, J. S., Nulsen, P. E. J., George, M. R., & Taylor, G. B. 2011, Science, 331, 1576

Smith, G. P., Khosroshahi, H. G., Dariush, A., Sanderson, A. J. R., Ponman, T. J., Stott, J. P., Haines, C. P., Egami, E., & Stark, D. P. 2010, MNRAS, 409, 169

Smith, R. K., Bautz, M. W., Edgar, R. J., Fujimoto, R., Hamaguchi, K., Hughes, J. P., Ishida, M., Kelley, R., Kilbourne, C. A., Kuntz, K. D., McCammon, D., Miller, E., Mitsuda, K., Mukai, K., Plucinsky, P. P., Porter, F. S., Snowden, S. L., Takei, Y., Terada, Y., Tsuboi, Y., & Yamasaki, N. Y. 2007, PASJ, 59, 141

Smith, R. K., Brickhouse, N. S., Liedahl, D. A., & Raymond, J. C. 2001, ApJ, 556, L91

Spergel, D. N., Verde, L., Peiris, H. V., Komatsu, E., Nolta, M. R., Bennett, C. L., Halpern, M., Hinshaw, G., Jarosik, N., Kogut, A., Limon, M., Meyer, S. S., Page, L., Tucker, G. S., Weiland, J. L., Wollack, E., & Wright, E. L. 2003, ApJS, 148, 175

Stanek, R., Evrard, A. E., Böhringer, H., Schuecker, P., & Nord, B. 2006, ApJ, 648, 956

Stott, J. P., Edge, A. C., Smith, G. P., Swinbank, A. M., & Ebeling, H. 2008, MNRAS, 384, 1502

Sun, M., Sehgal, N., Voit, G. M., Donahue, M., Jones, C., Forman, W., Vikhlinin, A., & Sarazin, C. 2010, ArXiv e-prints

Sun, M., Voit, G. M., Donahue, M., Jones, C., Forman, W., & Vikhlinin, A. 2009, ApJ, 693, 1142

Sunyaev, R. A., & Zeldovich, Y. B. 1970, Ap&SS, 7, 3

—. 1972, Comments on Astrophysics and Space Physics, 4, 173

Tyson, J. A., Wenk, R. A., & Valdes, F. 1990, ApJ, 349, L1

Umetsu, K., & Broadhurst, T. 2008, ApJ, 684, 177

Umetsu, K., Broadhurst, T., Zitrin, A., Medezinski, E., Coe, D., & Postman, M. 2011, ArXiv e-prints

Valdarnini, R. 2006, New A, 12, 71

Vazza, F., Brunetti, G., Kritsuk, A., Wagner, R., Gheller, C., & . Norman, M. 2009, ArXiv e-prints

Venturi, T., Giacintucci, S., Dallacasa, D., Cassano, R., Brunetti, G., Bardelli, S., & Setti, G. 2008, A&A, 484, 327

Vikhlinin, A. 2006, ApJ, 640, 710

Vikhlinin, A., Burenin, R., Forman, W. R., Jones, C., Hornstrup, A., Murray, S. S., & Quintana, H. 2007, in Heating versus Cooling in Galaxies and Clusters of Galaxies, ed. H. Böhringer, G. W. Pratt, A. Finoguenov, & P. Schuecker , 48–+

Vikhlinin, A., Burenin, R. A., Ebeling, H., Forman, W. R., Hornstrup, A., Jones, C., Kravtsov, A. V., Murray, S. S., Nagai, D., Quintana, H., & Voevodkin, A. 2009a, ApJ, 692, 1033

Vikhlinin, A., Forman, W., & Jones, C. 1999, ApJ, 525, 47

Vikhlinin, A., Kravtsov, A., Forman, W., Jones, C., Markevitch, M., Murray, S. S., & Van Speybroeck, L. 2006, ApJ, 640, 691

Vikhlinin, A., Kravtsov, A. V., Burenin, R. A., Ebeling, H., Forman, W. R., Hornstrup, A., Jones, C., Murray, S. S., Nagai, D., Quintana, H., & Voevodkin, A. 2009b, ApJ, 692, 1060

Vikhlinin, A., Markevitch, M., Murray, S. S., Jones, C., Forman, W., & Van Speybroeck, L. 2005, ApJ, 628, 655

Vikhlinin, A., Voevodkin, A., Mullis, C. R., van Speybroeck, L., Quintana, H., McNamara, B. R., Gioia, I., Hornstrup, A., Henry, J. P., Forman, W. R., & Jones, C. 2003, ApJ, 590, 15

Voevodkin, A., & Vikhlinin, A. 2004, ApJ, 601, 610

Werner, N., Zhuravleva, I., Churazov, E., Simionescu, A., Allen, S. W., Forman, W., Jones, C., & Kaastra, J. S. 2009, MNRAS, 398, 23

White, S. D. M., Navarro, J. F., Evrard, A. E., & Frenk, C. S. 1993, Nature, 366, 429

Xue, S.-J., & Wu, X.-P. 2002, ApJ, 576, 152

Yee, H. K. C., Ellingson, E., & Carlberg, R. G. 1996, ApJS, 102, 269

Young, O. E., Thomas, P. A., Short, C. J., & Pearce, F. 2011, MNRAS, 413, 691

Zhang, Y., Okabe, N., Finoguenov, A., Smith, G. P., Piffaretti, R., Valdarnini, R., Babul, A., Evrard, A. E., Mazzotta, P., Sanderson, A. J. R., & Marrone, D. P. 2010, ApJ, 711, 1033

Zwicky, F. 1933, Helvetica Physica Acta, 6, 110

—. 1937, ApJ, 86, 217